Technische Universität München
Fakultät für Maschinenwesen
Lehrstuhl für Aerodynamik und Strömungsmechanik

Interference Effects in Automotive, Open Jet Wind Tunnels

Christopher Collin

Vollständiger Abdruck der von der Fakultät für Maschinenwesen
der Technischen Universität München zur Erlangung des akademischen Grades
eines Doktor-Ingenieurs (Dr.-Ing.) genehmigten Dissertation.

Vorsitzender: Prof. Dr.-Ing. Florian Holzapfel

Prüfende der Dissertation:

1. Priv.-Doz. Dr.-Ing. habil. Thomas Indinger
2. Prof. Dr.-Ing. Jochen Wiedemann

Die Dissertation wurde am 23.01.2019 bei der Technischen Universität
München eingereicht und durch die Fakultät für Maschinenwesen
am 03.07.2019 angenommen.

— *"Talk about a dream, try to make it real"* —
(Bruce Springsteen)

Preface

The present work is the result of a collaboration of the Technical University of Munich and the AUDI AG, Ingolstadt. The common target was to achieve a better understanding about interference effects in automotive, open jet wind tunnels in order improve the accuracy of aerodynamic data from wind tunnels and to draw better guidelines for new facilities. I would like to thank Prof. Dr.-Ing. Nikolaus A. Adams, PD Dr.-Ing. habil. Thomas Indinger, Dr. Stefan Dietz (AUDI AG) and Dr. Joerg Mueller (AUDI AG) for providing me with the opportunity to be part of such a challenging project. Furthermore, I would like to thank Robby Pyttel, Stefan Eyring and Dr.-Ing. Thomas Birkner from the wind tunnel project team at Audi for the great cooperation.

This thesis is based on the results from many wind tunnel measurements, CFD simulations and technical discussions. Therefore, I would like thank all my colleagues, who were involved. In particular, I am grateful to Dr. Gerhard Wickern, Prof. Dr. Jochen Wiedemann, Dr. Edzard Mercker for several discussions about correction methods for wind tunnels, to my colleagues Steffen Mack, Lukas Haag, Marco Kiewat, Wolfgang Lützenburg and my colleagues from the Audi wind tunnel and workshop for their support in wind tunnel measurements, to Dr. Stefan Blume for his support in CFD methods.

I would like to thank my family: my father Uwe Collin and my mother Silvia Collin. They always encouraged me with their trust and support. Last but not least, I thank all my close friends for their understanding and appreciation for such an intensive time of my life.

Abstract

The evaluation of open jet wind tunnel interferences in real facilities is challenging as the aerodynamic properties of the testing object in unlimited flow conditions are typically not sufficiently known. That is why many approaches on wind tunnel corrections are based on potential flow models. The present work provides new methods for the evaluation of nozzle, open jet, collector and moving ground interferences with CFD using *OpenFOAM®*. Therefore, the full scale DrivAer reference model with estateback, notchback and fastback and an Audi RS5 DTM race car were selected to be representative automotive bodies. The aerodynamic simulations on these models were performed in both open road and wind tunnel conditions. The investigations on nozzle interferences focused on nozzle parameters such as the blockage ratio in the range of 2.4 % to 19.7 %, the longitudinal distance between the nozzle exit and model center from 3 m to 9 m as well as on the nozzle and the plenum method of dynamic pressure determination. Parameters for the collector interferences were the collector cross-sectional area in the range of 1 to 5 nozzle areas, the collector flap angle from 0 ° to 30 ° and the test section length of up to 4.0 hydraulic nozzle diameters. The studies on moving ground interferences returned the moving belt dimensions required for the aerodynamic development of the selected race car. Based on the results for the interference effects under investigation, potential design recommendations for a modern automotive open jet test section were derived. Furthermore, an extended, potential flow model was developed in order to account for the effect of the open jet expansion. A better agreement of the new correction method with the CFD results was achieved compared to the classical solid blockage correction.

Excerpts of this work have been published in the following journals and proceedings:

Collin, C., Mack, S., Indinger, T., & Mueller, J. (2016). A Numerical and Experimental Evaluation of Open Jet Wind Tunnel Interferences using the DrivAer Reference Model. In *SAE Int. J. Passeng. Cars - Mech. Syst.* (Vol. 9; No. 2, pp. 657–679).

Collin, C., Indinger, T., & Mueller, J. (2017). Moving Ground Simulation for High Performance Race Cars in an Automotive Wind Tunnel. In *International Journal of Automotive Engineering* (Vol. 8; No. 1, p. 15-21).

Collin, C., Mueller, J., Islam, M., & Indinger, T. (2018). On the Influence of Underhood Flow on External Aerodynamics of the DrivAer Model. In J. Wiedemann (Ed.), *Progress in Vehicle Aerodynamics and Thermal Management: 11th FKFS Conference* (pp. 201–215). Cham: Springer International Publishing.

Hupertz, B., Krueger, L., Chalupa, K., Lewington, N., Luneman, B., Costa, P., Kuthada, T., & Collin, C. (2018). Introduction of a New Full-Scale Open Cooling Version of the DrivAer Generic Car Model. In J. Wiedemann (Ed.), *Progress in Vehicle Aerodynamics and Thermal Management: 11th FKFS Conference* (pp. 35–60). Cham: Springer International Publishing.

Contents

1 Introduction

Wind tunnel interferences in general have been known effects for more than a hundred years as Prandtl (1919) was one of the first to perform investigations on airfoils. Several studies followed in order to achieve a better knowledge about the requirement to apply corrections to testing data obtained in wind tunnels. On the one hand, these studies include different kinds of wind tunnel boundaries such as closed wall, open jet or mixed types. On the other hand, different properties of the testing object (model), e.g. streamlined and bluff bodies, were subject of extensive evaluations of interferences between the model and the wind tunnel boundaries. The present work focuses on the particular application of near-ground vehicles in open jet wind tunnels with moving ground simulation for the development of automotive aerodynamics[1].

1.1 Motivation

Experimental testing in wind tunnels is often the essential approach to develop automotive aerodynamics even though Computational Fluid Dynamics (CFD) have been showing a remarkable improvement in accuracy and turn-around time for the last decades. Wind tunnel measurements remain the method of choice if a large number of model configurations are desired to be tested within a short time. However, as old as wind tunnel testing itself surely is the consideration of wind tunnel interferences in order to obtain representative results. Lock (1929) was the first to introduce a correction formula to account for the effect of the solid blockage[2] on the effective tunnel velocity the model is exposed to. Lock's correction method accounts for the interferences between the model and the wind tunnel for both two- and three-dimensional applications in closed wall and open jet wind tunnels. Lock (1929) considers different tunnel geometries such as circular and rectangular wind tunnel nozzles as well as different shapes of symmetrical[3] models. The principle idea of Lock to extract a correction formula for a sphere and to use a model shape factor for different model geometries is adopted and extended by Glauert (1933) and Young and Squire (1945). Glauert (1933) introduces two additional phenomena. Firstly, the effect of virtual mass created by the displacement of volume due to the wake of the model and, secondly, the effect from a gradient of static pressure along the wind tunnel test section. Glauert considers the virtual mass of the wake as an additional model volume in order to calculate the model shape factor using Lock's approach. Furthermore, he

[1] Sometimes also called the $^3/_4$ open jet wind tunnel, e.g. see Deutenbach (1995).

[2] Solid blockage denotes the blockage of the test section due to the solid boundaries of the model and does not include the blockage effects of the re-circulation zone and wake downstream the model.

[3] The model is not mandatory symmetric in stream-wise but in lateral directions. Thus, the symmetric model treated by Lock (1929) denotes a zero lift configuration.

introduced a correction formula in order to account for the horizontal buoyancy[1] induced by a longitudinal pressure gradient.

Apart from the potential flow based approaches from e.g. Lock (1929), Glauert (1933) and Young and Squire (1945) an empirical method is presented by Maskell (1961) focusing on a correction method for bluff bodies[2]. Maskell's method is based on momentum balance considerations presenting a blockage correction for closed wall wind tunnels. Therefore, he includes the retrospective effect of the blockage-induced wake distortion on the rear end base pressure of bluff bodies.

Mercker (1986) presents a blockage correction for automotive bodies in closed wall test sections. Therefore, the approaches above are combined in order to apply corrections for the solid blockage and wake blockage to measurements of passenger cars. A correction method for the automotive, open jet test section is presented by Mercker and Wiedemann (1996). Therefore, the open jet expansion correction from Lock (1929) and the horizontal buoyancy correction from Glauert (1933) for pressure gradients are adopted by suggesting appropriate model shape factors for automotive bodies. Furthermore, Mercker and Wiedemann (1996) derive dynamic pressure corrections to account for interference effects involving the nozzle and the collector in open jet test sections. These include a nozzle blockage, collector blockage and a jet deflection correction (partially) based on potential flow considerations. A separate correction of the nozzle blockage for the nozzle and the plenum method of dynamic pressure adjustment are introduced by Mercker et al. (1997). Later, an alternative approach for the horizontal buoyancy correction due to static pressure gradients is presented by Mercker and Cooper (2006). The so-called "Two Measurement Correction" applies a horizontal buoyancy correction based on drag measurements in two wind tunnel configurations with different static pressure gradients.

An alternative approach for automotive, open jet wind tunnels is presented by Wickern (2001). Compared to the work of Mercker et al., the correction methods by Wickern are entirely based on potential flow models. Therefore, Wickern (2001) adopts the model of Lock (1929) in order to calculate the model shape factor for automotive bodies. Furthermore, Wickern and Schwartekopp (2004) introduce a potential flow model in order to account for the induced velocity and horizontal buoyancy effects due to the nozzle interference. Later, Wickern (2014) introduces the "Self-Correcting Open Jet Wind Tunnel" based on the compensation of the open jet and the nozzle interference by selecting an appropriate longitudinal model position along the test section.

It is worth to mention that many other techniques apart from theoretical models were applied in order to achieve a better understanding for wind tunnel interferences. For example, on-road testing is a wide-spread method to compare aerodynamic data obtained in wind tunnels, see e.g. Zaccariotto (1991), Le Good and Passmore (1994), Howell et al. (2002) and Lawson et al. (2007). Furthermore, wind tunnel correlation tests are performed

[1] In closed wall wind tunnels the horizontal buoyancy correction includes both the virtual mass and empty tunnel gradients.

[2] From aerodynamic aspects the flow around a bluff body is characterized by regions of detached and re-circulating flow (downstream the model). In contrast, the term "wake" denotes flow regions with a significant loss of momentum present for both streamlined and bluff bodies.

to compare the results for selected vehicles in different facilities, see e.g. Guertler (2000) and Hennig and Mercker (2011). As an example, Figure 1.1 illustrates the results from the latest EADE correlation test for the uncorrected drag coefficients ΔC_D of seven production cars including moving ground simulation. The curves still show some significant differences in the range of $|\Delta C_\mathrm{D}| \leq 0.015$ even though a large amount of research work was already performed on wind tunnel interferences. Thus, the requirement of sufficient wind tunnel corrections and design rules for new facilities is still present in order to bring aerodynamic results closer together.[1]

1.2 Objectives

Testing a model in a wind tunnel is, by definition, merely a simulation of the aerodynamic conditions of a "real" application. Fundamentally, this is caused due to the transformation of the reference system of a moving model in, ideally, still air towards a resting model surrounded by a moving air flow and moving floor for ground vehicles. Thus, the exact evaluation of wind tunnel interferences requires either the comparison of the wind tunnel results with the real application in order to apply corrections or to ensure the elimination of potential interferences by the design of the facility. However, firstly the measurement of aerodynamic forces is often difficult in the real application, at least with the desired accuracy of typically $\Delta C_\mathrm{D} \approx \pm 0.002$. Secondly, entirely eliminating interference effects in a facility substantially requires the limitation of the blockage conditions and, hence,

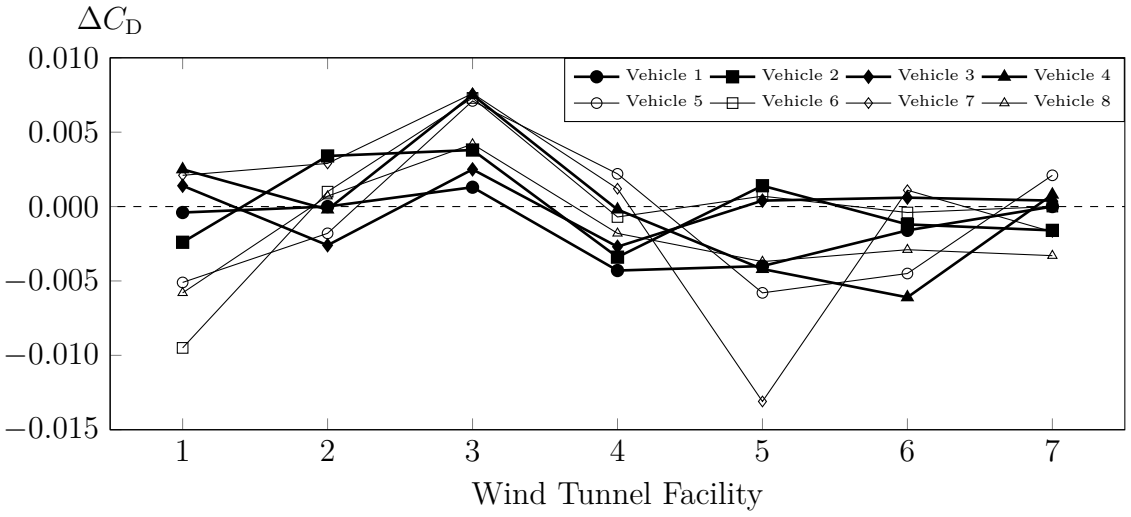

Figure 1.1: EADE Correlation Test 2011: Uncorrected drag coefficients ΔC_D for seven wind tunnel facilities compared to the average drag coefficient from all facilities. The curves represent seven selected vehicles in baseline configuration (with underhood flow) and moving ground simulation. The corresponding data is presented by Hennig and Mercker (2011).

[1] It is worth to mention, that existing correction methods already bring the results from Figure 1.1 closer together, see e.g. Hennig (2017) for more information.

certain minimum dimensions of the test section and its components. But what size, e.g. of a nozzle, is large enough to minimize interferences? In terms of a cost-effective development, is it reasonable to build a facility of that size or preferably apply corrections? Of course, the answers to these questions depend on the desired accuracy. Furthermore, the experimental evaluation of wind tunnel effects at realistic Reynolds-numbers is often restricted due to constructional limitations of a particular facility.

Compared to an experimental approach on a selected model, CFD offers the opportunity to vary the wind tunnel geometry and, hence, the blockage conditions within a larger range. Additionally, the simulations of a model at negligible blockage conditions is realizable in CFD by adjusting the size of the domain. Thus, the opportunity using CFD to compare both the flow field around the model and the resulting effects on the integral forces in wind tunnel and open road is expected to be a promising method to evaluate wind tunnel interferences. Furthermore, existing studies e.g. presented by Fischer et al. (2007), Fischer et al. (2010) and Hennig (2017) verify CFD to be a promising tool in order simulate wind tunnel aerodynamics of existing facilities.

Figure 1.1 shows that the results predicted in different wind tunnels significantly depend on the particular model geometry. That is why it is expected to be rather difficult to formulate a general rule valid for the whole range of automotive bodies. Nevertheless, it seems reasonable to classify automotive bodies with respect to some general shape properties, e.g. the rear end shape. For the present work, the DrivAer reference model was selected to serve as a rather detailed but generic vehicle geometry offering different rear end shapes. The DrivAer model is an open-source reference geometry for both research and industrial purposes. The geometry is available for download online at Technical University of Munich (2018). Heft et al. (2012) introduce the model as "a new realistic, generic car model for aerodynamic investigations". Since then, the model was adopted from different research institutions and industry. Both experimental and numerical investigations were applied to the model. After the upgrade of the large wind tunnel (WTA) of the Technical University of Munich (TUM) with moving ground simulation, presented by Mack et al. (2012), several aerodynamic tests were performed using a 40 % scale DrivAer model. Thus, experimental data is available in order to validate CFD.

The main objective of the present work is to achieve a better understanding of the essential interference effects in automotive, open jet wind tunnels using the DrivAer model in order to design a new facility. The past has shown, that real facilities offer a large number of potential sources, which may interfere with the model. That is why, the author focused on the interferences due to the wind tunnel nozzle and open jet, the collector and the moving ground simulation, which were estimated to be of the highest relevance. Essentially, the answers to the following questions were desired:

1. Which design rules are to be followed in order to either eliminate or confine interference effects?
2. In terms of a practical design, what are reasonable dimensions for a new facility?
3. In terms of a practical design, which wind tunnel corrections are necessary?

1.3 Approach and Structure

The general approach of the present work is illustrated in Figure 1.2. It contains the presentation of the state of the art (Chapter 2), three basic steps (Chapter 3-5) to achieve a better understanding for open jet wind tunnel interferences followed by a summary and suggestions for potential future work (Chapter 6).

Chapter 2 The state of the art towards the knowledge of interference effects in open jet wind tunnels is presented. It is well known, that wind tunnel interferences in general have been under investigation for more than a hundred years. Therefore, a description of the most essential aerodynamic interference effects in automotive, open jet wind tunnels and existing correction methods are presented.

Chapter 3 CFD was the tool to evaluate wind tunnel interferences. The numerical methods and the principle of the separation of interference effects are explained. Experimental data was produced in order to validate the numerical results for both the simulation of the flow around a vehicle and its interferences with a wind tunnel.

Chapter 4 The numerical model is applied to separate the effects of the nozzle and open jet, the collector and moving ground simulation on the model tested in an open jet test section. The studies were restricted to the DrivAer geometry and a limited amount of wind tunnel parameters.

Chapter 5 Existing wind tunnel corrections were extended towards a new correction method to account for additional effects connected to the open jet expansion. The correction models are compared to the CFD results. Finally, design criteria for potential facilities were derived.

Chapter 6 The most essential results of the present work are summarized and assessed with regard to the transfer-ability towards the design and correction of "real" facilities. Consequences and suggestions for potential future work are drawn in order to extend the range of parameters for wind tunnel studies.

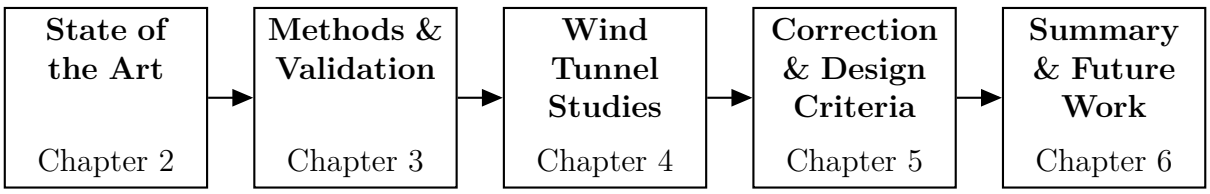

Figure 1.2: General approach of the present work.

2 Wind Tunnel Interferences and Corrections

Since the beginning of the 20th century the relevance of wind tunnel interferences has been observed in different technical applications of both aerodynamics and hydrodynamics. This includes investigations on conventional open jet and closed wall wind tunnels (classic closed wall and adaptive walls) as well as hybrid forms containing both solid and open test section boundaries. The present work focuses on interference effects in open jet wind tunnels for automotive aerodynamics. An overview of previous approaches is given in the current section. Therefore, the interferences under investigation are presented in Figure 2.1. An early general correction formula for the open jet interference is presented by Lock (1929) whereas Glauert (1933) was one of the first to work on an approach for the effects of empty test section gradients[1]. Both nozzle and collector interferences are introduced to be relevant for open jet test sections by Mercker and Wiedemann (1996). For these interferences the state of the art, namely the description and correction methods for the corresponding effect, is given. Of course, empty test section flow gradients are often associated with e.g. the nozzle or the collector, but treated separately here. It is worth to mention, that the current chapter does not cover the entire range of known wind tunnel interferences. Furthermore, the majority of correction methods is based on the assumption of an invariant flow under constraint wind tunnel conditions as discussed e.g. by Mercker and Cooper (2006)[2].

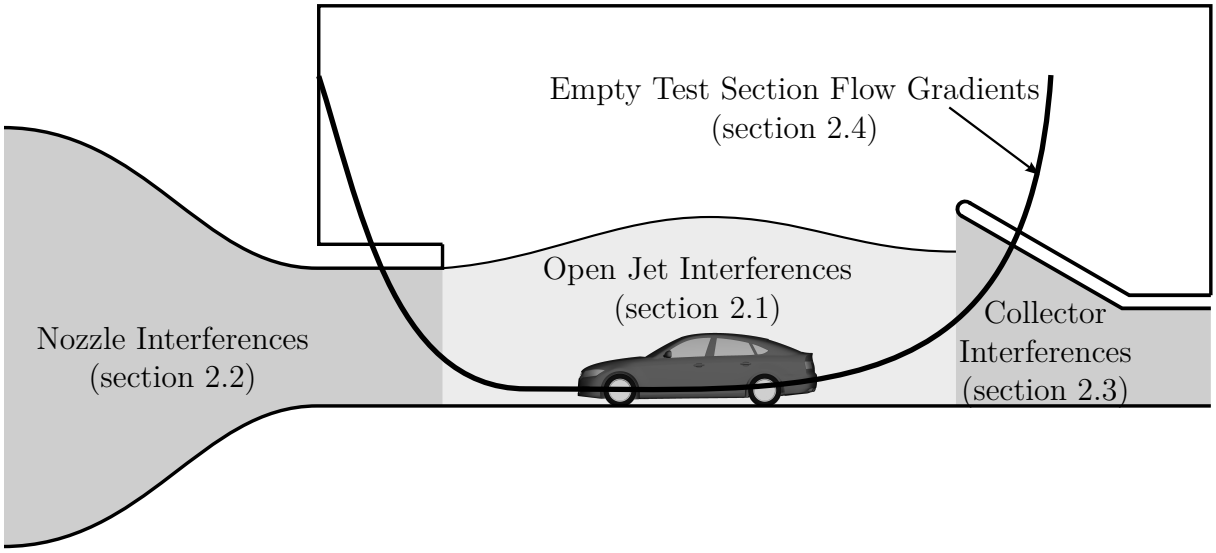

Figure 2.1: Schematic illustration of the interference effects under investigation.

[1]The work of Glauert (1933) focused on gradient effects in closed wall tunnels, but, later, the method was adopted by other researchers for open jet tunnels, too.

[2]The flow is invariant under constraint if typical flow phenomena, e.g. attached and detached regions, do not significantly change due to the presence of wind tunnel boundaries.

2.1 Open Jet Interferences

2.1.1 General Blockage Phenomena

The interference between a testing object with the jet boundary in a wind tunnel facility is caused by the practical limitation of the nozzle dimensions and hence the jet diameter. This interaction is mainly driven by the volume displacement due to the blockage of flow by both streamlined and bluff bodies. Consequently, the interference decays with increasing wind tunnel and/or decreasing model dimensions.

Jet Expansion by Solid Blockage

As evaluated by Lock (1929), wind tunnel interferences occur due to the flow field interaction between wind tunnel and the solid boundary of the model to test. In his investigations Lock (1929) focuses on symmetrical, streamlined bodies with attached flow and without lift induced flow deflection. For a considerable high blockage ratio the general effects of solid blockage on streamline paths and the velocity field[1] in both a closed wall and an open jet test section are given by Figure 2.2.

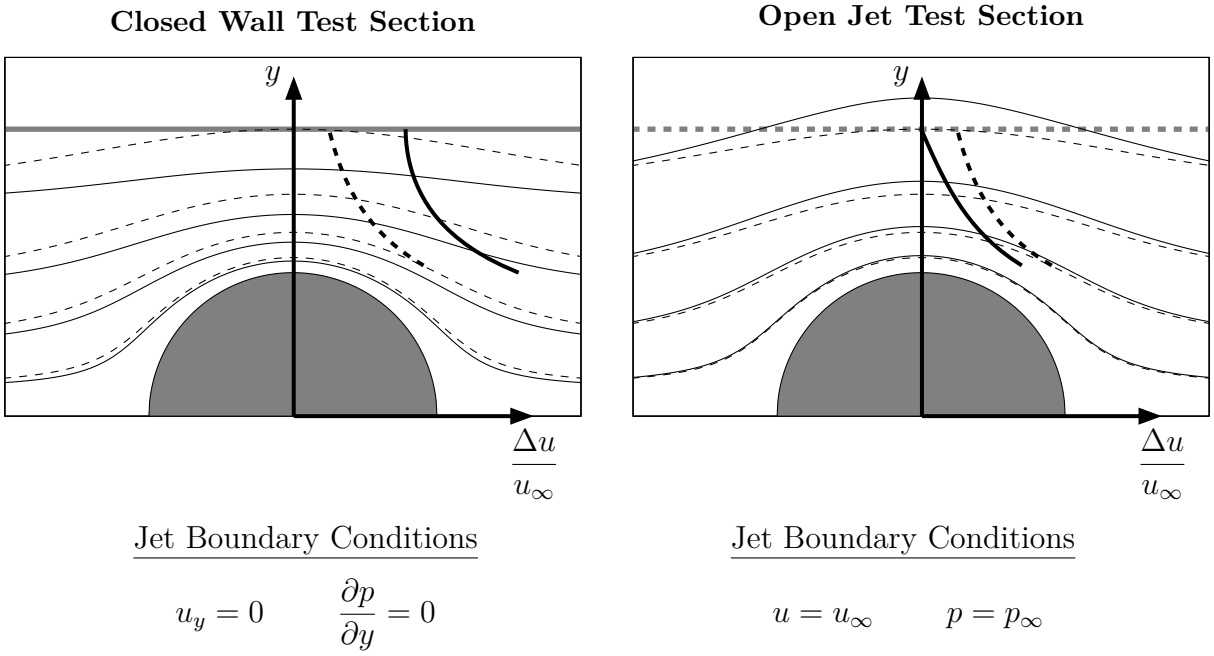

Figure 2.2: Effects of solid blockage of a cylindrical body in the closed wall (——) and the open jet (- - -) wind tunnel following the approach of Lock (1929); streamlines for the real flow (without interference) (- - -) and in wind tunnel conditions (——); corresponding velocity profiles $\Delta u/u_\infty$ (- - -) and (——).

[1] $\Delta u/u_\infty$ denotes the induced velocity from the dipole singularity and, in wind tunnel conditions, from the jet interference. Thus, the condition for the undisturbed flow is $\Delta u/u_\infty = 0$.

Figure 2.2 illustrates the general interference effects in both closed wall and open jet test sections for the attached[1], two dimensional flow around a symmetrical, cylindrical body. In closed wall test sections the furthest streamlines are defined by the geometry of the wind tunnel walls. For straight, friction-less test section walls the outer streamlines coincide with these walls. Thus, the corresponding boundary conditions at the jet boundary are defined by[2]:

$$\underline{\text{Closed wall test section:}} \qquad u_{\mathrm{y}} = 0, \quad \frac{\partial p}{\partial y} = 0 \quad \longrightarrow \quad \boxed{u_{\mathrm{WT}} = u_x \geq u_{\mathrm{Real}}} \tag{2.1}$$

The conservation of mass leads to an increase of the local flow velocity u_{WT} within the test section compared to the "real" flow velocity u_{Real} without any wind tunnel disturbance. In contrary, the location of the open jet boundary is not fixed by wind tunnel walls, but can be obtained from the constant static pressure condition $p = p_\infty$:

$$\underline{\text{Open jet test section:}} \qquad p = p_\infty, \quad u = u_\infty \quad \longrightarrow \quad \boxed{u_{\mathrm{WT}} \leq u_{\mathrm{Real}}} \tag{2.2}$$

The constant pressure boundary conditions $p = p_\infty$ leads to the condition of constant velocity at the jet boundary $u = u_\infty$ or $\Delta u / u_\infty = 0$. However, as illustrated in Figure 2.2, for a considerable blockage the local flow velocity at the equivalent location but in "real"[3] flow conditions is rather higher. The result is a decrease in effective flow velocity $u_{\mathrm{WT}} \leq u_{\mathrm{Real}}$ in open jet wind tunnel test sections compared to "real" flow conditions. Since based on a potential flow model, the velocity profile of an open jet is not sufficiently represented at the jet boundary. As shown by Miller and Comings (1957), friction effects at the jet boundary cause both an inner and an outer limit of the free shear layer. Consequently, Miller and Comings (1957) demonstrate flow gradients within the the open jet for both static pressure and velocity. These conditions are not covered by the potential flow model e.g. of Lock (1929).

Jet Expansion by Wake Blockage

As discussed above, the effect of solid blockage is caused by the displacement of volume due to the solid boundaries of a body. In case of automotive aerodynamics a typical model can be characterized as a bluff body. Flow separations at the rear end of the model typically produce regions of re-circulating flow and increase the loss of the momentum in the wake region[4]. A comparison of streamlines with the attached flow around a sphere is given in Figure 2.3. On the one hand the wake volume enhances the jet expansion and induces a further decrease of effective flow velocity; on the other hand a flow gradient between front and rear is created.

[1] Attached flow around a sphere denotes idealized, potential flow conditions and is not representative for the real flow conditions.

[2] The boundary conditions are formulated for a closed wall test section with constant cross section following $y = \text{const}$.

[3] "Real" flow denotes unlimited flow conditions of the real application (without wind tunnel interference).

[4] The term wake denotes regions with a loss of momentum downstream the model present for both sreamlined and bluff bodies.

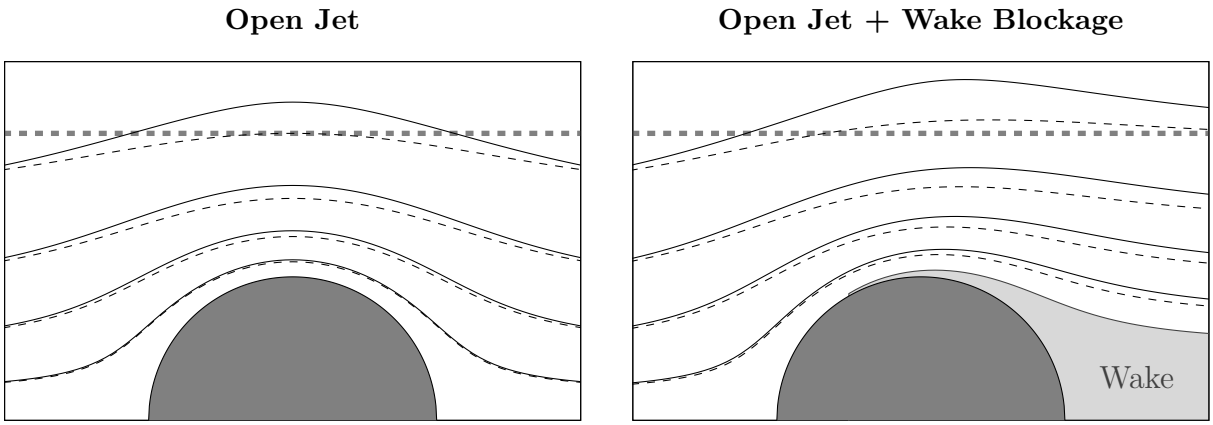

Figure 2.3: Effects of wake blockage of a cylindrical body in the open wind tunnel test section; streamlines for the real flow (- - -) and in wind tunnel conditions (——).

2.1.2 Open Jet Blockage Corrections

Open Jet Correction by Lock

Lock (1929) was the first to derive a general correction formula to account for the open jet interference of symmetrical, streamlined bodies. His work is a continuation of former, partially two-dimensional investigations in closed test sections e.g. by Fage (1929), Fage et al. (1929) and Ower and Hutton (1929). The model is based on the equations of potential flow for which the three-dimensional, vectorial velocity field $\underline{u} = (u_\mathrm{x}, u_\mathrm{y}, u_\mathrm{z})$ is defined as the gradient of the scalar velocity potential Φ:

$$\underline{u} = \begin{pmatrix} u_\mathrm{x} \\ u_\mathrm{y} \\ u_\mathrm{z} \end{pmatrix} = \nabla\Phi \tag{2.3}$$

For an irrotational $\nabla \times \underline{u} = 0$ and incompressible flow $\nabla \cdot \underline{u} = 0$ the velocity potential satisfies Laplace's equation:

$$\Delta\Phi = \frac{\partial^2\Phi}{\partial x^2} + \frac{\partial^2\Phi}{\partial y^2} + \frac{\partial^2\Phi}{\partial z^2} = 0 \tag{2.4}$$

The principle of superposition is permitted as (2.4) is a linear, differential equation. Thus, for a number n of velocity potentials Φ_i with $i = 1 \ldots n$ the "total" induced velocity $\underline{u}$ results from the summation of $\underline{u}_\mathrm{i}$:

$$\Delta\Phi = \sum_{i=1}^{n} \Delta\Phi_\mathrm{i} \quad \longrightarrow \quad \Phi = \sum_{i=1}^{n} \Phi_\mathrm{i} \quad \longrightarrow \quad \underline{u} = \sum_{i=1}^{n} \underline{u}_\mathrm{i} \tag{2.5}$$

The summation of the induced velocity for a number of singularities is an essential method for the classical solid blockage correction as it is based on the method of mirror images of singularities. The mirror images are applied to both open jet and closed wall test

sections as illustrated in Figure 2.4 for an arbitrary singularity in a rectangular wind tunnel. The induced velocity in wind tunnel conditions is calculated on the tunnel axis in the center of the model $x = 0$. In the following, the application for both different model and wind tunnel configurations is explained. The fundamental equations for the corresponding singularities are given in Table A.4 in appendix A.5 on page 164.

Sphere in a Square Tunnel (Lock (1929))

In general, the flow around a sphere is obtained from the combination of parallel flow and a dipole. The axial u_x and the radial u_r velocity components are:

$$u_\mathrm{x}(x,y,z) = \frac{M}{4\pi}\frac{1-3\dfrac{x^2}{x^2+y^2+z^2}}{(x^2+y^2+z^2)^{3/2}} + u_\infty \tag{2.6}$$

$$u_\mathrm{r}(x,y,z) = -\frac{3M}{4\pi}\frac{x\left(y^2+z^2\right)^{1/2}}{\left(x^2+y^2+z^2\right)^{5/2}} \tag{2.7}$$

The dipole moment M is set to achieve the stagnation point condition for a sphere with the radius R_M:

$$u_\mathrm{x}(x = R_\mathrm{M}, y = 0, z = 0) = 0 \quad \longrightarrow \quad M = 2\,\pi\,u_\infty\,{R_\mathrm{M}}^3 \tag{2.8}$$

Eq. (2.6) and (2.7) describe the flow around a sphere without wind tunnel disturbance. As shown in Figure 2.4 the flow field in wind tunnel conditions is represented by the application of mirror images. Thus, the induced velocity in the wind tunnel is calculated from the summation of mirror images. In the classical solid blockage correction the

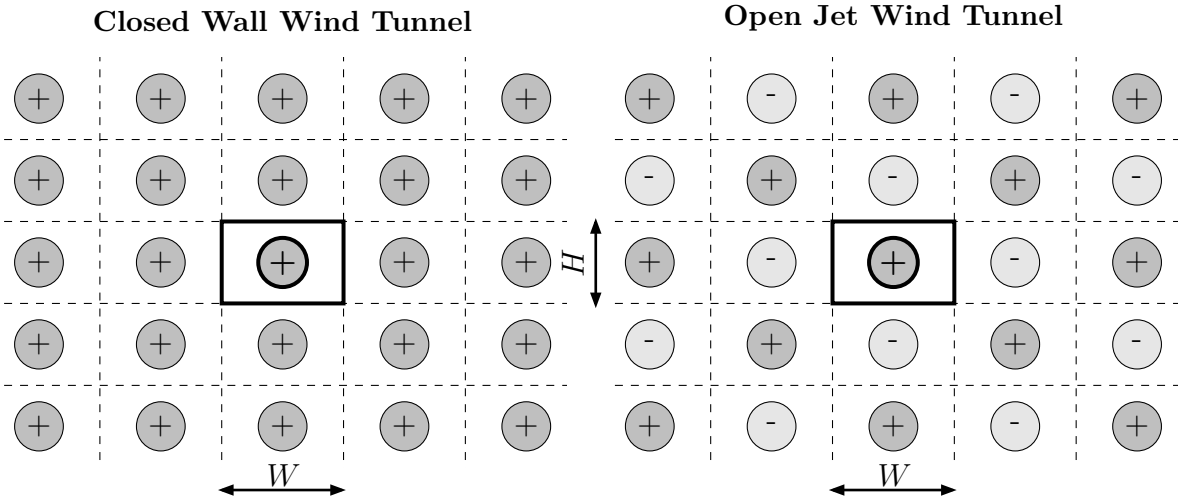

Figure 2.4: Series of images for both the closed wall (left) and the open jet (right) test section. The dashed lines (- - -) indicate the mirroring planes for a wind tunnel (——) of the width W and the height H.

velocity interference is calculated at $x = y = z = 0$. The dipole moment M in (2.6) and (2.7) is substituted with eq. (2.8).

$$\frac{\Delta u_\mathrm{x}}{u_\infty} = \frac{{R_\mathrm{M}}^3}{2} \underbrace{\sum_{m=-\infty}^{\infty} \sum_{n=-\infty}^{\infty}}_{\text{without } m=n=0} \frac{(-1)^{m+n}}{({y_\mathrm{m}}^2 + {z_\mathrm{n}}^2)^{3/2}} \tag{2.9}$$

$$\frac{\Delta u_\mathrm{r}}{u_\infty} = 0 \tag{2.10}$$

For a square, open jet with $W_\mathrm{N} = H_\mathrm{N}$ the coordinates y_m and z_n are calculated using the column index m and the row index n:

$$y_\mathrm{m} = m\, W_\mathrm{N} = m\, H_\mathrm{N}, \qquad z_\mathrm{n} = n\, H_\mathrm{N} \tag{2.11}$$

The relation between model radius R_M and model frontal area A_M as well as the tunnel cross section A_N is:

$$A_\mathrm{M} = \pi\, {R_\mathrm{M}}^2, \qquad A_\mathrm{N} = W_\mathrm{N}\, H_\mathrm{N} = {H_\mathrm{N}}^2 \tag{2.12}$$

Eq. (2.9) is substituted with eq. (2.11) and (2.12):

$$\frac{\Delta u}{u_\infty} = \frac{\Delta u_\mathrm{x}}{u_\infty} = \frac{1}{2} \left(\frac{R_\mathrm{M}}{H_\mathrm{N}}\right)^3 \underbrace{\sum_{m=-\infty}^{\infty} \sum_{n=-\infty}^{\infty}}_{\text{without } m=n=0} \frac{(-1)^{m+n}}{(m^2 + n^2)^{3/2}} \tag{2.13}$$

$$\frac{\Delta u}{u_\infty} = \frac{\Delta u_\mathrm{x}}{u_\infty} = \frac{1}{2\pi^{3/2}} \left(\frac{A_\mathrm{M}}{A_\mathrm{N}}\right)^{3/2} \underbrace{\sum_{m=-\infty}^{\infty} \sum_{n=-\infty}^{\infty}}_{\text{without } m=n=0} \frac{(-1)^{m+n}}{(m^2 + n^2)^{3/2}} \tag{2.14}$$

Rankine Ovoid in a Square Tunnel (Lock (1929))

To represent the flow field around a symmetric, streamlined body with the infinite flow u_∞ Lock (1929) used a combination of equal source and sink (doublet). Therefore, Figure 2.5 illustrates the flow field around a Rankine ovoid of length $2l$ and thickness $2t$ as well as the induced velocity Δu_x and Δu_r within the symmetry plane $x = 0$. Again, the flow field is rotational and symmetric with respect to the x-axis. Therefore, the radial distance $r = \sqrt{y^2 + z^2}$ is used. Figure 2.5 shows that the induced velocity from source and sink sums up with equal magnitude for the axial velocity component Δu_x. However, the radial component Δu_r for source and sink is also equal in magnitude but of opposite in sign. Thus, Δu_r sums up to zero for $x = 0$.

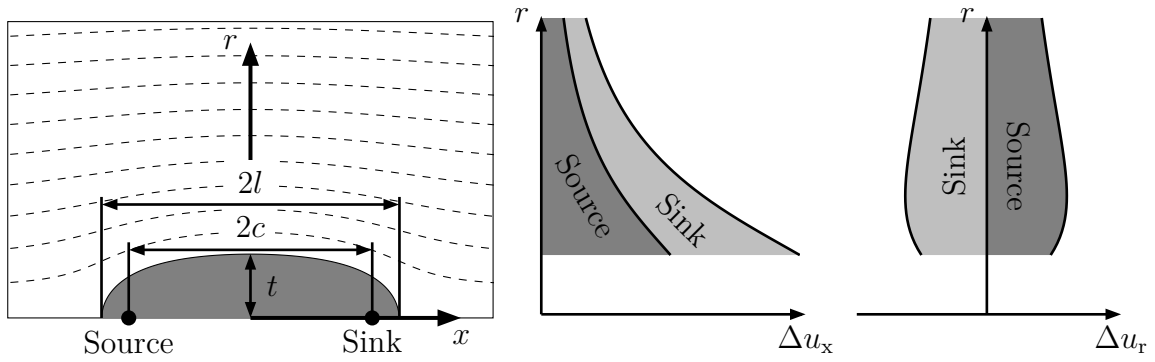

Figure 2.5: Flow field around a Rankine ovoid following the approach of Lock (1929); left: Streamline image; Right: Induced velocity Δu_x and Δu_y along y at $x = 0$)

In terms of potential flow equations the same approach as for the dipole is applied:

$$u_\mathrm{x}(x,y,z) = \frac{Q}{4\pi}\left[\frac{x+c}{\left((x+c)^2+y^2+z^2\right)^{3/2}} - \frac{x-c}{\left((x-c)^2+y^2+z^2\right)^{3/2}}\right] + u_\infty \tag{2.15}$$

$$u_\mathrm{r}(x,y,z) = \frac{Q}{4\pi}\left[\frac{(y^2+z^2)^{1/2}}{\left((x+c)^2+y^2+z^2\right)^{3/2}} - \frac{(y^2+z^2)^{1/2}}{\left((x-c)^2+y^2+z^2\right)^{3/2}}\right] \tag{2.16}$$

For $x = 0$ eq. (2.15) and (2.16) turn into:

$$x = 0: \quad u_\mathrm{x}(y,z) = \frac{Q}{2\pi}\frac{c}{(c^2+y^2+z^2)^{3/2}} + u_\infty \tag{2.17}$$

$$x = 0: \quad u_\mathrm{r}(y,z) = 0 \tag{2.18}$$

As for the dipole the radial velocity u_r at $x = 0$ for the doublet is zero. The velocity u_x in eq. (2.17) refers to the source strength Q and the source and sink positions c. To draw a connection to the thickness $2t$ and hence to the frontal area A_M the corresponding stream function Ψ is applied at $x = 0$ and $r = t$ and set to zero:

$$x = 0, r = t: \quad \Psi(y,z) = 0 = -\frac{Q}{2\pi}\frac{c}{(c^2+t^2)^{1/2}} + \frac{1}{2}u_\infty t^2 \tag{2.19}$$

$$Q = \pi u_\infty \frac{t^3}{c}\left(\left(\frac{c}{t}\right)^2 + 1\right)^{1/2} \tag{2.20}$$

The substitution of Q in eq. (2.17) with eq. (2.20) brings:

$$x = 0: \quad \frac{u_\mathrm{x}(y,z)}{u_\infty} = \frac{1}{2}t^3\left(\left(\frac{c}{t}\right)^2 + 1\right)^{1/2}\frac{1}{(c^2+y^2+z^2)^{3/2}} + 1 \tag{2.21}$$

As for the sphere, the induced velocity at the model center results from the mirror images:

$$\frac{\Delta u}{u_\infty} = \frac{\Delta u_\mathrm{x}}{u_\infty} = \frac{1}{2} t^3 \left(\left(\frac{c}{t} \right)^2 + 1 \right)^{1/2} \underbrace{\sum_{m=-\infty}^{\infty} \sum_{n=-\infty}^{\infty}}_{\text{without } m=n=0} \frac{(-1)^{m+n}}{\left(c^2 + {y_\mathrm{m}}^2 + {z_\mathrm{n}}^2 \right)^{3/2}} \tag{2.22}$$

The coordinates y_m and z_n are identical to equation (2.11). The induced velocity is then:

$$\frac{\Delta u}{u_\infty} = \frac{\Delta u_\mathrm{x}}{u_\infty} = \frac{1}{2} \left(\frac{t}{H_\mathrm{N}} \right)^3 \left(\left(\frac{c}{t} \right)^2 + 1 \right)^{1/2} \underbrace{\sum_{m=-\infty}^{\infty} \sum_{n=-\infty}^{\infty}}_{\text{without } m=n=0} \frac{(-1)^{m+n}}{\left(\left(\frac{c}{H_\mathrm{N}} \right)^2 + m^2 + n^2 \right)^{3/2}} \tag{2.23}$$

$$\frac{\Delta u}{u_\infty} = \frac{\Delta u_\mathrm{x}}{u_\infty} = \frac{1}{2\pi^{3/2}} \left(\frac{A_\mathrm{M}}{A_\mathrm{N}} \right)^{3/2} \left(\left(\frac{c}{t} \right)^2 + 1 \right)^{1/2} \underbrace{\sum_{m=-\infty}^{\infty} \sum_{n=-\infty}^{\infty}}_{\text{without } m=n=0} \frac{(-1)^{m+n}}{\left(\left(\frac{c}{H_\mathrm{N}} \right)^2 + m^2 + n^2 \right)^{3/2}} \tag{2.24}$$

Eq. (2.23) and (2.24) still refer to the source and sink position c rather than the model length $2l$. Lock (1929) calculated l from the stagnation point condition using eq. (2.15) and (2.20) at $y = z = 0$ and $x = l$:

$$\frac{u_\mathrm{x}}{u_\infty} = 0 = \frac{1}{4} \frac{t^3}{c} \left(\left(\frac{c}{t} \right)^2 + 1 \right)^{1/2} \left[\frac{1}{(l+c)^2} - \frac{1}{(l-c)^2} \right] + 1 \tag{2.25}$$

Lock (1929) re-arranged eq. (2.25) towards the bi-quadratic form:

$$\left(\left(\frac{l}{c} \right)^2 - 1 \right)^2 = \frac{l t^2}{c^3} \left(1 + \left(\frac{t}{c} \right)^2 \right)^{1/2} \tag{2.26}$$

The solution of eq. (2.26) returns the half-model length l for a given c and t.

Rectangular Tunnels (Wuest (1961))

Investigations for rectangular, open jet wind tunnels were conducted later, eq. by Wuest (1961). Therefore, the approach of Lock (1929) was adopted and extended for wind tunnels with $W_\mathrm{N} \neq H_\mathrm{N}$. The entire method is identical and the result for the induced velocity for the sphere (dipole) is:

$$\frac{\Delta u}{u_\infty} = \frac{1}{2\pi^{3/2}} \left(\frac{A_\mathrm{M}}{A_\mathrm{N}} \right)^{3/2} \underbrace{\sum_{m=-\infty}^{\infty} \sum_{n=-\infty}^{\infty}}_{\text{without } m=n=0} \frac{(-1)^{m+n}}{\left(m^2 \frac{W_\mathrm{N}}{H_\mathrm{N}} + n^2 \frac{H_\mathrm{N}}{W_\mathrm{N}} \right)^{3/2}} \tag{2.27}$$

and for the Rankine ovoid (doublet):

$$\frac{\Delta u}{u_\infty} = \frac{1}{2\pi^{3/2}} \left(\frac{A_\mathrm{M}}{A_\mathrm{N}}\right)^{3/2} \left(\left(\frac{c}{t}\right)^2 + 1\right)^{1/2} \underbrace{\sum_{m=-\infty}^{\infty} \sum_{n=-\infty}^{\infty}}_{\text{without } m=n=0} \frac{(-1)^{m+n}}{\left(\frac{c^2}{A_\mathrm{M}} \left(\frac{A_\mathrm{M}}{A_\mathrm{N}}\right) + m^2 \frac{W_\mathrm{N}}{H_\mathrm{N}} + n^2 \frac{H_\mathrm{N}}{W_\mathrm{N}}\right)^{3/2}} \tag{2.28}$$

The Correction Formula (Lock (1929))

As explained above, Lock (1929) performs calculations for different model shapes and tunnel shapes in order to propose a general correction formula for the jet expansion. For a given model geometry Lock (1929) derives the velocity correction to be proportional to the blockage ratio:

$$\frac{\Delta u}{u_\infty} \sim \left(\frac{A_\mathrm{M}}{A_\mathrm{N}}\right)^{3/2} \tag{2.29}$$

Furthermore, Lock (1929) separates the effects on the induced velocity for those applied by the model and the wind tunnel. Therefore, he uses the model shape factor λ and the tunnel shape factor τ:

$$\boxed{\frac{u_\mathrm{c}}{u_\infty} - 1 = \frac{\Delta u}{u_\infty} = \tau\lambda \left(\frac{A_\mathrm{M}}{A_\mathrm{N}}\right)^{3/2}} \tag{2.30}$$

The model shape factor λ refers to the model volume and is independent of the wind tunnel geometry. The reference is the sphere for which $\lambda = 1$. The tunnel shape factor τ takes into account the mirror images and is assumed to be independent from the model geometry. However, the results for a square tunnel are:

$$\boxed{\text{Dipole}} \qquad \tau = \frac{1}{2\pi^{3/2}} \underbrace{\sum_{m=-\infty}^{\infty} \sum_{n=-\infty}^{\infty}}_{\text{without } m=n=0} \frac{(-1)^{m+n}}{(m^2+n^2)^{3/2}} \tag{2.31}$$

$$\boxed{\text{Doublet}} \qquad \tau = \frac{1}{2\pi^{3/2}} \underbrace{\sum_{m=-\infty}^{\infty} \sum_{n=-\infty}^{\infty}}_{\text{without } m=n=0} \frac{(-1)^{m+n}}{\left(\frac{c^2}{A_\mathrm{M}} \left(\frac{A_\mathrm{M}}{A_\mathrm{N}}\right) + m^2 + n^2\right)^{3/2}} \tag{2.32}$$

Eq. (2.31) and (2.32) show that the summations for τ for both the dipole and the doublet are not identical. Lock (1929) assumes the effect of the model length and hence c negligible as the model dimensions are expected to be much smaller than the tunnel dimensions ($c^2/A_\mathrm{N} \approx 0$).

Equation (2.30) contains the following approximations for the open jet test section:

- The model of interference is symmetrical and no wake interference is existent.
- The jet boundary confirms the boundary conditions $p = p_\infty$ and $u = u_\infty$ as stated in equation (2.2).

- By its displacement, the model induces a velocity in the wind tunnel test section. The interference is calculated at the model center.
- Within the symmetry plane $x = 0$ the flow is parallel to the undisturbed flow and hence $u = u_\mathrm{x}$ and $u_\mathrm{r} = 0$.
- The tunnel dimensions are rather large compared to the model dimensions $c^2/A_\mathrm{N} \approx 0$.
- The jet boundary remains at its location. The model does not affect the open jet cross section.
- The tunnel shape factor τ accounts for a specific tunnel geometry whereas $\Delta u \sim \tau$.
- The model shape factor λ accounts for the shape of the body by using the reference of the sphere $\lambda = 1$ whereas $\Delta u \sim \lambda$.

The basic idea is to use a general equation to correct the velocity interference Δu. It is derived for a sphere in a circular tunnel and hence for a rotationally symmetric flow field. To consider different shapes of both the wind tunnel and the model geometry Lock (1929) performs calculations for τ and λ.

The only geometric length scale referred by equation (2.30) is the frontal area of the model A_M. Since it is based on a sphere with $\lambda = 1$, the additional volume of solid blockage for longer bodies but of equivalent frontal area is considered by λ. Lock (1929) determines λ for different two-dimensional shapes such as the ellipse, the Rankine oval as well as the simple and the generalized Joukowski shape. Furthermore he picks the Rankine ovoid and the spheroid for investigations in three dimensions as shown by Figure 2.6. The calculation of λ does not take into account any wind tunnel geometry but only returns the ratio of velocity interference for different model shapes. The extra volume for longer bodies of $l/t > 1$ generally also produces a model shape factor $\lambda > 1$.

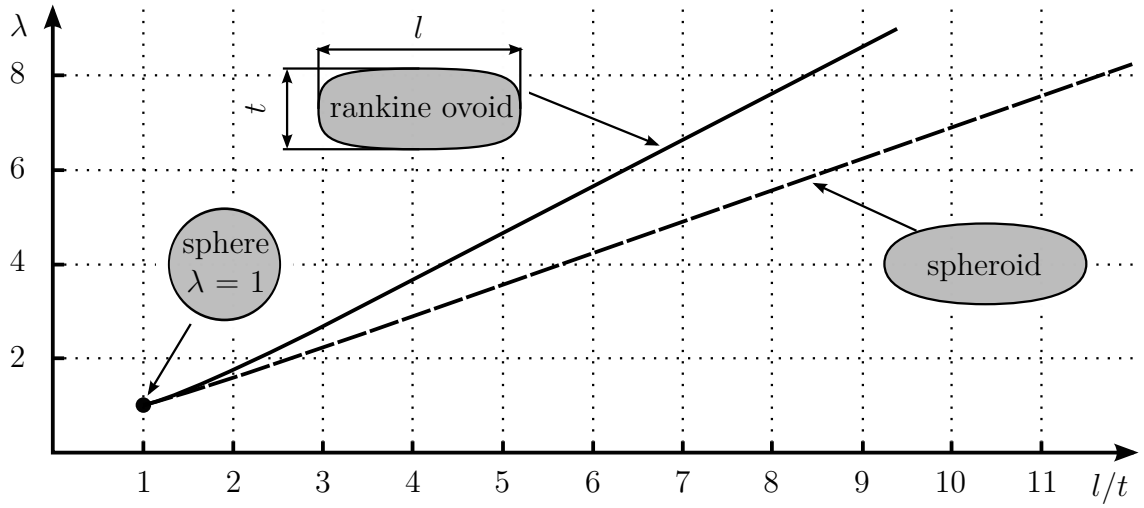

Figure 2.6: Model shape factor λ for a Rankine ovoid and a spheroid with the fineness ratio l/t as given by Lock (1929).

For the calculation of τ for a rectangular tunnel the following equation is given e.g. by Wuest (1961):

$$\boxed{\text{Closed Jet}} \quad \tau = \frac{1}{2\pi^{3/2}} \sum_{m=-\infty}^{\infty} \sum_{n=-\infty}^{\infty} \left(\frac{1^{m+n}}{m^2 \frac{W_\mathrm{N}}{H_\mathrm{N}} + n^2 \frac{H_\mathrm{N}}{W_\mathrm{N}}} \right)^{3/2} \tag{2.33}$$

$$\boxed{\text{Open Jet}} \quad \tau = \frac{1}{2\pi^{3/2}} \sum_{m=-\infty}^{\infty} \sum_{n=-\infty}^{\infty} \left(\frac{(-1)^{m+n}}{m^2 \frac{W_\mathrm{N}}{H_\mathrm{N}} + n^2 \frac{H_\mathrm{N}}{W_\mathrm{N}}} \right)^{3/2} \tag{2.34}$$

An empirical approximation for τ of rectangular, open jet wind tunnels is given e.g. by Wickern (2001):

$$\tau = -0.03 \left(\frac{W}{H} + \frac{H}{W} \right)^3 \tag{2.35}$$

An overview of tunnel shape factors for both open jet and closed wall tunnels is presented in Table 2.1.

Open Jet Correction by Mercker et al.

As stated above, most of the first wind tunnel corrections were applied in aerospace aerodynamics and for closed wall test sections. Later on, open jet wind tunnel interferences for ground vehicles were focused, too. Main aspects are the usage of an open jet test section and the bluff body characteristics of typical passenger cars. E. Mercker was one of the first to develop practical wind tunnel corrections for automotive wind tunnels. In the first paper Mercker (1986) introduces a correction procedure for closed wall wind tunnels including a solid blockage and a wake blockage correction. Therefore, the approach of Lock (1929) is adopted in order to calculate the corrected wind tunnel velocity using eq. (2.30). Later, also the open jet wind tunnel is considered by Mercker and Wiedemann (1996). Automotive, open jet wind tunnels have the solid wind tunnel boundary on the floor as part of the model. To apply the approach of Lock (1929) a duplex mirror image of the testing object is created as shown in Figure 2.7. For a rectangular nozzle the

Table 2.1: Tunnel shape factors τ for rectangular tunnels by Lock (1929) and Wuest (1961).

$\frac{W_\mathrm{N}}{H_\mathrm{N}}$	1.00	1.20	1.40	1.60	1.80	2.00
	1.00	0.83	0.71	0.63	0.56	0.50
Closed Wall	0.8061	0.8193	0.8521	0.8988	0.9562	1.0227
Open Jet	-0.2376	-0.2528	-0.2893	-0.3389	-0.3969	-0.4611

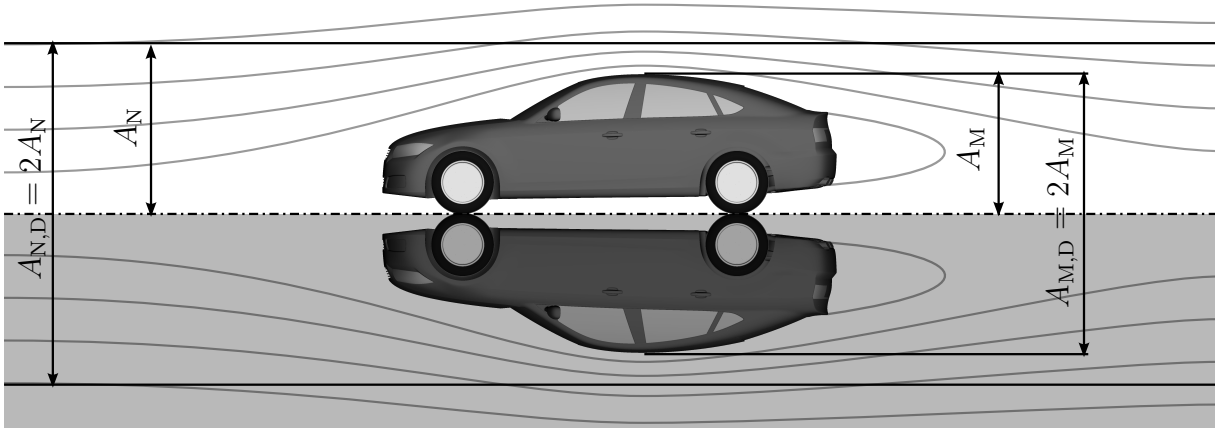

Figure 2.7: Duplex mirror image for an automotive, open jet wind tunnel as shown by Mercker and Wiedemann (1996).

dimensions change as following (duplex dimensions with index "D"):

$$\frac{A_{\mathrm{N,D}}}{A_{\mathrm{N}}} = \frac{H_{\mathrm{N,D}}}{H_{\mathrm{N}}} = \frac{A_{\mathrm{M,D}}}{A_{\mathrm{M}}} = 2, \qquad \frac{W_{\mathrm{N,D}}}{W_{\mathrm{N}}} = 1 \tag{2.36}$$

Mercker and Wiedemann (1996) apply a velocity correction for the effect of the jet expansion by following eq. (2.30) using the blockage factor ε_{S}:

$$\varepsilon_{\mathrm{S}} = \frac{\Delta u}{u_\infty} = \tau\lambda \left(\frac{A_{\mathrm{M}}}{A_{\mathrm{N}}}\right)^{3/2} = \tau \left(\frac{V_{\mathrm{M}}}{A_{\mathrm{M}}\, L_{\mathrm{M}}}\right) \left(\frac{A_{\mathrm{M}}}{A_{\mathrm{N}}}\right)^{3/2} = \tau \left(\frac{V_{\mathrm{M}}}{L_{\mathrm{M}}}\right) \frac{A_{\mathrm{M}}}{A_{\mathrm{N}}^{3/2}} \tag{2.37}$$

The model shape factor, introduced by Lock (1929), is replaced by an area ratio of using an effective, average model area $A_{\mathrm{M,eff}} = V_{\mathrm{M}}/L_{\mathrm{M}}$. Compared to Lock (1929), a value $\lambda = 1$ is not present for a sphere but for a cuboid. In a later approach Mercker (2013) adapts λ by additionally including the wake volume V_{W} and the wake length L_{W}:

$$\lambda = \left(\frac{V_{\mathrm{T}}}{A_{\mathrm{M}}\, L_{\mathrm{T}}}\right)^{1/2} = \left(\frac{V_{\mathrm{M}} + V_{\mathrm{W}}}{A_{\mathrm{M}}\ (L_{\mathrm{M}} + L_{\mathrm{W}})}\right)^{1/2} \tag{2.38}$$

The understanding of "wake" here is the re-circulation region of detached flow downstream the rear end of the car. The calculation of the wake volume V_{W} includes the separation area of the wake A_{W}:

$$V_{\mathrm{W}} = \frac{1}{2}\, k\ (A_{\mathrm{W}})^{3/2} \quad \text{with:} \quad k = 2.6 \tag{2.39}$$

The formula for the wake length L_{W} is taken from Garry et al. (1994):

$$L_{\mathrm{W}} = k\,\sqrt{A_{\mathrm{W}}} \tag{2.40}$$

Open Jet Correction by Wickern et al.

As a second example of automotive, open jet wind tunnel corrections Wickern (2001) also adopts the classical solid blockage correction using eq. (2.30) on page 14. For the correction of open jet interferences Wickern (2001) focuses on the calculation of the model shape factor λ for typical automotive shapes. The work of Young and Squire (1945) is referred who perform investigations on the calculation of λ:

$$\lambda = \frac{\sqrt{\pi}}{2} \frac{V_\mathrm{M}}{{A_\mathrm{M}}^{3/2}} \tag{2.41}$$

The displacement of the open jet by the wake volume is not considered as the approach of Young and Squire (1945) is limited to the solid blockage. To apply a correction for bluff bodies, Wickern (2001) uses the approach of Glauert (1933):

$$\lambda = G \frac{\sqrt{\pi}}{2} \frac{V_\mathrm{M}}{{A_\mathrm{M}}^{3/2}} \quad \text{with:} \quad G = \frac{V_\mathrm{M,real} + V_\mathrm{M,virtual}}{V_\mathrm{M,real}} \tag{2.42}$$

The Glauert-factor G relates the portion of total volume and solid volume whereas Wickern (2001) uses the approximation of G presented by Garner et al. (1966):

$$G = 1 + 0.4 \frac{t}{l} = 1 + 0.4 \frac{\sqrt{A_\mathrm{M}}}{\sqrt{\pi}\,(L_\mathrm{M} + L_\mathrm{W})} \quad \text{with:} \quad t = \sqrt{\frac{A_\mathrm{M}}{\pi}} \tag{2.43}$$

Thus, the Glauert-factor G is calculated from the equivalent model diameter t and the total length of the model L_M and the re-circulation area L_W. The calculation of L_W is equivalent to eq. (2.39) and (2.40) but using a $k = 2$. The final calculation for λ presented by Wickern (2001) is:

$$\lambda = G \frac{\sqrt{\pi}}{2} \frac{V_\mathrm{M} + V_\mathrm{W}}{{A_\mathrm{M}}^{3/2}} \tag{2.44}$$

2.2 Nozzle Interferences

2.2.1 Dynamic Pressure Determination

One of the most essential quantities for any wind tunnel measurement is the effective flow velocity u_∞ and, respectively, the dynamic pressure $p_{\mathrm{dyn},\infty}$ of the undisturbed flow. However, in typical facilities of automotive, open jet wind tunnels the velocity field inside the test section is overall affected by the testing object. Thus, a reference point to directly determine the undisturbed flow velocity is not at all available. This, in fact, becomes relevant as soon as the testing object is added to the test section. To overcome this issue the most common approach today is to perform a wind tunnel calibration for the empty test section. Therefore, the "natural" flow gradients of the wind tunnel itself are used to predict the dynamic pressure for a testing configuration. The wind tunnel nozzle turned

out to be an excellent source for that since it creates a remarkable change in both dynamic and static pressure along the converging region of the nozzle.

For long, two common methods are typically used in modern wind tunnels in order to adjust the speed of the open jet — the plenum method (PM) and the nozzle method (NM). Both methods are explained in Figure 2.8. The basic idea is to calibrate the pressure drop Δp in the empty wind tunnel for a preferred range of testing speed. The difference between the two methods is then the selection of the pressure taps. The plenum method uses the differential, static pressure between the settling chamber (high pressure side) and the plenum (low pressure side) whereas the nozzle method operates with a second nozzle reference on the low pressure side, see also Figure 2.8. Both methods are calibrated for the empty wind tunnel test section to achieve the dynamic pressure at a representative reference point in the test section $p_{\mathrm{dyn,ref}} = f(\Delta p_{\mathrm{PM}})$ and/or $p_{\mathrm{dyn,ref}} = f(\Delta p_{\mathrm{NM}})$ respectively. For configurations including a testing object the dynamic pressure of the undisturbed flow $p_\infty = p_{\mathrm{dyn,ref}}$ is then obtained from the wind tunnel calibration by measuring the tunnel gradients Δp_{PM} and/or Δp_{NM} for the particular method. Based on the working principle, both the plenum and the nozzle method are somewhat affected by flow gradients applied by the testing object. A simplified visualization of these effects is given by Figure 2.9. The plenum method (Figure 2.9 left) uses the pressure drop between settling chamber and plenum as the testing object is added. Following the theory explained in section 2.1 the constant pressure condition at the jet boundary enforces also a constant velocity at the same location. Assuming a sufficient large plenum, the pressure at the jet boundary then equals the plenum pressure p_{p}. This leads to the condition that

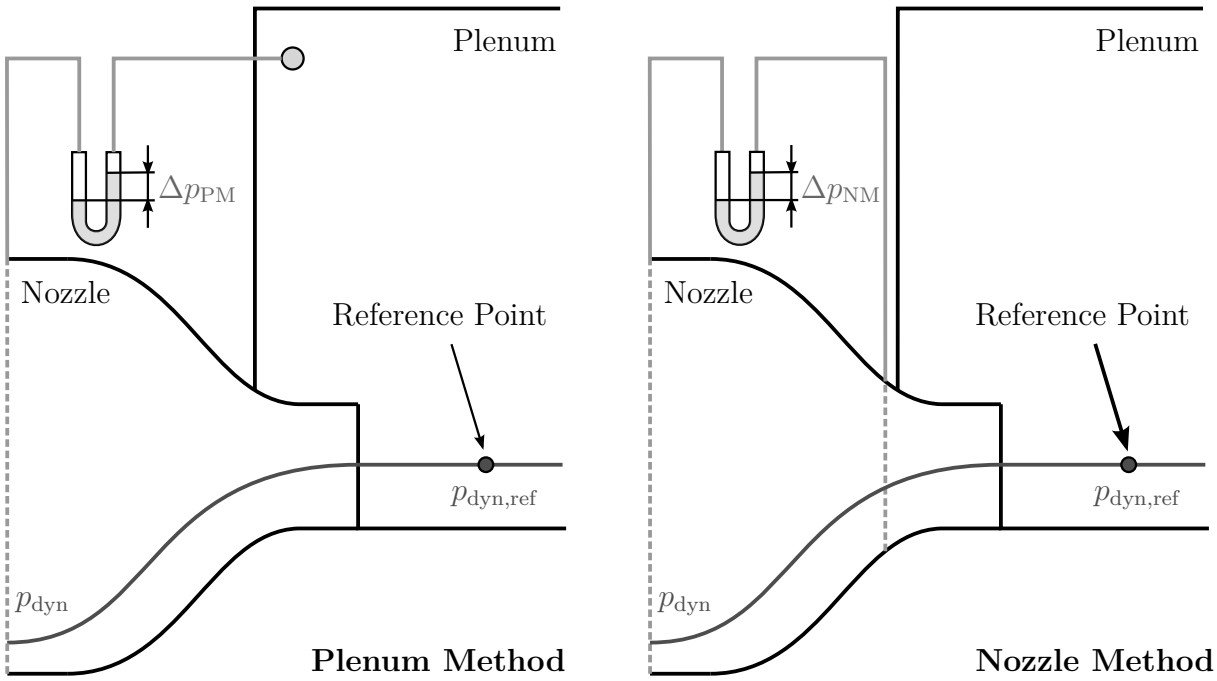

Figure 2.8: Approach for the calibration of an open jet wind tunnel for the plenum method (left) or the nozzle method (right), e.g. Nijhof and Wickern (2003).

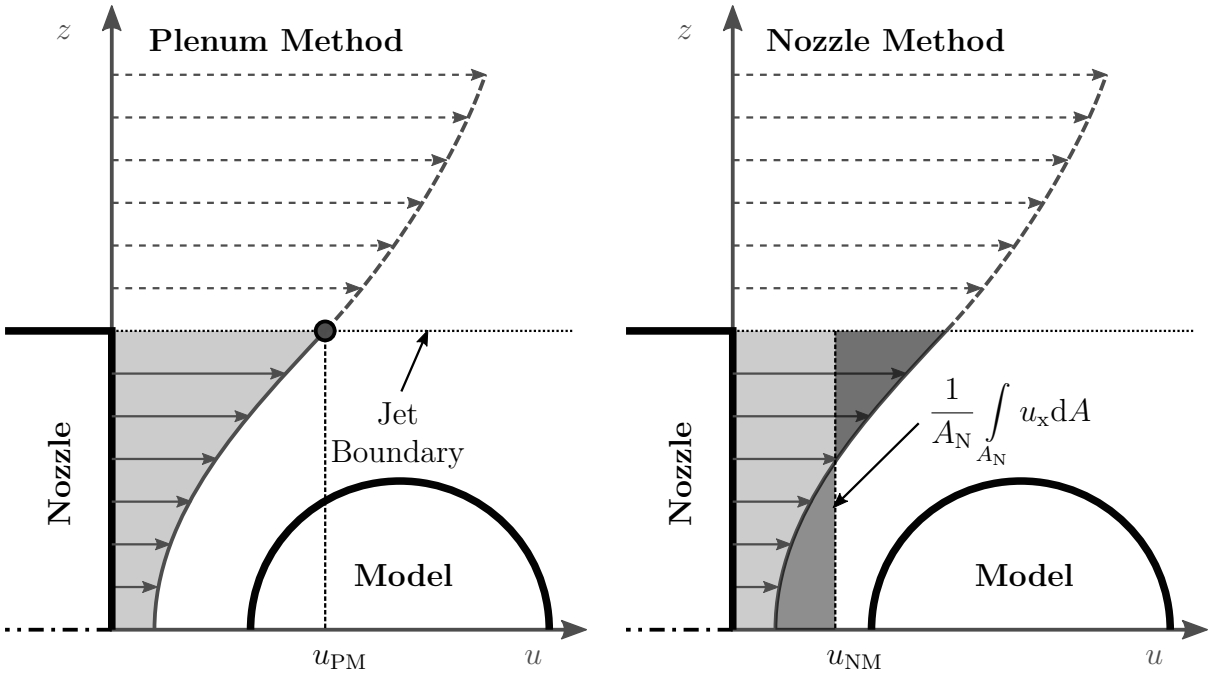

Figure 2.9: Schematic illustration of the velocity obtained by the plenum method u_{PM} (left) and the nozzle method u_{NM} (right). Assuming a velocity profile in the wind tunnel that is equivalent to open road conditions, the velocity of the undisturbed flow is given by u_{∞}. The plenum method determines the velocity at the jet boundary, wheres the nozzle method produces the integral average velocity for the nozzle exit.

a constant pressure drop for the plenum method Δp_{PM} returns a constant velocity at the jet boundary. Due to the presence of the testing object the upstream velocity is typically decreased compared to the undisturbed flow velocity u_{∞}. For significant blockage ratios $A_{\mathrm{M}}/A_{\mathrm{N}}$ the plenum method predicts a velocity u_{PM} lower than the undisturbed flow velocity u_{∞}. For the nozzle method (Figure 2.9 right) the pressure drop in the nozzle indicates the test section dynamic pressure. It is hence based on the continuity effect that provides a constant mass flow through the nozzle if the pressure drop Δp_{NM} is constant. Again the upstream flow of the model decelerated by the model blockage. For the same flow conditions as explained for the plenum method the nozzle method predicts the average velocity at the nozzle exit. It can be obtained from the integral of the velocity profile within the nozzle exit area. Thus, the velocity determined using the nozzle method u_{NM} is lower than both u_{PM} and u_{∞}.

For the measurement of the aerodynamic force coefficients C_{i} the following dependency is well known:

$$C_{\mathrm{i}} = \frac{F_{\mathrm{i}}}{A_{\mathrm{M}}\, p_{\mathrm{dyn}}} \tag{2.45}$$

F_{i} indicates the force acting in the corresponding direction and A_{M} the model frontal area. The dynamic pressure p_{dyn} now includes either the plenum or the nozzle method. Both methods predict a dynamic pressure that is lower than the "correct" value of the

undisturbed flow. An increase of the aerodynamic force coefficients, compared to the corrected force coefficients $C_{\mathrm{i,c}}$, is hence expected:

$$C_{\mathrm{i,NM}} \geq C_{\mathrm{i,PM}} \geq C_{\mathrm{i,c}} \tag{2.46}$$

Obviously, essential factors for this effect are the blockage ratio $A_{\mathrm{M}}/A_{\mathrm{N}}$ and the distance between nozzle and testing object.

2.2.2 Nozzle Interference Corrections

Nozzle Corrections by Mercker et al.

Mercker and Wiedemann (1996) developed an approach to account for the effects on the dynamic pressure created by the interference between testing object and nozzle. This paper considers interference effects for a wind tunnel operating with the nozzle method. Later, Mercker et al. (1997) extends this study as the plenum method is included as well. The method is based on a potential flow model whereas the testing object is represented as a half-infinite body using a source singularity in parallel flow, see Figure 2.10. The basic idea is to calculate the velocity interference at the nozzle exit for both the nozzle and the plenum method. Assuming a parallel flow at the nozzle exit the lateral velocity components u_{r} are eliminated. Thus, only the stream-wise velocity component u_{x} is relevant and can be expressed as:

$$u_{\mathrm{x}}(x,r) = u_{\infty} + \frac{Q}{4\pi}\frac{x}{\left(x^2+r^2\right)^{3/2}} \tag{2.47}$$

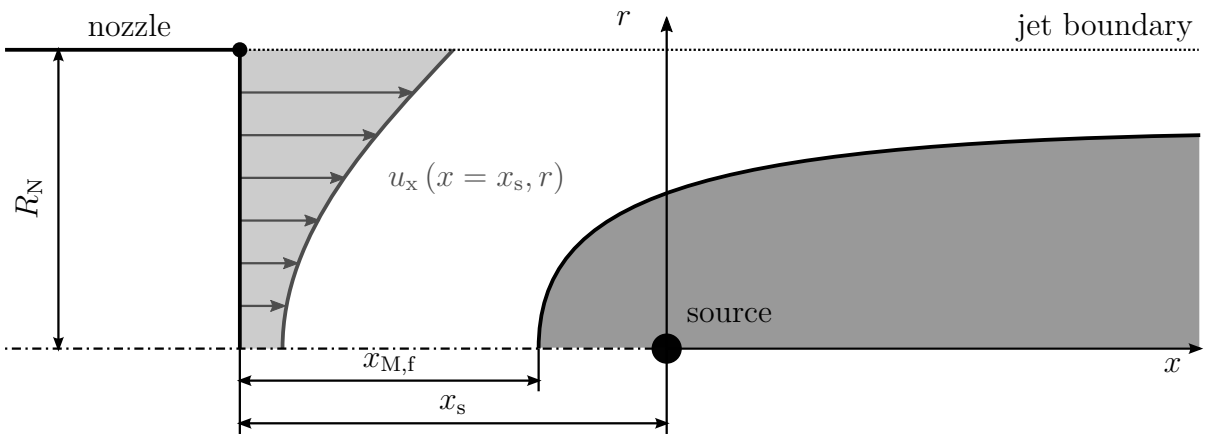

Figure 2.10: Principle of modeling nozzle blockage using a point source.

To express this equation in terms of the frontal area A_M of the model the source strength is substituted:

$$Q = A_\mathrm{M} u_\infty \tag{2.48}$$

$$\frac{u_\mathrm{x}(x,r)}{u_\infty} = 1 + \frac{A_\mathrm{M}}{4\pi} \frac{x}{\left(x^2 + r^2\right)^{3/2}} \tag{2.49}$$

According to Figure 2.9 the velocity interference for the plenum method is obtained at the jet boundary at the nozzle exit. For a circular tunnel with the radius R_n the location of interference is then at $x = -x_\mathrm{s}$. Eq. (2.49) results in:

$$\underline{\text{plenum method:}} \qquad \frac{1}{\varepsilon_\mathrm{q,PM}} = \frac{u_\mathrm{PM}}{u_\infty} = 1 - \frac{A_\mathrm{M}}{4\pi} \frac{x_\mathrm{s}}{\left(x_\mathrm{s}^2 + R_\mathrm{n}^2\right)^{3/2}} \tag{2.50}$$

The correction factor $\varepsilon_\mathrm{q,PM}$ for the plenum method is introduced. To calculate the interference velocity u_NM for the nozzle method eq. (2.49) is integrated over the nozzle exit area, which is considered to be a circular jet:

$$\frac{u_\mathrm{NM}}{u_\infty} = \frac{1}{A_\mathrm{N}} \int_0^{A_\mathrm{N}} \frac{u_\mathrm{x}(x,r)}{u_\infty} \,\mathrm{d}A = \frac{1}{A_\mathrm{N}} \int_0^{2\pi} \int_0^{R_\mathrm{N}} \frac{u_\mathrm{x}(x,r)}{u_\infty} r \,\mathrm{d}r \,\mathrm{d}\phi \tag{2.51}$$

Thus, the interference velocity for the nozzle method results from the integration of eq. (2.49). The correction factor $\varepsilon_\mathrm{q,NM}$ for the nozzle method is:

$$\underline{\text{nozzle method:}} \qquad 1 - \varepsilon_\mathrm{q,NM} = \frac{u_\mathrm{NM}}{u_\infty} = 1 - \frac{A_\mathrm{M}}{2A_\mathrm{N}} \left(1 - \frac{x_\mathrm{s}}{\left(x_\mathrm{s}^2 + R_\mathrm{n}^2\right)^{1/2}}\right) \tag{2.52}$$

To consider the effect of the flow constraint due to the proximity of the nozzle a ring vortex with the circulation Γ is placed along the nozzle exit plane, see Figure 2.11. The

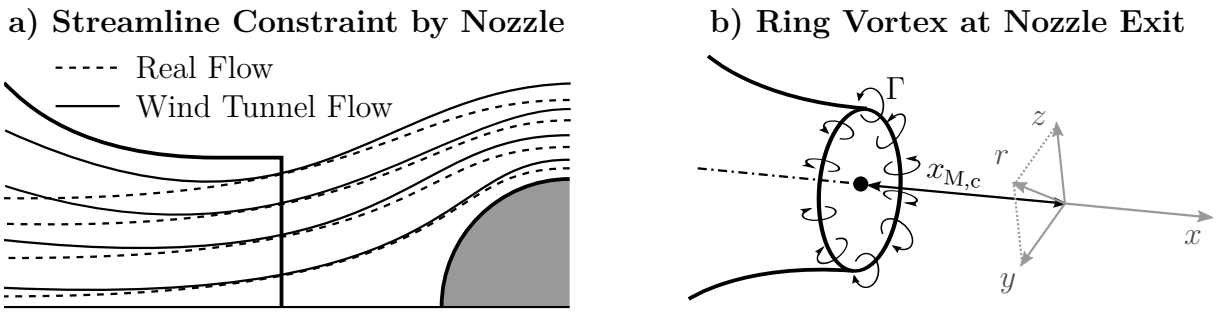

Figure 2.11: Streamline constraint by the nozzle (left) and modeling with a ring vortex (right) as given by Mercker et al. (1997).

result is a further expanding flow near the model and an increased stream-wise velocity u_x along the test section:

$$u_\mathrm{x} = \frac{\Gamma}{2} \frac{R_\mathrm{N}^2}{\left(R_\mathrm{N}^2 + x_\mathrm{M,c}^2\right)^{3/2}} \tag{2.53}$$

In the first papers Γ is assumed to be proportional to the perturbation velocity of the nozzle method $\varepsilon_\mathrm{q,NM}$, see Mercker et al. (1997):

$$\Gamma = 2\, R_\mathrm{N}\, u_\infty\, \varepsilon_\mathrm{q,NM} \tag{2.54}$$

The effective blockage factor for the nozzle method can then be obtained from the substitution of Γ in eq. (2.53).

$$1 - \varepsilon_\mathrm{NM} = \varepsilon_\mathrm{q,NM} \frac{R_\mathrm{N}^3}{\left(R_\mathrm{N}^2 + x_\mathrm{M,c}^2\right)^{3/2}} \tag{2.55}$$

The effective blockage factor $\varepsilon_\mathrm{q,PM}$ for the plenum method is approximated by Mercker et al. (1997) by:

$$\varepsilon_\mathrm{PM} = \varepsilon_\mathrm{q,PM} - \varepsilon_\mathrm{q,NM} + \varepsilon_\mathrm{NM} \tag{2.56}$$

In a later paper Mercker and Cooper (2006) apply different circulations for both methods of dynamic pressure determination:

$$\Gamma_\mathrm{NM} = 2\, R_\mathrm{N}\, u_\infty\, \varepsilon_\mathrm{q,NM}, \qquad \Gamma_\mathrm{PM} = 2\, R_\mathrm{N}\, u_\infty\, \varepsilon_\mathrm{q,PM} \tag{2.57}$$

The complete formula for the blockage factors ε_PM and ε_NM are now used as the reciprocate. The blockage factors to calculate the corrected velocity u_c are given by Mercker and Cooper (2006):

$$\varepsilon_\mathrm{q,PM} = \frac{u_\mathrm{c}}{u_\mathrm{PM}} - 1 = \frac{\dfrac{A_\mathrm{M,D}}{4\pi} \dfrac{x_\mathrm{s}}{\left(x_\mathrm{s}^2 + R_\mathrm{n}^2\right)^{3/2}}}{1 - \dfrac{A_\mathrm{M,D}}{4\pi} \dfrac{x_\mathrm{s}}{\left(x_\mathrm{s}^2 + R_\mathrm{n}^2\right)^{3/2}}} \left[\frac{R_\mathrm{N}^3}{\left(R_\mathrm{N}^2 + x_\mathrm{M,f}^2\right)^{3/2}} \right] \tag{2.58}$$

$$\varepsilon_\mathrm{q,NM} = \frac{u_\mathrm{c}}{u_\mathrm{NM}} - 1 = \frac{\dfrac{A_\mathrm{M,D}}{2A_\mathrm{N,D}} \left(1 - \dfrac{x_\mathrm{s}}{\left(x_\mathrm{s}^2 + R_\mathrm{n}^2\right)^{1/2}}\right)}{1 - \dfrac{A_\mathrm{M,D}}{2A_\mathrm{N,D}} \left(1 - \dfrac{x_\mathrm{s}}{\left(x_\mathrm{s}^2 + R_\mathrm{n}^2\right)^{1/2}}\right)} \left[\frac{R_\mathrm{N}^3}{\left(R_\mathrm{N}^2 + x_\mathrm{M,f}^2\right)^{3/2}} \right] \tag{2.59}$$

The application for automotive, open jet wind tunnels is realized using the duplex method ($A_\mathrm{M,D} = 2A_\mathrm{M}$, $A_\mathrm{N,D} = 2A_\mathrm{N}$) explained in section 2.1. The tunnel radius of the duplex, rectangular nozzle is then:

$$R_\mathrm{N,D} = \left(\frac{2A_\mathrm{N}}{\pi}\right)^{1/2} \tag{2.60}$$

Eq. (2.58) and (2.59) contain the position of the point source x_s as the reference for the distance between model and nozzle. The distance $x_\mathrm{M,f}$ of the front end of the half-infinite body is represented by the location of the stagnation point $u_\mathrm{x} = 0$ in eq. (2.49):

$$x_\mathrm{M,f} = x_\mathrm{s} - \left(\frac{A_\mathrm{M}}{4\pi}\right)^{1/2} \tag{2.61}$$

Furthermore, the position of the source x_s is selected to represent the front end of a car. In their first papers Mercker et al. (1997) decided for a fixed source location defined by the dimensions of the vehicle (L_M: length of the model; $x_\mathrm{M,c}$: distance between nozzle and center of the model):

$$x_\mathrm{s} = x_\mathrm{M,c} - \frac{L_\mathrm{M}}{2} + \left(\frac{A_\mathrm{M}}{2\pi}\right)^{1/2} \tag{2.62}$$

Later, Mercker and Cooper (2006) and Mercker (2013) use an iterative approach to calculate x_s, if both the dynamic pressure from plenum method $p_\mathrm{dyn,PM}$ and from the nozzle method $p_\mathrm{dyn,NM}$ are known from a wind tunnel measurement. The position of the point source is moved until the corrected dynamic pressure $p_\mathrm{dyn,c}$ is equal for both methods:

$$p_\mathrm{dyn,c} \equiv p_\mathrm{dyn,PM}\,(1+\varepsilon_\mathrm{PM})^2 = p_\mathrm{dyn,NM}\,(1+\varepsilon_\mathrm{NM})^2 \tag{2.63}$$

Another effect considered by (Mercker & Wiedemann, 1996) is the jet deflection, which is created by an increased flow angle at the jet boundary. Figure 2.12 depicts the increase of the jet deflection effect for decreasing distance to the nozzle using the example of a flat plate. In the approach of Mercker and Wiedemann (1996) the effect of jet deflection is

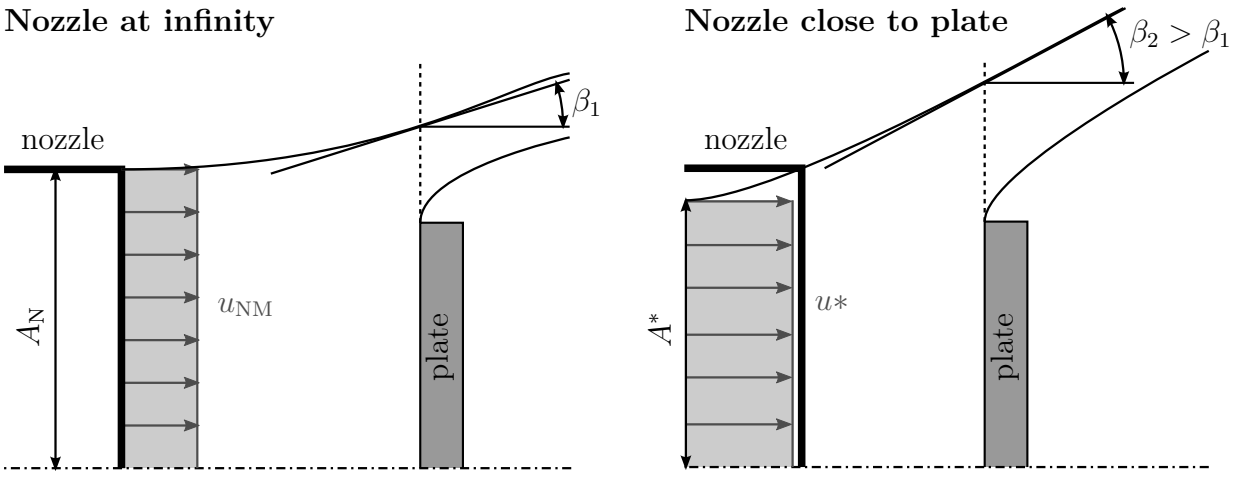

Figure 2.12: Jet deflection effect as given by Mercker and Wiedemann (1996). The interaction between the nozzle and the model enforces a flow acceleration in the nozzle as well as an increased flow angle at the jet boundary for a significantly small distance between nozzle and model.

considered by a substitution of the nozzle area A_N in the jet expansion correction, see eq. (2.37):

$$\varepsilon_\mathrm{S} = \tau \left(\frac{V_\mathrm{M}}{L_\mathrm{M}}\right) \frac{A_\mathrm{M}}{A^{*3/2}} \qquad \text{with:} \qquad A^* \leq A_\mathrm{N} \tag{2.64}$$

Since the jet deflection is assumed to be a velocity correction of the same sign as the jet expansion A^* is effectively smaller than the nozzle area A_N. The magnitude of A^* is calculated from the continuity of flow using the nozzle method, see Mercker and Wiedemann (1996):

$$A_\mathrm{N}\, u_\mathrm{NM} = A^*\, u^* \qquad \longrightarrow \qquad A^* = A_\mathrm{N} \frac{u^*}{u_\mathrm{NM}} = \frac{A_\mathrm{N}}{1+\varepsilon_\mathrm{q,NM}} \tag{2.65}$$

Nozzle Corrections by Wickern et al.

In his first paper Wickern (2001) introduces a correction method for the effect of the dynamic pressure determination due to the presence of the model. In principal, the method is identical to Mercker's correction above as it is based on the induced velocity of a potential flow singularity on the nozzle cross section. However, Wickern (2001) gives results for both a dipole and a doublet and also takes into account the mirror images. Furthermore, the correction is applied to a rectangular open jet and not to a circular such as the correction of Mercker, e.g. in Mercker and Cooper (2006). The flow at the nozzle exit is assumed to be parallel and hence the induced velocity is limited to the axial component. For the dipole in a rectangular tunnel Wickern (2001) formulates the induced velocity as:

$$\begin{aligned}\frac{\Delta u}{u_\infty} = \frac{\Delta u_\mathrm{x}(x,y,z)}{u_\infty} = \frac{1}{2\pi^{3/2}} \left(\frac{H_\mathrm{N}}{W_\mathrm{N}}\right)^{3/2} \left(\frac{A_\mathrm{M}}{A_\mathrm{N}}\right)^{3/2} \cdot \\ \sum_{m=-\infty}^{\infty} \sum_{n=-\infty}^{\infty} (-1)^{m+n} \frac{\left(\frac{y}{W_\mathrm{N}} - m\right)^2 + \left(\frac{z}{W_\mathrm{N}} - n\frac{H_\mathrm{N}}{W_\mathrm{N}}\right)^2 - 2\left(\frac{x}{W_\mathrm{N}}\right)^2}{\left(\left(\frac{x}{W_\mathrm{N}}\right)^2 + \left(\frac{y}{W_\mathrm{N}} - m\right)^2 + \left(\frac{z}{W_\mathrm{N}} - n\frac{H_\mathrm{N}}{W_\mathrm{N}}\right)^2\right)^{5/2}}\end{aligned} \tag{2.66}$$

From eq. (2.66) Wickern (2001) recognized the same dependency of Δu from the blockage ratio as the classical solid blockage correction presented in eq. (2.30) and introduced a new tunnel shape factor τ_2 for the nozzle blockage:

$$\frac{\Delta u}{u_\infty} = \tau_2(x)\, \lambda \left(\frac{A_\mathrm{M}}{A_\mathrm{N}}\right)^{3/2} \tag{2.67}$$

The tunnel factor $\tau_2(x)$ is not constant as the nozzle blockage effect depends on the distance between model and nozzle. For the nozzle method Wickern (2001) applies the condition of constant mass flow at the nozzle exit and integrates eq. (2.66):

$$\tau_{2,\mathrm{NM}}(x_\mathrm{c}) = \frac{1}{2\pi^{3/2}} \left(\frac{H_\mathrm{N}}{W_\mathrm{N}}\right)^{3/2} \cdot \int_{A_\mathrm{N}} \left[\sum_{m=-\infty}^{\infty} \sum_{n=-\infty}^{\infty} (-1)^{m+n} \frac{\left(\frac{y}{W_\mathrm{N}} - m\right)^2 + \left(\frac{z}{W_\mathrm{N}} - n\frac{H_\mathrm{N}}{W_\mathrm{N}}\right)^2 - 2\left(\frac{x_\mathrm{c}}{W_\mathrm{N}}\right)^2}{\left(\left(\frac{x_\mathrm{c}}{W_\mathrm{N}}\right)^2 + \left(\frac{y}{W_\mathrm{N}} - m\right)^2 + \left(\frac{z}{W_\mathrm{N}} - n\frac{H_\mathrm{N}}{W_\mathrm{N}}\right)^2\right)^{5/2}} \right] \frac{\mathrm{d}A}{A_\mathrm{N}} \quad (2.68)$$

The effect of the singularity on the dynamic pressure for a wind tunnel operating with the plenum method is assumed to be negligible. Thus, the tunnel shape factor is zero:

$$\tau_{2,\mathrm{PM}}(x_\mathrm{c}) = 0 \quad (2.69)$$

The same approach for the doublet is given in appendix A.1.1 on page 141. Wickern (2001) computes results for $\tau + \tau_{2,\mathrm{NM}}$ in order to compare the effect of the model on the dynamic pressure for the nozzle method. Figure 2.13 depicts the curves given by Wickern (2001) as a function of the distance between nozzle exit and model center x_c for the dipole and different doublets in a square tunnel. Figure 2.13 depicts that the summation of τ and $\tau_{2,\mathrm{NM}}$ is possible as both the nozzle blockage and the solid blockage are considered

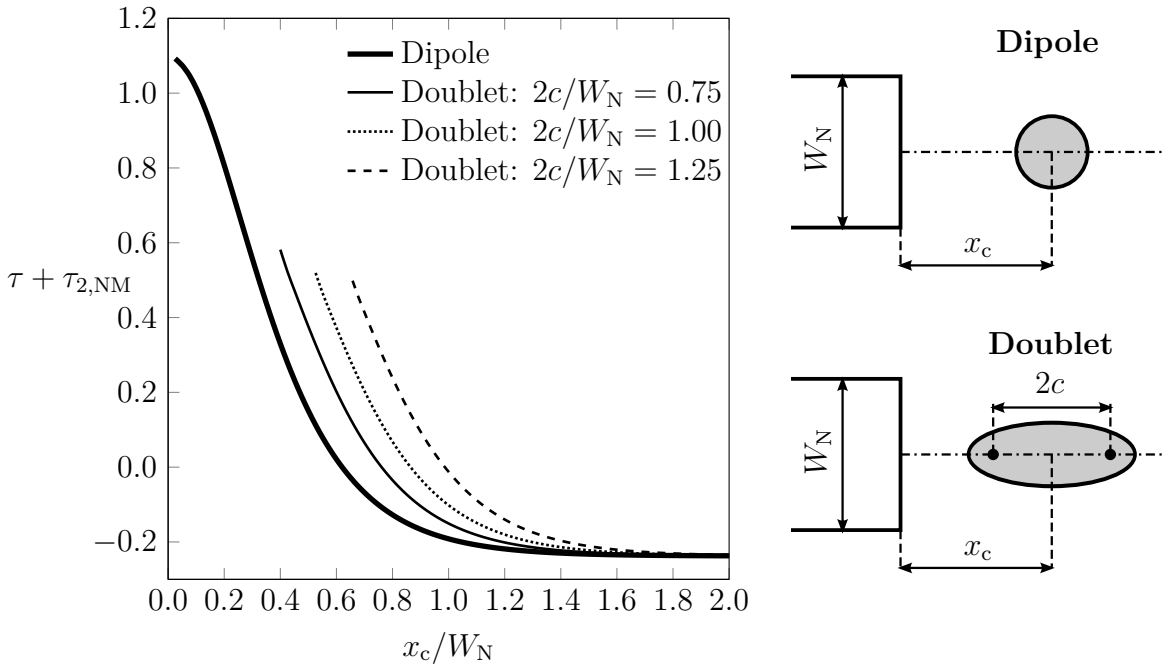

Figure 2.13: Tunnel shape factors $\tau + \tau_{2,\mathrm{NM}}$ given by Wickern (2001) for a square, open jet ($W_\mathrm{N}/H_\mathrm{N} = 1$) for a dipole and doublets with different spacing between source and sink.

with a velocity correction. The correction formula is based on the classical solid blockage correction.

The dynamic pressure correction for the nozzle method by Wickern (2001) is a similar approach to Mercker et al. However, the difference is that Wickern (2001) uses a doublet for automotive corrections in a rectangular tunnel. Furthermore, a dynamic pressure correction is applied only for the nozzle method.

In a later paper Wickern and Schwartekopp (2004) upgrade the nozzle correction by an additional effect. For a better understanding the principle effect is given in Figure 2.14 for a streamlined body in rather extreme blockage conditions. As explained above, the nozzle method returns the average velocity within the nozzle exit. Far upstream in the nozzle the velocity is assumed to be uniform and equivalent to the velocity of the nozzle method u_{NM}. The flow is accelerated at the nozzle exit up to a higher magnitude. The jet boundary velocity is equivalent to the plenum method u_{PM}. Due to the contracting flow behind the model the jet cross section is reduced whereas the jet boundary velocity remains constant as u_{PM}. Far downstream the flow behind the streamlined body is expected to be uniform again. The pressure equates the room pressure p_∞. Wickern and Schwartekopp (2004) balance the increase of momentum with a force F_{x} acting on the model. This force is the same for a wind tunnel operating with both the plenum and the nozzle method as it results from a model induced pressure gradient. Thus, Wickern and Schwartekopp (2004) call it the nozzle gradient effect. The correction formula is hence not a dynamic pressure but a gradient correction to account for the drag increase due to the interference between model and nozzle:

$$\Delta C_{\mathrm{D}} = \frac{F_{\mathrm{x}}}{\frac{\rho}{2} {u_\infty}^2 A_{\mathrm{M}}} \tag{2.70}$$

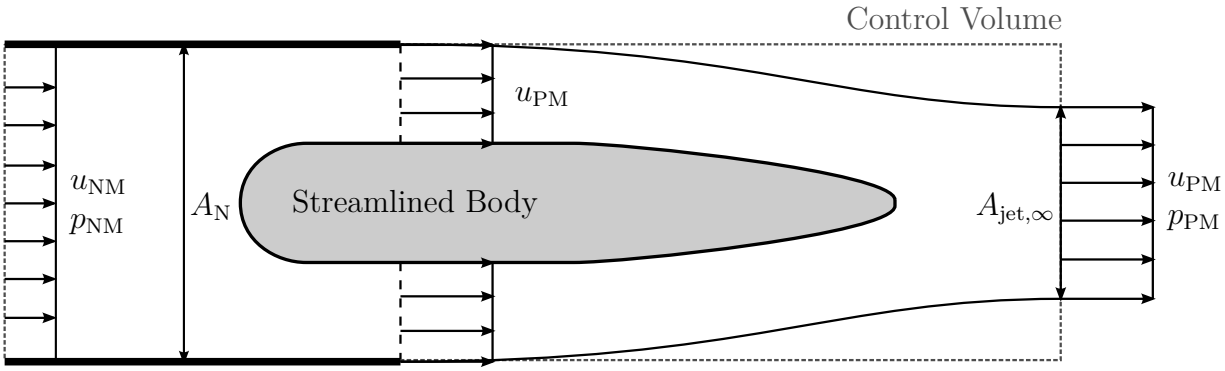

Figure 2.14: Simplified velocity conditions in the wind tunnel due to the nozzle blockage by a streamlined model Wickern and Schwartekopp (2004).

The force F_x is calculated from the momentum balance within the control volume. This approach is given in appendix A.1.1. The result is given by Wickern and Schwartekopp (2004):

$$\Delta C_D = \left[\frac{u_{PM}}{u_{NM}} - 1\right]^2 \frac{A_N}{A_M} \tag{2.71}$$

It is obvious that the drag correction requires the input of the velocity from both methods. Wickern and Schwartekopp (2004) combine the momentum balance with the potential flow model from eq. (2.67):

$$\frac{u_{PM}}{u_{NM}} = \frac{\Delta u}{u_\infty} + 1 = \tau_{2,NM}\,\lambda \left(\frac{A_M}{A_N}\right)^{3/2} + 1 \tag{2.72}$$

The substitution of u_{PM}/u_{NM} in eq (2.71) with eq. (2.72) brings:

$$\Delta C_D = {\tau_{2,NM}}^2\,\lambda^2 \left(\frac{A_M}{A_N}\right)^2 = \tau_{NG}\,\lambda^2 \left(\frac{A_M}{A_N}\right)^2 \quad \text{with:} \quad \tau_{NG} = {\tau_{2,NM}}^2 \tag{2.73}$$

The final set of equations for the method of Wickern et al. is:

$$\boxed{\text{Nozzle Blockage:}} \qquad \frac{\Delta u}{u_\infty} = \tau_{2,NM}\,\lambda \left(\frac{A_M}{A_N}\right)^{3/2} \tag{2.74}$$

$$\boxed{\text{Nozzle Gradient:}} \qquad \Delta C_D = \tau_{NG}\,\lambda^2 \left(\frac{A_M}{A_N}\right)^2 \tag{2.75}$$

In his latest paper Wickern (2014) formulates an approach towards the self-correcting open jet wind tunnel. The basic idea is to balance the drag increasing effect of nozzle blockage and nozzle gradient with the drag decreasing effect due to the jet expansion. As the result, Wickern (2014) recommends particular longitudinal positions for the model for which the corrections of open jet and nozzle cancel out each other.

2.3 Collector Interferences

2.3.1 Collector Blockage

The collector serves as an essential component in any open jet wind tunnel test section. The design of the collector is strongly connected to the dimensions of the wind tunnel nozzle as it operates as a flow stabilizer for the open jet. Flow fluctuations increase along the propagation of an open jet due to the instabilities within the free shear layers. For example, Wickern (2014) recommends not to exceed a test section length L_{TS} of three hydraulic jet diameters $L_{\mathrm{TS}} \leq 3\,d_{\mathrm{N}}$. Otherwise, problems with tunnel resonances and/or energy losses may occur as also discussed by Wiedemann et al. (1993), Arnette et al. (1999) and Lacey (2002). Due to the restriction of the test section length collector interferences are of significant importance in many wind tunnel facilities. For bluff body aerodynamics with detached flow wake distortion due to the collector can be present especially for rather short test sections. At this point it is worth to mention that the collector often affects the static pressure distribution along the test section. This effect is discussed in section 2.4. A second effect of importance is the collector blockage caused by the momentum loss in the near and far wake region of the model. A better understanding of this effect is

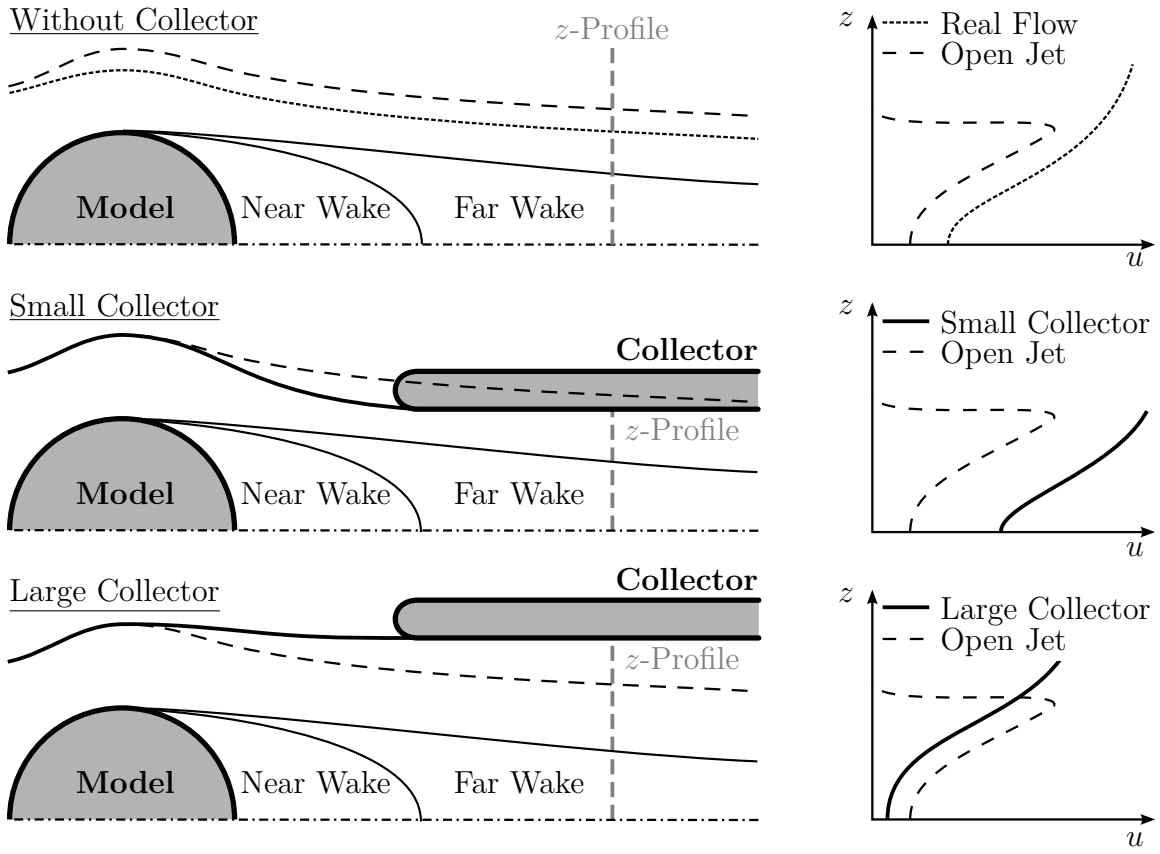

Figure 2.15: Collector blockage and its effect on the jet boundary (left) and on the velocity distribution $u(z)$ in the wake of the model (right); schematic illustration for a small and a large collector inlet area.

presented by Figure 2.15 by comparing the velocity interference for a small and a large collector inlet area A_C.

Assuming attached flow downstream the collector inlet Figure 2.15 depicts the expansion or constriction of the open jet by the collector compared to a half-infinite test section. The conservation of mass enforces an acceleration of flow for the small collector and a deceleration for the large collector even for a streamlined model, for which no wake is present. For bluff bodies an additional acceleration of flow is expected due to blockage of the near and/or the far wake at the collector inlet. These interferences can affect both lift and drag measurements whereas a general tendency of increase or decrease of forces, such as for the nozzle, is not possible. An extensive study to evaluate the effect of test section length L_{TS} and collector area A_C is provided by von Schulz-Hausmann and Vagt (1988), see Figure 2.16. von Schulz-Hausmann and Vagt (1988) give results for automotive bodies evaluated in a model scale tunnel using the 1:4 scaled Porsche 944 as well as the 1:4 and 1:5 scaled MIRA Van. The curves in Figure 2.16 are representative for the 1:4 scale models. As stated in Figure 2.15, the effect of the collector on the measured drag coefficient C_D is strongly connected to the collector area (here normalized to the nozzle area A_C/A_N). For the short test section configuration $L_{TS}/d_N = 2$ a steep drag gradient is visible within the range $1.0 \leq A_C/A_N \leq 1.7$. Based on Bernoulli's equation von Schulz-Hausmann and Vagt (1988) derive a theory to predict the influence of the collector. For the shortest test section this model matches well for $A_C/A_N \approx 1.2$. However, the curves diverge with increasing collector area. Accordingly, with increasing test section length the collector interference decreases and turns out to be almost negligible for $L_{TS}/d_N = 2.96$.

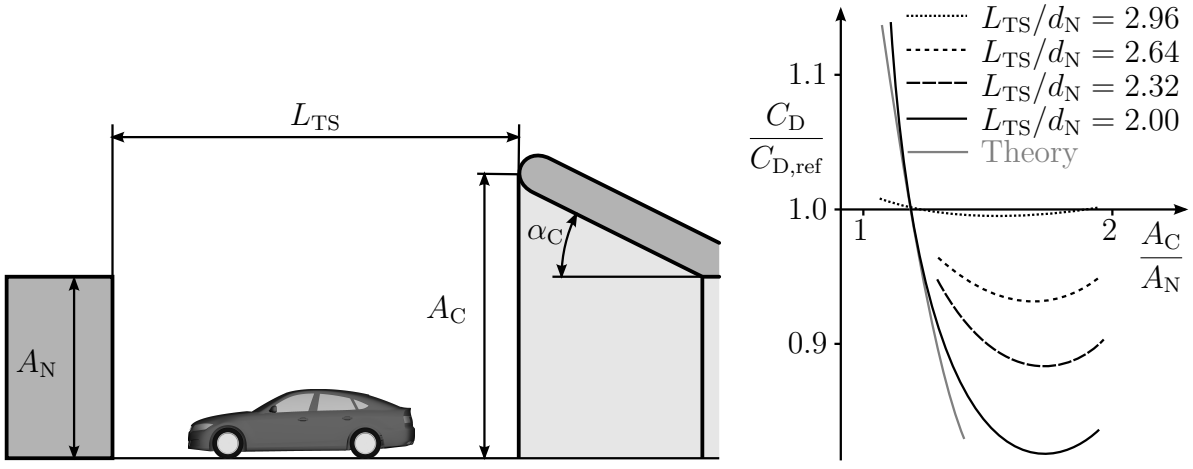

Figure 2.16: Approach by von Schulz-Hausmann and Vagt (1988) to evaluate the collector interference on an automotive body. The parameters under investigation are the test section length L_{TS} and the collector inlet area A_C adjusted by the flap angle α_C (left). The results are plotted for the normalized drag coefficient $C_D/C_{D,ref}$ (right).

2.3.2 Collector Interference Corrections

The principle blockage phenomena for the collector interference are similar to those for the nozzle interference. However, in typical facilities the influence of the collector on the static pressure gradient in the empty test section is significantly higher than those of the nozzle. Furthermore, the effects of empty test section flow gradients is discussed in section 2.4. For now, the collector interferences are treated to be blockage effects only present if the model is placed inside the test section.

Mercker and Wiedemann (1996) introduce a correction method to account for the collector blockage. They adopt the approach of Mercker (1986) for closed jet test sections, which is based on the work of Maskell (1961) and Glauert (1933):

$$\varepsilon_{\mathrm{W}} = \frac{A_{\mathrm{M}}}{A_{\mathrm{C}}} \left(\frac{C_{\mathrm{D}}}{4} + 0.41 \right) \tag{2.76}$$

$$\varepsilon_{\mathrm{C}} = \frac{\varepsilon_{\mathrm{W}} {R_{\mathrm{C}}}^3}{\left(\left(L_{\mathrm{TS}} - x_{\mathrm{c}} \right)^2 + R_{\mathrm{C}}^2 \right)^{3/2}} \quad \longrightarrow \quad \frac{\Delta u}{u_\infty} = \varepsilon_{\mathrm{C}} \tag{2.77}$$

The wake blockage factor ε_{W} is used to account for the velocity increase at the collector inlet due to the momentum loss in the wake of bluff bodies. As for the nozzle interference in eq. (2.55) on page 23, Mercker and Wiedemann (1996) use the ring vortex method also to represent the flow constraint by the collector, see eq. (2.77). The induced velocity Δu at the model center is calculated from ε_{C}. The ring vortex is placed at the equivalent collector radius R_{C}:

$$R_{\mathrm{C}} = \sqrt{\frac{2A_{\mathrm{C}}}{\pi}} \tag{2.78}$$

Later, the set of equations is adapted in order to distinguish between collector blockage and wake distortion. An overview of the entire correction approach is presented by Mercker (2013).

2.4 Empty Test Section Flow Gradients

All the effects discussed above for the open jet, the nozzle and the collector occur if the model is installed inside the test section. Thus, these effects are not recognized in the flow field of the empty wind tunnel test section. However, many facilities show flow gradients even if no model is installed, e.g. as provided by Hennig and Mercker (2011). Empty wind tunnel gradients can be the result of components to control and/or stabilize the test section flow. The static pressure gradient is a widely used term in order to characterize gradients in wind tunnel test sections.

2.4.1 Static Pressure Gradient

Wind tunnel testing is a simulation of open road conditions. The transformation of a moving car through stationary air/ground towards a resting car with moving air/ground requires to ensure a flow field of constant velocity and static pressure along the test section. Due to limitations of wind tunnel dimensions, e.g. test section length, the realization of zero gradient test section is often challenging. Figure 2.17 depicts two typical examples of reasons for the presence of a gradient in static pressure as also presented by Hennig and Mercker (2011).

For a realistic moving ground simulation in a wind tunnel the near ground flow needs to be uniform and hence without any boundary layer. Different methods were established to remove the boundary layer profile at the nozzle exit. The most common techniques are the boundary layer suction, scoop and tangential blowing. More information are presented by Wickern et al. (2003). As shown in Figure 2.17, a gradient in static pressure can be created by a boundary layer suction. Furthermore, the collector typically influences the static pressure at the end of the test section. Obviously, these empty test section gradients change with test section length and specific collector design. It is worth to mention, that several further design criteria are of importance to achieve a wind tunnel flow free of gradients. Those are e.g. the nozzle, the plenum dimensions and the design of the moving ground simulation. However, in the scope of this work the main focus is on the collector design.

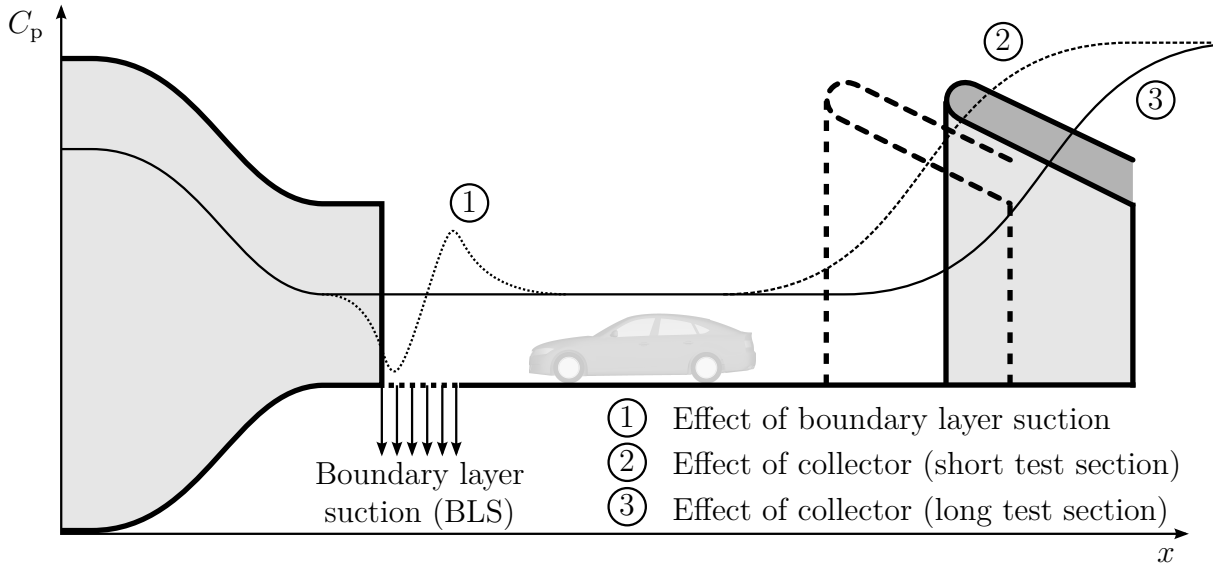

Figure 2.17: Static pressure coefficient c_p along the empty test section. Flow gradients are added by the boundary layer suction and the collector (short and long test section setup). Schematic illustration following the data presented by Hennig and Mercker (2011) for the Audi Aeroacoustic Wind Tunnel.

2.4.2 Static Pressure Gradient Corrections

For automotive applications Mercker and Wiedemann (1996) formulated a general horizontal buoyancy correction to account for the effect of a static pressure gradient. The correction is applied to the drag coefficient $\Delta C_{\mathrm{D,HB}}$ that is manipulated by a horizontal gradient $\mathrm{d}c_{\mathrm{p}}/\mathrm{d}x$:

$$\Delta C_{\mathrm{D,HB}} = \frac{1}{A_{\mathrm{M}}} \frac{\mathrm{d}c_{\mathrm{p}}}{\mathrm{d}x} V_{\mathrm{eff}} \tag{2.79}$$

A_{M} again denotes the frontal area of the model and V_{eff} represents the effective model volume including the displacement of volume in the wake region. Mercker and Wiedemann (1996) refer to the work of Glauert (1928), who focuses on simple bodies such as a sphere, and recommended to calculate the effective model volume from the model volume as $V_{\mathrm{eff}} = 1.75\, V_{\mathrm{M}}$. A similar approach is presented by Wickern (2001) whereas he uses the Glauert factor G from eq. (2.43) in order to calculate the effective model volume:

$$\Delta C_{\mathrm{D,HB}} = \frac{1}{A_{\mathrm{M}}} \frac{\mathrm{d}c_{\mathrm{p}}}{\mathrm{d}x} \left(V_{\mathrm{M}} + V_{\mathrm{W}}\right) G \tag{2.80}$$

Later, Mercker et al. (2005) separate the effects of static pressure gradient into a portion solid-body buoyancy force $\Delta C_{\mathrm{D,HB}}$ and wake distortion $\Delta C_{\mathrm{D,W}}$ to apply the correction to the drag coefficient C_{D}:

$$C_{\mathrm{D,c}} = C_{\mathrm{D}} + \Delta C_{\mathrm{D,HB}} + \Delta C_{\mathrm{D,W}} \tag{2.81}$$

$$\Delta C_{\mathrm{D,HB}} = G \frac{V_{\mathrm{M}}}{A_{\mathrm{M}}} \frac{\mathrm{d}c_{\mathrm{p}}}{\mathrm{d}x} \tag{2.82}$$

$$\Delta C_{\mathrm{D,W}} = c_{\mathrm{p,Wc}} - c_{\mathrm{p,Mb}} \tag{2.83}$$

Mercker et al. (2005) defines the wake distortion, e.g. due to a positive pressure gradient by the collector, as a projection of pressure increase at the position of wake closure on the rearward model surface and hence as an increase in model base pressure. Therefore, the difference of empty test section static pressure at the position of the model base $c_{\mathrm{p,Mb}}$ and the location of wake closure $c_{\mathrm{p,Wc}}$ is applied to the drag correction.

For the method above, the location of wake closure must be known. To overcome this issue, Mercker and Cooper (2006) introduce a method to apply the drag correction on the base of two measurements with different static pressure gradients, e.g. by using two different collector positions. Both static pressure gradients must be known to obtain the corrected drag coefficient $C_{\mathrm{D,c,i}}(x)$ for the pressure distributions $i = 1$ and $i = 2$:

$$C_{\mathrm{D,c,i}}(x) = \left(C_{\mathrm{D}} + \Delta c_{\mathrm{p,i}}(x)\right) \frac{p_{\mathrm{dyn,c}}}{p_{\mathrm{dyn}}} \quad \text{with:} \quad \Delta c_{\mathrm{p,i}}(x) = c_{\mathrm{p,i}}(x_{\mathrm{fb}}) - c_{\mathrm{p,i}}(x) \tag{2.84}$$

The drag correction equals the difference of static pressure coefficient $\Delta c_{\mathrm{p,i}}(x)$ in the empty test section between the front bumper location x_{fb} and a downstream location x. Additionally, a dynamic pressure correction $p_{\mathrm{dyn,c}}/p_{\mathrm{dyn}}$ is applied to account for the effects

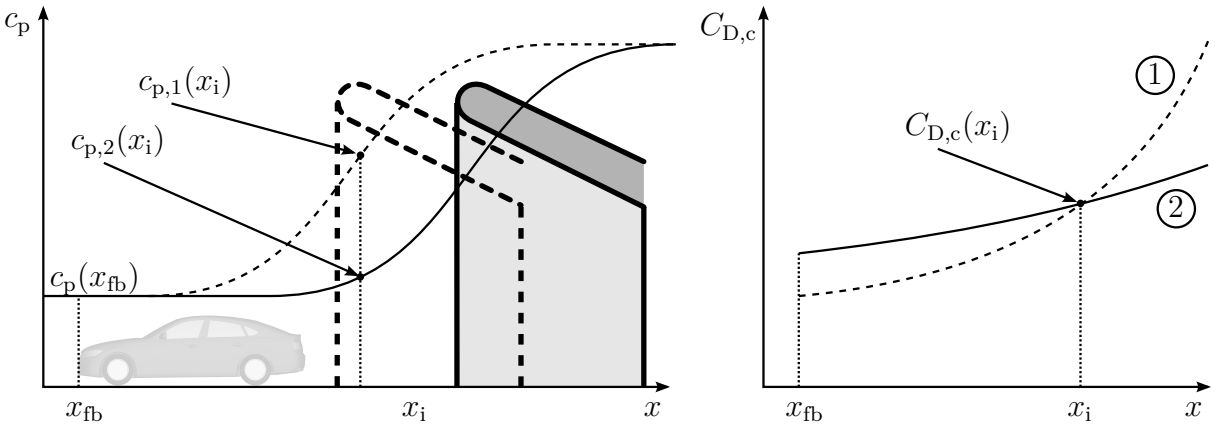

Figure 2.18: "Two-Measurement Correction" approach as presented by Mercker and Cooper (2006) to account for the effect of an empty wind tunnel static pressure gradient (left). The corrected drag coefficient for the pressure distribution 1 and 2 is identical at the position x_i (right).

of nozzle, open jet and collector interference. Starting from the front bumper location, Mercker and Cooper (2006) move the location of x further downstream until the corrected drag for both pressure distributions is identical. This position represents the sensitivity length x_i, see Figure 2.18.

3 Numerical Methods and Validation

One of the essential steps on the way to a modern open jet wind tunnel concept for automotive aerodynamics is to identify and quantify all relevant interference effects for a particular wind tunnel design. The overall system of a closed circle wind tunnel was experienced to be of high complexity. However, the base of every wind tunnel concept is to define the general tunnel dimensions, e.g. the nozzle area A_{N}, the test section length L_{TS} and the longitudinal position of the model x_{c}.

The evaluation of particular interferences applied by the nozzle, the open jet expansion, collector and empty tunnel flow gradients was realized using CFD simulations. The CFD model was developed in order to return the flow around a vehicle for both open road and wind tunnel conditions. The comparison of integral forces and local flow field phenomena returned information about the corresponding interference effects. The full scale DrivAer model was selected to be an appropriate representative for a typical mid-size production car.

3.1 Numerical Methods

Initially, the numerical methods to simulate the flow around a vehicle in open road and wind tunnel conditions were selected. In general, the flow conditions for both the open jet and automotive aerodynamics are highly unsteady. One important aspect were the instabilities within the free mixing shear layer at the boundary of the open jet. An unsteady numerical method was desirable in order to cover these conditions. However, time-resolved simulations such as the Direct Numerical Simulation (DNS) or the Large Eddy Simulation (LES) require a huge amount of computational time and, hence are not (yet) reasonable methods for the simulations of a vehicle inside an open jet wind tunnel in several configurations. Thus, the Delayed Detached-Eddy Simulation (DDES) as a hybrid RANS/LES-method was selected in order to examine open jet interferences. In the following, the simulation method and the setup are explained more in detail.

3.1.1 Delayed Detached-Eddy Simulation (DDES)

The biggest challenge for the simulation of high Reynolds number flows is the effect of turbulence, see e.g. Pope (2000). In the last decades, different CFD methods were applied in order to overcome the requirement of fully resolved turbulence. Simulations based on the Navier-Stokes-Equations were simplified to reduce computational costs. The Reynolds-averaged Navier-Stokes equations (RANS) are based on an averaging of the

Reynolds stress terms within the conservation of momentum. Consequently, the use of turbulence models is necessary. The classical RANS returns a time-averaged solution for an unsteady flow field as all turbulent structures are modeled. The principle of Large Eddy Simulations (LES) is to solve turbulence length scales on grid scale (GS). Accordingly, smaller length scales are modeled using a sub-grid scale (SGS) turbulence model.

Spalart et al. (1997) introduces the Detached-Eddy Simulations (DES) as a hybrid RANS/ LES-method. The DES combines the advantages of partially resolved turbulence of the LES with the considerably lower computational effort of RANS. The principle of the DES is to assign both RANS and LES regions of the flow field. Near wall regions, especially within the boundary layer, are solved using RANS whereas LES is applied to the rest of the flow field. The main advantage of DES is to apply wall functions to the boundary layers and, hence a coarser grid spacing of $y^+ > 1$ is applicable in near wall regions. Spalart et al. (1997) suggests to use the Smagorinsky model for the SGS eddy viscosity and the Spalart-Allmaras (SA) one-equation turbulence model by Spalart and Allmaras (1992) within the RANS regions. The turbulent viscosity $\nu_\mathrm{t} = \tilde{\nu} f_\mathrm{v1}$ is calculated from the transport equation presented by Spalart and Allmaras (1992). Spalart et al. (1997) uses the distance to the closest wall d as well as the grid spacing filter Δ as a criteria in order to adjust the turbulent length scale $\tilde{d}$:

$$\tilde{d} = MIN\left(d, C_\mathrm{DES}\,\Delta\right) \tag{3.1}$$

Thus, the model works as the SA model for $d \ll \Delta$ and as the SGS model for $d \gg \Delta$. C_DES is a model constant whereas Shur et al. (1999) recommends to use $C_\mathrm{DES} = 0.65$. For the SA model the switch between RANS and LES region is independent from the local flow field, but only defined by the local grid spacing Δ. Spalart et al. (1997) presents two methods to calculate Δ for a particular volume cell:

$$\text{maximum length:} \qquad \Delta = MAX\left(\Delta x, \Delta y, \Delta z\right) \tag{3.2}$$

$$\text{equivalent cube:} \qquad \Delta = \sqrt[3]{\Delta x\,\Delta y\,\Delta z} \tag{3.3}$$

The work of Spalart et al. (2006) and Spalart (2009) shows that grid-induced separation may occur if the LES regions are (partially) located inside the boundary layers. Menter and Kuntz (2004) also propose a shielding function to overcome this effect. The Delayed Detached-Eddy Simulation (DDES), as a further development of the DES, applies a shielding function to ensure that the boundary layers are covered by the RANS regions. The shielding function f_d is presented by Spalart et al. (2006) and takes into account the molecular ν and the turbulent viscosity ν_t, the wall distance d as well as the velocity gradients $u_\mathrm{i,j}$ and the Kármán constant κ:

$$r_\mathrm{d} = \frac{\nu_\mathrm{t} + \nu}{\sqrt{u_\mathrm{i,j} u_\mathrm{i,j}}\kappa^2 d^2} \tag{3.4}$$

$$f_\mathrm{d} = 1 - \tanh\left(\left[8 r_\mathrm{d}\right]^3\right) \tag{3.5}$$

$$\tilde{d} = d - f_\mathrm{d}\,MAX\left(0, d - C_\mathrm{DES}\,\Delta\right) \tag{3.6}$$

3.1.2 Numerical Setup

Islam et al. (2009) introduce the application of DES for automotive aerodynamics using the open-source CFD toolbox *OpenFOAM®*. In principle, the CFD method applied in the present work was based on the work of Islam et al. (2009) but includes further development. Consequently, *OpenFOAM®* version 2.3.x distributed by *ESI-OpenCFD* was used in order to run DDES simulations whereas the SA model was applied within the RANS regions. Near the wall the Spalding wall function was used, see Shih et al. (2000).

Grid Generation

The numerical grids were generated with the *snappyHexMesh* utility provided by *OpenFOAM®*, see ESI-OpenCFD (2017). Based on a structured, hexahedral grid *snappyHexMesh* generates a hexa-dominant volume mesh with the option of surface-parallel layers in particular regions. The near-wall layers were spaced in order to achieve a non-dimensional wall distance in the range of $30 \leq y^+ \leq 300$.

CFD Domains

Three general types of CFD domains were used to separate the interference effects for wind tunnel nozzle, open jet, collector and moving ground simulation, see Figure 3.1. The open road (OR) domain was set up as a rectangular shaped box. With a blockage ratio of $A_M/A_N \approx 0.084\,\%$ for the full scale DrivAer model the domain was considered to be quasi-infinite and, hence, free of interference effects. The half-infinite wind tunnel (HIWT) included both a nozzle and an open jet of variable cross section A_N whereas the jet is not restricted at the outlet. Thus, the interference effects were limited to those from the nozzle and the open jet as the plenum dimensions correlated to those of the OR domain. As an upgrade of the half-infinite wind tunnel the finite wind tunnel (FWT) additionally included a collector and a diffusor geometry. Both collector interference and empty tunnel flow gradients were added depending on the particular dimensions. An additional plenum outlet was used in order to define the reference pressure inside the plenum. The plenum dimensions remained quasi-infinite.

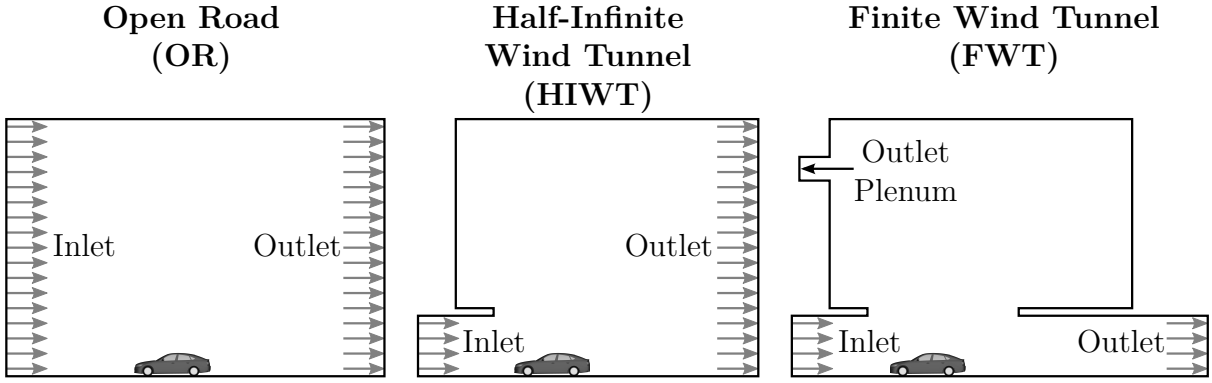

Figure 3.1: CFD domains to cover open road and wind tunnel conditions.

Simulation Procedure and Specifications

The flow field for each simulation was initialized with the potential flow solution calculated with *potentialFoam*, see Figure 3.2 a). For an open jet wind tunnel the *potentialFoam* solution did not return a realistic flow field. However, this initialization was experienced to be the most stable approach. Based, on the initial, in-compressible fields the DDES were run using the PISO-algorithm (Pressure-Implicit with Splitting of Operators), see ESI-OpenCFD (2017). The flow fields were averaged for a time range of 7 s, see Figure 3.2 b) - d) for different wind tunnel configurations. Regarding run time the simulations were split into two phases – the starting and the final phase. The basic idea was to reduce the computational time for the starting phase of the simulation until the flow fields were fully developed. Therefore, a rather large time step of $\Delta t = 10^{-3}$ s was used. After 6 s of physical time, the time step was reduced to $\Delta t = 10^{-4}$ s to increase the accuracy of the simulation. The physical run time for all wind tunnel simulations was 15 s, whereas the flow fields and aerodynamics force coefficients were averaged between $8\,\text{s} \leq t \leq 15\,\text{s}$. For the standard, DrivAer simulations this averaging range was selected in

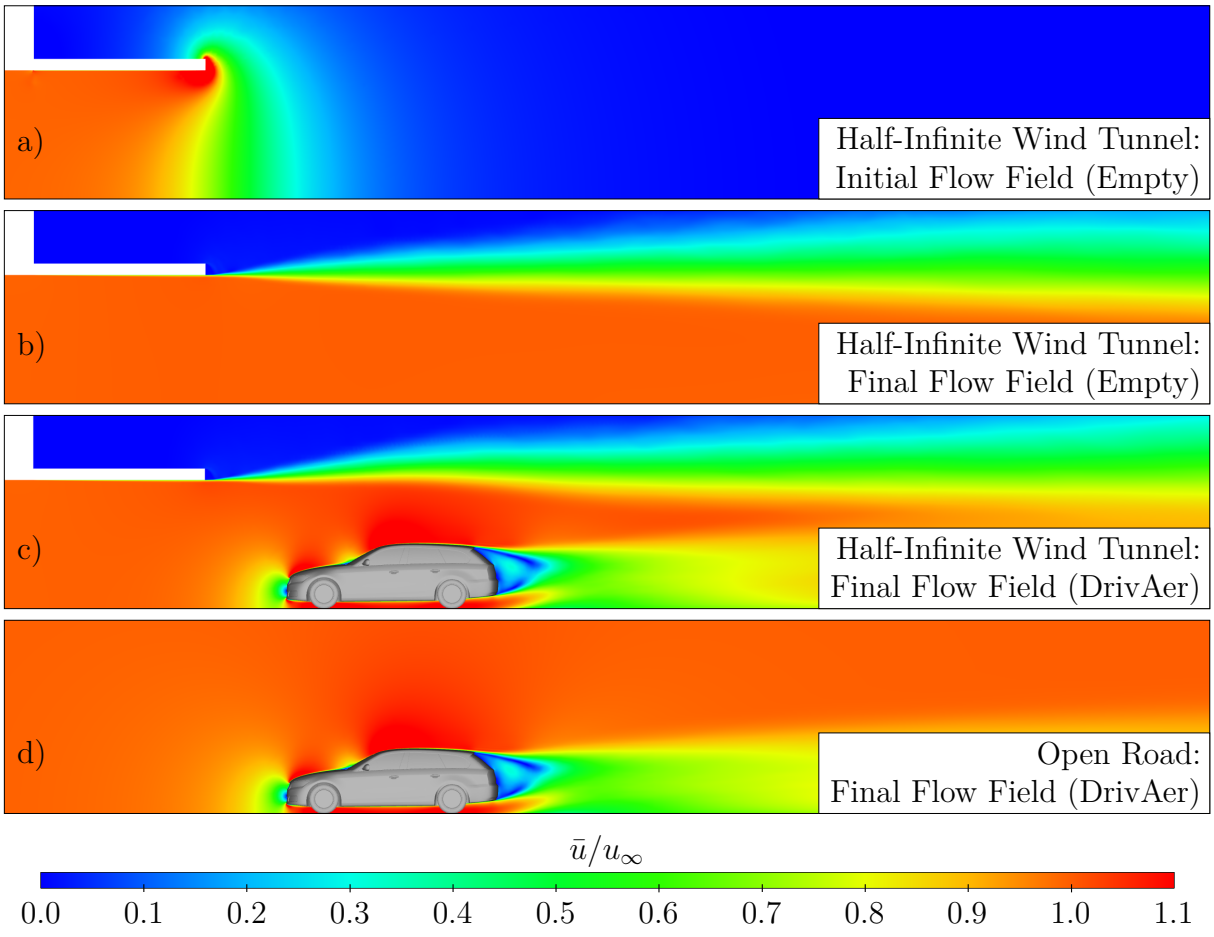

Figure 3.2: Average flow field $\bar{u}/u_\infty$ for different domain configurations: a) Empty, half-infinite wind tunnel after initialization with *potentialFoam*; b) Final field for the half-infinite wind tunnel; c) Final field for the half-infinite wind tunnel with DrivAer; d) Final field for the open road with DrivAer.

order to achieve an average accuracy for each force coefficient of ±0.001. An example for the temporal sequence of the drag and lift coefficient C_D and C_L is presented in Figure 3.3. Furthermore, an overview of the most relevant simulation settings is given in Table 3.1. The discretization of the numerical grid is presented in Table 3.2. It is worth to mention, that the discretization scheme for the convection term of u was adjusted for the starting phase in order to enhance stability. Therefore, a Linear Upwind Stabilized Transport (LUST) was applied to allow high Courant-numbers in the starting phase.

Boundary Conditions

Depending on the CFD domain (open road, half-infinite wind tunnel, finite wind tunnel), different boundary conditions were applied to the domain inlets and outlets, see Table 3.3. For all domain types the inlet boundary was defined as a velocity inlet and with a constant value for the turbulent viscosity, calculated from the inlet velocity as well as from turbulent length and turbulent intensity. Furthermore, a zeroGradient pressure condition was used at the inlet.

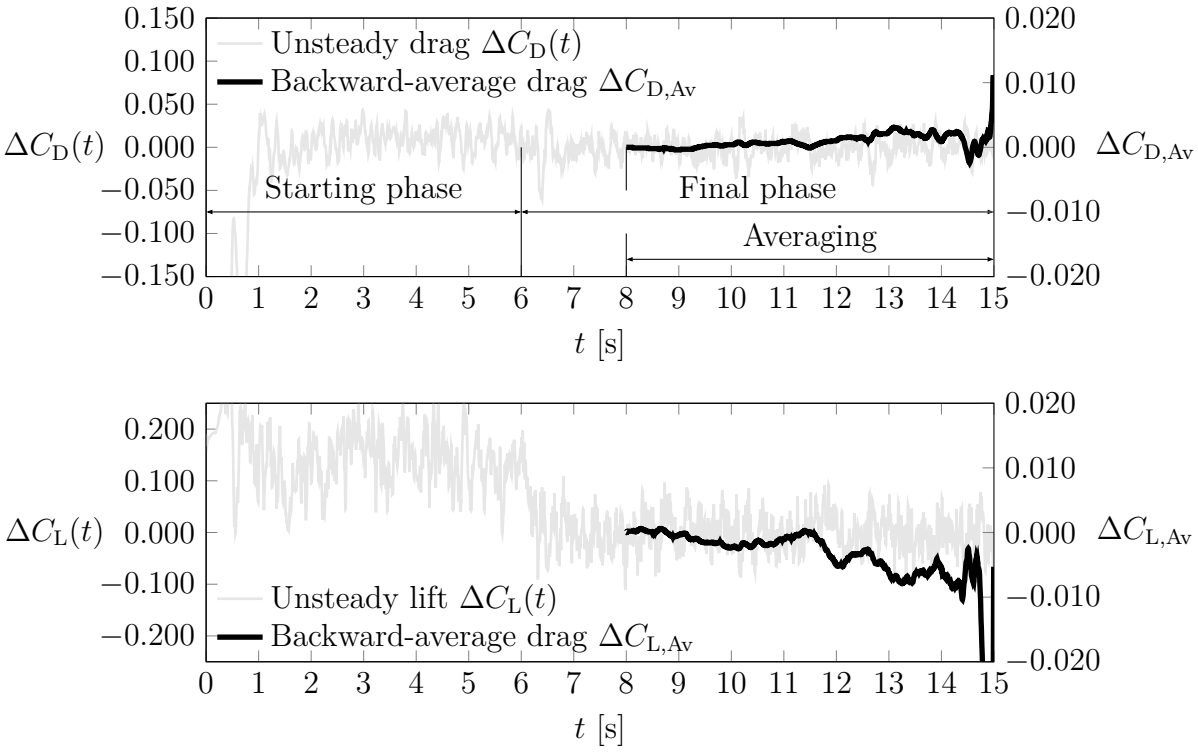

Figure 3.3: Time resolved sequence of the force coefficients C_D and C_L for the starting and the final phase of the simulation. $\Delta C_\mathrm{D}(t)$ and $\Delta C_\mathrm{L}(t)$ denote the unsteady, raw coefficients whereas $\Delta C_\mathrm{D,Av}$ and $\Delta C_\mathrm{L,Av}$ represent the backward average coefficients from $t = 15\,\mathrm{s}$. ΔC_i refer to the overall average of the corresponding coefficient C_i.

Table 3.1: Simulation settings and specifications for the CFD wind tunnel studies using the mock-up DrivAer Geometry.

		Open Road OR	**Half-Infinite Wind Tunnel HIWT**	**Finite Wind Tunnel FWT**
Number of Volume Cells		$7 - 10 \cdot 10^7$	$9 - 16 \cdot 10^7$	$10 - 12 \cdot 10^7$
Computational Run Time		$50 - 100\,\mathrm{h}$	$80 - 120\,\mathrm{h}$	$110 - 120\,\mathrm{h}$
Number of Cores			512	
Density	ϱ		$1.1584\,{}^{\mathrm{kg}}/_{\mathrm{m}^3}$	
Kinematic Viscosity	ν		$1.5711 \cdot 10^{-5}\,{}^{\mathrm{m}^2}/_{\mathrm{s}}$	
Reynolds-Number	Re		$\approx 1.1 \cdot 10^7$	
Velocity	u_∞		$38.888888\,{}^{\mathrm{m}}/_{\mathrm{s}}$	
Turbulence Length	L_{turb}		$0.01\,\mathrm{m}$	
Turbulence Intensity	T_{U}		$0.5\,\%$	
Starting Phase			$0\,\mathrm{s} \leq t \leq 6\,\mathrm{s}; \Delta t = 10^{-3}\,\mathrm{s}$	
Final Phase			$6\,\mathrm{s} \leq t \leq 15\,\mathrm{s}; \Delta t = 10^{-4}\,\mathrm{s}$	
Time Averaging			$8 - 15\,\mathrm{s}$	

Table 3.2: Discretization of the numerical grid for DDES. The keywords conform to the nomenclature of *OpenFOAM®* as presented by ESI-OpenCFD (2017).

Mathematical Term	**Keyword**
$\partial/\partial t$	backward
∇u, $\nabla \tilde{\nu}$	cellLimited Gauss linear
∇p	Gauss linear
$\nabla \cdot (\Phi u)$	Gauss CoBlended: LUST, linearUpwind (start)
	Gauss CoBlended: filteredLinear2V, linearUpwind (final)
$\nabla \cdot (\Phi \tilde{\nu})$	linearUpwind
$\nabla^2()$	Gauss linear limited corrected

The outlet boundary conditions were identical for the open road and half-infinite wind tunnel domain. For the half-infinite wind tunnel domain the pressureInletOutletVelocity was the only stable approach for u to deal with the entrainment of the free shear layer. Furthermore, it was essential to use also the totalPressure condition, which defined the reference pressure $p_\infty = 0$ at the outlet. For the finite wind tunnel domain, the definition of the reference pressure was set at the plenum outlet in order to achieve $p_\infty = 0$ in the plenum chamber. Therefore, a zeroGradient condition was used at the outlet of the high speed wind tunnel diffusor. To ensure real, closed circle wind tunnel conditions, the mass flow through the collector and the diffusor was enforced using a fixedMean condition for u at the outlet, which was calculated from the mass flow through the nozzle. With this approach the final mass flow through the plenum outlet was controlled to be zero.

All other boundaries related to the wind tunnel and the model were either slip or friction walls. For slip walls the slip keyword was used for all fields p, u, $\tilde{\nu}$ and ν_{SGS}. For friction

Table 3.3: Boundary conditions of p, u, $\tilde{\nu}$ and ν_{SGS} for the different domains (OR: Open Road, HIWT: Half-Infinite Wind Tunnel, FWT: Finite Wind Tunnel) expressed as *OpenFOAM®* keywords, see ESI-OpenCFD (2017).

Boundary	Domain	p	u	$\tilde{\nu}$, ν_{SGS}
Inlet	**OR** **HIWT** **FWT**	zeroGradient	surfaceNormalFixedValue	fixedValue
Outlet	**OR** **HIWT**	totalPressure	pressureInletOutletVelocity	zeroGradient
	FWT	zeroGradient	fixedMean	
Outlet Plenum	**FWT**	totalPressure	pressureInletOutletVelocity	zeroGradient

walls such as parts of the nozzle and the collector as well as the model the conditions zeroGradient for p, fixedValue for $u = 0$ and $\tilde{\nu} = 0$ and the nutUSpaldingWallFunction for ν_{SGS} were applied. An additional condition was used for the wheels for u. The wheels were treated as friction walls, but the rotatingWallVelocity condition simulated the wheel rotation. It was well known that this approach requires a rotationally symmetrical rim design, which was present for the DrivAer but not for the race car simulations. Waeschle (2007) shows methods to increase the accuracy, e.g. by using sliding mesh simulations. However, computational time was limited and sliding mesh hence not reasonable. The moving belt in case of ground simulation was simulated with translatingWallVelocity.

3.2 Validation of the CFD Model

The numerical methods introduced in section 3.1 were validated using test cases and experimental data. The DrivAer reference model was selected to evaluate the basic wind tunnel interferences for nozzle, open jet and collector in chapter 4. In preparation, the following section describes both the simulation of the DrivAer aerodynamics and of the wind tunnel aerodynamics for the Audi Aeroacoustic Wind Tunnel (AAWK). The validation included the comparison of flow field characteristics such as velocity and static pressure. Furthermore, the interaction of the AAWK with an Audi A4 series production car was validated with respect to the aerodynamic force coefficients measured with different wind tunnel characteristics, e.g. longitudinal model position in the test section.

3.2.1 DrivAer Simulations

In the present work, two general configurations of the DrivAer model were considered to validate the numerical methods – the mock-up and the open cooling model. Both the results from experimental and numerical investigations, using the 40 % scale model of the TUM, are presented below.

Mock-up DrivAer Model

Collin et al. (2016) present results of CFD simulations of the mock-up DrivAer with generic, closed rims and smooth underfloor inset with different rear ends. The 40 % scale model was tested in the WTA and in the AAWK whereas the measurement equipment for the force measurements were identical in both tunnels. Furthermore, the model setup was comparable as the main body was attached to a top strut and each wheel was supported by wheel struts, see Figure 3.4. A six-component, internal balance and four one-component, wheel balances measured the aerodynamic forces. Following this approach, both drag and lift forces acting on the main body were measured, whereas only drag was captured for the wheels[1]. The rear ends for the main body were modular for estateback, notchback and fastback. Figure 3.5 shows the experimental setup in the wind tunnels WTA and AAWK. The main differences for the testing conditions in both facilities were the blockage ratio, test section length and the moving ground simulation (e.g. moving belt width). The main specifications for WTA and AAWK are presented in Table 3.4.

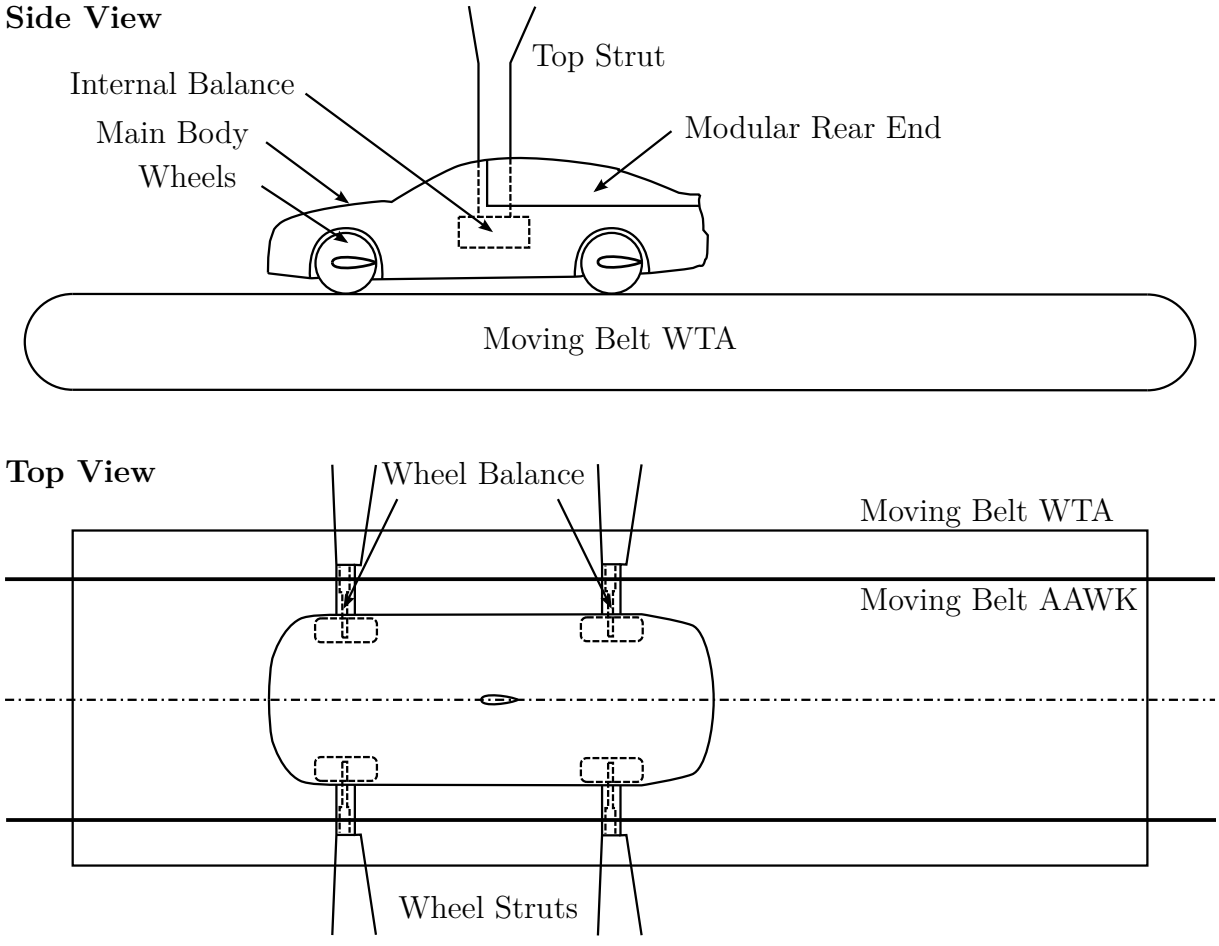

Figure 3.4: Methodology for the model support for the DrivAer model. The main body with modular rear ends was attached to a top strut using an internal, six-component balance. The wheels were supported separately by one-component balances via wheel struts.

[1]Due to the wheel support via wheel struts the wheels were decoupled from the main body.

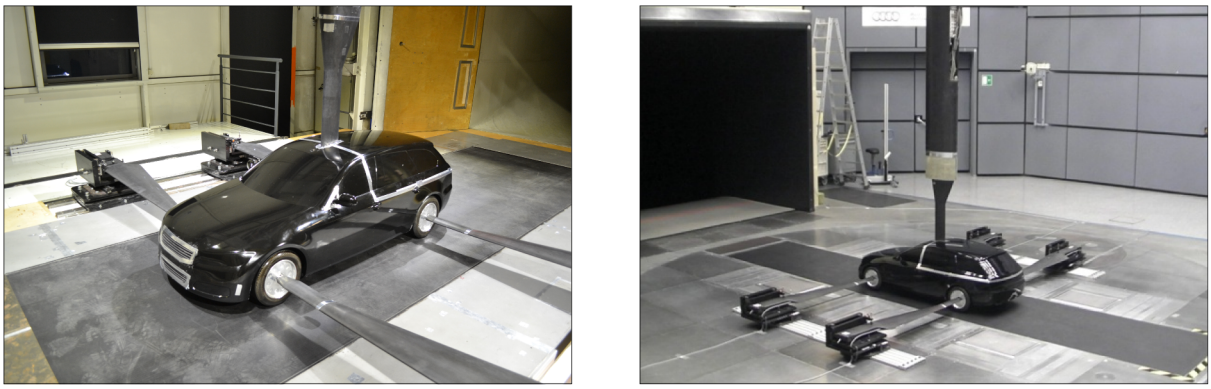

Figure 3.5: Experimental setup as presented by Collin et al. (2016) and Collin et al. (2018) of the 40 % scale DrivAer model of the TUM in the WTA (left) and in the AAWK (right).

Table 3.4: Specifications of the wind tunnel facilities WTA and AAWK as presented by Collin et al. (2016), Wickern and Lindener (2000) and Mack et al. (2012).

	WTA at TUM	**AAWK at Audi**
Nozzle Size W_N x H_N	1.80 m x 2.40 m	2.79 m x 3.94 m
Nozzle Cross Section A_N	4.32 m^2	11.00 m^2
Contraction Ratio	7.0:1	5.5:1
Length of Test Section	4.80 m	9 m – 10 m
Collector Cross Section	7.54 m^2	37.5 m^2
Model Position	$x_c = 2$ m	$x_c = 4$ m
Belt Dimensions L_B x W_B	4.53 m x 1.39 m	5.50 m x 1.00 m
Max. Speed of Belt	50 m/s	65.3 m/s
Material of Belt	Polyester-Based	Polyester-Based
Boundary Layer Treatment	Scoop (adjustable)	Suction System (adjustable)
Max. Inflow Velocity	65.0 m/s	83.3 m/s
Turbulence Level	< 0.4 %	< 0.3 %
Displacement Thickness [a]	1.9 mm	< 1.0 mm
Boundary Layer Thickness [a]	29 mm	23 mm

[*] Measured at the center of the turntable/model at $y = 0$ m.

The wind tunnel interference effects were expected to be negligible[1] for the AAWK as the solid blockage was in the range of $A_M/A_N \approx 3\,\%$. Thus, for the simulations the open road domain, presented in Figure 3.1 in section 3.1.2, was selected. Furthermore, Heft (2014) shows that the proximity of the model support is known to affect the aerodynamics of the DrivAer model significantly. Thus, both simulations with and without top strut and wheel struts were run in order to evaluate the effect in CFD. An overview of the experimental and numerical tests is presented in Table 3.5.

[1]The blockage ratio was considered to be negligible. However, interferences due to e.g. boundary layer treatment and/or empty tunnel flow gradients could not be sufficiently excluded.

Table 3.5: Conditions in experiments and CFD for the validation of the DrivAer simulations as presented by Collin et al. (2016).

	Experiment TUM	**Experiment Audi**	**CFD with Struts**	**CFD w/o Struts**
Model Scale	1:2.5	1:2.5	1:1	1:1
Reynolds Number	$5.2 \cdot 10^6$	$5.2 \cdot 10^6$	$1.1 \cdot 10^7$	$1.1 \cdot 10^7$
Dynamic Pressure	NM	NM	Inlet Velocity	Inlet Velocity
Domain	WTA	AAWK	Open Road	Open Road
Blockage Ratio	8.02 %	3.15 %	< 0.084 %	< 0.084 %
Moving Ground	Single Belt	Single Belt	Infinite Belt	Slip
Struts	yes	yes	yes	no

It is worth to mention, that the CFD simulations were run on a Reynolds number of $Re \approx 1.1 \cdot 10^7$ as it was representative for a full scale production car case at $u \approx 38.9\,\mathrm{m/s}$. However, Collin et al. (2016) show that the effect of $Re > 5.5 \cdot 10^6$ is expected to be negligible.

The model support using top strut and wheel struts was expected to cause interference effects with the model. Thus, the CFD simulations were set up with and without the struts. In the simulations without struts a slip ground condition was applied as it matched the latter simulation setup, which was used to evaluate the open jet interferences in chapter 4. The setup with struts was selected to cover the experiments as good as possible. Therefore, a moving ground was applied to the simulations instead of the slip floor condition without struts. For all simulations and experiments the DrivAer model was tested with different rear ends: estateback (EB), fastback (FB) and notchback (NB).

In general, no wind tunnel corrections were applied for the comparison between experiments and CFD. It is well known that, especially for the wind tunnel measurements in the WTA, corrections might be required as the blockage ratio of approximately 10 %, the gradient in static pressure as well as nozzle and collector interference were not negligible. However, for the measurements in the AAWK the blockage ratio was rather low and interference effects expected to be negligible.

The results for the experiments at TUM and Audi as well as for the CFD simulations with and without struts are given in Table 3.6 and Table 3.7. Table 3.6 contains the absolute coefficients for drag C_D, front lift $C_\mathrm{L,f}$ and rear lift $C_\mathrm{L,r}$. The drag coefficient at TUM and WTA matches in the range of ± 0.001 for all rear ends investigated. This result was somewhat surprising as larger interference effects were expected for the WTA. However, the model position was selected in order to balance the static pressure gradient between the front and the rear end and the nozzle method was used, following the self-correcting approach of Wickern (2014). Thus, a compensation of the overall interferences for drag was possible. Larger differences of up to 0.020 - 0.030 occurred for the front lift coefficient. However, reasons for the can be the differences in moving belt width as the belt in the AAWK barely covered the model. Collin et al. (2017) experience a significant influence of belt width especially on the $C_\mathrm{L,f}$. Furthermore, a high sensitivity of front lift with respect

Table 3.6: Aerodynamic force coefficients for drag C_D, front lift $C_{L,f}$ and rear lift $C_{L,r}$ from experimental and numerical data as presented by Collin et al. (2016). DrivAer configuration: mock-up, smooth underfloor, generic wheels (closed), with mirrors.

		Experiment TUM	**Experiment Audi**	**CFD with Struts**	**CFD w/o Struts**
C_D	Estateback	0.299	0.298	0.299	0.295
	Fastback	0.252	0.251	0.251	0.244
	Notchback	0.255	0.255	0.255	0.247
$C_{L,f}$	Estateback	−0.093	−0.069	−0.122	−0.107
	Fastback	−0.063	−0.039	−0.090	−0.085
	Notchback	−0.057	−0.033	−0.087	−0.078
$C_{L,r}$	Estateback	−0.061	−0.062	−0.093	−0.098
	Fastback	0.055	0.063	0.039	0.044
	Notchback	0.029	0.037	0.014	0.024

Table 3.7: Rear end deltas for drag ΔC_D, front lift $\Delta C_{L,f}$ and rear lift $\Delta C_{L,r}$ from experimental and numerical data as presented by Collin et al. (2016). DrivAer configuration: mock-up, smooth underfloor, generic wheels (closed), with mirrors.

		Experiment TUM	**Experiment Audi**	**CFD with Struts**	**CFD w/o Struts**
ΔC_D	EB - FB	0.048	0.047	0.048	0.052
	EB - NB	0.044	0.043	0.044	0.048
	FB - NB	−0.004	−0.004	−0.004	−0.003
$\Delta C_{L,f}$	EB - FB	−0.030	−0.030	−0.032	−0.022
	EB - NB	−0.036	−0.036	−0.035	−0.029
	FB - NB	−0.005	−0.005	−0.003	−0.007
$\Delta C_{L,r}$	EB - FB	−0.116	−0.125	−0.132	−0.142
	EB - NB	−0.090	−0.099	−0.107	−0.122
	FB - NB	0.026	0.026	0.025	0.020

to the pitching angle was investigated during the measurements in the WTA. The match for $C_{L,r}$ was in the range of lower than 0.010.

Comparing the CFD results with the measurements, a good agreement of $\Delta C_D = \pm 0.001$ was achieved by adding the struts to the model. Bigger differences occurred for both $\Delta C_{L,f} \approx \pm 0.030$ and $\Delta C_{L,f} \approx \pm 0.030$. However, CFD generally showed a better match if the struts were included, especially for the rear end deltas, see Table 3.7.

Open Cooling DrivAer Model

In addition to the DrivAer mock-up model, the existing 40 % scale model of the TUM was upgraded with the latest open cooling geometry presented by Wittmeier and Kuthada (2015). A comparison of the geometry for mock-up and open cooling DrivAer is given in Figure 3.6. In principle, the underfloor did not change significantly except for the transmission tunnel. The open cooling version includes an adapted engine and gearbox combination in order to create a cooling outlet at the rear end of the engine under-shield. Additional outlets were located inside the front wheel houses. This model update included a set of new parts such as upper and lower grille, radiator package, engine compartment, engine, gearbox, exhaust pipes as well as a new underfloor inset. More information about the upgrade is presented by Collin et al. (2018).

The radiator package was designed as a stack of two honeycombs, a perforated sheet and the fan shroud, see Figure 3.7 left. Sealing frames were applied between these components in order to prevent leakage flow. The perforated sheets were parametric with respect to the position (W_0, H_0, a), the diameter d and the number of holes N, see Figure 3.7 right. The parameters were adjusted to achieve different openness ratios in the range of $5\,\% < A_\mathrm{o}/A_\mathrm{c} < 50\,\%$:

$$A_\mathrm{o}/A_\mathrm{c} = \frac{\frac{\pi}{4} d^2 N}{W\ H} \tag{3.7}$$

The corresponding pressure drop curves of the package including honeycombs and perforated sheets were determined experimentally, see Figure 3.8. Additionally, the curve of Wittmeier and Kuthada (2015) is given, which is located in the middle range of the investigated sheets.

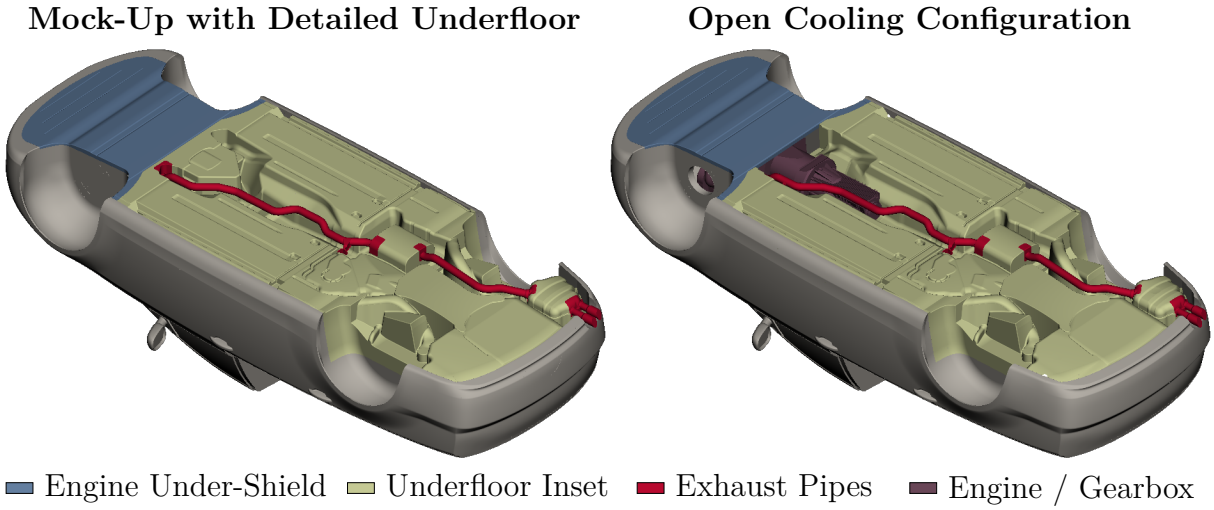

Figure 3.6: Geometry changes from the mock-up DrivAer with detailed underfloor inset (left) towards the open cooling DrivAer model (right) as presented by Collin et al. (2018).

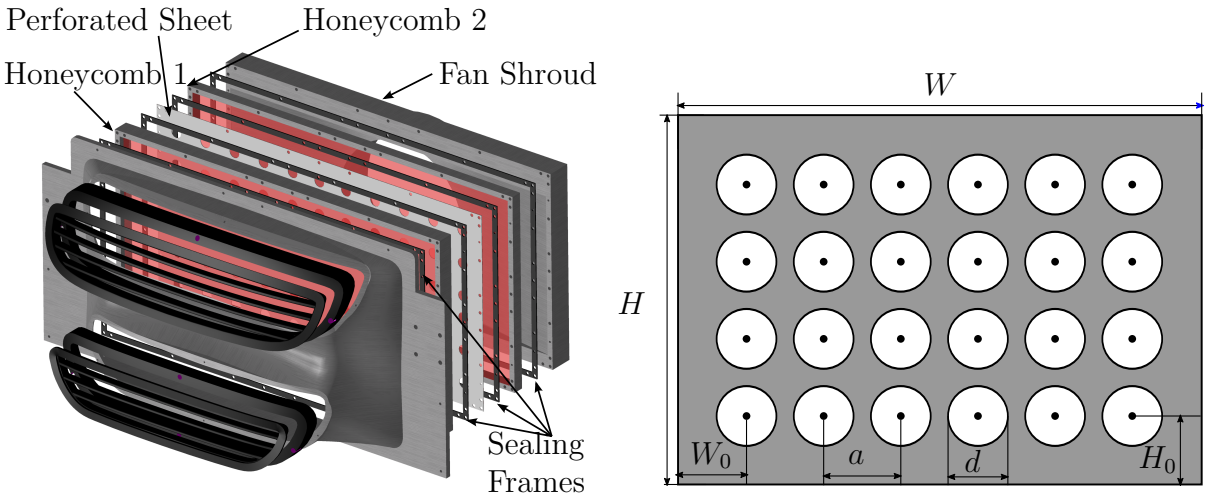

Figure 3.7: Radiator package assembly for the 40 % scale model (left) and parameters for the perforated sheet dimensions (right) as presented by Collin et al. (2018).

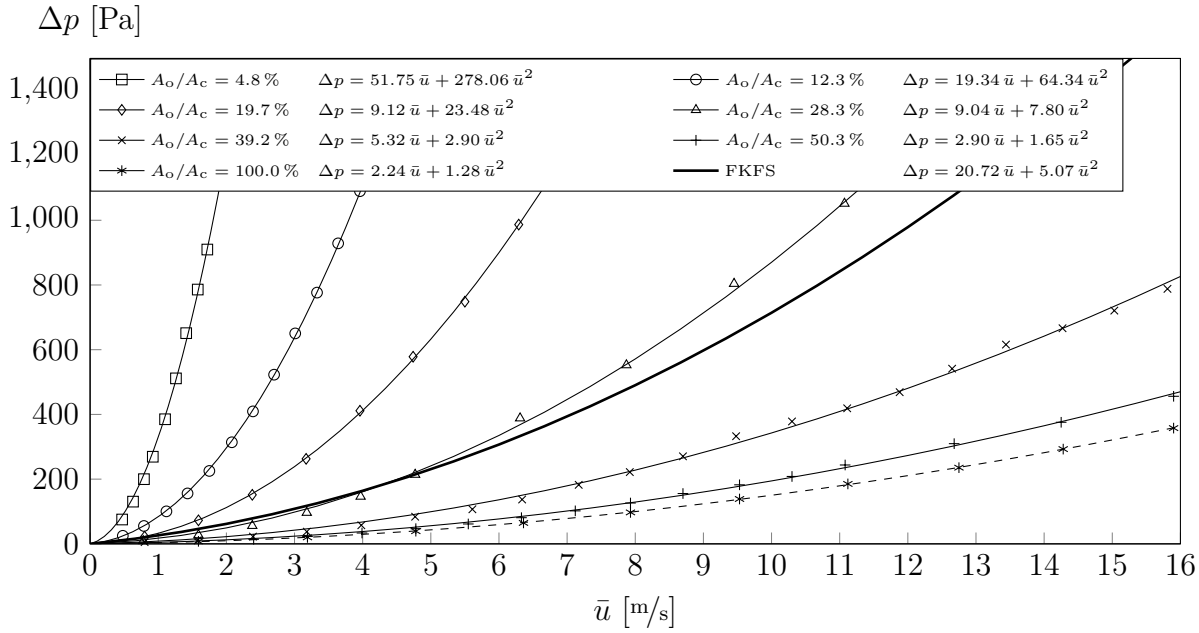

Figure 3.8: Pressure drop curves for different perforated sheets in the radiator assembly as presented by Collin et al. (2018). A_o/A_c denotes the openness ratio of the sheets. The FKFS data is based on the work of Wittmeier and Kuthada (2015).

After upgrading the DrivAer model with open cooling the first measurements were obtained using the new geometry with closed cooling in order to compare the results with existing data. Therefore, the model was set up in the WTA of the TUM using the same approach as described above for the mock-up model, see e.g. Figure 3.5 left. The results for both the absolute values for C_D, $C_{L,f}$ and $C_{L,r}$ and the cooling deltas $\Delta C_{D,c}$, $\Delta C_{L,f,c}$ and $\Delta C_{L,r,c}$ are presented in Table 3.8.

Table 3.8: Aerodynamic force coefficients for drag C_D, front lift $C_{L,f}$ and rear lift $C_{L,r}$. The TUM values are presented by Collin et al. (2018), the FKFS 2015 values by Wittmeier and Kuthada (2015) and both the FKFS 2018 and Ford 2018 by Hupertz et al. (2018).

Wind Tunnel Facility		**TUM**	**FKFS 2015**	**FKFS 2018**	**Ford**
Dynamic Pressure		**NM**	**PM**	**PM**	**NM**
Model Scale		**1:2.5**	**1:4**	**1:4**	**1:1**
C_D	Estateback	0.314	0.312		
	Fastback	0.279			
	Notchback	0.279	0.277	0.273	0.252
$C_{L,f}$	Estateback	−0.078	−0.070		
	Fastback	−0.045			
	Notchback	−0.040	−0.039	0.035	−0.026
$C_{L,r}$	Estateback	−0.001	0.011		
	Fastback	0.109			
	Notchback	0.087	0.098	0.117	0.114
$\Delta C_{D,c}$		0.008	0.007	0.012	0.011
$\Delta C_{L,f,c}$	Notchback	0.031	0.026	0.041	0.032
$\Delta C_{L,r,c}$		−0.032	−0.030	−0.019	−0.032

Table 3.9: Characteristics of perforated sheets. The coefficients C_1 and C_2 denote the coefficients from Figure 3.8. D and F denote the Darcy-Forchheimer coefficients determined at 27 °C and $p_\infty = 990\,\mathrm{hPa}$, $\varrho = 1.135\,\mathrm{kg/m^3}$, $\mu = 1.85 \cdot 10^{-5}\,\mathrm{Pa\,s}$.

A_o/A_c	d	a	W_0	H_0	C_1	C_2	D	F
%	mm	mm	mm	mm	kg/s	kg/m	1/m²	1/m
50.3	4.0	5.0	7.5	7.5	2.90	1.65	$6.03 \cdot 10^6$	$1.12 \cdot 10^2$
39.2	2.5	3.5	8.3	7.8	5.32	2.90	$1.10 \cdot 10^7$	$1.96 \cdot 10^2$
28.3	1.5	2.5	6.3	6.3	9.04	7.80	$1.88 \cdot 10^7$	$5.29 \cdot 10^2$
19.7	1.0	2.0	5.5	6.0	9.12	23.48	$2.67 \cdot 10^7$	$1.54 \cdot 10^3$
12.3	1.0	2.5	7.5	7.5	19.34	64.34	$5.26 \cdot 10^7$	$4.23 \cdot 10^3$
4.8	1.0	4.0	7.5	8.0	51.75	278.06	$1.07 \cdot 10^8$	$1.89 \cdot 10^4$

Summarizing, a good agreement of the absolute coefficients measured in this work was achieved compared to the FKFS 2015. Bigger differences occurred in comparison to the FKFS 2018 and Ford 2018. However, explanations for this are differences in model scale and, hence, Reynolds number as well as the wind tunnel facilities. Apart from this, a better agreement for all selected models and wind tunnel was gained in terms of cooling deltas. More details for these comparisons are presented by Collin et al. (2018) and Hupertz et al. (2018).

For the CFD simulations of the open cooling DrivAer, in principle, the setup for the mock-up DrivAer was adopted but the Reynolds-number was reduced to 4.9 million in order to

meet the conditions from the experiments. The simulations were performed with moving ground simulation including the moving belt dimensions of the WTA as well as the model support of the 40 % scale model. Two particular DrivAer configurations were selected – the estateback and the notchback with open wheel houses and different perforated sheets. Therefore, the Darcy-Forchheimer law was used, see ESI-OpenCFD (2017):

$$\frac{\Delta p}{\Delta x} = -\left(\mu\, u\, D + \frac{1}{2}\varrho\, u^2\, F\right) \tag{3.8}$$

An overview of the specifications for the perforated sheets is presented in Table 3.9.

The results for the cooling deltas of the estateback and the notchback in both experiments and CFD are illustrated in Figure 3.9. A good agreement of $\Delta C_{\mathrm{D,c}} < 0.001$ and $\Delta C_{\mathrm{L,i,c}} < 0.010$ between CFD and experiments was achieved in all configurations investigated.

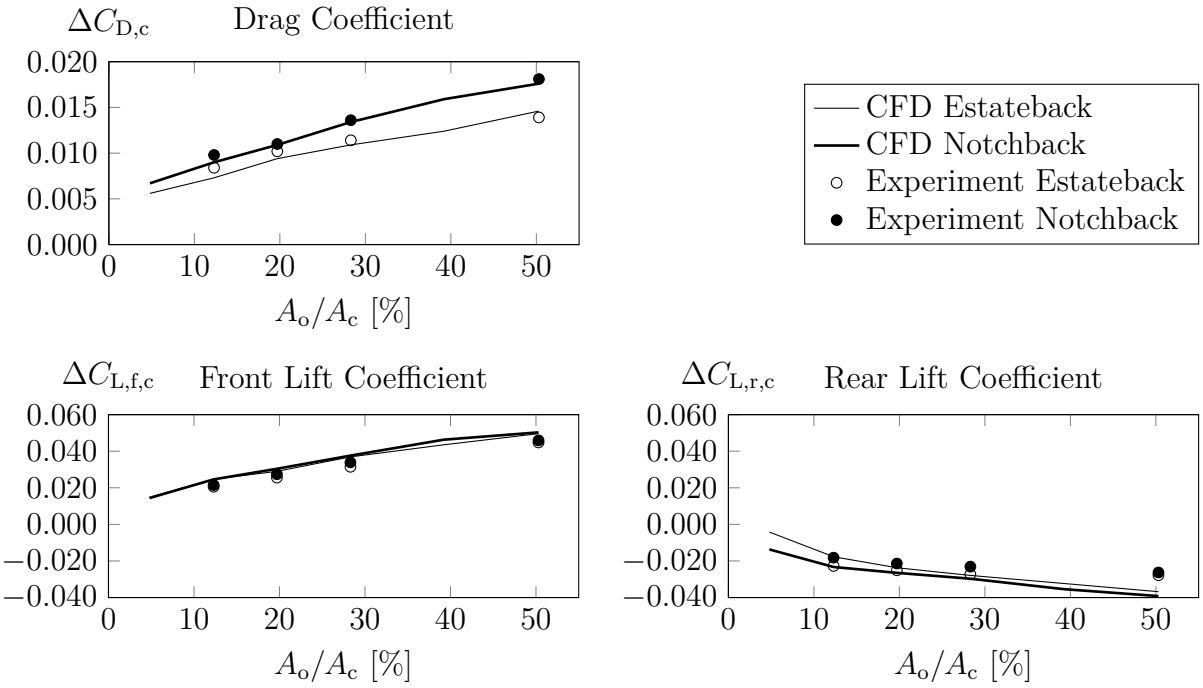

Figure 3.9: CFD and experiment: Effects of underhood flow on aerodynamic force coefficients for drag $\Delta C_{\mathrm{D,c}}$, front lift $\Delta C_{\mathrm{L,f,c}}$ and rear lift $\Delta C_{\mathrm{L,r,c}}$ as presented by Collin et al. (2018). $A_{\mathrm{o}}/A_{\mathrm{c}}$ denotes the openness ratio of the perforated sheets.

3.2.2 Wind Tunnel Simulations

In the second step of the validation for the CFD methods the interference between model and wind tunnel was tested. This approach started with the simulation of an empty, half-infinite open jet test section in order to evaluate the sensitivities and challenges in the prediction of the open jet propagation. After that the simulation of the Audi Aeroacoustic Wind Tunnel with and without a production car will be presented.

Half-Infinite Wind Tunnel Domain

As already introduced in section 3.1.2 the half-infinite wind tunnel domain was selected to reduce the relevant wind tunnel interferences to those applied by the wind tunnel nozzle and the open jet. The most important dimensions are shown in Figure 3.10.

The wind tunnel nozzle was simplified towards a rectangular channel and, hence, no converging region was present to formulate a general condition, independent from a specific nozzle geometry. However, the fixed condition in terms of the nozzle was the width-to-height ratio, which constant with $W_N/H_N = 1.4$. The length of the nozzle was 13.7 m, which was determined to be a sufficient distance to prevent any upstream interference of the inlet with the model. The length of the test section was 60 m and, hence, considered to be infinite.

For the simulations of the empty, half-infinite test section the grid resolution of the free shear layer at the jet boundary turned out to be an essential factor as it had a strong impact on the free jet propagation. This effect is presented in Figure 3.11 for the unsteady velocity field u/u_∞ and Figure 3.12 for the average velocity field $\bar{u}/u_\infty$ in the symmetry plane of the tunnel $y = 0$ up to $x = 10$ m downstream of the nozzle exit.

In general, the grid size in the empty test section was constant at ≈ 46.8 mm. However, the grid resolution was partially increased to properly resolve the velocity gradients in the free shear layer in y- and z-direction. Figure 3.11 and 3.12 a) present the field for the coarsest grid investigated. In the first 2-3 m downstream the nozzle exit the shear layer appeared to be rather stable as the grid was too coarse to resolve the turbulent structure on grid scale. Further downstream the eddies were (partially) resolved. The point of firstly resolving eddies in the shear layer led to an abrupt expansion of the shear layer velocity profile, see Figure 3.12. Comparing the result for the high resolution mesh with a grid spacing of 2.9 mm, the first turbulent structures appeared further upstream

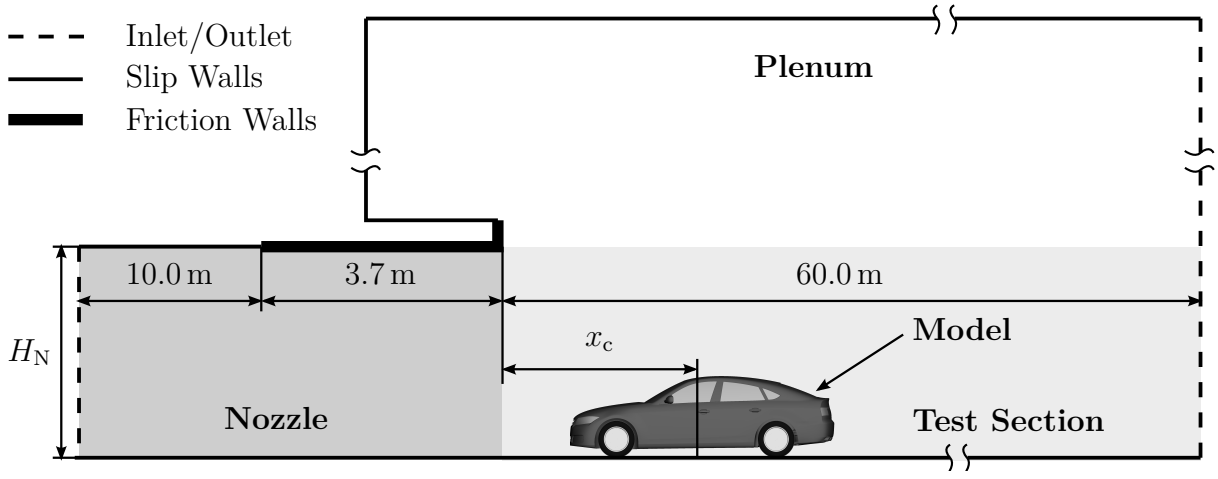

Figure 3.10: Dimensions of the half-infinite wind tunnel in the plane $y = 0$. H_N denotes the nozzle height and x_c the distance between nozzle exit to the wheel base center of the model.

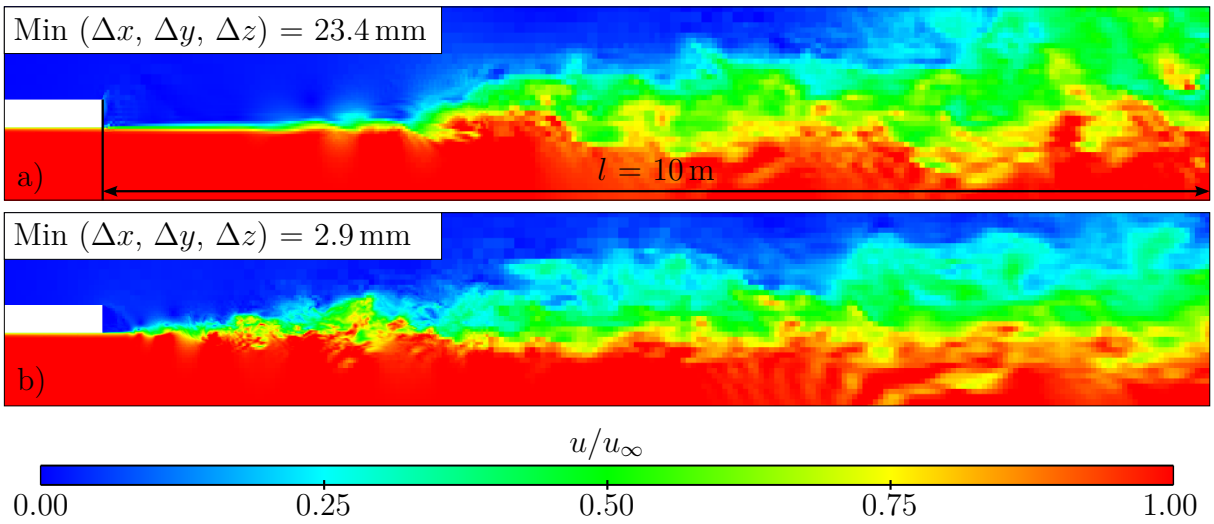

Figure 3.11: Unsteady velocity field u/u_∞ for different grid resolutions Δx, Δy, Δz within the free shear layer downstream a nozzle with 11 m^2: a) 23.4 mm; b) 2.9 mm.

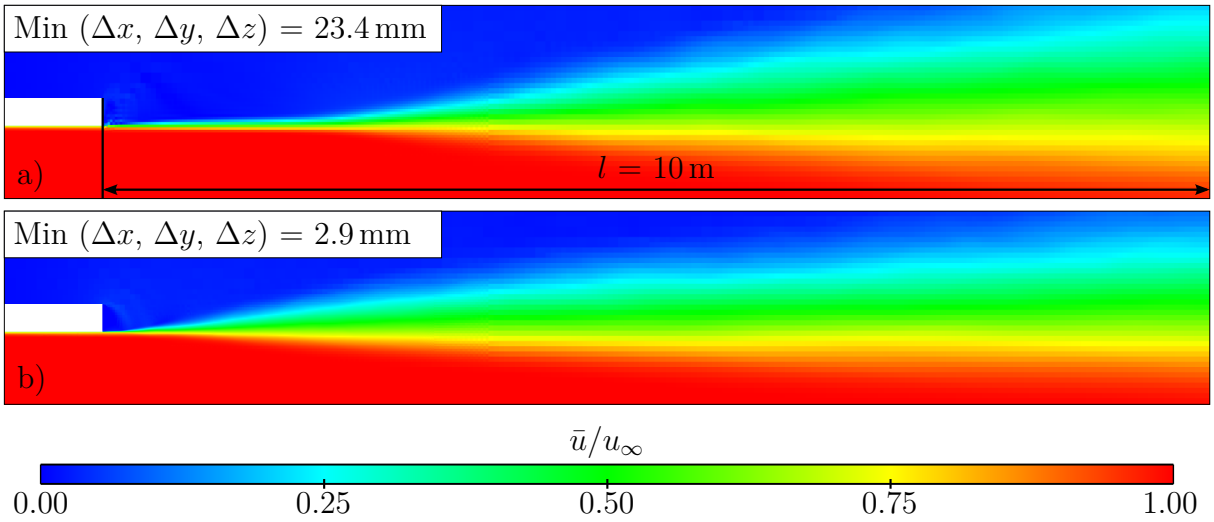

Figure 3.12: Average velocity field u/u_∞ for different grid resolutions Δx, Δy, Δz within the free shear layer downstream a nozzle with 11 m^2: a) 23.4 mm; b) 2.9 mm.

(≈ 0.2 m downstream the nozzle exit). The result was a more consistent expansion of the free, turbulent shear layer, also in the average velocity field.

A grid size of 2.9 mm turned out to be the highest, reasonable resolution for a full wind tunnel simulation including a vehicle model, even though a grid-converged solution could not be guaranteed. This condition was applied not only because of the number of cells but also due to the fact that a higher resolution forced a further decrease of the time step $< 10^{-4}$ s. Furthermore, also for 2.9 mm the shear layer was only partially resolved with the highest resolution, see Figure 3.13. The basic idea was to use the highest resolution only in the area of the largest velocity gradients close to the nozzle exit.

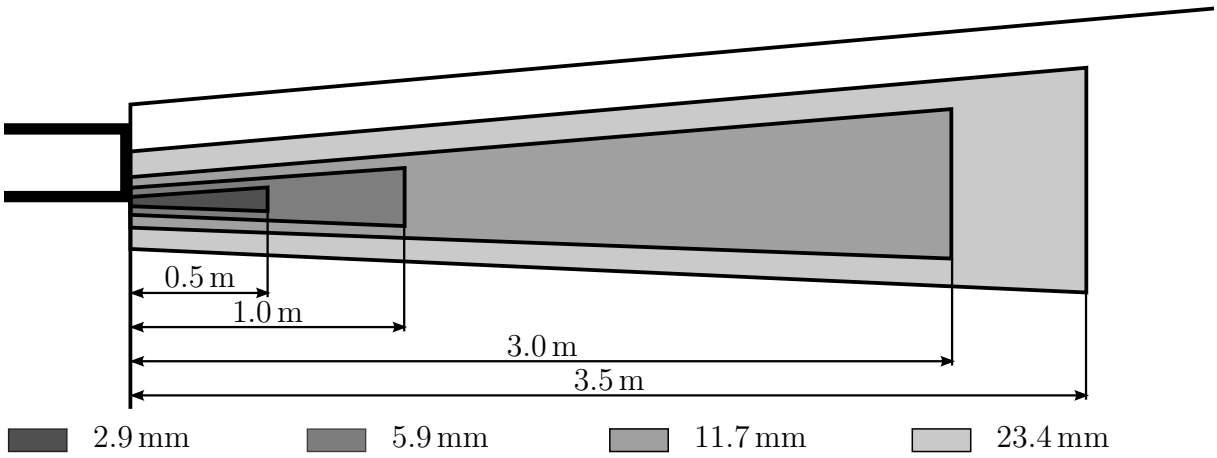

Figure 3.13: Final grid refinement and length of the refinement regions.

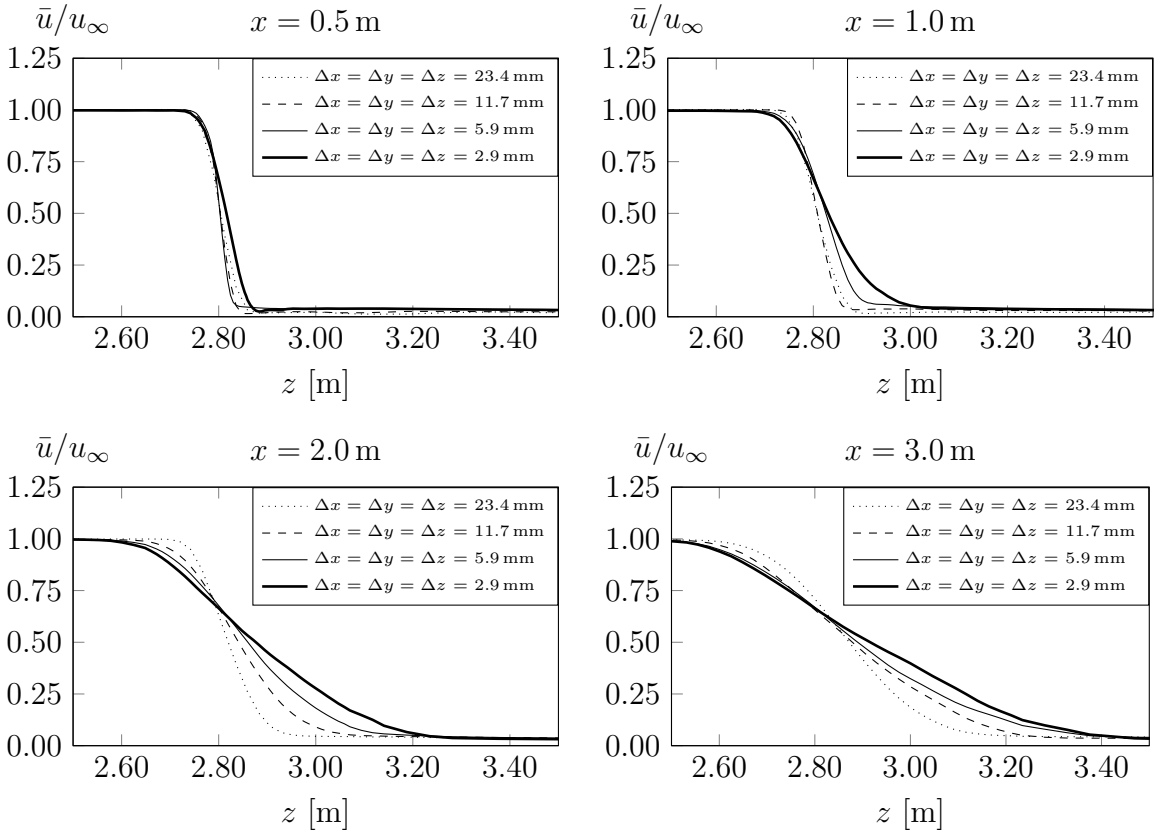

Figure 3.14: Average velocity $\bar{u}/u_\infty$ at $y = 0$ for different x-locations and grid refinements.

As stated above, depending on the grid size within the free shear layer, the location y and z respectively of the jet boundary was significantly affected. Figure 3.14 illustrates the average velocity profiles at $y = 0$ at 0.5 m, 1.0 m, 2.0 m and 3.0 m downstream the nozzle exit for four grid densities. Therefore, based on the highest resolution, the refinement regions were removed step-wisely. In general, a lower grid resolution led to a lower shear layer thickness further downstream, e.g. at $x = 2.0\,\mathrm{m}$ and $x = 3.0\,\mathrm{m}$. The effect on

the static pressure coefficient $C_\mathrm{p}(x)$ is shown in Figure 3.15 once in the symmetry plane of the test section at $z = 0.6\,\mathrm{m}$ and $y = 0.0\,\mathrm{m}$ as well as in a more lateral region at $y = 1.0\,\mathrm{m}$ and $y = 1.5\,\mathrm{m}$ which is representative for the range where the model is located. The abrupt resolving of turbulent structures acted as a singularity inside the test section followed by a positive peak in the static pressure. This effect appeared to be of numerical nature and, hence, not to be physically plausible. However, for the most critical nozzle with $A_\mathrm{N} = 11\,\mathrm{m}^2$ with the highest resolution the gradient of the static pressure coefficient was in the range of $\Delta C_\mathrm{p} < \pm 0.002$ for $x \leq 10.0\,\mathrm{m}$, $|y| \leq 1.0\,\mathrm{m}$ and $|z| \leq 1.5\,\mathrm{m}$. A plot for the range of up to $x = 10\,\mathrm{m}$ and for a selection of four different nozzle cross sections is presented in Figure 3.16.

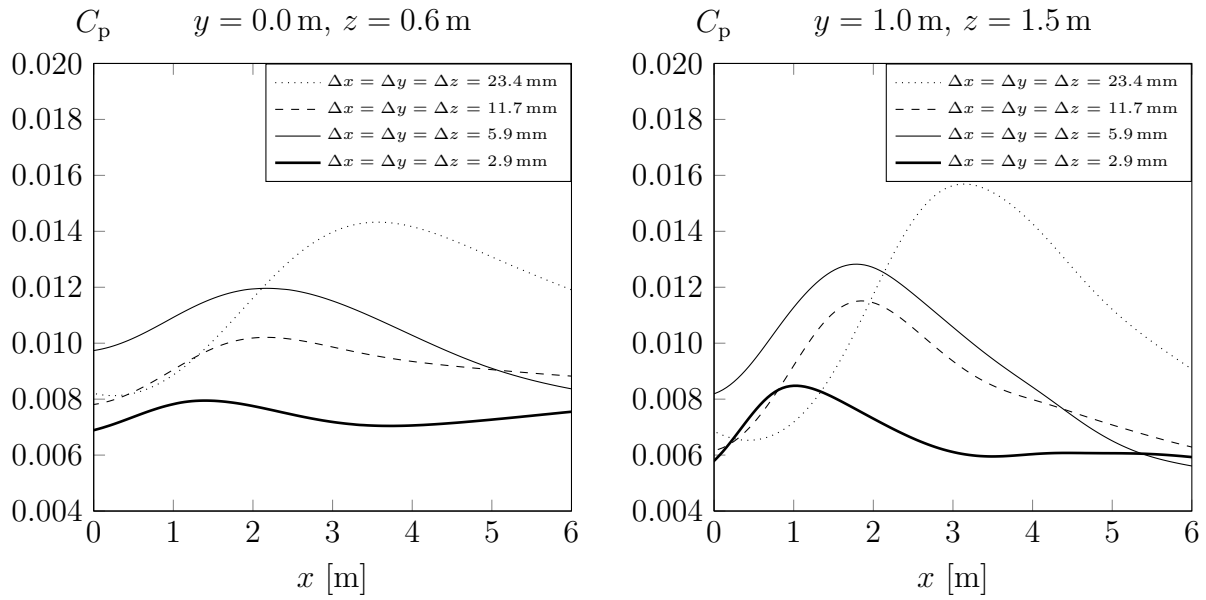

Figure 3.15: Static pressure C_p in the empty test section of the half-infinite wind tunnel for different refinement levels in the free shear layer. $x = 0$ is the nozzle exit. The profiles were extracted at different positions (left and right).

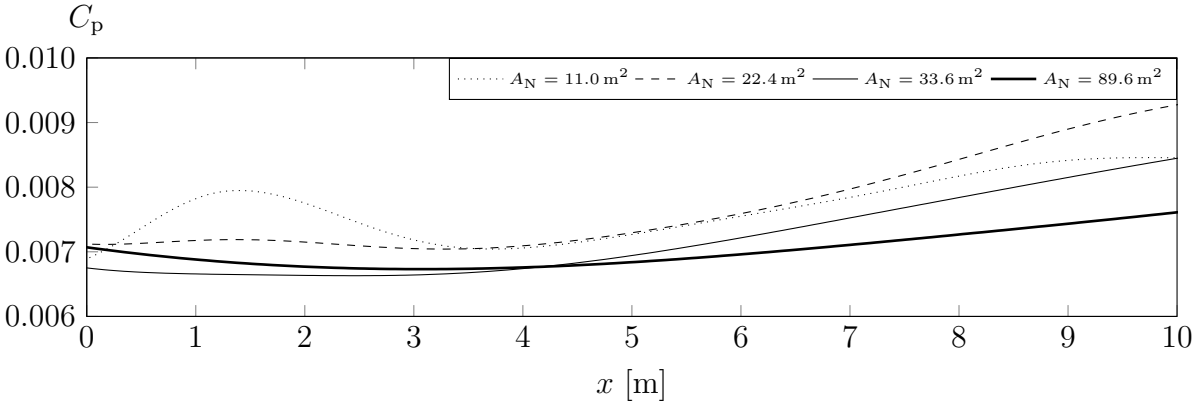

Figure 3.16: Static Pressure C_p in the empty test section of the half-infinite wind tunnel for different nozzle cross sections $11.0\,\mathrm{m}^2 \leq A_\mathrm{N} \leq 89.6\,\mathrm{m}^2$. $x = 0$ denotes the nozzle exit. The profiles were extracted at $y = 0.0\,\mathrm{m}$ and $z = 0.6\,\mathrm{m}$.

Audi Aeroacoustic Wind Tunnel (AAWK)

Based on the knowledge presented for the CFD simulations for the empty, half-infinite wind tunnel test section a simulation setup for the Audi Aeroacoustic Wind Tunnel (AAWK) was created. Therefore, not the entire airline was included. The CFD domain included settling chamber, wind tunnel nozzle, plenum and test section, collector as well as the high speed diffusor. Thus, the domain correlated to the finite wind tunnel, see Figure 3.17. In the first step the empty test section was simulated for the wind tunnel setup with a velocity of 140 $^{\mathrm{km}}/_{\mathrm{h}}$, static ground and without boundary layer suction. Therefore, the test section length was adjusted using the collector position of $L_{\mathrm{TS}} = 9.5\,\mathrm{m}$, see Figure 3.18 for the static pressure gradient.

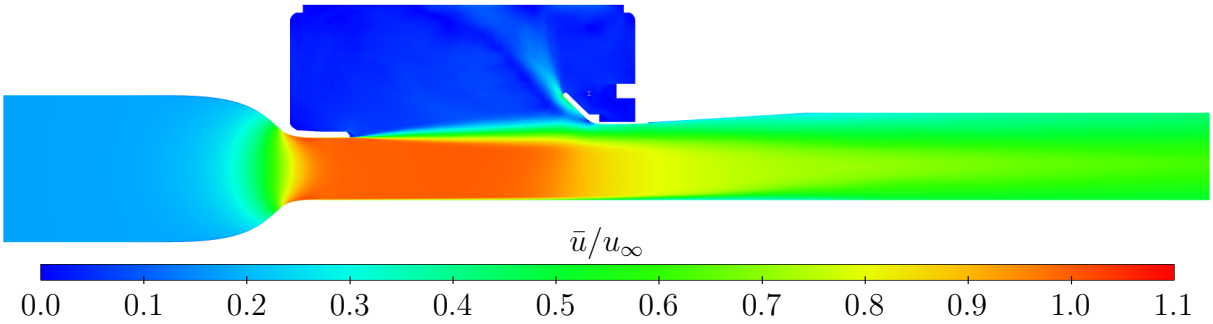

Figure 3.17: Velocity field $\bar{u}/u_\infty$ for the empty AAWK test section in CFD.

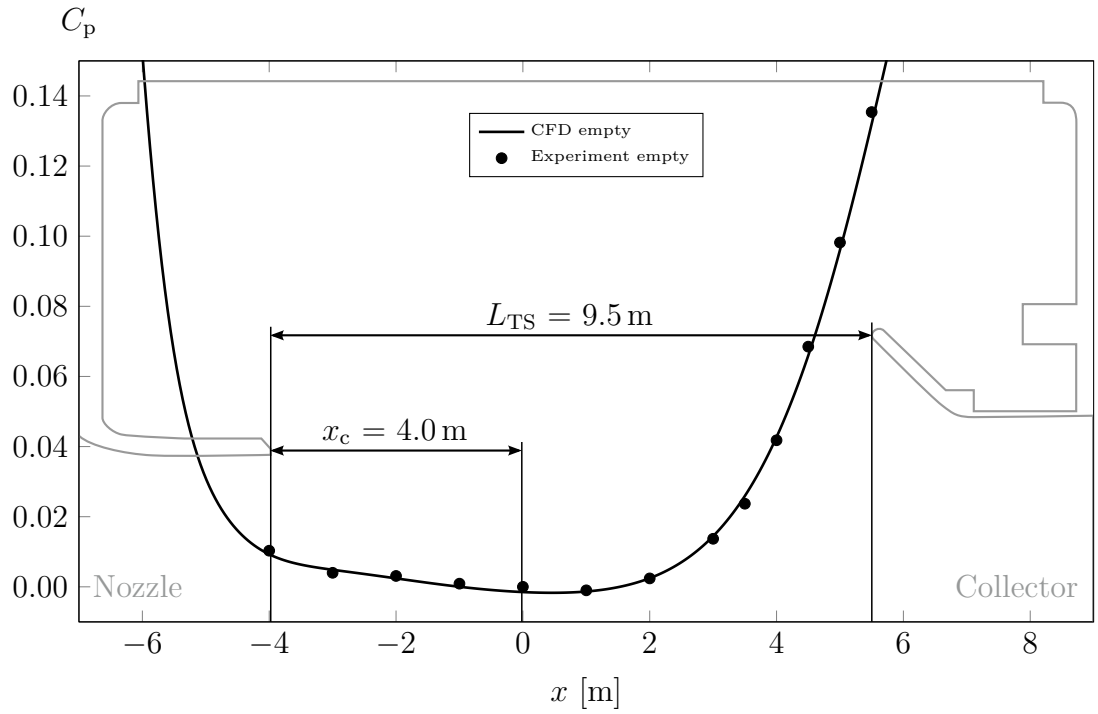

Figure 3.18: Static Pressure C_p in the empty test section of the AAWK with static ground, boundary layer suction off and a test section length of $L_{\mathrm{TS}} = 9.5\,\mathrm{m}$. The profiles from both experiment and CFD were extracted at $y = 0.0\,\mathrm{m}$ and $z = 0.8\,\mathrm{m}$.

Figure 3.18 compares the static pressure coefficient $C_p(x)$ for both experiment and simulation at $y = 0$ and $z = 0.8\,\mathrm{m}$. A reasonable agreement of CFD with the experiments was achieved. Figure 3.18 also shows the later standard location of the vehicle in the test section at $x_c = 4.0\,\mathrm{m}$.

Furthermore, a validation of the velocity field inside the open jet test section, in particular close to the jet boundary, was desired. Therefore, three-component, hot wire measurements were performed in both the empty test section and with an Audi A4 Avant, see Figure 3.19 and Figure 3.20. These measurements were extracted as velocity profiles for $\bar{u}/u_\infty(y)$ at $z = 0.7\,\mathrm{m}$ and $\bar{u}/u_\infty(z)$ at $y = 0.0\,\mathrm{m}$ (symmetry plane). The velocity profiles

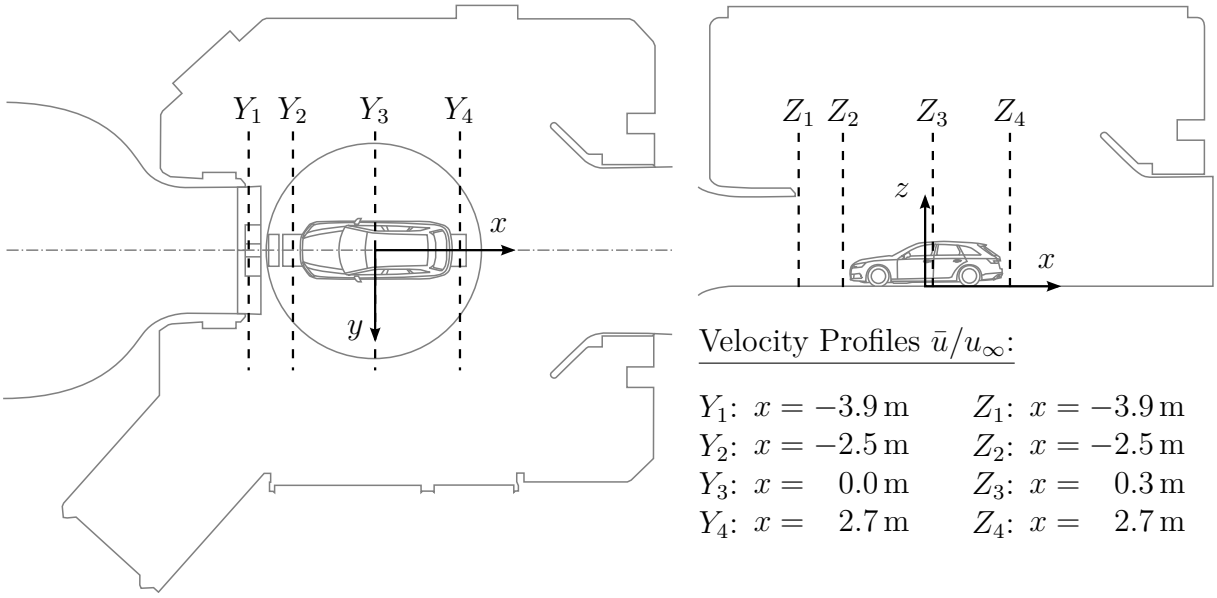

Figure 3.19: Positions for velocity profiles $\bar{u}/u_\infty$ for the experiments with hot wire anemometers. The y-profiles Y_i were extracted from a height $z = 0.7\,\mathrm{m}$, the z-profiles Z_i were extracted at the symmetry plane $y = 0.0\,\mathrm{m}$. The Audi A4 Avant was located at the standard AAWK position at $x_c = 4.0\,\mathrm{m}$.

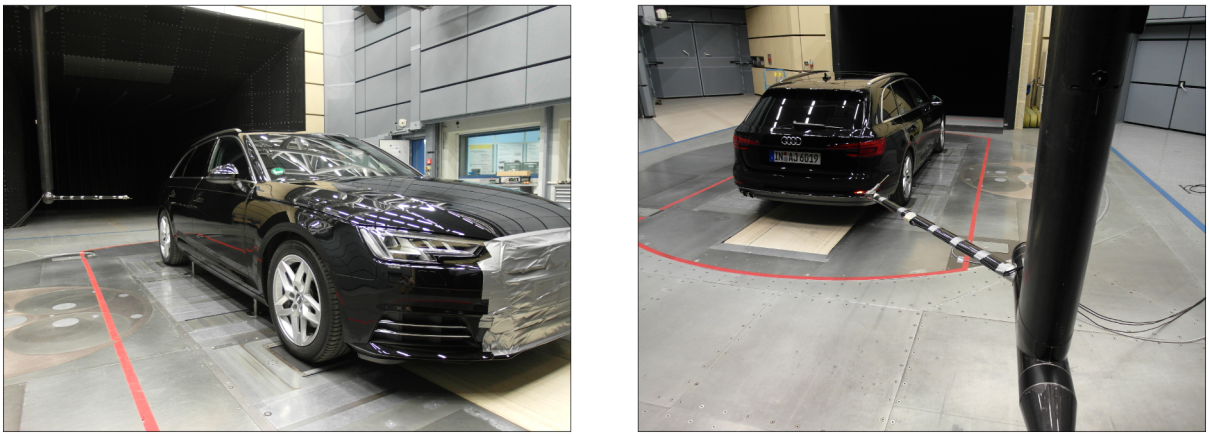

Figure 3.20: Experimental setup of an Audi A4 series estateback car in the test section of the full scale Audi Aeroacoustic Wind Tunnel (AAWK). The hot wire probe is attached to a traversing arm.

were measured 0.1 m downstream the nozzle exit, in the center of the turntable as well as directly in front of and behind the car. The hot wire probe was attached to a z-arm and was traversed around the car. For both the measurements and simulations of the Audi A4 Avant the cooling inlets were closed. The results for experiments and CFD are presented in Figure 3.21 for the profiles Y_i and Figure 3.22 for the profiles Z_i. The comparison between CFD and experiments for the y-profiles shows a good agreement close to the nozzle at Y_1 but a slightly increasing difference for the location of the jet boundary further downstream for both empty test section and with model. The offset of the most downstream position at $x = 2.7\,\mathrm{m}$ (Y_4) was about 0.1 m. However, this offset was detected to be equal for both empty configuration and with the model. Thus, the displacement of the jet boundary in y-direction was adequately predicted in CFD.

Comparing the profiles Z_1, Z_2,Z_3 and Z_4, the agreement of CFD with the experiments was better and no increasing discrepancy downstream in z-direction for the location of the jet boundary was determined. This was a good confirmation of the refinement strategy for the free shear layer presented above. Furthermore, an explanation for the shift of profile Y_4 of about 0.1 m can be a slight difference of the angle of the nozzle side wall of about 0.5 ° either in CFD or experiments. A lateral effect of the z-arm in the experiments due to a displacement of the flow only y-direction can not be reliably ruled out as well.

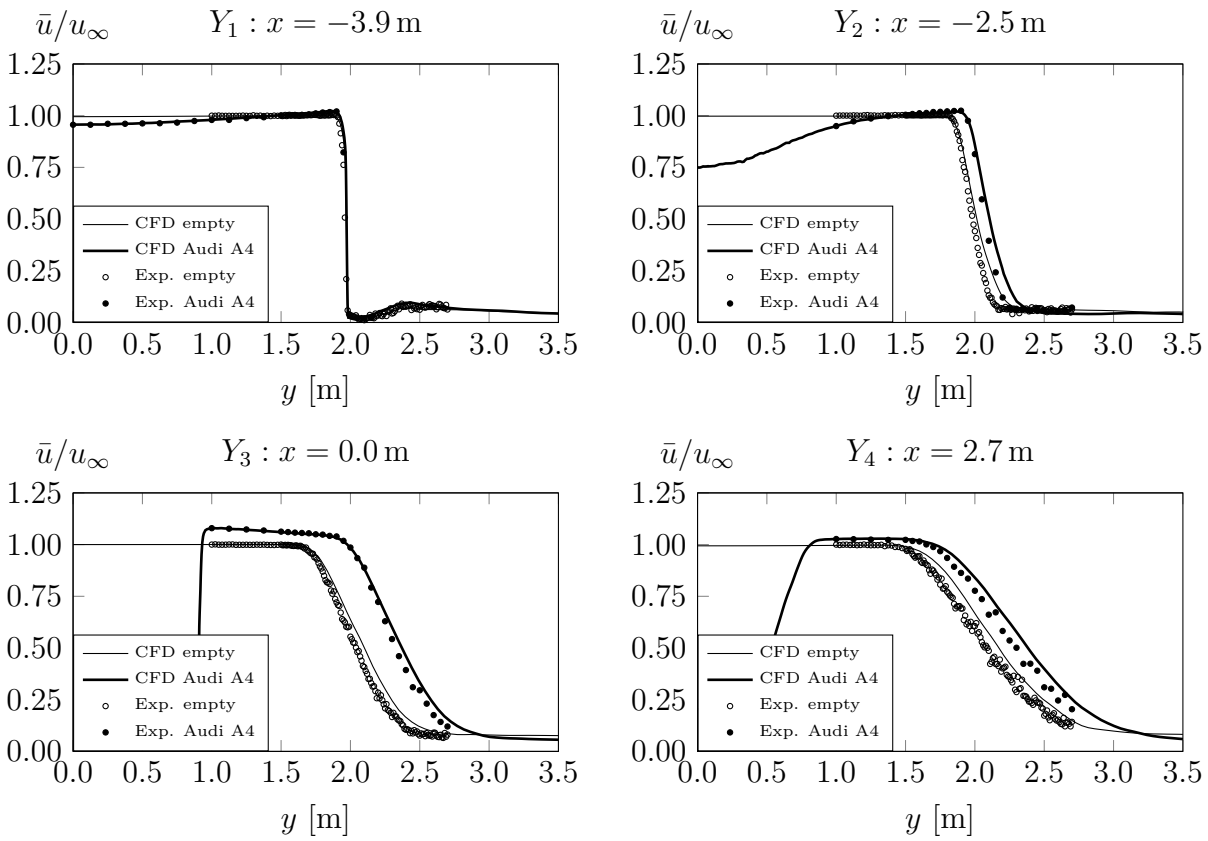

Figure 3.21: Horizontal velocity profiles $\bar{u}/u_\infty$ for different x-locations in CFD and experiments.

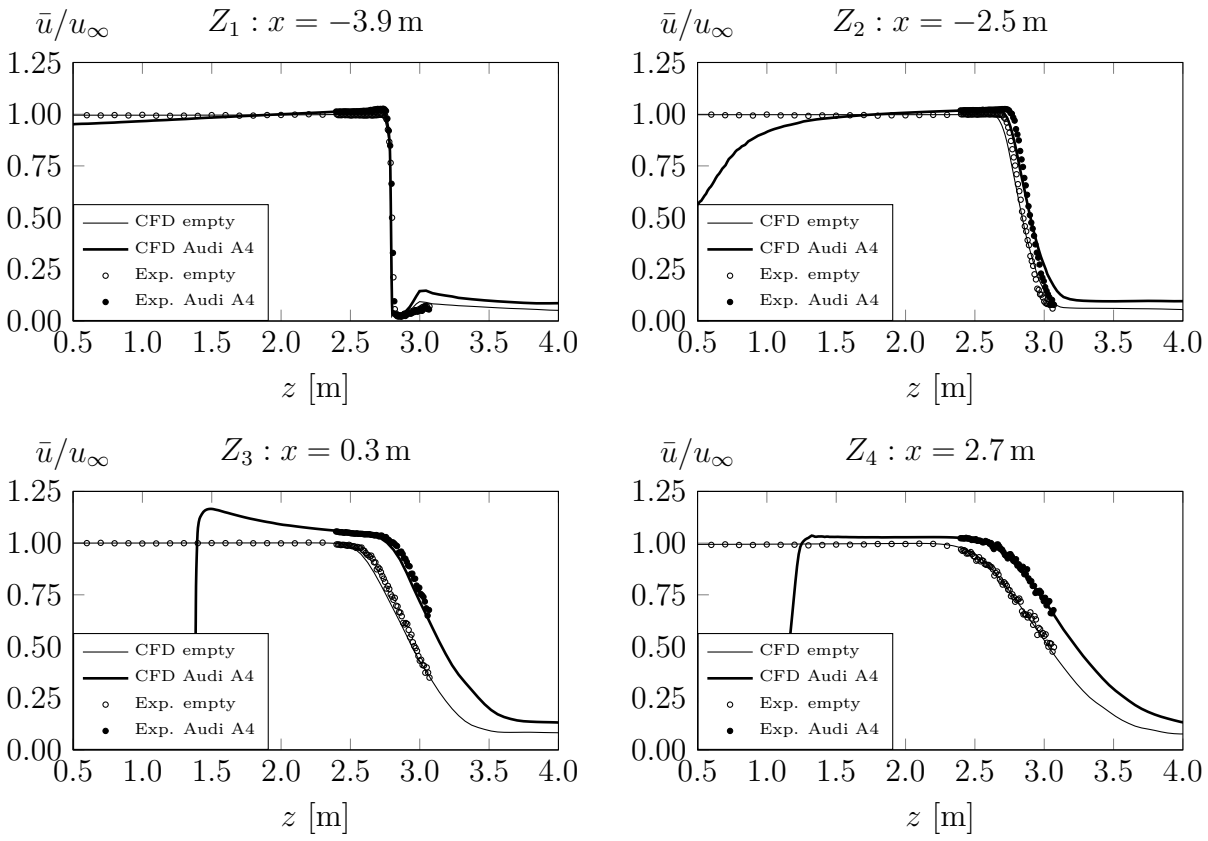

Figure 3.22: Vertical velocity profiles $\bar{u}/u_\infty$ for different x-locations in CFD and experiments.

In the last step of the validation of wind tunnel interferences in CFD a comparison of the effect of the longitudinal model position on the aerodynamic forces was drawn. Therefore, the Audi A4 Avant was set up at different positions x_c in the experiments. These positions were limited by the adjustment range of the AAWK wheel drive units and the wheel base of the model. The maximum range, which was achieved in the experiments, was $\Delta x_\mathrm{c} = \pm 0.3\,\mathrm{m}$ originating from the standard model position $x_\mathrm{c} = 4.0\,\mathrm{m}$. Finally, five measurements were performed in the experiments covering both nozzle and plenum method for the determination of the dynamic pressure. The wind tunnel was set up with static ground and without boundary layer treatment. Based on the standard position $x_\mathrm{c} = 4.0\,\mathrm{m}$, the collector was located at $x_\mathrm{coll} = 9.5\,\mathrm{m}$. For each change in model position x_c the collector position was adjusted by the same distance in order to keep a constant distance between the model and the collector. The same approach was applied in CFD including the positioning of the wheel drive units.

Figure 3.23 shows the velocity field $\bar{u}/u_\infty$ in the symmetry plane $y = 0$ for two selected model positions $x_\mathrm{c} = 3.7\,\mathrm{m}$ (top) and $x_\mathrm{c} = 4.3\,\mathrm{m}$ (bottom). Furthermore, the varying position of the collector at $x_\mathrm{coll} = 9.2\,\mathrm{m}$ (top) and $x_\mathrm{coll} = 9.8\,\mathrm{m}$ (bottom) is presented. The effects of the model position on the aerodynamic force coefficients is given in Figure 3.24. The coefficients are presented as deltas referring to the standard position. The largest effect of model position was determined for ΔC_D in both experiments and CFD.

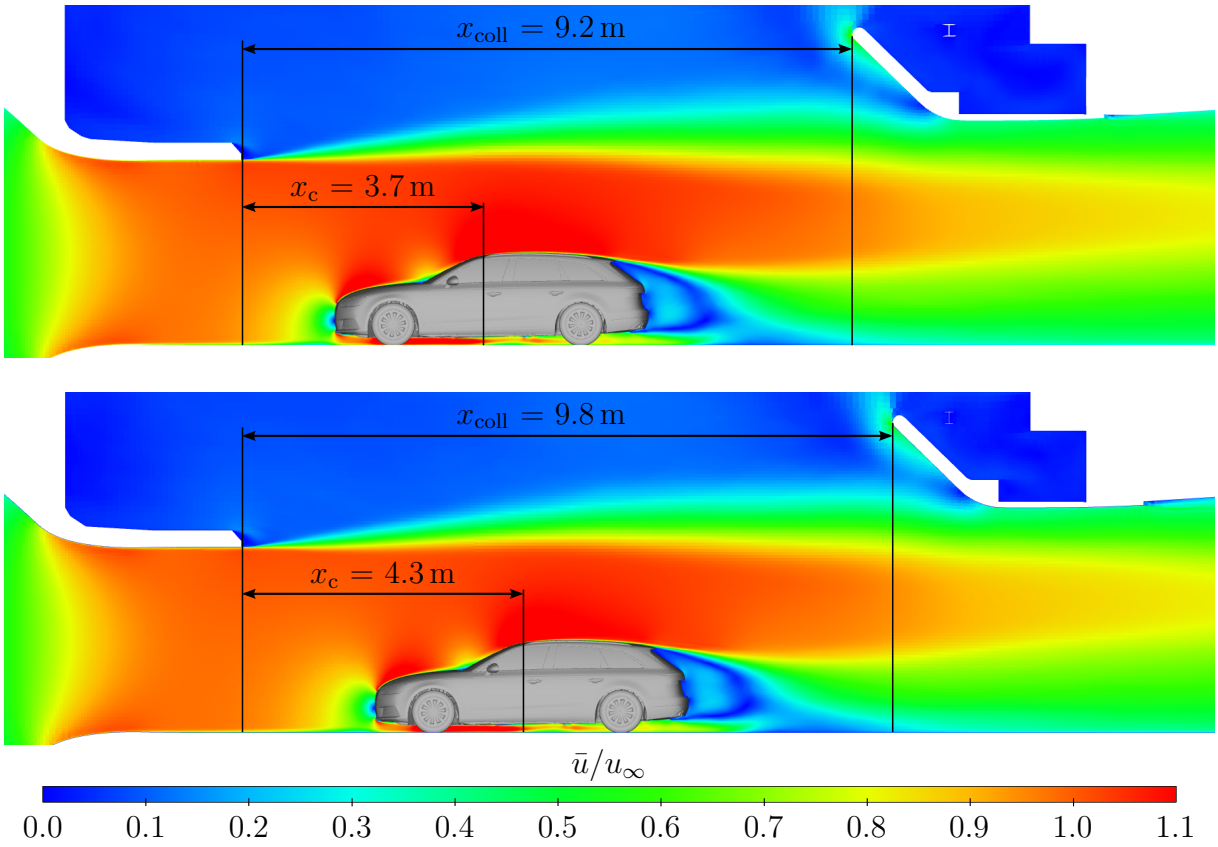

Figure 3.23: Velocity field $\bar{u}/u_\infty$ for the AAWK test section with Audi A4 Avant in CFD in the symmetry plane $y = 0.0\,m$. The images show the car located at different distance to nozzle: $x_c = 3.7\,m$ (top) and $x_c = 4.3\,m$ (bottom).

The maximum delta between $x_c = 3.7\,m$ (top) and $x_c = 4.3\,m$ was $\Delta C_D \approx \pm 0.015$ for the nozzle method and $\Delta C_D \approx 0.006$ for the plenum method. The prediction of the monotonous gradient in CFD correlated well with a maximum discrepancy of < 0.001. For $\Delta C_{L,f}$ and $\Delta C_{L,r}$ not a clear trend such as for ΔC_D was determined neither in experiments nor in CFD. The maximum effect of model position on the lift coefficients was in the range of five counts. However, also for front and rear lift coefficient the agreement of CFD and experiments was acceptable.

Summarizing, the study on model position confirms the prediction of Wickern (2014) expecting a higher nozzle interference with the model using the nozzle method. However, it is worth to mention that a variation of the model position along the rather short test section of the AAWK certainly involves further wind tunnel interferences as well. For example, the boundary layer thickness is larger if the model is located at $x_c = 4.3\,m$ rather than for $x_c = 3.7\,m$. Furthermore, the static pressure gradient caused by the collector was known not to be shifted by the same distance as the shift of collector position. Thus, the variation of the longitudinal model position was expected to include a change of several wind tunnel interferences, which was predicted well in CFD.

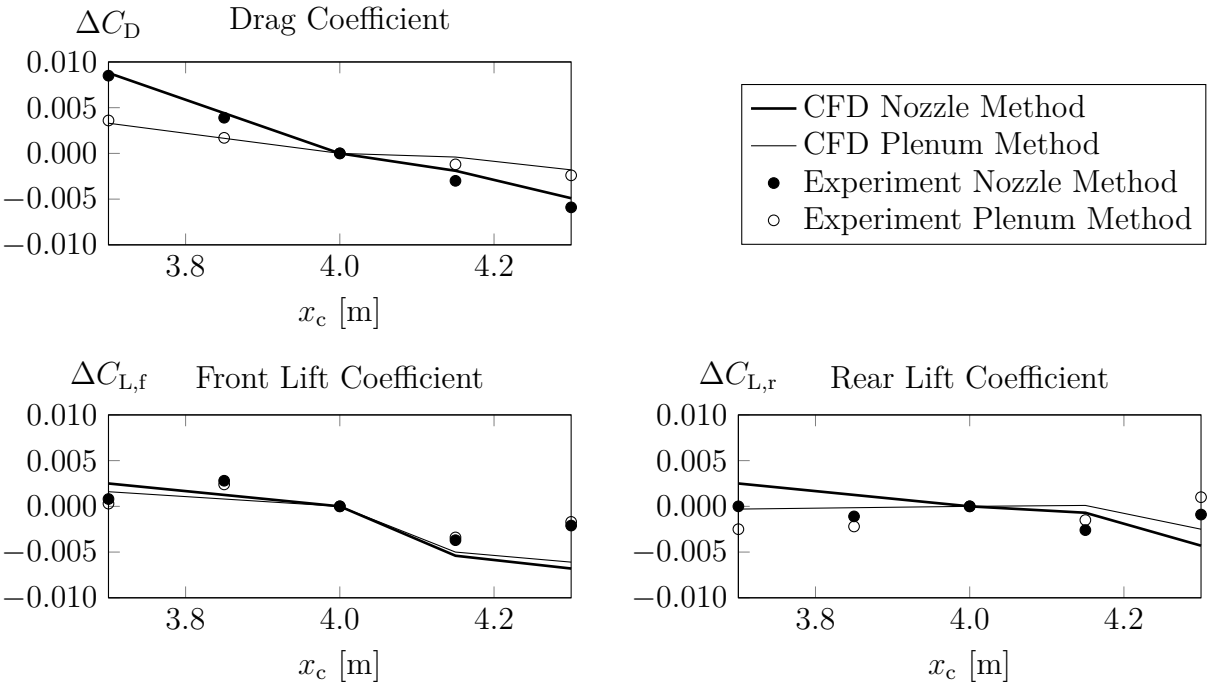

Figure 3.24: Effect of model position in the AAWK in CFD and experiments.

4 Numerical Evaluation of Open Jet Wind Tunnel Interferences

In the following section, the numerical methods introduced in chapter 3 are applied to some selected wind tunnel interferences created by the nozzle and the open jet (section 4.1), the collector (section 4.2) and moving ground simulation (section 4.3). The investigations included flow field analysis in order to draw a connection to the effects on the corresponding aerodynamic force coefficients.

4.1 Nozzle and Open Jet Interferences

With the objective to perform wind tunnel simulations, for which only interferences between the nozzle, the open jet and the model are relevant, the approach is presented in section 4.1.1, followed by the general results in section 4.1.2. A more detailed analysis to separate the effects for the nozzle and the open jet is given in section 4.1.3.

4.1.1 Methodology

The setup for the half-infinite wind tunnel (HIWT), presented in section 3.2.2, was adopted in order to evaluate the nozzle and the open jet interferences. The basic methodology was to perform simulations for the mock-up DrivAer with smooth underfloor and rotating wheels at different longitudinal positions along the test sections $3.0\,\mathrm{m} \leq x_\mathrm{c} \leq 9.0\,\mathrm{m}$ and for different blockage ratios $2.4\,\% \leq A_\mathrm{M}/A_\mathrm{N} \leq 19.7\,\%$. The same model configuration was simulated in open road, corrected conditions ($C_\mathrm{i,c}$) in order to evaluate the absolute effect for the aerodynamic force coefficients ΔC_i ($\Delta C_\mathrm{D}, \Delta C_\mathrm{L,r}, \Delta C_\mathrm{L,f}$) in the wind tunnel ($C_\mathrm{i}$):

$$\Delta C_\mathrm{i} = C_\mathrm{i} - C_\mathrm{i,c} \tag{4.1}$$

The dynamic pressure p_dyn in order to calculate the force coefficients in the wind tunnel was extracted for both the nozzle method $p_\mathrm{dyn,NM}$ and the plenum method $p_\mathrm{dyn,PM}$. In real facilities, both $p_\mathrm{dyn,NM}$ and $p_\mathrm{dyn,PM}$ are calculated from an empty test section calibration by using the corresponding measurement for the pressure drop when the model is present. Thus both methods require a converging region and a settling chamber upstream the nozzle exit. However, the nozzle of the half-infinite wind tunnel was defined to have a constant cross section A_N in order to remain independent from a specific nozzle geometry except for the constant width-to-height ratio $W_\mathrm{N}/H_\mathrm{N} = 1.4$, see Figure 4.1.

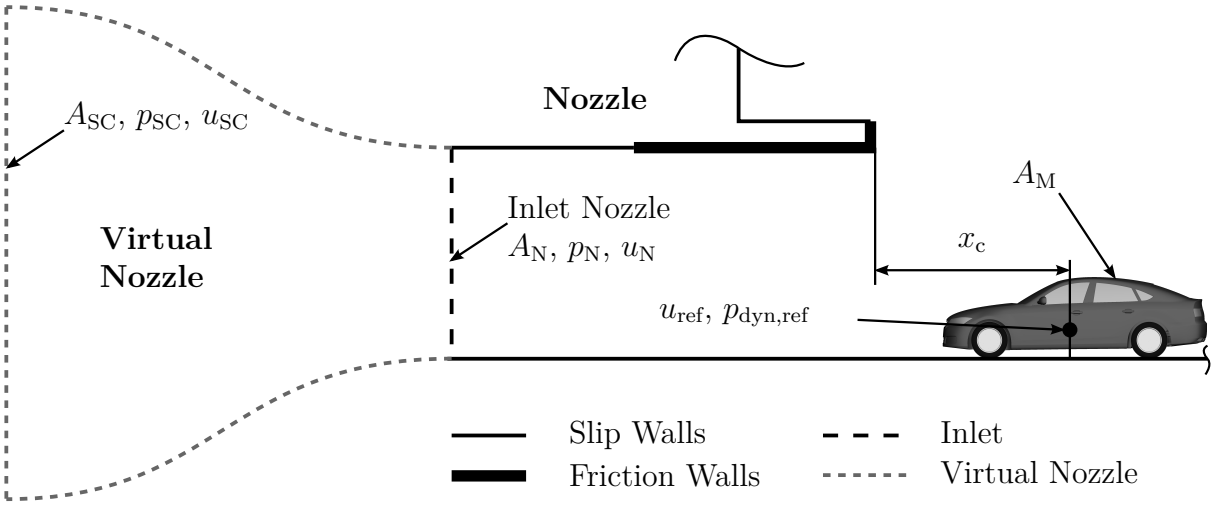

Figure 4.1: Schematic image of the "virtual nozzle" approach to calculate the dynamic pressure $p_{\mathrm{dyn,NM}}$ and $p_{\mathrm{dyn,PM}}$ in the half-infinite wind tunnel in CFD.

In the present study, a "virtual nozzle"[1] was attached to the existing nozzle to determine the dynamic pressure $p_{\mathrm{dyn,NM}}$ and $p_{\mathrm{dyn,PM}}$, see Figure 4.1. This approach followed some theoretical assumptions:

- The reference static pressure in the plenum remained constant: $p_\infty = 0$.
- The static pressure p_N at the inlet upstream the nozzle exit was increased according to the plenum due to the proximity of the model: $p_\mathrm{N} \geq p_\infty$.
- The virtual pressure probes in the nozzle were not contaminated by the model. The pressure built-up in the virtual nozzle was equal for both the empty test section and with the model.
- Reynolds effect due to the change in velocity were negligible.

Based on these assumptions, the adjustment of the dynamic pressure using the nozzle method sets a constant mass flow through the nozzle. Thus, the dynamic pressure $p_{\mathrm{dyn,NM}}$ was calculated from the inlet velocity u_N as it was constant for all simulations. However, the friction wall section of the nozzle caused a slight increase of the actual test section velocity compared to the inlet conditions of $\leq 0.4\,\%$. Therefore, for each simulation with the model the dynamic pressure for the nozzle method was used from a reference point at $x_\mathrm{ref} = x_\mathrm{c}$, $y_\mathrm{ref} = 0$ and $z_\mathrm{ref} = 0.6\,\mathrm{m}$ from the empty test section simulation. This approach considered a potential, longitudinal gradient of test section velocity, which was lower than $0.1\,\%$ in the investigated range. For the simulations with the DrivAer model the calculation of the nozzle method dynamic pressure $p_{\mathrm{dyn,NM}}$ was based on the reference velocity (empty test section) at the corresponding model position:

$$p_{\mathrm{dyn,NM}}\left(x_\mathrm{c}\right) = \frac{\varrho}{2}\, u_{\mathrm{ref}}\left(x_\mathrm{c}\right)^2 = p_{\mathrm{dyn,ref}}\left(x_\mathrm{c}\right) \qquad \text{with:} \qquad u_{\mathrm{ref}}\left(x_\mathrm{c}\right) > u_\mathrm{N} \tag{4.2}$$

[1]The virtual nozzle extends the physical nozzle, included in CFD, by a converging region in order to determine the dynamic pressure for the plenum method.

The index "ref" denotes the flow conditions in the empty test section. Therefore, for each simulation with the DrivAer model $p_{\mathrm{dyn,NM}}(x_\mathrm{c}) = p_{\mathrm{dyn,ref}}(x_\mathrm{c})$ was used at the corresponding reference point x_c from the empty tunnel simulation as u_N remained constant for all simulations[1]. Thus, the CFD model of the wind tunnel simulated a facility operating with the nozzle method. The calculation of the plenum method dynamic pressure $p_{\mathrm{dyn,PM}}$ for configurations with the DrivAer model required further input data from the particular simulation. By definition, the dynamic pressure for plenum method is determined from the pressure drop between the settling chamber and the plenum $p_\mathrm{SC} - p_\infty$. Using the approach of the virtual nozzle p_SC was calculated from p_N using Bernoulli's equation:

$$p_\mathrm{SC} = p_\mathrm{N} + \frac{\varrho}{2}\left({u_\mathrm{N}}^2 - {u_\mathrm{SC}}^2\right) = p_\mathrm{N} + \frac{\varrho}{2}{u_\mathrm{N}}^2\left[1 - \left(\frac{A_\mathrm{N}}{A_\mathrm{SC}}\right)^2\right] \tag{4.3}$$

The assumption of negligible Reynolds effects brought a linear approach for the dynamic pressure $p_{\mathrm{dyn,PM}} \sim p_\mathrm{SC}$:

$$C_{\mathrm{p,SC}} = \frac{p_\mathrm{SC} - p_\infty}{p_\mathrm{dyn}} = \frac{p_\mathrm{SC}}{p_\mathrm{dyn}} = \text{const.} \qquad \longrightarrow \qquad \frac{p_{\mathrm{dyn,PM}}}{p_{\mathrm{dyn,ref}}} = \frac{p_\mathrm{SC}}{p_{\mathrm{SC,ref}}} \tag{4.4}$$

The static pressure in the plenum chamber was known to be zero $p_\infty = 0$. Thus, the dynamic pressure $p_{\mathrm{dyn,PM}}$ for the plenum method was calculated from the ratio of static pressure in the virtual settling chamber with model p_SC and in the empty test section $p_{\mathrm{SC,ref}}$ using equation (4.3):

$$p_{\mathrm{dyn,PM}} = \frac{p_\mathrm{SC}}{p_{\mathrm{SC,ref}}}\, p_{\mathrm{dyn,ref}} = \frac{p_\mathrm{N} + \frac{\varrho}{2}{u_\mathrm{N}}^2\left[1 - \left(\frac{A_\mathrm{N}}{A_\mathrm{SC}}\right)^2\right]}{p_{\mathrm{N,ref}} + \frac{\varrho}{2}{u_\mathrm{N}}^2\left[1 - \left(\frac{A_\mathrm{N}}{A_\mathrm{SC}}\right)^2\right]}\, p_{\mathrm{dyn,ref}} \tag{4.5}$$

Therefore, p_N was extracted from each simulation as the integral average for the inlet patch of the nozzle. The calculation of $p_{\mathrm{dyn,PM}}$ includes the assumption of a particular converging ratio $A_\mathrm{SC}/A_\mathrm{N}$ as it affects the remaining dynamic pressure in the virtual settling chamber $p_{\mathrm{dyn,SC}}$. Figure 4.2 shows the decay of $p_{\mathrm{dyn,SC}}$ with increasing converging ratio and the corresponding decay of dynamic pressure predicted by the plenum method $p_{\mathrm{dyn,PM}}$ for a selected simulation with the largest nozzle interference investigated $A_\mathrm{M}/A_\mathrm{N} = 19.7\,\%$ and $x_\mathrm{c} = 3.0\,\mathrm{m}$. The dotted line indicates the asymptotic limit. For a typical converging ratio $A_\mathrm{SC}/A_\mathrm{N} = 6$ the remaining offset was $\approx 0.3\,\%$ and, hence, considerably accurate. Thus, a virtual converging ratio of $A_\mathrm{SC}/A_\mathrm{N} = 6$ was selected to calculate $p_{\mathrm{dyn,PM}}$ in the CFD simulations. Collin et al. (2016) propose an alternative approach to calculate the plenum method dynamic pressure using a different assumption. Following the correction model of Wickern (2014) the dynamic pressure correction for the plenum method is negligible, as he only applies a gradient correction. Consequently, Collin et al. (2016) assume that the dynamic pressure for the plenum method can be directly calculated from the stagnation point pressure. However, both approaches returned almost identical values for $p_{\mathrm{dyn,PM}}$

[1] This approach was based on the assumption that the pressure taps for the nozzle method were not contaminated by the upstream effect of the model.

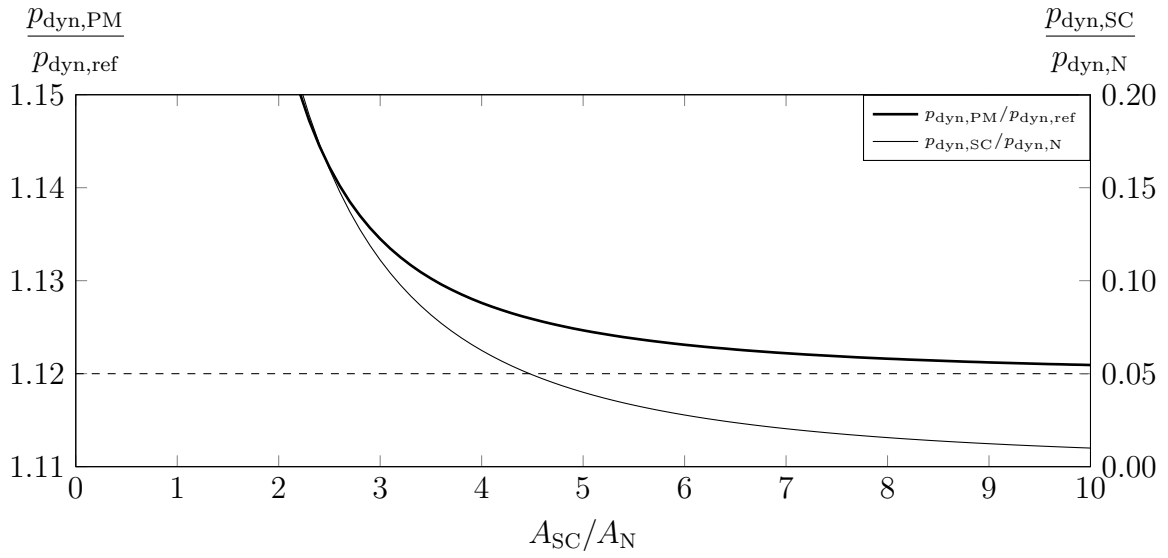

Figure 4.2: Sensitivity analysis for the predicted dynamic pressure for the plenum method $p_{\mathrm{dyn,PM}}$ depending on the converging ratio of the virtual nozzle $A_{\mathrm{SC}}/A_{\mathrm{N}}$. $p_{\mathrm{dyn,SC}}/p_{\mathrm{dyn,N}}$ denotes the dynamic pressure in the virtual settling chamber. The values are presented for the simulation with the largest nozzle interference: $A_{\mathrm{M}}/A_{\mathrm{N}} = 19.7\,\%$, $x_{\mathrm{c}} = 3.0\,\mathrm{m}$.

as the maximum difference between the method of Collin et al. (2016) and the method described above was $< 0.3\,\%$.

4.1.2 General Effects on Aerodynamic Force Coefficients

Based on the method explained above, the mock-up DrivAer with mirrors, smooth underfloor and generic closed wheel was selected for the simulations in both open road and wind tunnel conditions. Therefore, different rear end shapes (estateback, fastback and notchback) were investigated. The results for open road conditions set the reference to evaluate the interference effects in the half-infinite wind tunnel, see Table 4.1. Based on these results, the interferences for the wind tunnel simulations were derived.

Table 4.1: Aerodynamic force coefficients C_{D}, C_{L}, $C_{\mathrm{L,f}}$ and $C_{\mathrm{L,r}}$ for the DrivAer with estateback, fastback and notchback in open road conditions. A_{M} denotes the frontal area of the model. The slip boundary condition was applied to the floor of the domain.

	A_{M}	C_{D}	C_{L}	$C_{\mathrm{L,f}}$	$C_{\mathrm{L,r}}$
Estateback	2.166	0.299	−0.202	−0.101	−0.101
Fastback	2.162	0.247	−0.034	−0.075	0.041
Notchback	2.165	0.251	−0.051	−0.073	0.021

Drag Contributions for Nozzle and Open Jet Interferences

The most detailed investigations were performed for the estateback as it was expected to be, in terms of drag, the rear end shape with the largest wind tunnel interference effects. The simulations included four cross sections for the nozzle ($A_N = 11.0\,m^2$, $A_M/A_N = 19.7\,\%$; $A_N = 22.4\,m^2$, $A_M/A_N = 9.7\,\%$; $A_N = 33.6\,m^2$, $A_M/A_N = 6.4\,\%$ and $A_N = 89.6\,m^2$, $A_M/A_N = 2.4\,\%$) as well as different longitudinal model positions $3.0\,m \leq x_c \leq 9.0\,m$, see Figure 4.3 for some selected vector fields. The results for the drag coefficients are presented in Figure 4.4 for the nozzle and the plenum method.

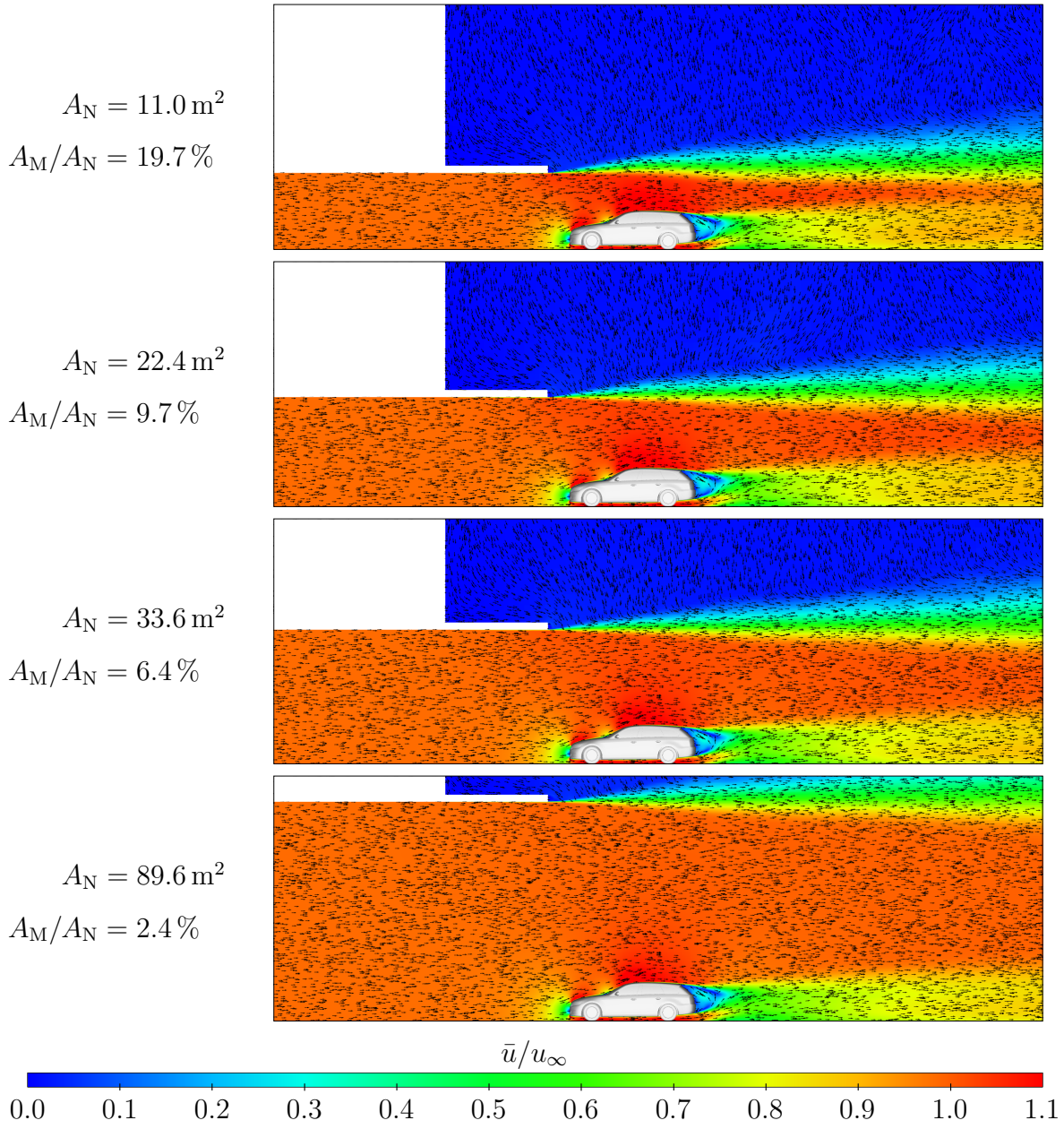

Figure 4.3: Velocity field $\bar{u}/u_\infty$ in the plane $y = 0$ for different nozzle cross sectional areas A_N and blockage ratios A_M/A_N and $x_c = 3.0\,m$.

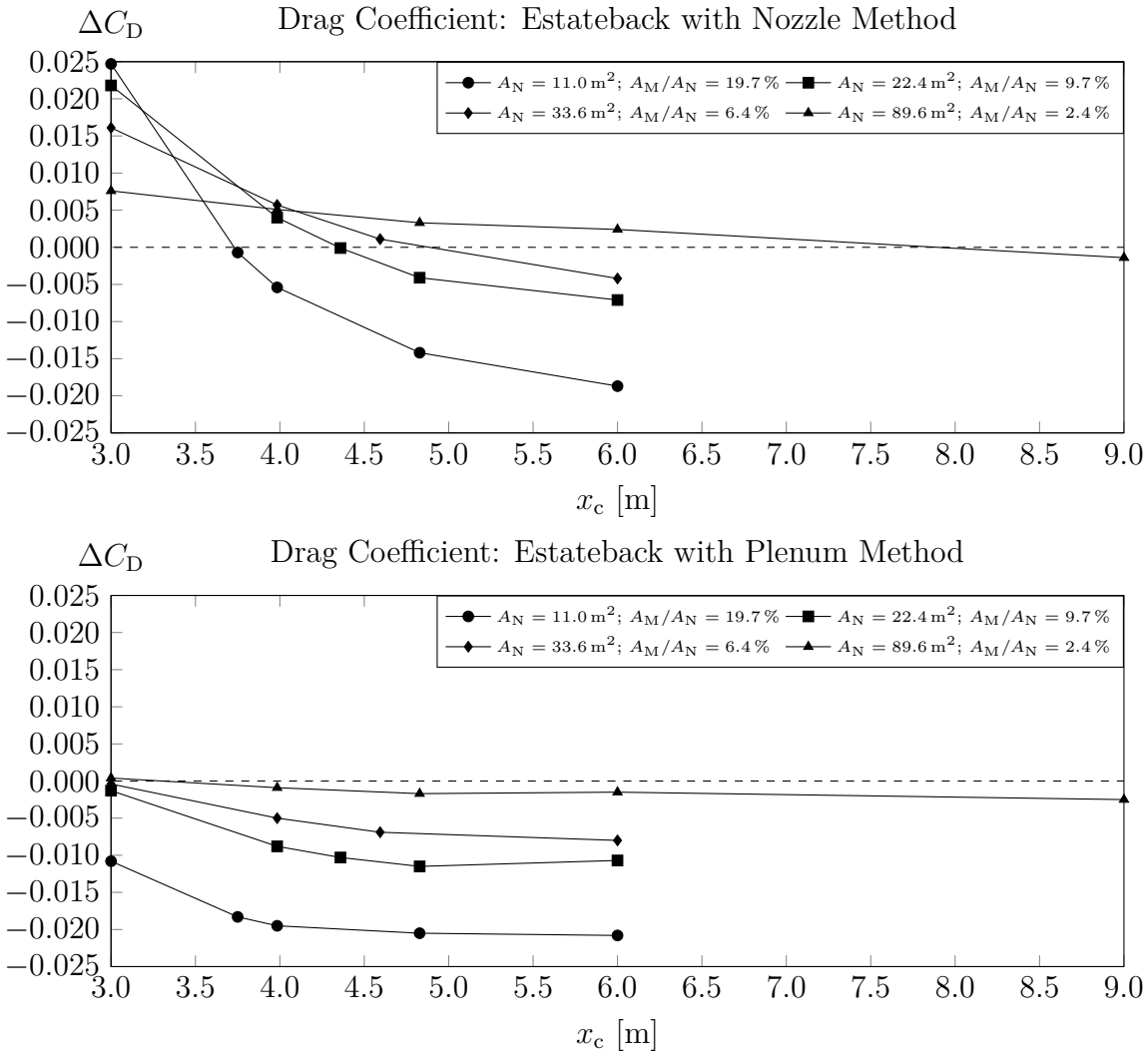

Figure 4.4: Drag coefficients ΔC_D for the DrivAer estateback referring to open road conditions for the nozzle method (top) and the plenum method (bottom). The curves represent the dependency on the longitudinal model position x_c for different blockage ratios A_M/A_N.

As presented by Collin et al. (2016), for both the nozzle and the plenum method the drag coefficient was lower than in open road conditions if the model was located "far" away from the nozzle (here $x_c = 6.0\,m$ and $x_c = 9.0\,m$ respectively). This effect was explained with the jet expansion by the model as it decays for the larger nozzles selected. The drag increased with decreasing distance to the nozzle. The drag increase due to the proximity of the nozzle was larger for the nozzle method and partially resulted in a compensation of drag increasing and decreasing effects $\Delta C_D = 0$. This was in good agreement with the theory of the self-correcting wind tunnel by Wickern (2014) although $\Delta C_D = 0$ was not achieved for all tunnels using the plenum method.

Additional simulations were performed to compare the effects on drag presented above for different rear ends of the DrivAer, see Figure 4.5 for the nozzle with $A_N = 11.0\,m^2$, $A_M/A_N = 19.7\,\%$ and Figure A.6 in appendix A.3.2 on page 147 for $A_N = 22.4\,m^2$,

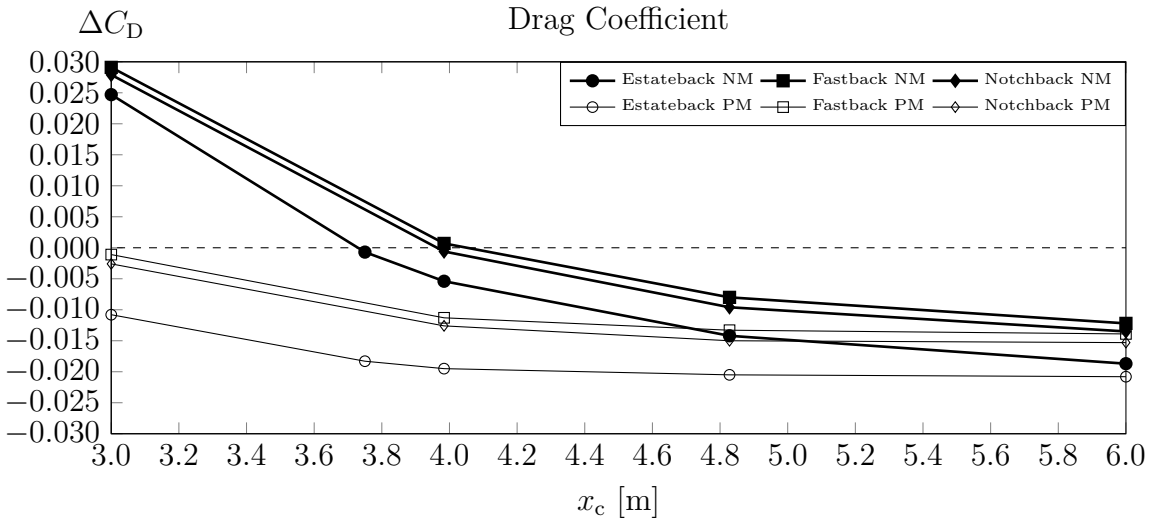

Figure 4.5: Drag coefficients ΔC_D for the DrivAer referring to open road conditions. The curves represent different rear end shapes for a nozzle with $A_N = 11.0\,m^2$ and $A_M/A_N = 19.7\,\%$. Thick lines denote the nozzle method (NM) and thin lines the plenum method (PM).

$A_M/A_N = 9.7\,\%$. The trends of drag for the fastback and the notchback were almost identical as the biggest differences between both rear ends were $\Delta C_D \leq 0.002$. Comparing fastback and notchback with the estateback "far" away from the nozzle exit plane, e.g. $x_c = 6.0\,m$, the estateback remained with a higher drag deficit due to the jet expansion. Furthermore, the estateback is exposed to a higher absolute drag increase if the model is located closer to the nozzle and the nozzle method is used. Thus, the distance to the nozzle for the drag compensation with the nozzle method was lower for the estateback ($x_c \approx 3.7\,m$) than for both fastback an notchback ($x_c \approx 4.0\,m$).

Lift Contributions for Nozzle and Open Jet Interferences

Figure 4.6 depicts the effects on both front and rear lift of the estateback for the plenum method and different blockage ratios. The results for the nozzle method were comparable and are attached in appendix A.3.2 on page 148. Except for a rather low distance to the nozzle $x_c < 4.0\,m$, both $\Delta C_{L,f}$ and $\Delta C_{L,r}$ were positive in all simulations, which was an effective deficit of negative lift as both coefficients were negative in open road conditions, see Table 4.1. Thus, the theoretic expectation of an effective reduction of all aerodynamic forces due to the jet expansion was confirmed. In general, the longitudinal gradient for the lift coefficients was, if at all present, significantly lower than for the drag coefficient. A self-compensating effect such as for drag was not investigated. Summarizing, the results for the lift coefficients of the estateback were reasonable. However, the remaining offset of the rear lift coefficient for the largest nozzle of $\Delta C_{L,r}(x_c > 6.0\,m) \approx 0.005$ was somewhat suspicious.

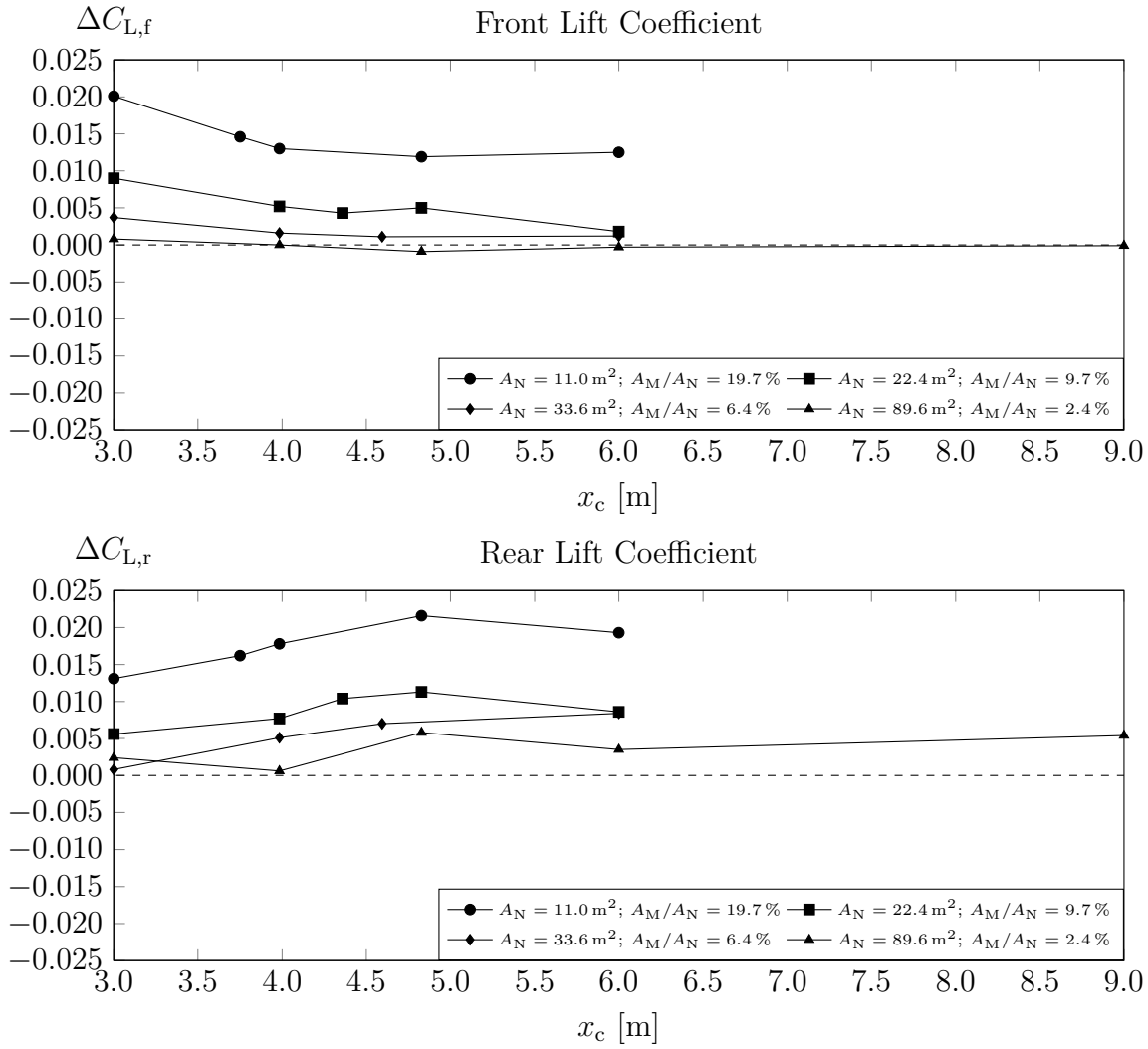

Figure 4.6: Lift coefficients $\Delta C_{\mathrm{L,f}}$ and $\Delta C_{\mathrm{L,r}}$ using the plenum method for the DrivAer estateback referring to open road conditions. The curves represent the dependency on the longitudinal model position x_{c} for different blockage ratios $A_{\mathrm{M}}/A_{\mathrm{N}}$.

The comparison of lift effects on different rear ends are given in Figure 4.7 for the highest blockage ratio $A_{\mathrm{M}}/A_{\mathrm{N}} = 19.7\,\%$ and in Figure A.8 in appendix A.3.2 on page 149 for $A_{\mathrm{M}}/A_{\mathrm{N}} = 9.7\,\%$. For all rear ends the longitudinal gradients for both $\Delta C_{\mathrm{L,f}}$ and $\Delta C_{\mathrm{L,r}}$ were significantly smaller than for the corresponding drag coefficients. Furthermore, these gradients died out with increasing distance to the nozzle. In contrast with $\Delta C_{\mathrm{L,f}}$, the absolute change of rear lift was of opposite sign for both the fastback and the notchback ($\Delta C_{\mathrm{L,r}} \leq 0$) compared to the estateback ($\Delta C_{\mathrm{L,r}} \geq 0$). Furthermore, the rear lift interference "far" away from the nozzle was larger for the estateback. Considering the lift coefficients in open road conditions in Table 4.1, the explanation was the negative, absolute rear lift of the estateback compared to positive for both fastback and notchback. Again, this confirmed the expectation of an absolute deficit of aerodynamic forces due to the jet expansion. The same effect was experienced for lower blockage ratios.

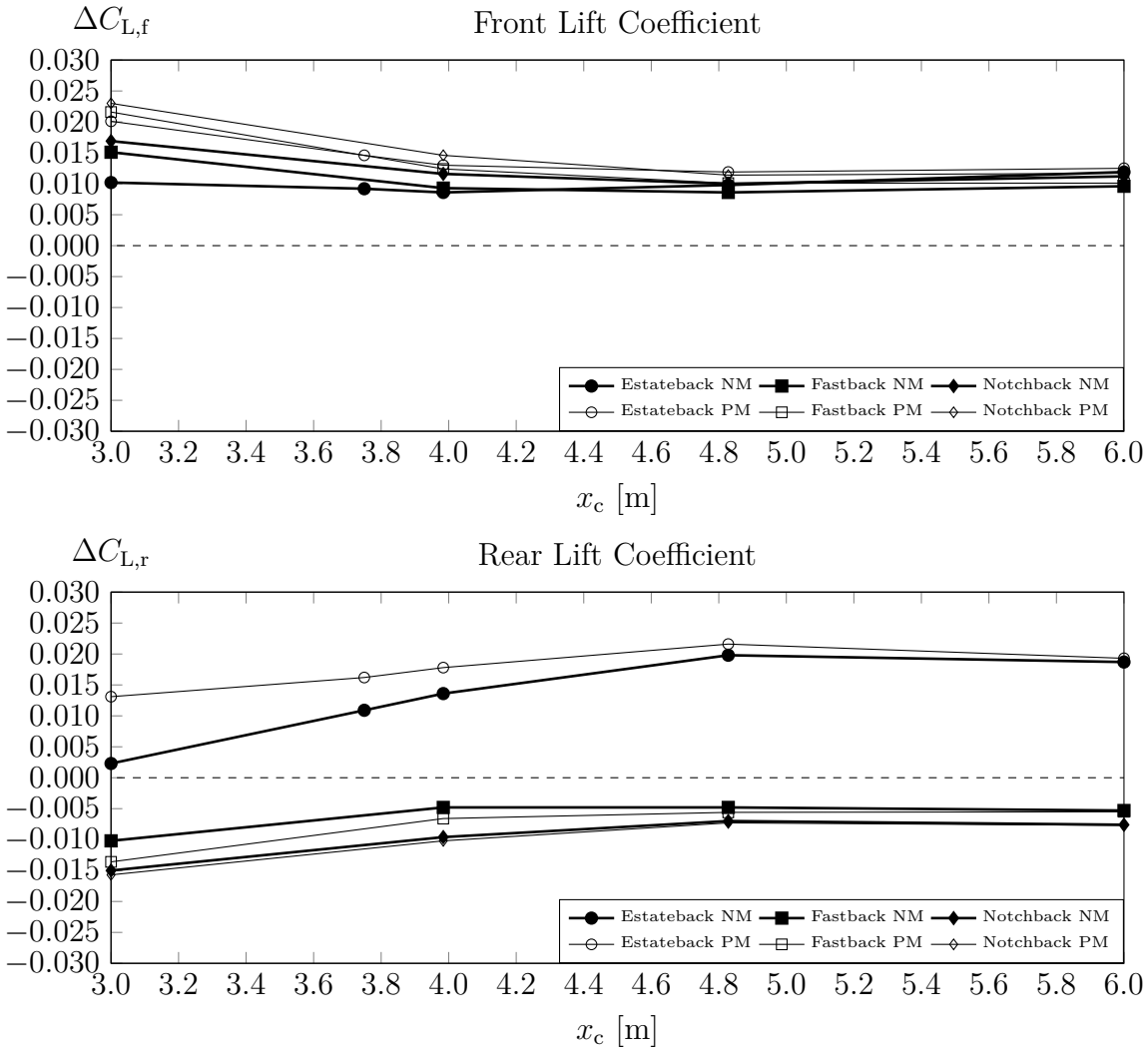

Figure 4.7: Lift coefficients $\Delta C_{\mathrm{L,f}}$ and $\Delta C_{\mathrm{L,r}}$ for the DrivAer referring to open road conditions. The curves represent different rear end shapes for a nozzle with $A_{\mathrm{N}} = 11.0\,\mathrm{m}^2$ and $A_{\mathrm{M}}/A_{\mathrm{N}} = 19.7\,\%$. Thick lines denote the nozzle method (NM) and thin lines the plenum method (PM).

4.1.3 Separation of Interferences with Nozzle and Open Jet

The results presented for the half-infinite wind tunnel included interferences with both the nozzle and the open jet. For all blockage ratios under investigation the overall interferences were not negligible. However, for all nozzle cross sections and rear ends under investigation the nozzle interference decayed with increasing distance to the model. The consequence was, that only open jet interferences remained further downstream. For the practical design of a wind tunnel operating with the plenum method the correction of the nozzle interference can be dispensable if the model position is selected accordingly. Thus, the separation of the particular effects was desired in order to obtain a correction approach for a later design.

Separation of Nozzle Interferences

The most essential interference between the nozzle and the model is the prediction of the dynamic pressure in the open jet test section and, hence, the effective velocity of the on-coming flow. Therefore, it was assumed that the velocity profiles upstream the model were itself similar in shape but scaled compared to open road conditions.

The basic idea of the approach to define an effective on-coming velocity was to use a reference point $P_{\mathrm{ref}}\,(x_{\mathrm{ref}} = -3.0\,\mathrm{m}, y_{\mathrm{ref}} = 0.0\,\mathrm{m}, z_{\mathrm{ref}} = 0.5\,\mathrm{m})$ upstream the model to calculate the effective test section velocity u_{eff}:

$$u_{\mathrm{eff}} = \frac{\bar{u}\,(x_{\mathrm{ref}}, y_{\mathrm{ref}}, z_{\mathrm{ref}})}{\bar{u}_{\mathrm{c}}\,(x_{\mathrm{ref}}, y_{\mathrm{ref}}, z_{\mathrm{ref}})}\,u_{\infty} \tag{4.6}$$

The result was a non-dimensional velocity field $u_{\infty}/u_{\mathrm{eff}}$ in the wind tunnel, which was in good agreement with open road conditions upstream the model. A comparison of the infinite velocity u_{∞} predicted by both the nozzle and the plenum method with the calculated, effective velocity u_{eff} is presented in Figure 4.8 for different blockage ratios and model positions.

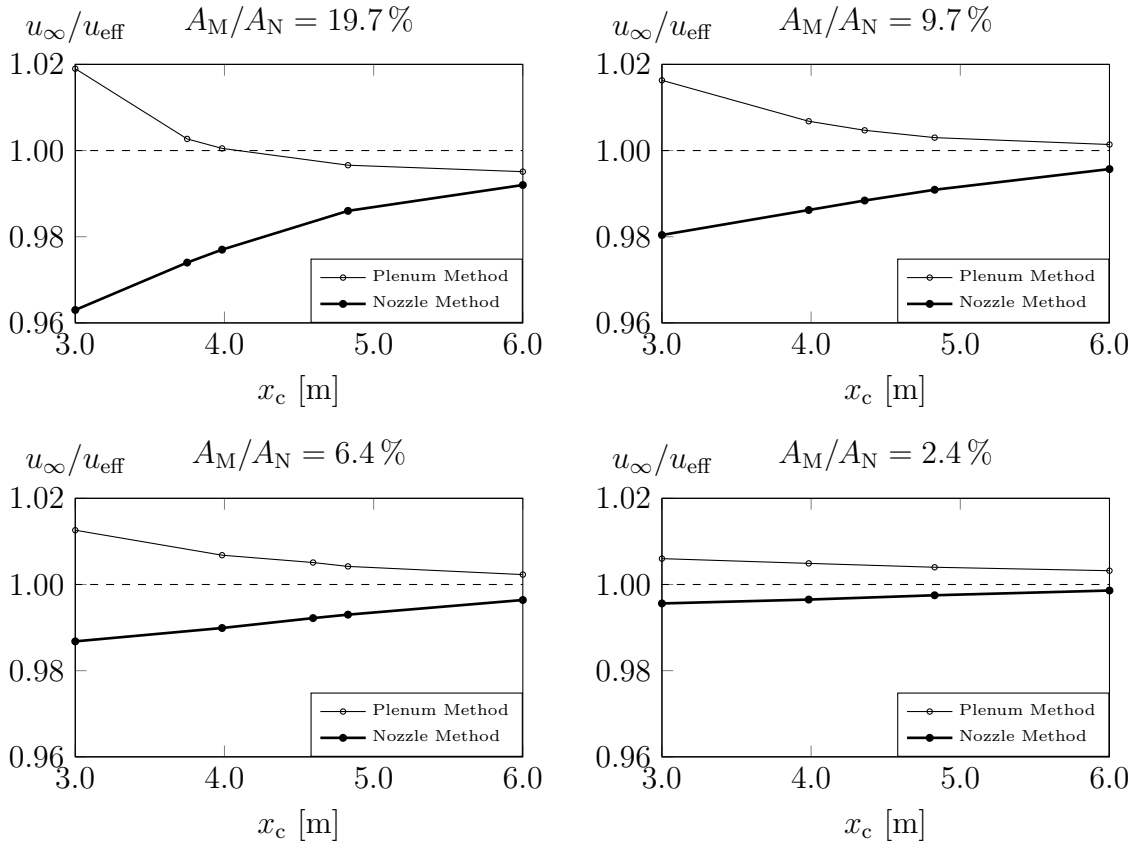

Figure 4.8: Comparison of the infinite velocity u_{∞} predicted by the plenum and the nozzle method to the effective velocity u_{eff} for different blockage ratios $A_{\mathrm{M}}/A_{\mathrm{N}}$ model locations x_{c}.

As expected from the considerations in chapter 2 (Figure 2.9 on page 20), the velocity predicted by the nozzle method was lower than the effective velocity. However, the results for the plenum method were somewhat surprising. In contrary to Figure 2.9, the plenum method predicted an infinite velocity marginally higher than the effective velocity. The opposite effect was expected due to the deceleration of the flow upstream the model. Therefore, a comparison of the upstream velocity profile at the nozzle exit in z-direction is presented in Figure 4.9 for a selected configuration ($A_\mathrm{M}/A_\mathrm{N} = 19.7\,\%$ and $x_\mathrm{c} = 3.0\,\mathrm{m}$). Figure 4.9 depicts the vertical, non-dimensional velocity profiles $\bar{u}/u_\mathrm{eff}(z)$ for both wind tunnel and open road conditions. Obviously, the main differences were given by the restrictions in nozzle height $H_\mathrm{N} \approx 2.8\,\mathrm{m}$ in the wind tunnel simulation. Up to a height of $H_\mathrm{N} \leq 1.5\,\mathrm{m}$ the velocity was identical. However, both profiles showed significant differences close to the jet boundary as the velocity in the wind tunnel deviated from the asymptotic profile in open road conditions. The result was a velocity at the jet boundary higher than infinite velocity $\bar{u}/u_\mathrm{eff} > 1$. This explained the effects presented above as the plenum method predicts the velocity at the jet boundary. Another explanation is presented by Wickern (2014) describing the nozzle gradient effect. For a rather high blockage, the nozzle gradient creates a pressure built-up inside the nozzle, which also explains the effect on the plenum method dynamic pressure.

Summarizing, it is worth to mention that the differences between the effective velocity and those predicted by the plenum method were rather small for a larger distance to the nozzle: $1 \leq u_\infty/u_\mathrm{eff} \leq 1.004$. Thus, the correction required for drag was in the range of one drag count. The results for both the drag and the total lift coefficient using the effective on-coming velocity are illustrated in Figure 4.10. It is worth to mention that the curves in Figure 4.10 still contain the effect of the open jet expansion. Compared to the results for the plenum method in Figure 4.4, the longitudinal gradients on drag were significantly larger. Figure 4.10 shows that nozzle-induced interferences were in the range of the accuracy of the CFD ($\Delta C_\mathrm{D} \approx \pm 0.002$, $\Delta C_\mathrm{L} \approx \pm 0.005$) for $x_\mathrm{c} > 5.0\,\mathrm{m}$.

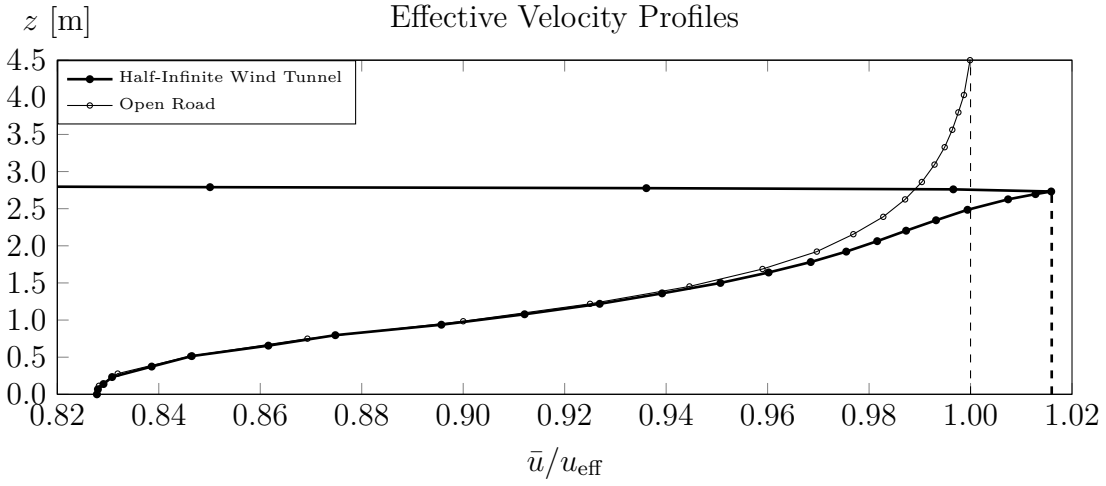

Figure 4.9: Effective velocity z-profile $\bar{u}/u_\mathrm{eff}$ in open road conditions and in the half-infinite wind tunnel with $A_\mathrm{M}/A_\mathrm{N} = 19.7\,\%$ and $x_\mathrm{c} = 3.0\,\mathrm{m}$.

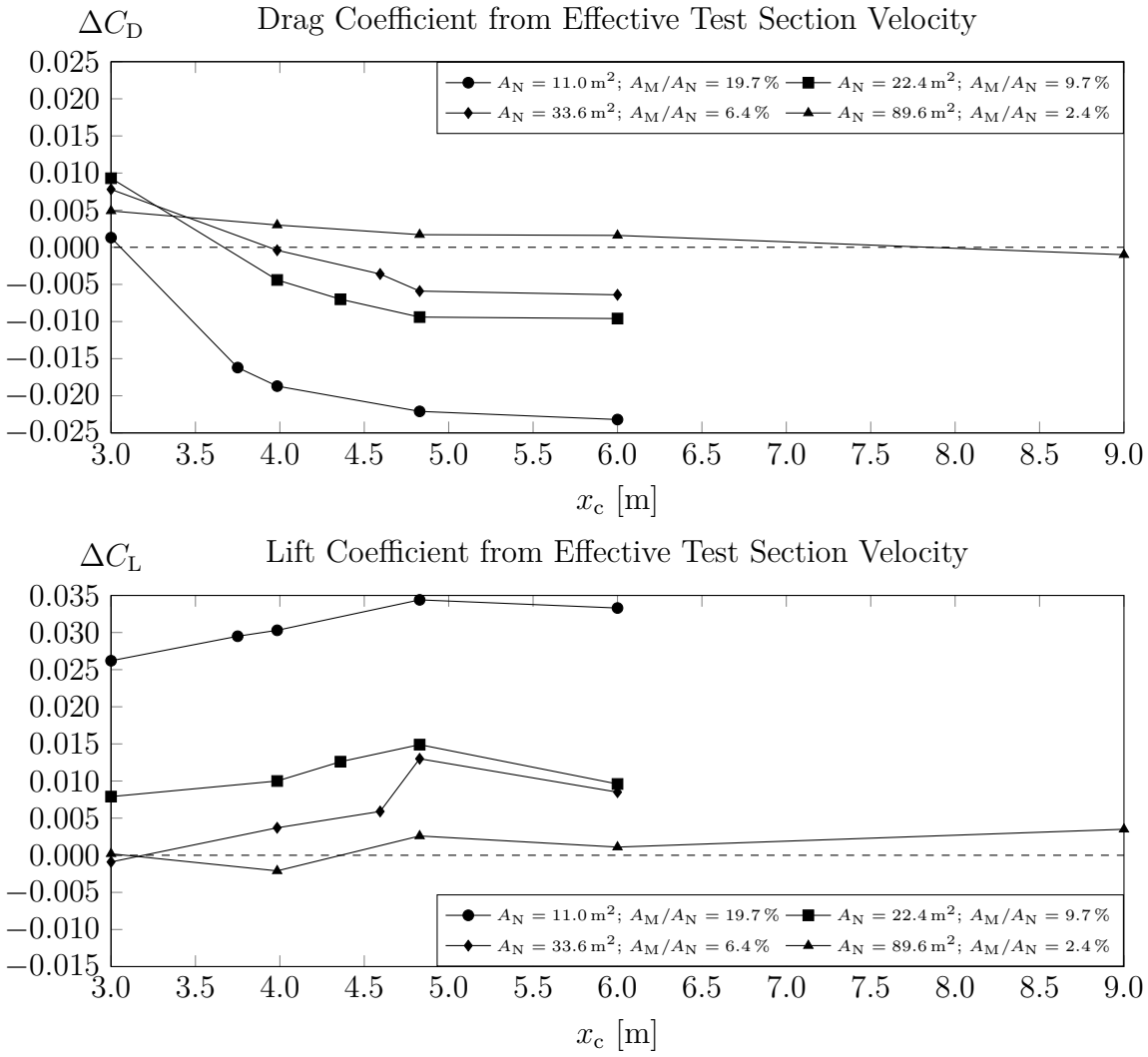

Figure 4.10: Drag and lift coefficients ΔC_D and ΔC_L using the effective velocity for the DrivAer estateback referring to open road conditions. The curves represent the dependency on the longitudinal model position x_c for different blockage ratios $A_\mathrm{M}/A_\mathrm{N}$.

Open Jet Interferences

Based on the results from Figure 4.10, it was assumed, that the effects at the really downstream position for the corresponding nozzle cross section were those applied by the jet expansion and, hence, resulted from interferences with the open jet. Therefore, the remaining difference to open road conditions for ΔC_D and ΔC_L were extracted for $\Delta x_\mathrm{c} = 6.0\,\mathrm{m}$ and $\Delta x_\mathrm{c} = 9.0\,\mathrm{m}$ respectively in order to draw the effect of the open jet over blockage ratio, see Figure 4.11. Figure 4.11 presents the effect of the jet expansion in comparison for CFD and the classical solid blockage of Lock (1929) using $\lambda = 2$ as suggested by Wickern (2014), see also equation (2.30) in section 2.1.2 on page 14:

$$\frac{\Delta u}{u_\infty} = \tau\lambda\left(\frac{A_\mathrm{M}}{A_\mathrm{N}}\right)^{3/2} \tag{4.7}$$

The results for drag show a good agreement up to $A_M/A_N \approx 10\,\%$ but the curves diverged for a further increase of the blockage ratio. The same trends were determined for the fastback and the notchback, see Figure A.9 and Figure A.10 in appendix A.3.2 on page 150 and 151. For the largest blockage ratio under investigation CFD predicted a significantly lower drag reduction due to the jet expansion as expected from the classical solid blockage correction. The opposite effects were investigated for the lift correction. It is worth to mention again, that the accuracy in lift prediction in CFD was estimated to be in the range of five counts. Furthermore, the total lift of both the fastback and the notchback was rather small and the corresponding correction was in the range of accuracy of CFD.

The classical solid blockage correction from Lock (1929) applies velocity correction induced in the model center. However, Collin et al. (2016) show that, in fact, a stream-wise velocity gradient was determined in the CFD simulations. Depending on the local block-

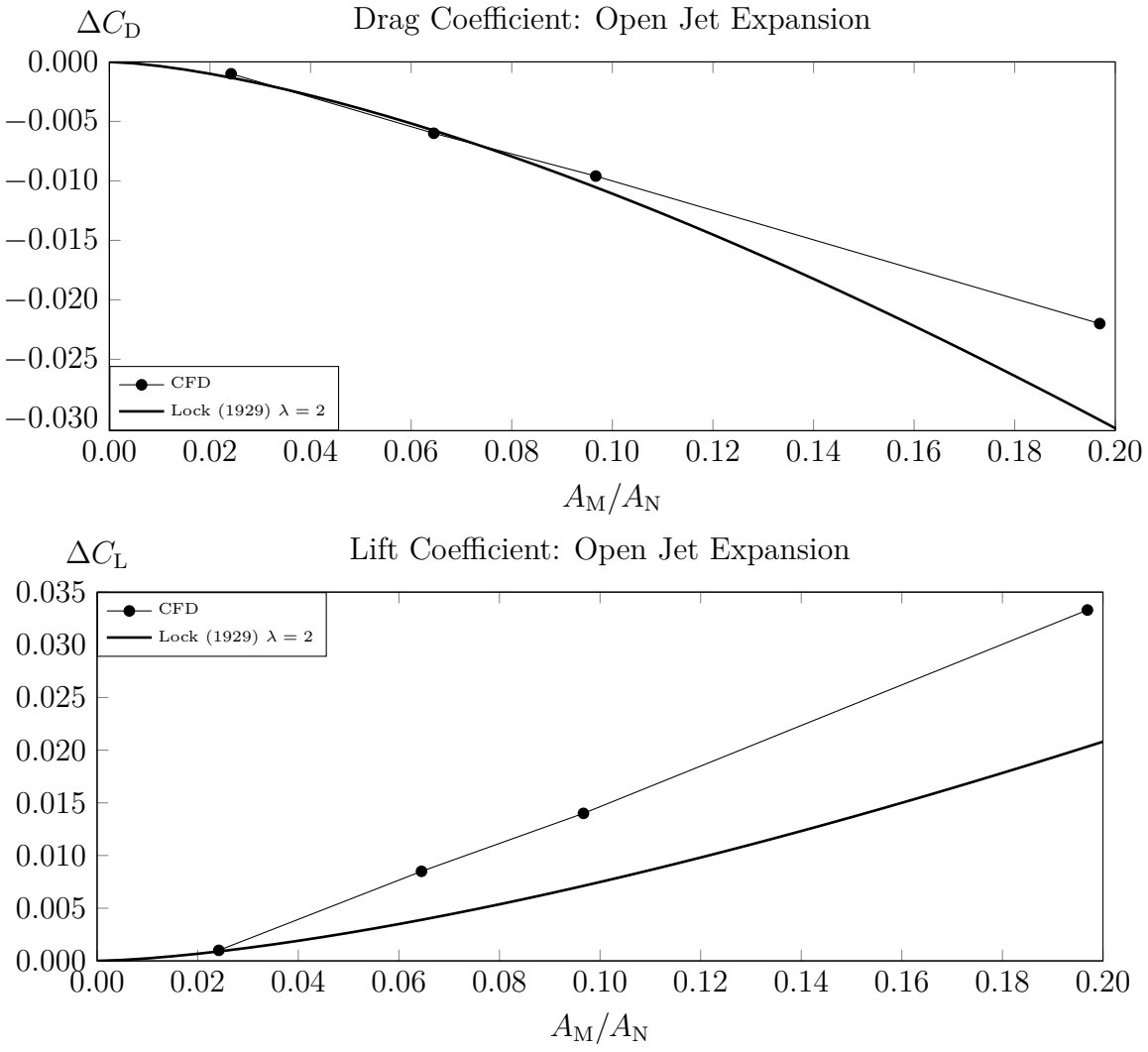

Figure 4.11: Estateback: Effect of open jet expansion on drag ΔC_D and lift coefficient ΔC_L depending on the blockage ratio A_M/A_N. The curves denote the results from CFD and the classical correction from Lock (1929) using $\lambda = 2$ as proposed by Wickern (2014).

age ratio the model is exposed to a gradient in jet expansion. Therefore, Figure 4.12 illustrates the induced velocity $\Delta u/u_\infty$ due to the jet expansion for the estateback and the notchback. As a reference, the comparison of the velocity profile at $y = 0.0\,\mathrm{m}$ and $z = 1.7\,\mathrm{m}$ the normalized velocity was scaled to be identical at $x = -3.0\,\mathrm{m}$. The curves show a decrease in effective test section velocity around the model up to $x \approx 0.5\,\mathrm{m}$, which is, approximately, the location of the largest blockage along the model. For both the estateback and the notchback the velocity deficit decreases again for $x > 0.5\,\mathrm{m}$. Due to the bluff body characteristics of the DrivAer body the re-acceleration of the flow around the rear region of the model did not reach the same velocity as in front of the model. Thus, a velocity deficit remained in the wake region of the model. The result was a reduction of both drag and lift.

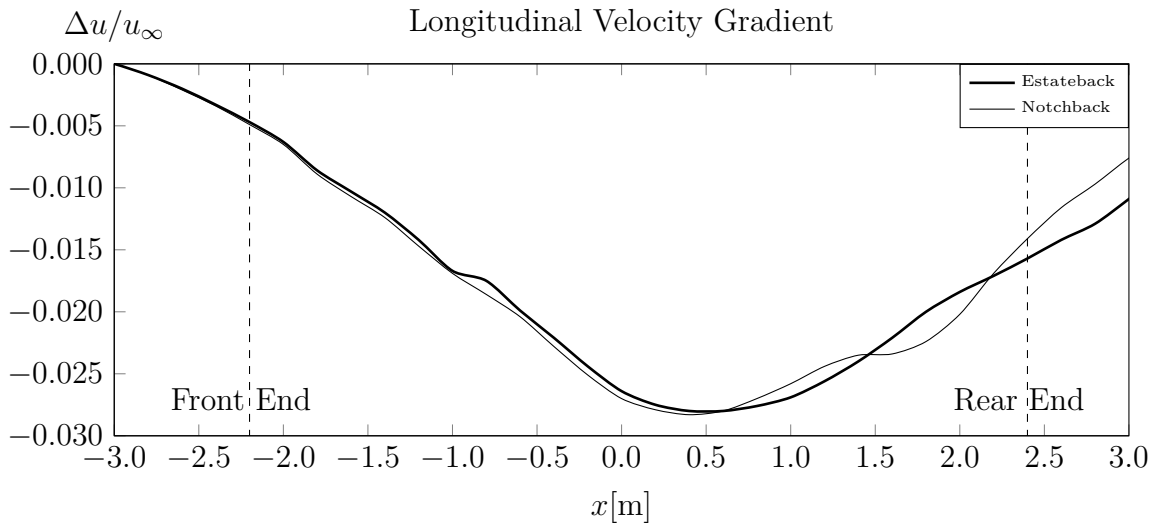

Figure 4.12: Longitudinal velocity gradient $\Delta u/u_\infty$ along the model extracted from the simulation with $A_\mathrm{N} = 11.0\,\mathrm{m}^2$ and $x_\mathrm{c} = 3.984\,\mathrm{m}$. The profiles were extracted from the $y = 0.0\,\mathrm{m}$ and $z = 1.7\,\mathrm{m}$ and normalized at $x = -3.0\,\mathrm{m}$.

4.2 Collector Interferences

Based on the results for the interference between nozzle and model in section 4.1 the half-infinite wind tunnel was "upgraded" towards a more realistic finite wind tunnel by adding a collector. The methodology is discussed in detail in section 4.2.1. For the present study, two general shapes of collector geometry were considered, the generic and the generic, converging collector. The results for both types are presented in section 4.2.2 and 4.2.3 respectively.

4.2.1 Methodology

The objective of the collector studies was mainly to achieve a better understanding about design parameters for the wind tunnel collector and its interaction with the model depending on the test section length. However, the collector interference was expected to decay as the longitudinal distance between the model and the collector increases. Thus, one of the key achievements was to determine the requirement of a minimum test section length in order to eliminate an effect on the aerodynamics of the model. The parameters under investigations were the test section length L_{TS} and the distance between model center and collector inlet x_{coll} respectively, the collector cross sections A_{C}, $A_{\mathrm{C,in}}$ and $A_{\mathrm{C,out}}$ and the flap angle α_{coll}.

The CFD simulations for the collector interference comprised about 140 configurations. Thus, this approach was decided to be applied only for one wind tunnel nozzle. Considering both the results from section 4.1 and the practical feasibility for a real facility, the nozzle cross section was selected with $A_{\mathrm{N}} = 22.4\,\mathrm{m}^2$. Thus, for the full scale DrivAer model, representing a mid-size production car, the corresponding blockage ratio was $A_{\mathrm{M}}/A_{\mathrm{N}} = 9.7\,\%$. It is worth to mention, that wind tunnel interferences with the nozzle and the open jet were determined to be not negligible at this blockage ratio. However, it turned out to be a sufficient compromise of accuracy and feasibility.

The second step was to specify the distance x_{c} between nozzle exit plane and the model center as it was desired to be constant for the collector investigations. On the one hand the premise was to eliminate longitudinal gradients originating from the nozzle as much as possible, but on the other hand, to limit the distance to the nozzle in order not to "waste" test section length. Comparing the results for the estateback, fastback and notchback for the nozzle $A_{\mathrm{N}} = 22.4\,\mathrm{m}^2$ operating with the plenum method, the longitudinal drag gradient was lower than 0.001 at the model position $x_{\mathrm{c}} = 4.8\,\mathrm{m}$. Thus, no nozzle interference corrections were expected to be required.

For the upcoming investigations the wind tunnel test section was set up with two general collector shapes, see Figure 4.13. The basic idea was to use a simple collector geometry, although it was well known that the collector design is often rather complex. Figure 4.13 depicts both a generic collector (top) with a constant cross section A_{C} and a generic, converging collector (bottom) with a stream-wise decreasing cross section from $A_{\mathrm{C,in}}$ to $A_{\mathrm{C,out}}$. The essential parameters of the generic collector were, as stated above, the cross sectional area A_{C} as well as its x-position in the test section x_{coll}. Furthermore, the width-to-height ratio $W_{\mathrm{C}}/H_{\mathrm{C}}$ was a possible parameter, but it was selected to be constant and equivalent to the nozzle:

$$\frac{W_{\mathrm{C}}}{H_{\mathrm{C}}} = \frac{W_{\mathrm{N}}}{H_{\mathrm{N}}} = 1.4 \tag{4.8}$$

Additional geometric parameters such as the thickness (0.4 m) and the specific shape of the flap's tip were expected to be of minor importance. The collector surface was (only) partially treated as a friction wall in order to limit the computational effort. Therefore,

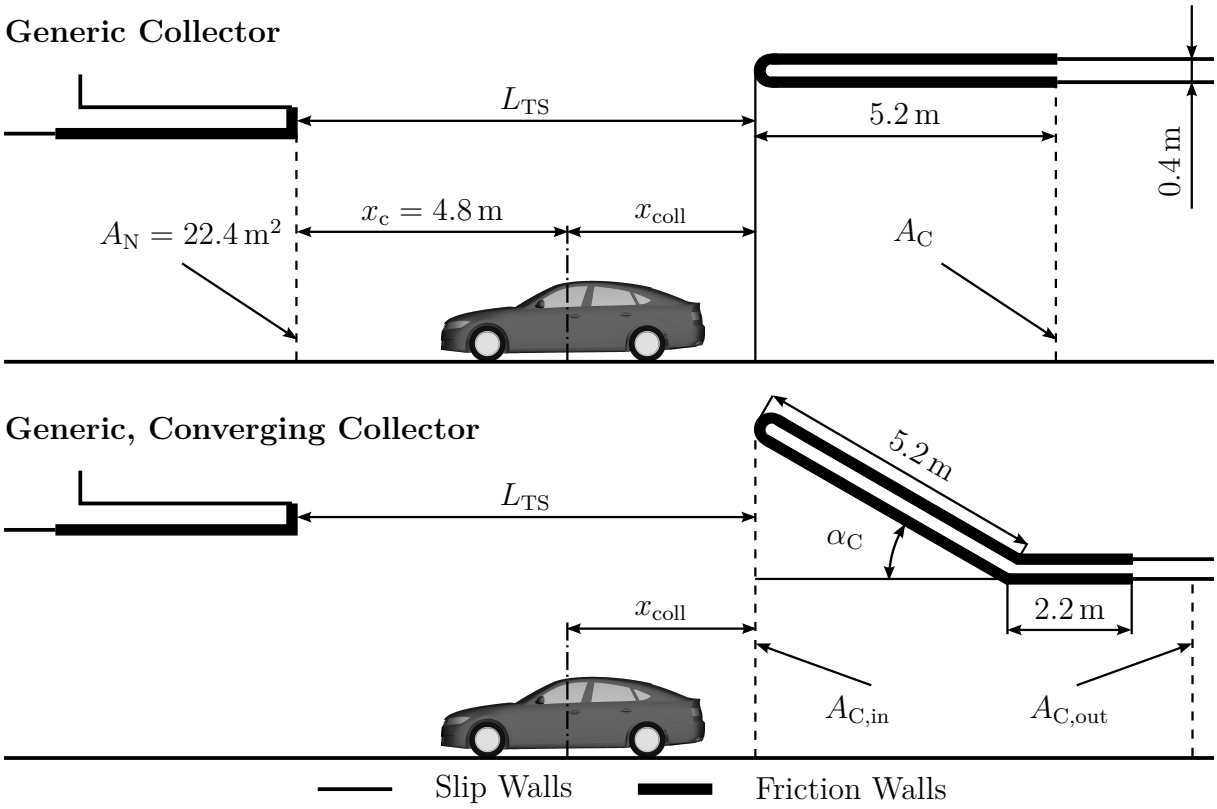

Figure 4.13: Collector geometry for parametric studies using a generic collector (top) and a generic, converging collector (bottom). The parameters under investigation were the test section length L_{TS} and the distance between model center and collector inlet x_{coll} respectively, the collector cross sections A_C, $A_{C,in}$ and $A_{C,out}$ and the flap angle α_C. Both the cross section of the nozzle A_N and the model position x_c were constant.

5.2 m inlet length were applied with friction followed by a slip wall treatment all the way through the outlet.

Obviously, the converging collector exposed a larger number of additional parameters such as the flap angle α_C and the flap length. However, the flap length was defined to be 5.2 m and the flap angle was selected to be equal for the side flaps and the top flap. Therefore, the width-to-height ratio above was set for the inlet area $W_{C,in}/H_{C,in} = 1.4$. Thus, depending on $A_{C,in}$ and α_{coll} the outlet ratio was $W_{C,in}/H_{C,in} < 1.4$. Additionally, 2.2 m of friction wall were added for the converging collector in order to cover the transition into the high-speed diffusor sufficiently.

As stated above, the test section setup was based on the half-infinite test section with $A_N = 22.4\,m^2$ and $x_c = 4.8\,m$. Thus, the evaluation of collector interferences in the finite wind tunnel (FWT) referred to the corresponding simulation in the half-infinite wind tunnel (HIWT), see Table 4.2:

$$\Delta C_i = C_{i,FWT} - \Delta C_{i,HIWT} \tag{4.9}$$

Table 4.2: Reference for collector interferences in the finite wind tunnel (FWT). Aerodynamic force coefficients C_D, C_L, $C_{L,f}$ and $C_{L,r}$ for the DrivAer with estateback, fastback and notchback from the simulations with $A_N = 22.4\,m^2$ and $x_c = 4.8\,m$ (plenum method).

	A_M	C_D	C_L	$C_{L,f}$	$C_{L,r}$
Estateback	2.166	0.288	−0.186	−0.096	−0.090
Fastback	2.162	0.239	−0.029	−0.070	0.041
Notchback	2.165	0.243	−0.050	−0.066	0.017

4.2.2 Results for the Generic Collector

The generic collector with constant cross section A_C was subject of a first, detailed investigation regarding the effects of test sections length L_{TS} and A_C on the model for the test section configuration explained above. Therefore, again the estateback was selected for a wide range of these parameters: $8.2\,m \leq L_{TS} \leq 18.7\,m$ and $1.0 \leq A_C/A_N \leq 3.0$. Based on these results, some selected configurations were performed for both the fastback and the notchback, too. The results are discussed below separately for the drag and the lift coefficients.

Drag Contributions for Collector Interferences: Generic Collector

Figure 4.14 depicts the effects on the drag coefficient ΔC_D over the collector cross section A_C/A_N. The particular curves denote different test section lengths. The results are presented in a similar form as given by von Schulz-Hausmann and Vagt (1988) described in section 2.3 on page 30.

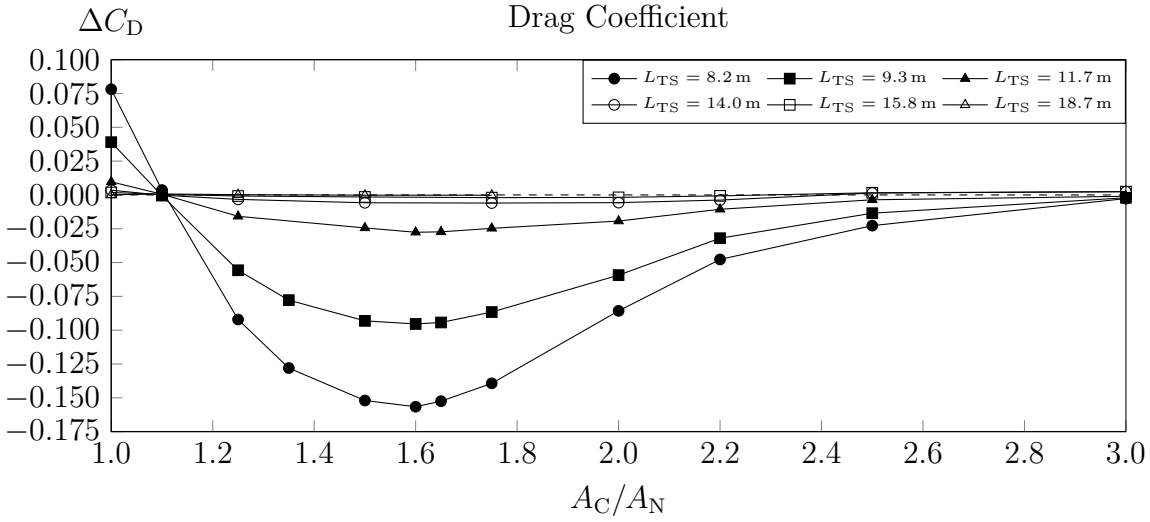

Figure 4.14: Aerodynamic drag coefficient ΔC_D for the DrivAer with estateback referring to the half-infinite wind tunnel $A_N = 22.4\,m^2$ and $x_c = 4.8\,m$. The curves represent different test section lengths L_{TS}.

Figure 4.14 illustrates two characteristic sections regarding the dependency of ΔC_D on A_C/A_N, which were divided approximately at $A_C/A_N \approx 1.6$. For $A_C/A_N < 1.6$ the drag increased with decreasing collector cross section, which correlates well with the theory of von Schulz-Hausmann and Vagt (1988) based on Bernoulli's equation. A decrease of collector cross section induced a larger average velocity at the collector inlet (and upstream of it) as the mass flow was defined by the nozzle to be constant. Accordingly, at least for rather short test sections, the model was exposed to a higher velocity. For all lengths of the test section investigated, the cross section with no effective drag interference was $A_C/A_N \approx 1.1$. Figure 4.15 provides a better understanding to explain the effects from

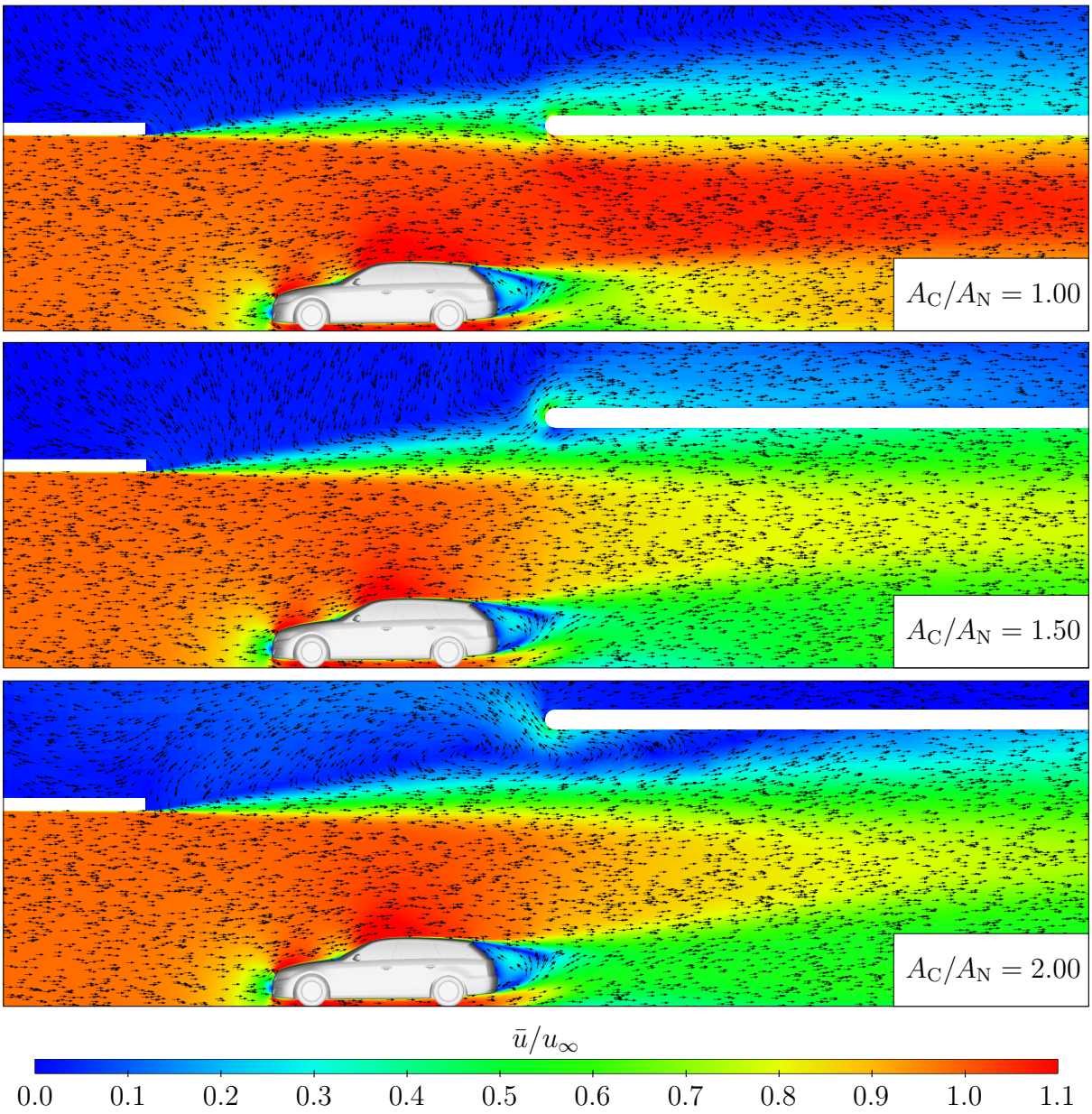

Figure 4.15: Velocity field $\bar{u}/u_\infty$ in the symmetry plane $y = 0$ for a test section length $L_{TS} = 8.2\,\text{m}$. Top: $A_C/A_N = 1.0$; Middle: $A_C/A_N = 1.5$; Bottom: $A_C/A_N = 2.0$. The arrows denote the local direction of the vector field.

Figure 4.14. The decrease of drag with increasing collector cross section for $A_C/A_N < 1.6$ was explained with an expanding or, respectively, compressing effect of the open jet due to the collector boundaries. Thus, a disturbance of the propagation of the "free" open jet was investigated. Following the results from Figure 4.14 the ratio $A_C/A_N = 1.1$ correlated well with the half-infinite wind tunnel results. Figure 4.15 (top) depicts the flow field for $A_C/A_N = 1.0$, for which an acceleration of the flow due to the collector cross section was investigated. For the plane $y = 0$, the entrainment in the free shear layer was mainly precipitated over the top of the collector and the jet basically filled the whole cross section of the collector. Comparing the flow field for $A_C/A_N = 1.5$ (middle), which was the configuration close to the drag minimum in Figure 4.14, the jet boundary barely follows the larger cross section of the collector with an expansion of the jet. The jet still "fills" most of the collector area, whereas a small flow separation was determined at the collector inlet. This "over-expansion" caused an average deceleration of the jet velocity due to the collector and, hence, an effective reduction of drag at the model. For a further increase to $A_C/A_N = 2.0$, see Figure 4.15 (top), the jet boundary was no longer attached to the collector walls at the collector inlet but further downstream inside the collector. Furthermore, the entrained mass flow in the free shear layer of the jet partially entered the collector and generated significant re-circulating zones around the collector tip. At the same time the jet expansion due to the collector started to decay with increasing A_C for $A_C/A_N > 1.6$. With this decay the flow around the model was accelerated with increasing collector area compared to $A_C/A_N = 1.6$, which was connected to an effective drag recovery at the model. Summarizing, with the effects explained above depending on the cross sectional area of the collector, an attached region and a detached region for A_C for A_C/A_N were classified. An increase of the collector cross section in the detached region was experienced as an effective extension of test section length L_{TS}. This effect was consistent for all test section lengths investigated. Figure 4.16 illustrates the results

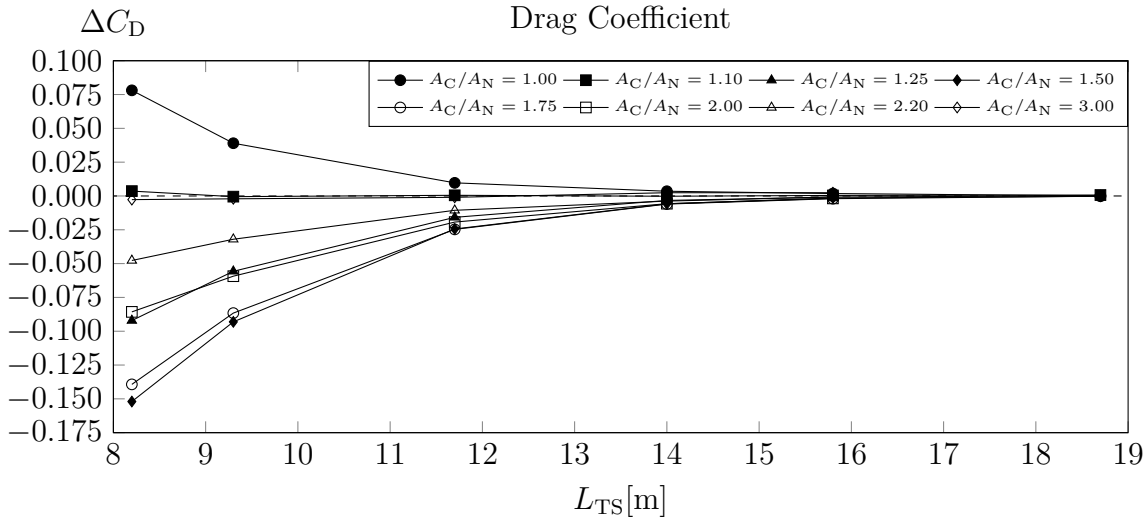

Figure 4.16: Drag coefficient ΔC_D for the DrivAer with estateback referring to the half-infinite wind tunnel $A_N = 22.4\,m^2$ and $x_c = 4.8\,m$. The curves represent different collector inlet cross sections A_C/A_N.

for the estateback in terms of L_{TS}. A consistent decay of collector interference with increasing test section length was observed. As a first intermediate result, the maximum drag interference determined for the estateback was $|\Delta C_{\mathrm{D,max}}| = 0.028$ for $L_{\mathrm{TS}} = 11.7\,\mathrm{m}$, $|\Delta C_{\mathrm{D,max}}| = 0.006$ for $L_{\mathrm{TS}} = 14.0\,\mathrm{m}$, $|\Delta C_{\mathrm{D,max}}| = 0.002$ for $L_{\mathrm{TS}} = 15.8\,\mathrm{m}$ and $|\Delta C_{\mathrm{D,max}}| < 0.001$ for $L_{\mathrm{TS}} = 18.7\,\mathrm{m}$.

Comparing the estateback with both the fastback and the notchback, some selected configurations were simulated. In terms of drag dependency on test section length, Figure 4.17 depicts the comparison of the estateback with the notchback. The results for the fastback were similar, see Figure A.11 in appendix A.3.3 on page 152. In general, the trends for all rear ends were consistent to the effects explained above. The drag interference was determined to be slightly lower for both the notchback and the fastback compared to the estateback. However, the decay of drag interference with increasing test section length was still comparable.

Lift Contributions for Collector Interferences: Generic Collector

Figure 4.18 depicts the corresponding lift results $\Delta C_{\mathrm{L,f}}$ and $\Delta C_{\mathrm{L,r}}$ from Figure 4.14 for the estateback. As expected, the interference of the collector with the front lift $\Delta C_{\mathrm{L,f}}$ was significantly lower than for the rear lift $\Delta C_{\mathrm{L,r}}$. For a test section length $L_{\mathrm{TS}} \geq 11.7\,\mathrm{m}$ the influences on $\Delta C_{\mathrm{L,f}}$ were already < 0.005 and, hence within the range of accuracy. Thus, the focus was put on $\Delta C_{\mathrm{L,r}}$ for the following investigations. Comparing the rear lift results from Figure 4.18 with the drag results from Figure 4.14, similar trends but of opposite, absolute sign were identified. According to the reference without a collector, the negative shift in rear lift for $A_{\mathrm{c}}/A_{\mathrm{N}} < 1.1$ and positive for $A_{\mathrm{c}}/A_{\mathrm{N}} > 1.1$ was explained with an increase and a decrease respectively of effective flow velocity, especially at the

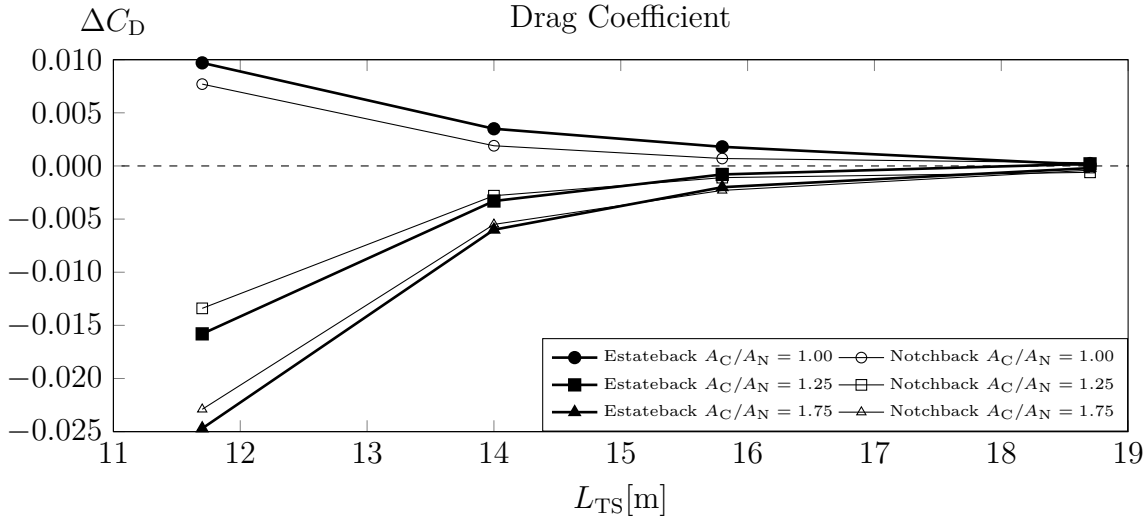

Figure 4.17: Drag coefficient ΔC_{D} for the DrivAer with estateback and notchback referring to the half-infinite wind tunnel $A_{\mathrm{N}} = 22.4\,\mathrm{m}^2$ and $x_{\mathrm{c}} = 4.8\,\mathrm{m}$. The curves represent different collector inlet cross sections $A_{\mathrm{C}}/A_{\mathrm{N}}$.

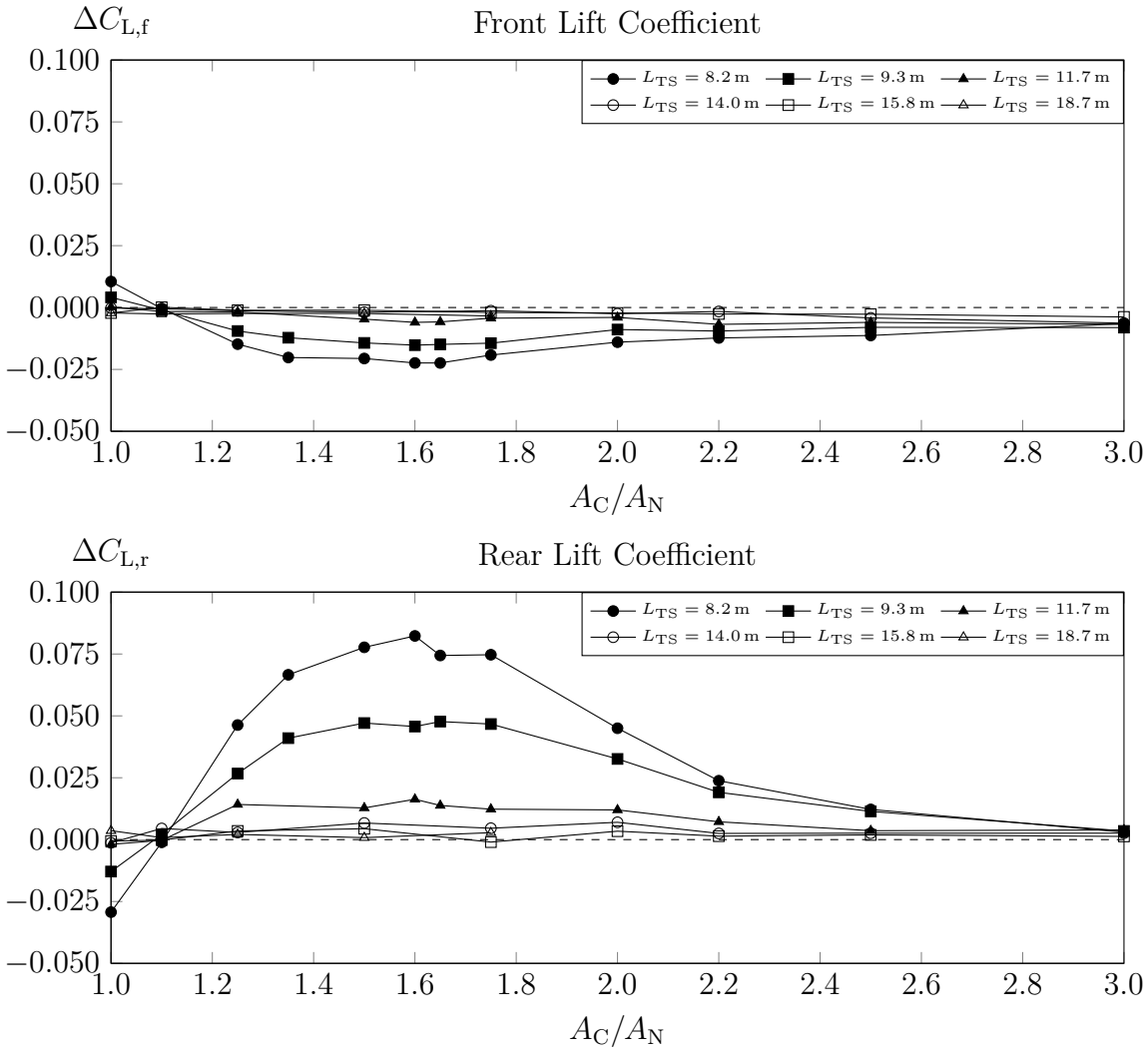

Figure 4.18: Lift coefficients $\Delta C_{\mathrm{L,f}}$ and $\Delta C_{\mathrm{L,r}}$ for the DrivAer with estateback referring to the half-infinite wind tunnel $A_{\mathrm{N}} = 22.4\,\mathrm{m}^2$ and $x_{\mathrm{c}} = 4.8\,\mathrm{m}$. The curves represent different test section lengths L_{TS}.

rear end of the model, see also Figure 4.15. Thus, the absolute down-force was reduced if the model was exposed to decelerated flow due to the collector.

Comparing the rear lift interferences for different rear ends, Figure 4.19 presents the results for the estateback and the notchback. The corresponding results for the fastback showed similar trends, see Figure A.12 in appendix A.3.3 on page 152. In general, the rear lift data was noisier than the drag data as the experienced accuracy was in the range $\Delta C_{\mathrm{L,r}} \pm 0.005$. However, considering the scale in Figure 4.19, some trends could be derived though. In principle, both the fastback and the notchback showed, in terms of positive or negative sign, the same trends for $\Delta C_{\mathrm{L,r}}$. That was somewhat surprising, following the line of arguments above for the estateback using an effective velocity increase or decrease due to the collector. Considering the absolute rear lift from the reference case, see Table 4.2, a decrease of rear lift was expected for both the fastback and the notchback with decreasing velocity. However, both Figure 4.19 and Figure A.12 show the opposite trend. Going back

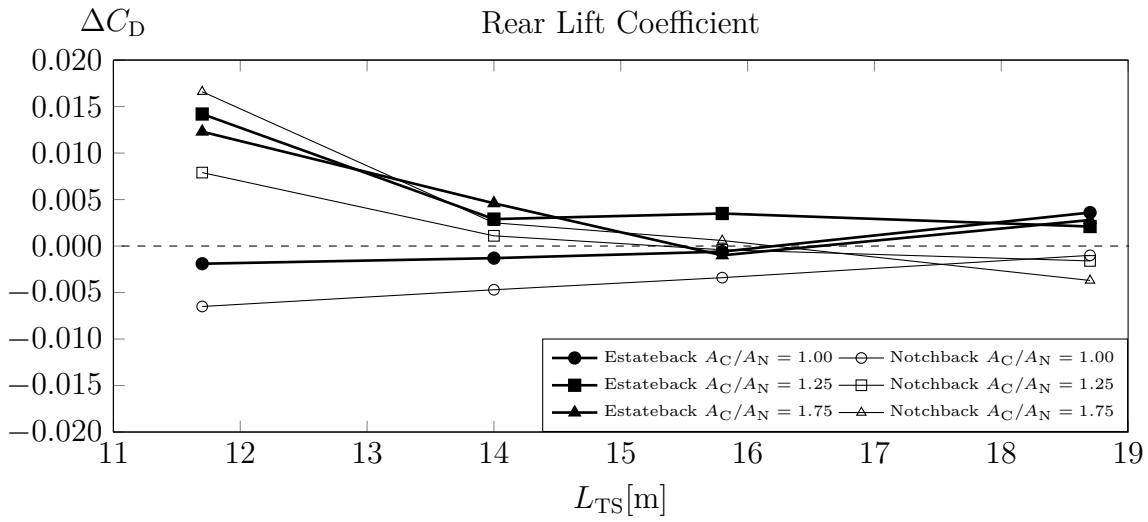

Figure 4.19: Rear lift coefficient $\Delta C_{L,r}$ for the DrivAer with estateback and notchback referring to the half-infinite wind tunnel $A_N = 22.4\,m^2$ and $x_c = 4.8\,m$. The curves represent different collector cross sections A_C/A_N.

to the argument concerning the attached and detached collector and the corresponding expansion or compression of the open jet, it was worth take into account the effect of the flow angle. Figure 4.20 illustrates both the effect of the collector on local velocity $\bar{u}/u_\infty$ and the vertical flow angle $\alpha_{u,z}$ downstream the model compared to the reference without

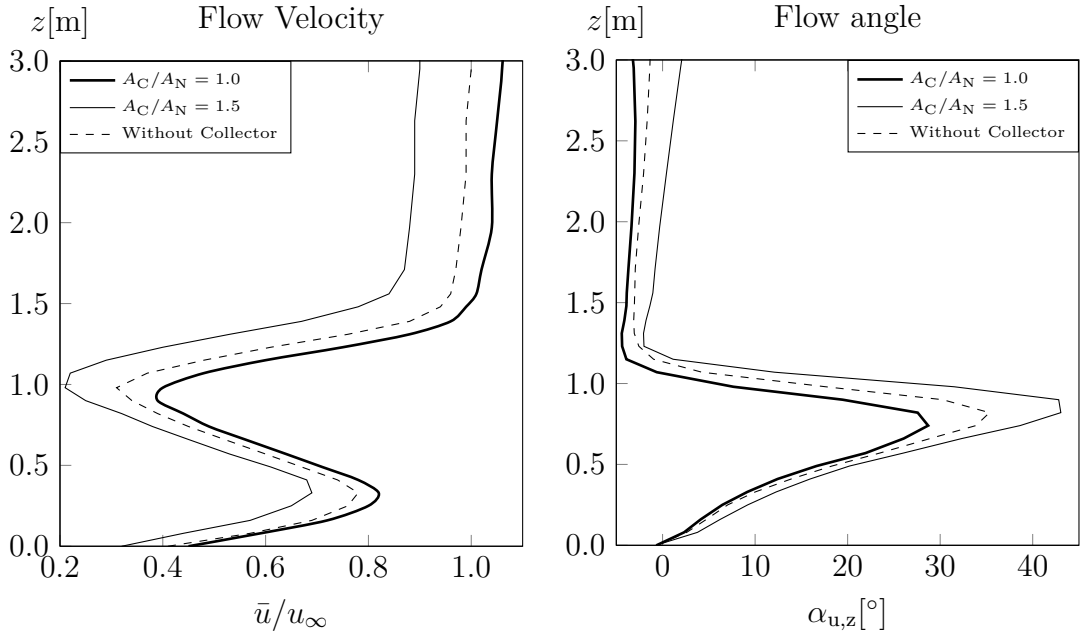

Figure 4.20: z-profiles at the collector inlet ($x = 3.5\,m$) for the velocity $\bar{u}/u_\infty$ (left) and the vertical flow angle $\alpha_{u,z}$ (right). The test section length was $L_{TS} = 8.2\,m$. The curves denote two cross sectional areas of the collector as well as the reference without collector.

collector (half-infinite test section). As discussed above, a small cross sectional area of the collector induced an over-velocity in the plane under investigation whereas the opposite effect occurred for a large collector. Comparing the flow angle, the small collector induced a negative shift in flow angle and, accordingly, the large collector a positive shift, also present in the wake region of the model. Thus, a combination of velocity and flow angle interference was determined for simulations with collector, especially for rather short test sections. A positive, induced flow angle for $A_C/A_N > 1.1$ explained an increase of rear lift $\Delta C_{L,r}$ for all rear ends under investigation.

4.2.3 Results for the Generic, Converging Collector

Based on the results for the generic collector, some selected configurations were set up for the generic, converging collector. Firstly, a similar approach as for the generic collector using the shortest test section $L_{TS} = 8.2\,m$ was performed by varying both the cross section $A_{C,in}/A_N$ and the flap angle α_C and, secondly, the decay of interference due to the generic, converging collector with increasing test section length was evaluated. Figure 4.21 depicts the flow field at $y = 0$ for $L_{TS} = 8.2\,m$, $A_{C,in}/A_N = 2.0$ and for three different flap angles α_C. The velocity field for $\alpha_C = 0\,°$ (top) represented the detached collector as the flow attached not at the tip of the collector but further downstream. Comparing, the result for the flap angle $\alpha_C = 10\,°$ (middle) the open jet attached at the downstream end of the flap and for $\alpha_C = 30\,°$ (bottom) approximately at the middle of the flap. The effect of the collector on the velocity field close to the model seemed comparable for $\alpha_C = 0\,°$ and $\alpha_C = 10\,°$, but a significant acceleration of the flow, especially in the wake region of the model, was investigated for $\alpha_C = 30\,°$.

Drag Contributions for Collector Interferences: Generic, Converging Collector

As stated above, the general approach for the generic collector was repeated for the generic, converging collector and for the estateback. The effect on drag of both the collector inlet area $A_{C,in}/A_N$ and the flap angle α_C is presented in Figure 4.22. It is worth to mention, that the reference area for the converging collector was the inlet area $A_{C,in}/A_N$. For the following discussion the focus is put on the sections, for which the collector had drag decreasing effect, as this range was expected to be more relevant for the practical solution in a real facility. In principle, the collectors with different flap angle showed the same trends as determined for the generic collector. Two general effects were:

1. The maximum drag reduction (= minimum drag) due to the generic collector ($\alpha_C = 0\,°$) was at $A_C/A_N \approx 1.6$ and representative for the corresponding test section length L_{TS}. The maximum drag reduction $\Delta C_{D,max}$ decreased with increasing flap angle: $\Delta C_{D,max} = -0.157$ for $\alpha_C = 0\,°$, $\Delta C_{D,max} = -0.118$ for $\alpha_C = 10\,°$, $\Delta C_{D,max} = -0.065$ for $\alpha_C = 20\,°$, $\Delta C_{D,max} = -0.028$ for $\alpha_C = 30\,°$.
2. For the converging collector, the location of A_C/A_N of maximum drag interference $\Delta C_{D,max}$ was shifted towards $A_C/A_N > 1.6$ if the reference area was the collector inlet $A_{C,in}$. The opposite effect was present if the outlet $A_{C,out}$ was the reference.

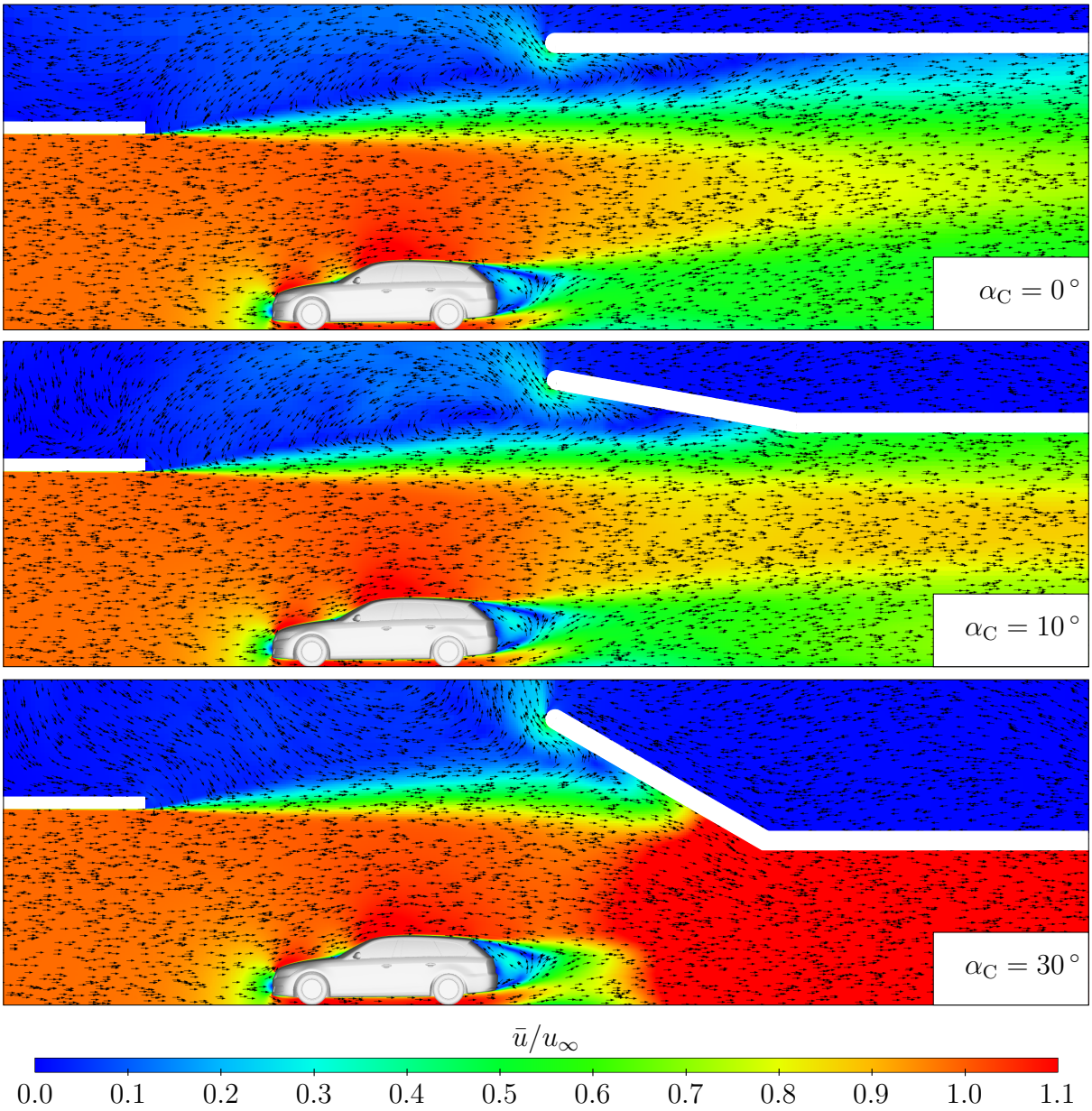

Figure 4.21: Velocity field $\bar{u}/u_\infty$ in the symmetry plane $y = 0$ for a test section length $L_{TS} = 8.2\,\text{m}$ and a collector inlet area of $A_{C,in}/A_N = 2.0$. Top: $\alpha_C = 0\,°$; Middle: $\alpha_C = 10\,°$; Bottom: $\alpha_C = 30\,°$. The arrows denote the local direction of the vector field.

Thus, an effective extension of test section length, depending on the flap angle, was determined for the converging collectors under investigation. Therefore, the decay of maximum drag interference $\Delta C_{D,max}$ with increasing test section length was taken from the generic collector ($\alpha_C = 0\,°$) in order to calculate the effective test section length $L_{TS,eff}$ for each converging collector. Figure 4.23 shows that, although L_{TS} was constant with $L_{TS} = 8.2\,\text{m}$, the effective test section length increased with increasing flap angle α_C up to 11.7 m for $\alpha_{coll} = 30\,°$. In the next step, the corresponding curve, as presented in Figure 4.22, was interpolated for each effective test section length $L_{TS,eff}$ from Figure 4.23. Furthermore, the curves were shifted with respect to A_C in order to match the maximum

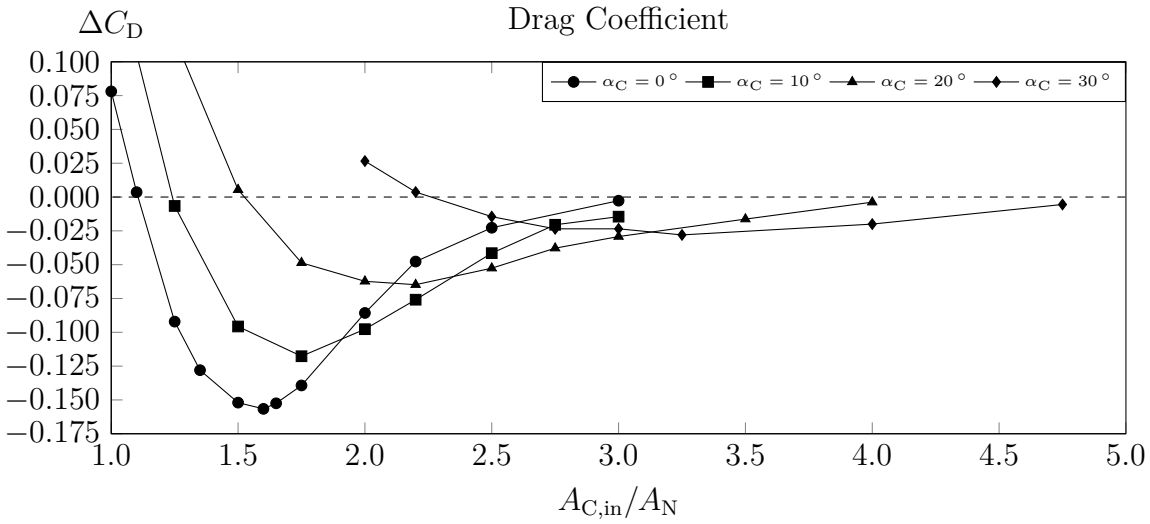

Figure 4.22: Drag coefficient ΔC_D for the DrivAer with estateback referring to the half-infinite wind tunnel $A_\mathrm{N} = 22.4\,\mathrm{m}^2$ and $x_\mathrm{c} = 4.8\,\mathrm{m}$. The curves represent different flap angles α_C for a test section length $L_\mathrm{TS} = 8.2\,\mathrm{m}$.

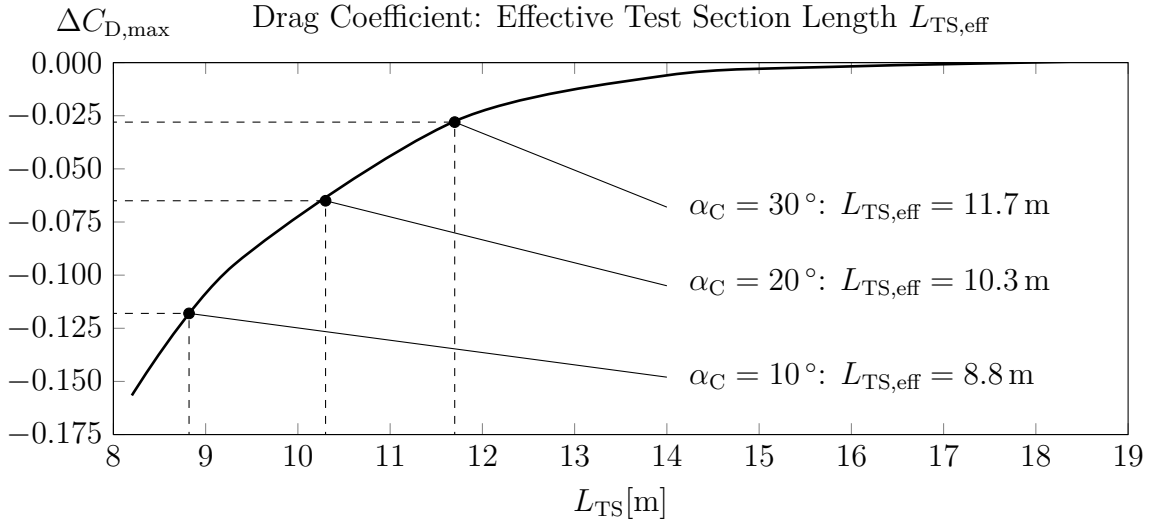

Figure 4.23: Maximum drag reduction ΔC_D for the generic collector depending on the test section length. Based on the generic collector, the effective test section length $L_\mathrm{TS,eff}$ for the configurations of the converging collector at $L_\mathrm{TS} = 8.2\,\mathrm{m}$ was interpolated.

drag reduction at $A_\mathrm{C}/A_\mathrm{N} = 1.6$. Figure 4.24 depicts the results using the example of the collector with $\alpha_\mathrm{C} = 10\,°$ and an effective test section length of $L_\mathrm{TS,eff} = 8.8\,\mathrm{m}$. The solid line represents the interpolated data for the generic collector with $\alpha_\mathrm{C} = 0\,°$ for $L_\mathrm{TS} = 8.8\,\mathrm{m}$. Two different references were used for the collector area of the converging collector, the inlet area $A_\mathrm{C,in}$ (circle markers) and the outlet area $A_\mathrm{C,out}$ (square markers). After shifting the curves in order to match the maximum interference, a good agreement with the generic collector was achieved on the left branch (attached collector: $A_\mathrm{C}/A_\mathrm{N} < 1.6$) using $A_\mathrm{C,in}$ and, respectively on the right branch (detached collector: $A_\mathrm{C}/A_\mathrm{N} > 1.6$)

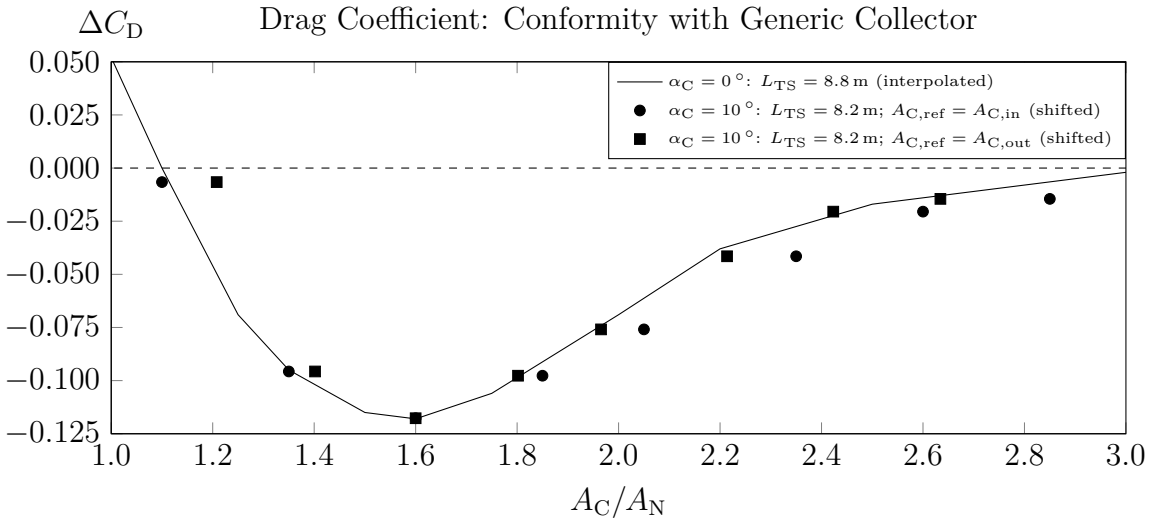

Figure 4.24: Conformity of generic $\alpha_C = 0\,°$ and the generic, converging collector $\alpha_C = 10\,°$ by interpolation of the drag interference for $\alpha_{coll} = 0\,°$ at the effective test section length $L_{TS,eff} = 8.8\,m$ for $\alpha_C = 10\,°$. The marks denote the choice of reference cross section $A_{C,in}$ and $A_{C,out}$ respectively.

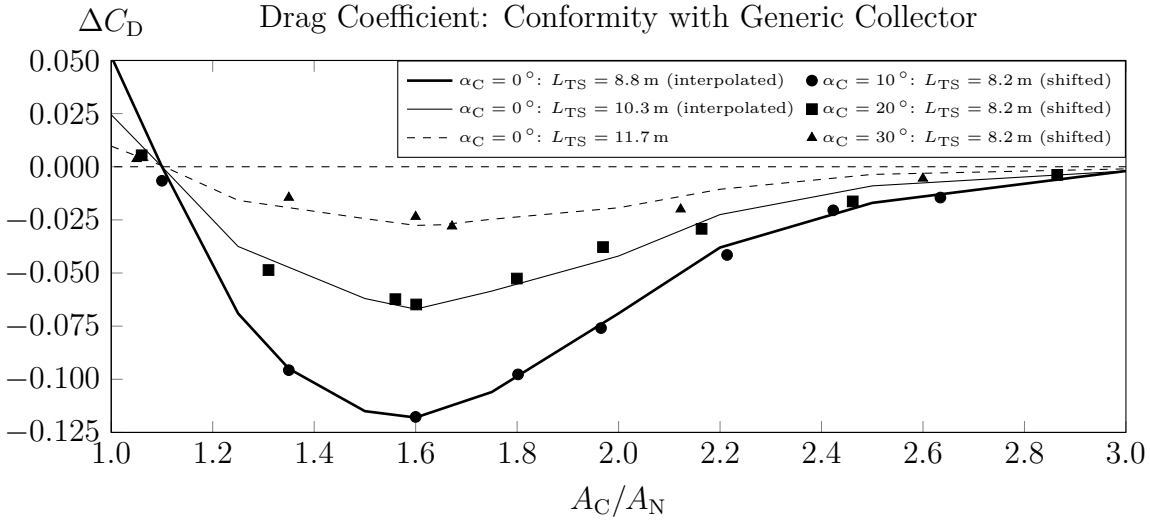

Figure 4.25: Drag conformity of the generic $\alpha_C = 0\,°$ and the generic; converging collector for $\alpha_C = 10\,°$, $\alpha_C = 20\,°$ and $\alpha_C = 30\,°$.

using $A_{C,out}$. Thus, $A_{C,in}$ turned out to be appropriate for the attached and $A_{C,out}$ for the detached collector in order to show the conformity of interference with the generic collector. Therefore, Figure 4.25 brings this knowledge together, comparing the results for the larger angles $\alpha_C > 10\,°$ as well. Figure 4.25 depicts the comparison of conformity between the generic and the generic, converging collector using the approach above. In general, the results showed good agreement for the range under investigation. Based on the knowledge about of an effectively extended test section due to the collector angle, the configurations of the converging collectors with the maximum interference were selected for simulations with increased test section length $L_{TS} \leq 15.8\,m$. Figure 4.26 shows that

the effect of collector interference decayed "faster" with increasing test section length if the flap angle was increased. Consequently, the maximum collector interference determined was reduced by increasing the flap angle in the range under investigation.

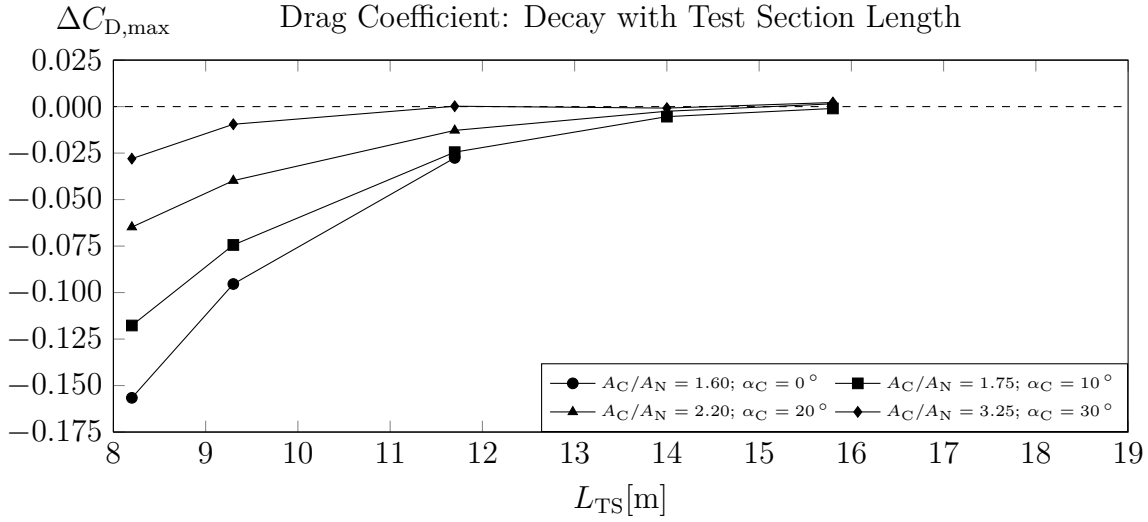

Figure 4.26: Decay of drag interference $\Delta C_{\mathrm{D,max}}$ for the DrivAer with estateback referring to the half-infinite wind tunnel $A_{\mathrm{N}} = 22.4\,\mathrm{m}^2$ and $x_{\mathrm{c}} = 4.8\,\mathrm{m}$. The curves represent the maximum expected drag reduction for the corresponding flap angle α_{C}.

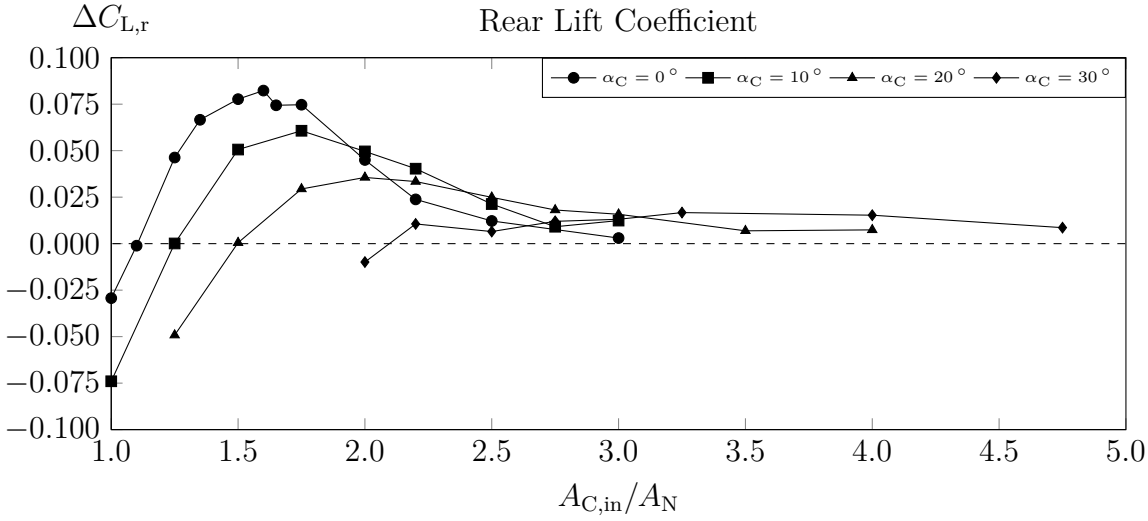

Figure 4.27: Rear lift coefficient $\Delta C_{\mathrm{L,r}}$ for the DrivAer with estateback referring to the half-infinite wind tunnel $A_{\mathrm{N}} = 22.4\,\mathrm{m}^2$ and $x_{\mathrm{c}} = 4.8\,\mathrm{m}$. The curves represent different flap angles α_{C} for a test section length $L_{\mathrm{TS}} = 8.2\,\mathrm{m}$.

Lift Contributions for Collector Interferences: Generic, Converging Collector

The same approach as presented for the interferences regarding drag was applied to evaluate the effects for the rear lift coefficients $\Delta C_{\mathrm{L,r}}$. As discussed above, the effects of the collector on front lift were significantly smaller and, hence, are not discussed here further in detail. In, principle, the rear lift interferences for the converging collectors confirmed the trends investigated for drag. Therefore, Figure 4.27 presents the results for the test section length $L_{\mathrm{TS}} = 8.2\,\mathrm{m}$, including three different flap angles and referring to the collector inlet area $A_{\mathrm{C,in}}$. The same effect of an extended effective test section length as for

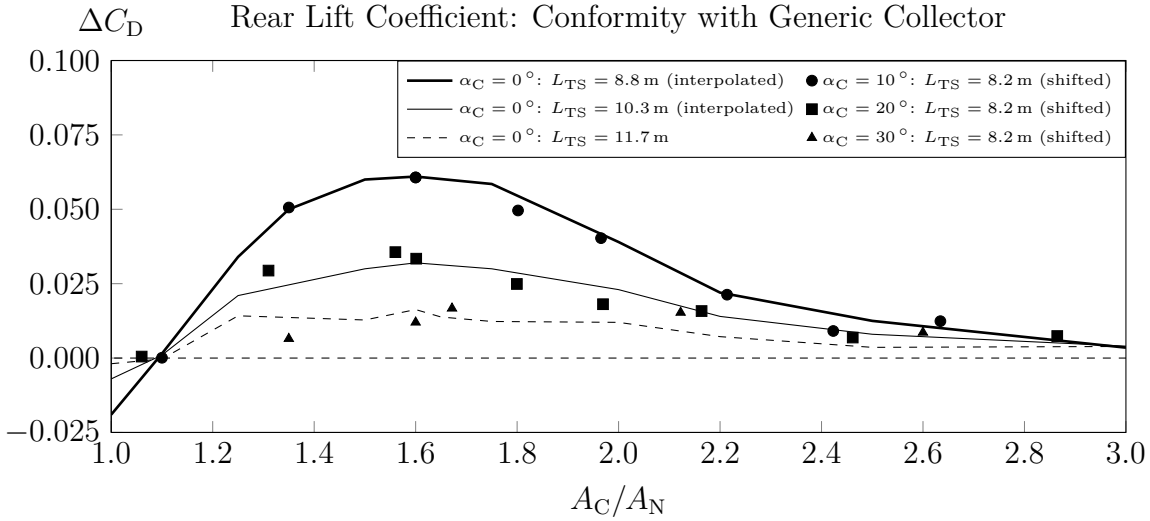

Figure 4.28: Rear lift conformity of generic $\alpha_{\mathrm{C}} = 0\,^{\circ}$ and the generic, converging collector for $\alpha_{\mathrm{C}} = 10\,^{\circ}$, $\alpha_{\mathrm{C}} = 20\,^{\circ}$ and $\alpha_{\mathrm{C}} = 30\,^{\circ}$.

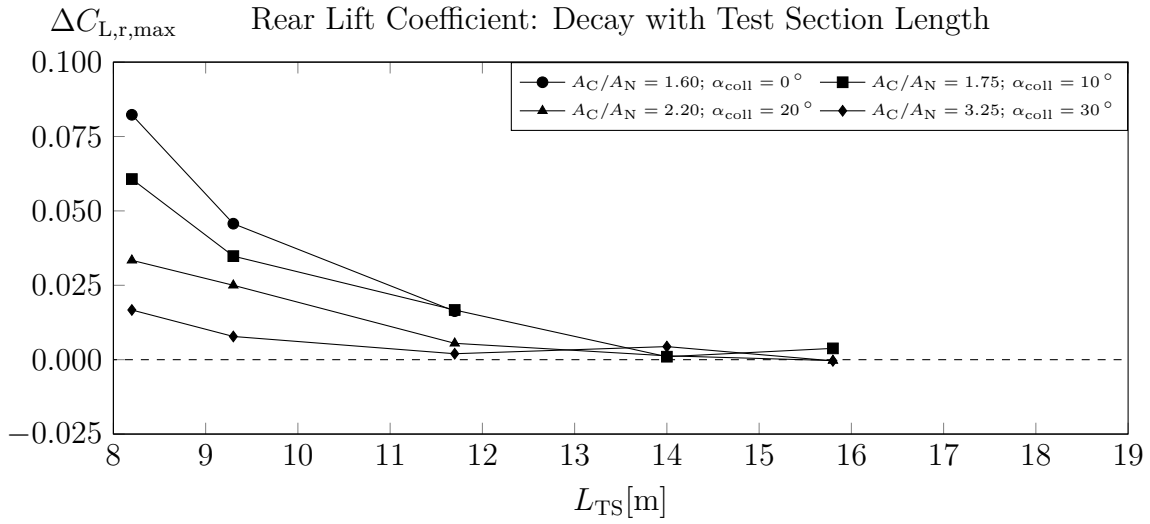

Figure 4.29: Decay of rear lift interference $\Delta C_{\mathrm{L,r,max}}$ for the DrivAer with estateback referring to the half-infinite wind tunnel $A_{\mathrm{N}} = 22.4\,\mathrm{m}^2$ and $x_{\mathrm{c}} = 4.8\,\mathrm{m}$. The curves represent the maximum expected drag reduction for the corresponding flap angle α_{coll}.

drag was investigated for the rear lift coefficient, too. Furthermore, also conformity with the generic collector was confirmed, see Figure 4.28, although the accuracy (± 0.010) was not as good as for the drag coefficient (± 0.002). However, the rear lift coefficient was experienced to be more sensitive. Furthermore, the decay of maximum rear lift interference was in good in agreement with the results for drag. For larger flap angles of the converging collector the interference died out at a shorter test section length, see Figure 4.29.

4.3 Moving Ground Interferences

The third basic interference under investigation in this work was the effect of moving ground simulation in an automotive wind tunnel due to the relative movement between a car and the street in open road conditions. An essential requirement for the current wind tunnel concept was to be applicable to the development of both production and race cars. Due to the rather low ground clearance, modern race cars were expected to be the essential application of wind tunnel testing in terms of the design of a potential moving ground system. In the following, the methodology and the results of the approach to define design criteria for a moving ground system for the aerodynamic development of race cars are presented. They were based on the work of Collin et al. (2017).

4.3.1 Methodology

A basic assumption to evaluate the interference between moving ground and vehicle aerodynamics was to trade the effects to be independent from general blockage phenomena in both open and closed jet facilities. Thus, the open road domain was selected in order to run simulations on moving belt configurations. Obviously, this was a rather idealized approach as methods of boundary layer treatment in a real facility were entirely not considered. A detailed discussion of the present approach is presented by Collin et al. (2017).

Based on the CFD methods for the open road domain, presented in section 3.1.2, some small adjustments were applied to the numerical setup in order to meet the requirements of the race car configuration. Due to the desired Reynolds number of $Re \approx 12.4$ million the final time step was reduced to $5 \cdot 10^{-5}$ s in order to limit the local CFL-number. Furthermore, the total, physical simulation time was reduced to 10 s whereas both flow field and integral forces were averaged during the last 7 s. This brought an averaging accuracy of $\Delta C_\mathrm{D} \approx \pm 0.002$ and $\Delta C_\mathrm{L,f} \approx \Delta C_\mathrm{L,r} \approx \pm 0.005$. Both drag and lift coefficients were validated using experimental data of the corresponding DTM race car and were in a range of 5 % accuracy, see Collin et al. (2017).

The first approach was to compare the results for a typical 5-belt system and a single-belt system, see Figure 4.30. The length of both the center belt (5-belt) and the single-belt were selected with $L_\mathrm{B,f}/L_\mathrm{M} = L_\mathrm{B,r}/L_\mathrm{M} = 0.9$. The width of the single-belt was $W_\mathrm{B}/W_\mathrm{M} = 1.6$. The wheel drive units (WDU) for the 5-belt had $W_\mathrm{WDU}/W_\mathrm{M} = 0.2$ and $L_\mathrm{WDU}/L_\mathrm{M} = 0.06$,

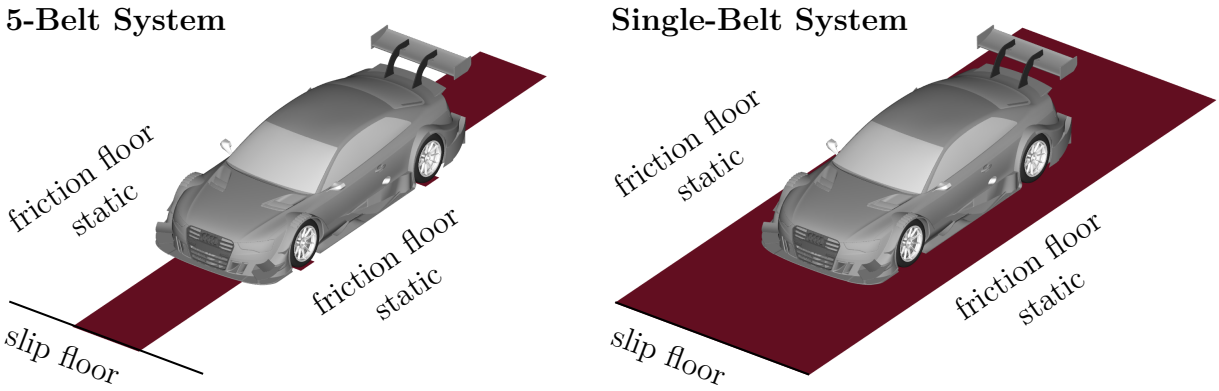

Figure 4.30: Schematic illustration of the floor boundaries of the domain for the 5-belt (left) and the single-belt (right) simulation as presented by Collin et al. (2017).

see Collin et al. (2017). For all simulations the same numerical grid was used and the moving ground regions were set by changing the floor boundary to either friction static floor or translating wall, see Figure 4.30. The beginning of the moving ground was treated to be idealized as the further upstream condition was always selected to be slip floor. The results, for the 5-belt system are presented in Figure 4.31, referring to the single-belt results. As expected, the moving ground simulation using a 5-belt brought a significant loss of aerodynamic, negative lift, especially on the front axis ($\Delta C_{\mathrm{L,f}} = 0.529$) compared to the single-belt simulation. Although, not negligible, the effects on both drag and rear lift were a lot smaller. Summarizing, the requirement of a single-belt for the selected race car was confirmed. Thus, the objective was to determine the characteristic belt dimensions of the single-belt for the selected race car, see Figure 4.32.

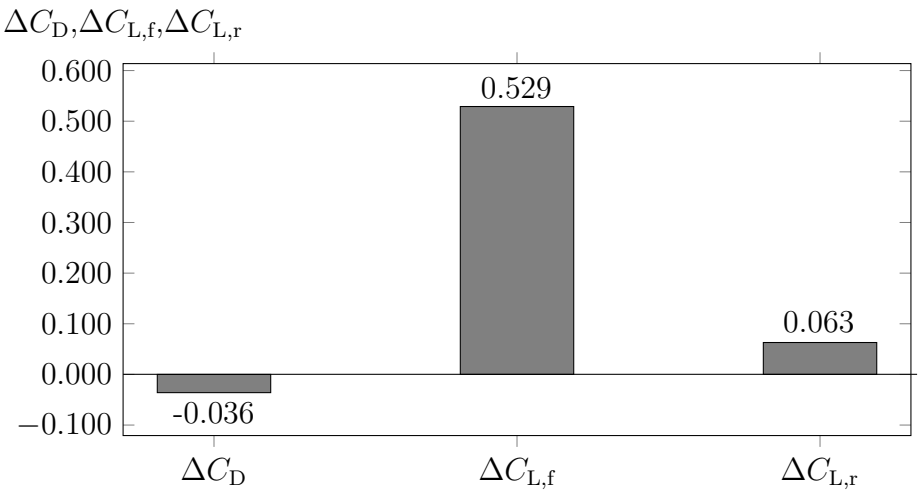

Figure 4.31: Aerodynamic force coefficients ΔC_{D}, $\Delta C_{\mathrm{L,f}}$ and $\Delta C_{\mathrm{L,r}}$ for a selected 5-belt moving ground system. The deltas ΔC_{i} refer to the results for a single-belt system.

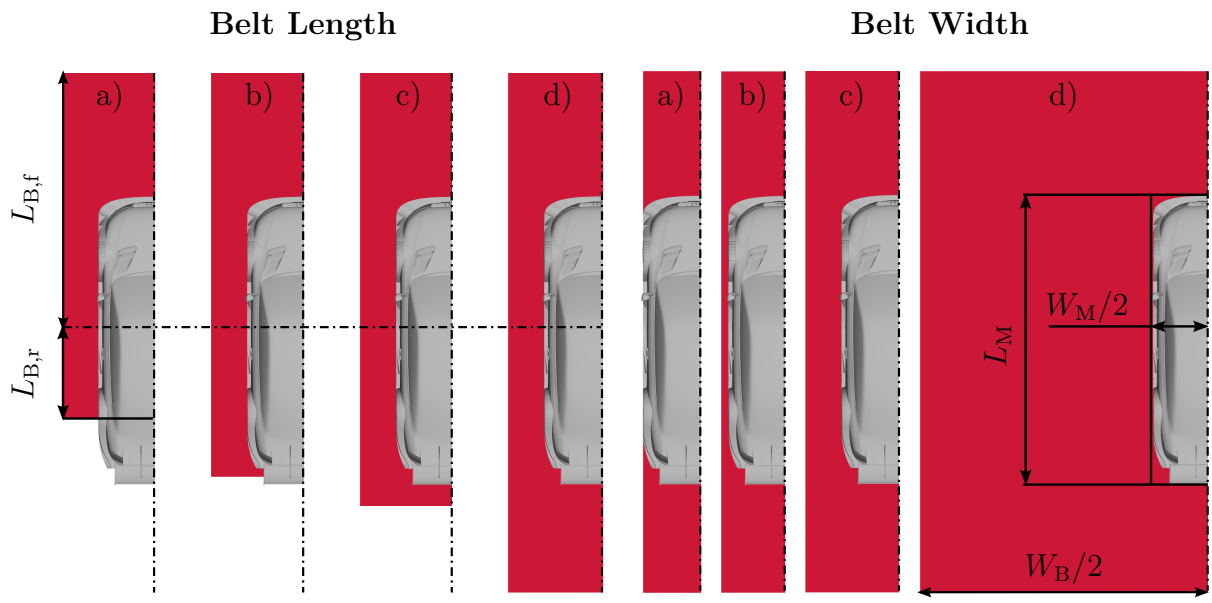

Figure 4.32: Schematic illustration of the methodology for the variation of the moving belt rear length (left) and the width (right) as presented by Collin et al. (2017). Moving belt rear length using $W_B/W_M = 1.6$ and $L_{B,f}/L_M = 0.9$: a) $L_{B,r}/L_M = 0.3$, b) $L_{B,r}/L_M = 0.5$, c) $L_{B,r}/L_M = 0.6$, d) $L_{B,r}/L_M = 0.9$. Moving belt width using $L_{B,f}/L_M = L_{B,r}/L_M = 0.9$: a) $W_B/W_M = 0.975$, b) $W_B/W_M = 1.100$, c) $W_B/W_M = 1.250$, d) $W_B/W_M = 5.000$.

The present study included the parameters of the rear length $L_{B,r}/L_M$ of the moving belt as well as the belt width W_B/W_M. The front belt length was set to be constant with $L_{B,f}/L_M = 0.9$. This approach was based on the assumption of an idealized flow at the upstream end of the moving belt as the biggest effects were expected due to the boundary layer treatment rather than from the moving ground itself. The study concerning the rear belt length was performed using a constant belt width $W_B/W_M = 1.6$ and, correspondingly, the belt length was constant $L_{B,r}/L_M = 0.9$ for the study of the belt width. Figure 4.32 depicts selected configurations of dimensions under investigation:

- $0.30 \leq L_{B,r}/L_M \leq 2.00$
- $0.98 \leq W_B/W_M \leq 5.00$

The lower limits were applied by the dimensions of the model, particularly by the wheels. A similar CFD approach, comparing different systems for moving ground simulation, is presented by Hennig et al. (2011) for the latter wind tunnel upgrade at FKFS explained by Hennig et al. (2012). Hennig et al. (2011) show results for both passenger cars and race cars using different moving belt alignments. In principle, higher effects are investigated for race cars and especially the lift coefficients were affected. Hennig et al. (2011) recognized different effects on the lift balance $\Delta C_{L,f}$ and $\Delta C_{L,r}$ depending on the particular race car. For the generic F3 race car the interferences for $\Delta C_{L,r}$ were larger than for $\Delta C_{L,f}$ whereas the results for the generic LMP race car show the opposite trend. That is why, no general rule can be derived for the interferences in lift as the results are strictly connected to the particular vehicle geometry.

4.3.2 Results for the Single-Belt Dimensions

The results for the interference of both the belt length and width are shown below in Figure 4.33 and Figure 4.34 respectively. The value for ΔC_{D}, $\Delta C_{\mathrm{L,f}}$ and $\Delta C_{\mathrm{L,r}}$ refer to the maximum belt dimension selected.In general, the effects were significantly smaller for the belt length. The maximum interferences were investigated for the rear lift coefficient $\Delta C_{\mathrm{L,r,max}} = 0.013$. However, even the maximum interference was relatively small compared to the total amount of down-force for the selected race car. For a belt length of $L_{\mathrm{B,r}}/L_{\mathrm{M}} \geq 0.9$ the deltas were in the range of the averaging accuracy of the simulation and, hence, estimated to be negligible.

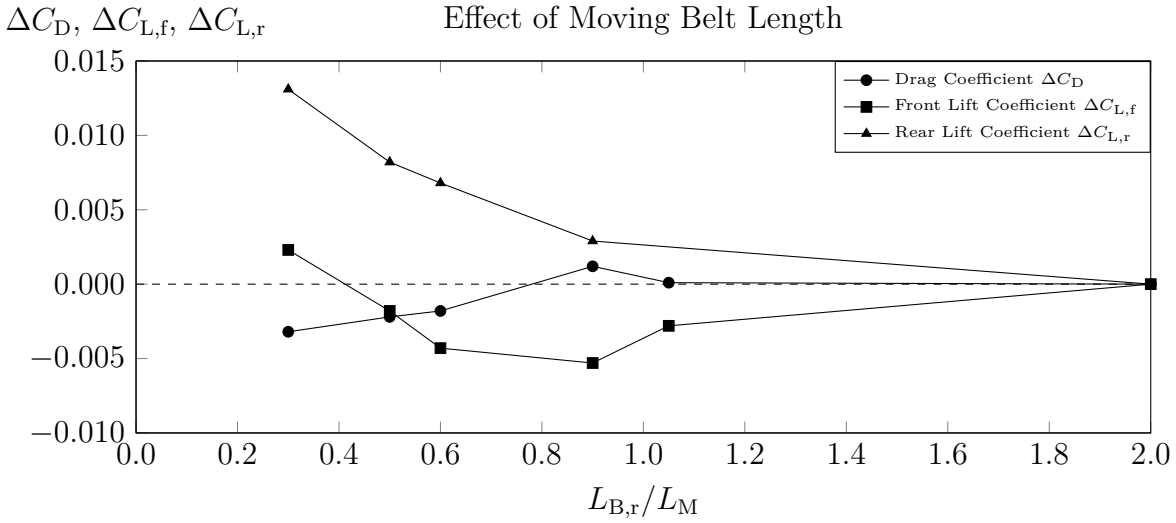

Figure 4.33: Effect of the rear length of the moving belt on aerodynamic force coefficients ΔC_{D}, $\Delta C_{\mathrm{L,f}}$ and $\Delta C_{\mathrm{L,r}}$.

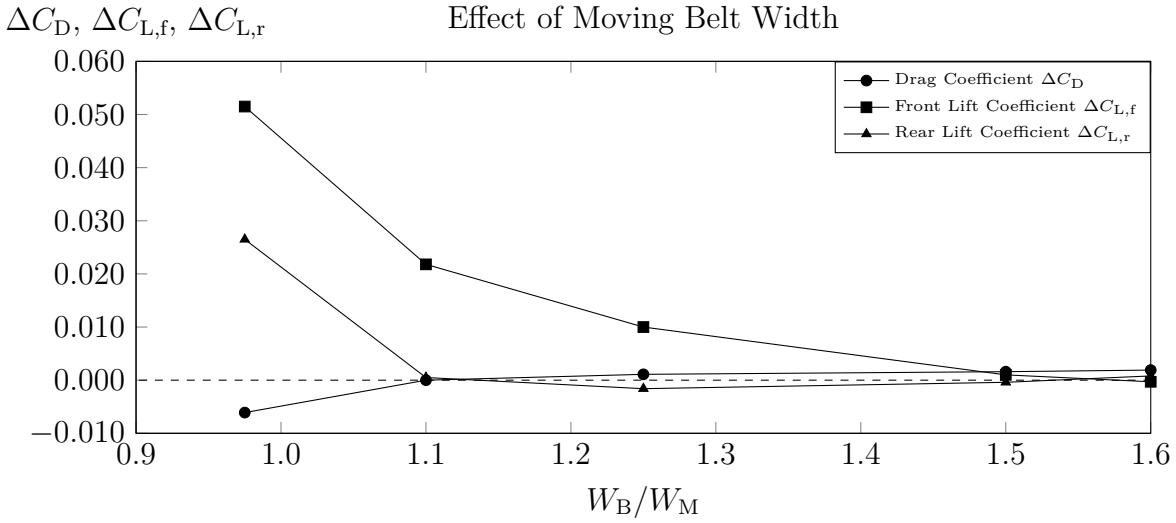

Figure 4.34: Effect of the width of the moving belt on aerodynamic force coefficients ΔC_{D}, $\Delta C_{\mathrm{L,f}}$ and $\Delta C_{\mathrm{L,r}}$.

Based on these results, for a typical race car of a model length of $L_\mathrm{M} \approx 5\,\mathrm{m}$ a rear belt length of $L_\mathrm{B,r} \approx 4.5\,\mathrm{m}$ was expected to be sufficient. Assuming the model to be located at the longitudinal center of the moving belt, a total belt length of $L_\mathrm{B} \approx 9.0\,\mathrm{m}$ was required. Comparing the results for the belt width, the largest effects were determined for the front lift coefficient $\Delta C_\mathrm{L,r,max} = 0.051$, approximately twice as big as for the rear lift coefficient $\Delta C_\mathrm{L,r,max} = 0.026$. This was obviously only representative for the selected race car and configuration. However, the interferences decayed with increasing belt width and were in the range of accuracy for $W_\mathrm{B}/W_\mathrm{M} \geq 1.5$. Assuming a car with a typical width of $W_\mathrm{M} \approx 2.0\,\mathrm{m}$, the required belt length derived from the results was $W_\mathrm{B} \approx 3.0\,\mathrm{m}$. Summarizing, the CFD simulation concerning the single-belt moving ground simulation yielded in a requirement of belt dimensions of approximately $L_\mathrm{B} \approx 9.0\,\mathrm{m}$ and $W_\mathrm{B} \approx 3.0\,\mathrm{m}$.

5 Consequences for the Design of Open Jet Wind Tunnels

The results of the CFD wind tunnel studies, presented in chapter 4, provided a more detailed knowledge about the interferences between model and nozzle, open jet, collector and moving ground simulation. Apart from local flow phenomena, the effects on the aerodynamic forces measured at the model are certainly the aspects of highest priority for a practical facility. Summarizing the results from chapter 4, a practical design of an automotive, open jet wind tunnel by entirely eliminating all discussed interferences did not appear to be reasonable. The interference due to the open jet expansion turned out to be the limiting factor as it was determined to be negligible (e.g. $\Delta C_\mathrm{D} \pm 0.001$) for a blockage ratio of $A_\mathrm{M}/A_\mathrm{N} \approx 2 - 3\,\%$. For a range of typical production cars with $2\,\mathrm{m}^2 \leq A_\mathrm{M} \leq 3\,\mathrm{m}^2$ a wind tunnel nozzle with $A_\mathrm{N} \approx 100\,\mathrm{m}^2$ will be required in order to be free of corrections. A rather realizable size is surely in the range of $20\,\mathrm{m}^2 \leq A_\mathrm{N} \leq 30\,\mathrm{m}^2$. Therefore, a new approach to apply a jet expansion correction is presented in section 5.1 and compared to both the classical correction from Lock (1929) and the CFD results. Final design criteria for an open jet wind tunnel are discussed in section 5.2.

5.1 Correction Methods for the Open Jet Expansion

The CFD simulations of the flow around the DrivAer model in several open jet test sections allowed to draw conclusions regarding the effect of jet expansion with respect to the blockage conditions. The discrepancies between the CFD results and the classical blockage correction were obvious. In this chapter, a new approach to account for the effects of jet expansion is proposed and explained below. A comparison of the results for the new method with both the classical approach and the CFD results is presented in section 5.1.3.

The details of the classical solid blockage correction, first introduced by Lock (1929), were described in section 2.1.2. Figure 5.1 illustrates the principle of this approach. The

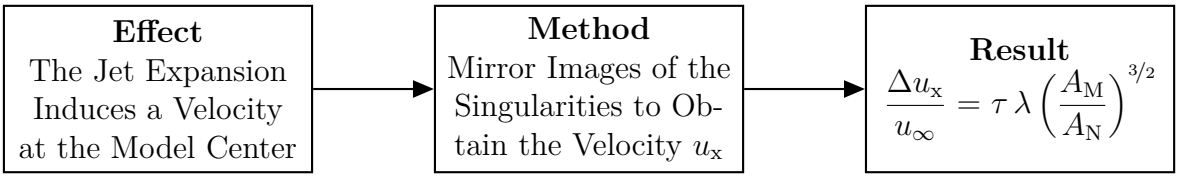

Figure 5.1: Principle approach of the classical correction for the open jet expansion.

strategy of applying mirror images at the wind tunnel boundaries satisfies the theoretical boundary condition for an open jet as stated in eq. (2.2) on page 8:

$$p = p_\infty, \quad u = u_\infty$$

The effectively decreased velocity of the flow around a model in the open jet test section is corrected by the application of a velocity correction. The classical correction method calculates the velocity interference from the mirror images with respect to the center of the model $(x, y, z) = (0, 0, 0)$. Based on the flow around a sphere ($\lambda = 1$) the mirror images return the tunnel shape factor τ for different tunnel geometries. The effective increase in jet diameter in proximity of the model is neglected and hence the tunnel cross section (nozzle height H_N and width W_N) is equivalent to the one from the mirror images.

Based on these approximations the classical solid blockage correction, stated in Figure. 5.1 was derived. However, the discrepancies in CFD and the classical approach for rather high blockage ratios are expected to be connected to an insufficient coverage of the jet expansion effects by the classical theory. However, an alternative approach was developed in this thesis. An overview of the considered effects is given by Figure 5.2. The main difference between closed and open jet test sections is the jet boundary condition. For closed jets the location of the jet boundary is fixed due to the solid walls. For an open jet the velocity at the jet boundary in potential flow theory is known and equates u_∞ of the undisturbed flow. However, the displacement of the jet boundary by the model causes the wind tunnel interference. It is not known, but can be calculated from the mirror images using the stream function Ψ, see method 1 in Figure 5.2. This correction accounts for the change in effective jet cross section $A_\mathrm{N,e}$ for an expanding jet and is discussed in detail in section 5.1.1. This effect is not included in the classical solid blockage correction. For the correction of the velocity interference Δu two methods were applied. Method 2.1 is identical to the classical solid blockage correction. The induced velocity is calculated from

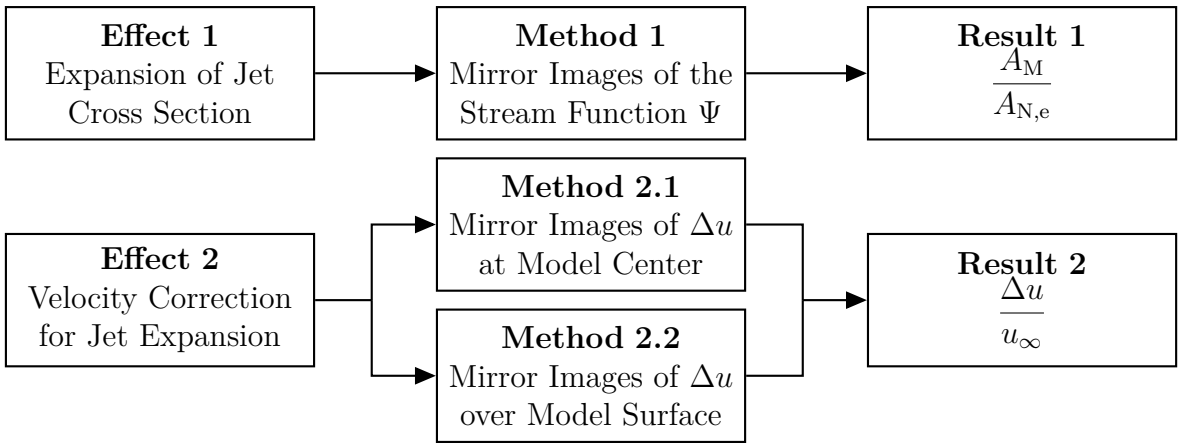

Figure 5.2: Overview of the effects and the methods to develop a new correction for the open jet expansion. The methods for effect 1 and 2 were based on a potential flow model for the wind tunnel flow around a sphere and returned either a velocity correction or an adaption of the blockage ratio.

the sum of mirror images at the model center. Method 2.2 takes into account that the induced velocity at a particular location is not constant. For example, the maximum jet expansion for a sphere is located in the plane at the model center $x = 0$ and is smaller for any other x-normal plane $x > 0$ and $x < 0$. Thus, the induced velocity is a gradient field. Both method 2.1 and 2.2 are discussed in section 5.1.2. The effects and methods, presented in this chapter, were applied to the flow around a sphere in both two and three dimensions. The general idea to use a model shape factor λ is adopted to compare the results with the results from CFD.

5.1.1 Expansion of Jet Cross Section

In the approach of Lock (1929) the effective displacement of the jet boundary is not considered. In fact, the jet expansion leads to an increase of the jet cross section in the proximity of the model. Thus, the location of wind tunnel interference is effectively displaced away from the model. Method 1 takes into account the increase of the jet cross section by computing mirror images of the stream function Ψ. The equations were derived for both two- and three dimensional blockage conditions. The essential equations were

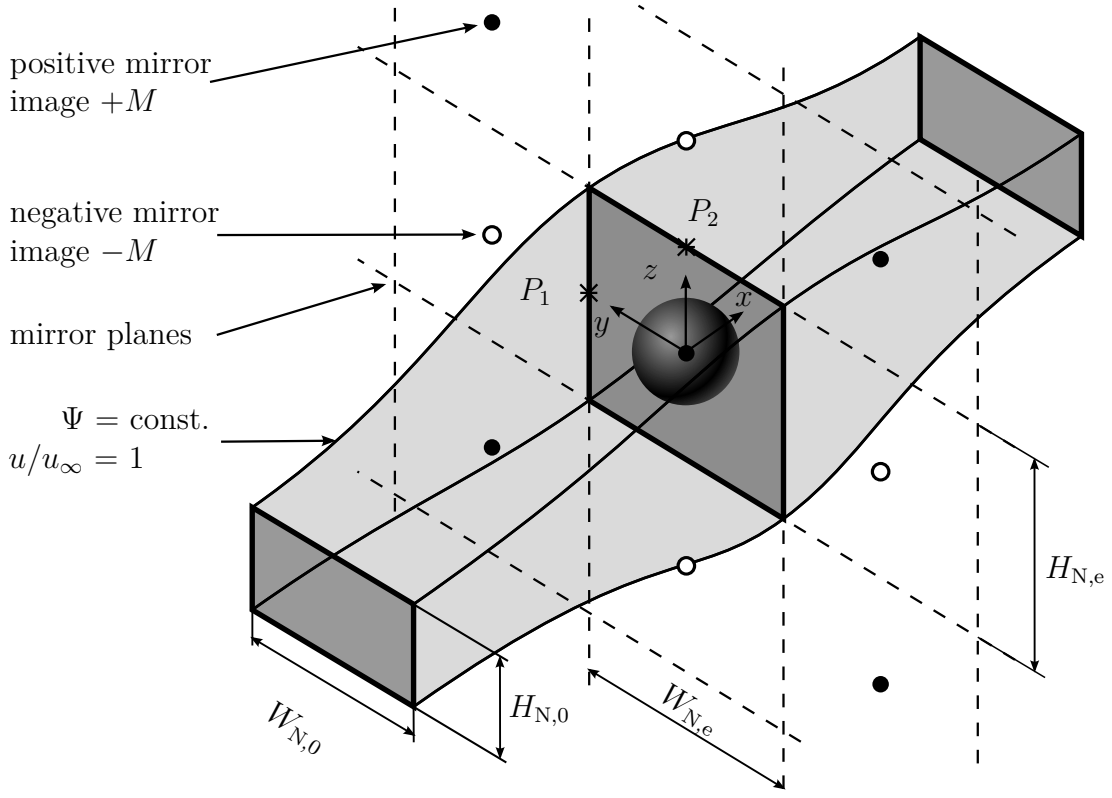

Figure 5.3: Jet expansion for a sphere in a rectangular wind tunnel. The mirror images alternate in sign $\pm M$ enforcing a constant velocity $u/u_\infty = 1$ at the jet boundary ($\Psi = \text{const.}$). The cross section $x = 0$ of the mirror images denotes the dimensions ($W_{\mathrm{N,e}}$ and $H_{\mathrm{N,e}}$) of the expanded jet. The dimensions of the initial jet are $W_{\mathrm{N,0}}$ and $H_{\mathrm{N,0}}$.

taken from Table A.3 and A.4 in appendix A.5. Figure 5.3 shows the general effect of the jet expansion and the placement of mirror images for a sphere in a rectangular, open jet. The mirror images are extracted in the x-normal plane of the model center ($x = 0$). The approach of alternating sign for the singularities enforces the jet boundary condition $u/u_\infty = 1$. The jet boundary is represented by streamlines and hence the stream function Ψ for each streamline is constant. The method below used the mirror images to calculated the effective stream function of the expanded jet at $x = 0$. Based on this knowledge the corresponding jet dimensions $W_{\mathrm{N},0}$ and $H_{\mathrm{N},0}$ for the undisturbed flow ($x \to \infty$) were calculated. Figure 5.4 illustrates the method of extracting mirror images in both two and three dimensions. The indices for the columns m and the rows n design the level of the corresponding image. In two dimensions only one index, here n, was sufficient. For the rectangular tunnel both indices were applied. It is important to mention that the mirror images for the rectangular jet satisfy the jet boundary condition $u = u_\infty$ at $y = \pm W_{\mathrm{N,e}}/2$ and $z = \pm H_{\mathrm{N,e}}/2$ respectively. Thus, the shape of the expanded jet cross section at $x = 0$ is rectangular as also shown in Figure 5.3. This is an approximation as the displacement in y- and z-direction is assumed to be constant.

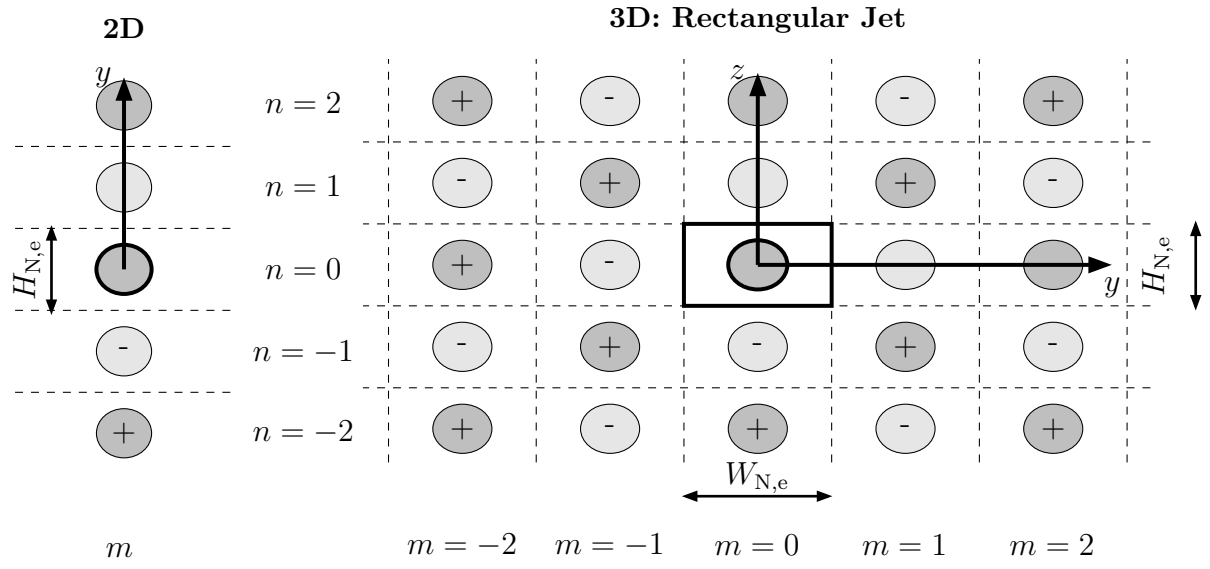

Figure 5.4: Mirror images at $x = 0$ for two and three dimensions. The indices m and n denote the level of the corresponding image. Two levels are illustrated but for the calculation the condition $m, n \to \infty$ is considered.

Two Dimensions

The two-dimensional example of a dipole in parallel flow represents the flow around an infinitely long cylinder. The flow field is characterized by a stream-wise coordinate x and a lateral coordinate y. The field variables Ψ_c and $u_\mathrm{x,c}$ represent the flow field without wind tunnel interference:

$$\Psi_\mathrm{c}(x,y) = u_\infty y - \frac{M}{2\pi}\frac{y}{x^2+y^2} \tag{5.1}$$

$$u_\mathrm{x,c}(x,y) = u_\infty - \frac{M}{2\pi}\frac{x^2-y^2}{\left(x^2+y^2\right)^2} \tag{5.2}$$

The dipole moment was calculated from the stagnation point $u_\mathrm{x,c} = 0$ by using the radius of the cylinder R_M:

$$u_\mathrm{x,c}(x=-R_\mathrm{M}, y=0) = 0 \quad \longrightarrow \quad M = 2\,\pi\,u_\infty\,{R_\mathrm{M}}^2 \tag{5.3}$$

For the model center $x = 0$ eq. (5.1) and (5.2) can be simplified towards:

$$\frac{\Psi_\mathrm{c}(x,y)}{u_\infty} = y - {R_\mathrm{M}}^2\frac{y}{x^2+y^2} \quad \longrightarrow \quad \frac{\Psi_\mathrm{c}(x=0,y)}{u_\infty} = y - \frac{{R_\mathrm{M}}^2}{y} \tag{5.4}$$

$$\frac{u_\mathrm{x,c}(x,y)}{u_\infty} = 1 - {R_\mathrm{M}}^2\frac{x^2-y^2}{\left(x^2+y^2\right)^2} \quad \longrightarrow \quad \frac{u_\mathrm{x,c}(x=0,y)}{u_\infty} = 1 + \frac{{R_\mathrm{M}}^2}{y^2} \tag{5.5}$$

For wind tunnel conditions, the second term in both equations of Ψ_c and $u_\mathrm{x,c}$ is added by the mirror images of the dipole. The vertical distance of each dipole was calculated using the mirror index n and the tunnel height $H_\mathrm{N,e}$:

$$y_\mathrm{n} = \frac{H_\mathrm{N,e}}{2} - H_\mathrm{N,e}\,n = \frac{H_\mathrm{N,e}}{2}\,(1-2\,n) \tag{5.6}$$

The substitution of y in eq. (5.4) and (5.5) with eq. (5.6) and the expansion of the mirror images returned the field variables in wind tunnel conditions:

$$\frac{\Psi(x=0, y=H_\mathrm{N,e}/2)}{u_\infty} = \frac{H_\mathrm{N,e}}{2} - 2\,\frac{{R_\mathrm{M}}^2}{H_\mathrm{N,e}}\sum_{n=-\infty}^{\infty}\frac{(-1)^n}{1-2n} \tag{5.7}$$

$$\frac{u_\mathrm{x}(x=0, y=H_\mathrm{N,e}/2)}{u_\infty} = 1 + 4\left(\frac{R_\mathrm{M}}{H_\mathrm{N,e}}\right)^2\sum_{n=-\infty}^{\infty}\frac{(-1)^n}{(1-2n)^2} \tag{5.8}$$

The solution of the infinite summations for Ψ and u_x returned:

$$\sum_{n=-\infty}^{\infty}\frac{(-1)^n}{1-2n} = \frac{\pi}{2} \qquad \sum_{n=-\infty}^{\infty}\frac{(-1)^n}{(1-2n)^2} = 0 \tag{5.9}$$

As shown by Lock (1929) the result of the mirror images for the u_x is 0. Thus the velocity at the wind tunnel boundary equates to the velocity of the undisturbed flow u_∞. For Ψ the summation results in $\pi/2$. Eq. (5.7) and (5.8) turn into:

$$\frac{\Psi(x=0, y=H_{N,e}/2)}{u_\infty} = \frac{H_{N,e}}{2} - \pi \frac{{R_M}^2}{H_{N,e}} \tag{5.10}$$

$$\frac{u_x(x=0, y=H_{N,e}/2)}{u_\infty} = 1 \tag{5.11}$$

The reduction of the stream function at the jet boundary by the summation of the set of dipoles gives the increase of the jet diameter in the center line of the model. Furthermore, the streamline with the stream function in eq. (5.10) represents the jet boundary. With increasing longitudinal distance $x \to \infty$ the effect of the dipole decays. The effective tunnel height $H_{N,0}$ was calculated from the stream function of the parallel flow:

$$\frac{\Psi(x \to \infty, y=H_{N,0}/2)}{u_\infty} = \frac{H_{N,0}}{2} \tag{5.12}$$

For the streamline at the jet boundary the condition (5.12) = (5.10) is valid. The effective blockage ratio can be obtained by rearranging the variables:

$$\frac{H_{N,0}}{H_{N,e}} = 1 - 2\pi \left(\frac{R_M}{H_{N,e}}\right)^2 = 1 - \frac{\pi}{2}\left(\frac{H_M}{H_{N,e}}\right)^2 \tag{5.13}$$

$$\frac{A_M}{A_{N,0}} = \frac{H_M}{H_{N,0}} = \frac{1}{\frac{A_{N,e}}{A_M}\left[1 - \frac{\pi}{2}\left(\frac{A_M}{A_{N,e}}\right)^2\right]} \tag{5.14}$$

Eq. (5.13) and (5.14) are analytic solutions of the increase of jet cross section at $x = 0$ for a cylinder in a two-dimensional tunnel. Figure 5.5 depicts the dependency of the radius and the blockage ratio within the maximum jet cross section. Furthermore, a comparison to the assumption without jet expansion is given. For low blockage ratios $A_M/A_{N,0} < 0.15$ the difference appears to be negligible, at least on the selected scale. In fact, the error of $A_{N,e}/A_{N,0} < 1.01$ was determined to be valid for $A_M/A_{N,0} < 0.08$. Thus, the increase of jet cross section cannot be generally neglected.

Three Dimensions: Rectangular Open Jet

The flow field in around a sphere in a rectangular tunnel changes with the ratio of tunnel height H_N to tunnel width W_N and is in general not rotational symmetric. Thus, the y-normal and z-normal wind tunnel boundaries are evaluated separately in order to achieve the nominal jet expansion for each direction. Therefore, the stream functions Ψ_y and Ψ_z are calculated as vector components of Ψ_r:

$$\Psi_y = \frac{y}{r}\Psi_r \quad \text{and} \quad \Psi_z = \frac{z}{r}\Psi_r \quad \text{with} \quad r = \sqrt{y^2 + z^2} \tag{5.15}$$

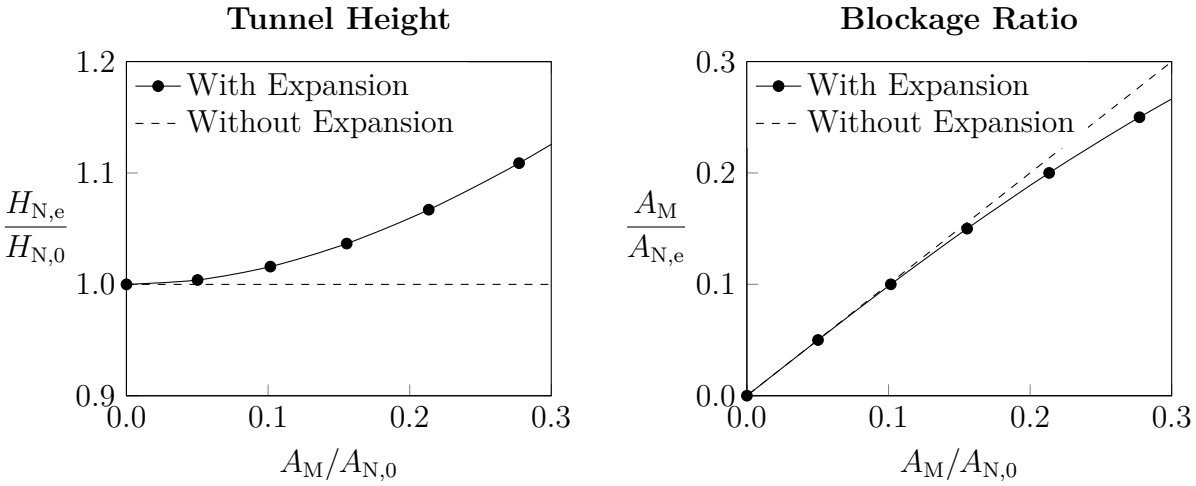

Figure 5.5: Two Dimensions: Effect of blockage ratio $A_M/A_{N,0}$ on the height $H_{N,e}/H_{N,0}$ of the expanded, open jet (left) and on the corresponding, effective blockage ratio $A_M/A_{N,e}$ (right). The results were extracted from eq. (5.13) and (5.14).

Using the same approach as shown above for the two-dimensional tunnel, eq. (5.4) was adapted:

$$\frac{\Psi_{y,c}(x=0,y,z)}{u_\infty} = \frac{1}{2} y \sqrt{y^2+z^2} - \frac{{R_M}^3}{2} \frac{y}{y^2+z^2} \tag{5.16}$$

$$\frac{\Psi_{z,c}(x=0,y,z)}{u_\infty} = \frac{1}{2} z \sqrt{y^2+z^2} - \frac{{R_M}^3}{2} \frac{z}{y^2+z^2} \tag{5.17}$$

The effective stream function at the jet boundary was again calculated from the mirror images of the dipole terms:

$$\frac{\Psi_y(x=0,y=W_{N,e}/2,z=0)}{u_\infty} = \frac{1}{8}{W_{N,e}}^2 - \frac{{R_M}^3}{2} \sum_{m=-\infty}^{\infty} \sum_{n=-\infty}^{\infty} (-1)^{m+n} \frac{y_m}{{y_m}^2+{z_n}^2} \tag{5.18}$$

$$\frac{\Psi_z(x=0,y=0,z=H_{N,e}/2)}{u_\infty} = \frac{1}{8}{H_{N,e}}^2 - \frac{{R_M}^3}{2} \sum_{m=-\infty}^{\infty} \sum_{n=-\infty}^{\infty} (-1)^{m+n} \frac{z_n}{{y_m}^2+{z_n}^2} \tag{5.19}$$

The coordinates y_m and z_n denote the distance between a specific point (x,y,z) and a dipole mirror image with the index m and n:

$$y_m = y - m\,W_{N,e} \quad \text{and} \quad z_n = z - n\,H_{N,e} \tag{5.20}$$

Eq. (5.18) and (5.19) can be re-written as:

$$\sum_{m=-\infty}^{\infty}\sum_{n=-\infty}^{\infty}(-1)^{m+n}\frac{y_\mathrm{m}}{{y_\mathrm{m}}^2+{z_\mathrm{n}}^2}=\sum_{m=-\infty}^{\infty}\sum_{n=-\infty}^{\infty}(-1)^{n}\frac{W_\mathrm{N,e}\left(\frac{1}{2}-m\right)}{{W_\mathrm{N,e}}^2\left(\frac{1}{2}-m\right)^2+\left(nH_\mathrm{N,e}\right)^2} \tag{5.21}$$

$$\sum_{m=-\infty}^{\infty}\sum_{n=-\infty}^{\infty}(-1)^{m+n}\frac{z_\mathrm{n}}{{y_\mathrm{m}}^2+{z_\mathrm{n}}^2}=\sum_{m=-\infty}^{\infty}\sum_{n=-\infty}^{\infty}(-1)^{n}\frac{H_\mathrm{N,e}\left(\frac{1}{2}-n\right)}{\left(mW_\mathrm{N,e}\right)^2+{H_\mathrm{N,e}}^2\left(\frac{1}{2}-n\right)^2} \tag{5.22}$$

Compared to eq. (5.9) the double-infinite series of sums are related to the ratio of tunnel width $W_\mathrm{N,e}$ and tunnel height $H_\mathrm{N,e}$. Thus, no general, analytic solution was found here, but a numerical solution was applied. A substitution of χ_y and χ_z for the sums was applied:

$$\chi_\mathrm{y}=\sum_{m=-\infty}^{\infty}\sum_{n=-\infty}^{\infty}(-1)^{m+n}\frac{\frac{1}{2}-m}{\left(\frac{1}{2}-m\right)^2+\left(n\frac{H_\mathrm{N,e}}{W_\mathrm{N,e}}\right)^2} \tag{5.23}$$

$$\chi_\mathrm{z}=\sum_{m=-\infty}^{\infty}\sum_{n=-\infty}^{\infty}(-1)^{m+n}\frac{\frac{1}{2}-n}{\left(m\frac{W_\mathrm{N,e}}{H_\mathrm{N,e}}\right)^2+\left(\frac{1}{2}-n\right)^2} \tag{5.24}$$

An analytic solution for the double infinite summations χ_y and χ_z was not found in this work. However, both factors can be calculated using a numerical approach. Therefore, a MATLAB script was created to calculate solutions for χ_y and χ_z in a selected range of tunnel aspect ratio $W_\mathrm{N,e}/H_\mathrm{N,e}$. As also mentioned by Wickern (2001), the summation of alternating sign converges quickly and $n = 10$ levels of mirror images turned out to be sufficient for realistic aspect ratios, see Figure 5.6 left. Furthermore, the values of χ_y and χ_z were plotted in Figure 5.6 right. The infinite limits are:

$$\lim_{W/H\to 0}\chi_\mathrm{y}=\pi,\qquad \lim_{W/H\to\infty}\chi_\mathrm{y}=0,\qquad \lim_{W/H\to 0}\chi_\mathrm{z}=0,\qquad \lim_{W/H\to\infty}\chi_\mathrm{z}=\pi \tag{5.25}$$

In the next step, eq. (5.18) and (5.19) were adapted in order to fit the streamline condition for the original tunnel dimensions $W_\mathrm{N,0}$ and $H_\mathrm{N,0}$:

$$\frac{\Psi_\mathrm{y}(x=0,y=W_\mathrm{N,e}/2,z=0)}{u_\infty}=\frac{1}{8}{W_\mathrm{N,e}}^2-\frac{{R_\mathrm{M}}^3}{2}\frac{\chi_\mathrm{y}}{W_\mathrm{N,e}}=\frac{1}{8}{W_\mathrm{N,0}}^2 \tag{5.26}$$

$$\frac{\Psi_\mathrm{z}(x=0,y=0,z=H_\mathrm{N,e}/2)}{u_\infty}=\frac{1}{8}{H_\mathrm{N,e}}^2-\frac{{R_\mathrm{M}}^3}{2}\frac{\chi_\mathrm{z}}{H_\mathrm{N,e}}=\frac{1}{8}{H_\mathrm{N,0}}^2 \tag{5.27}$$

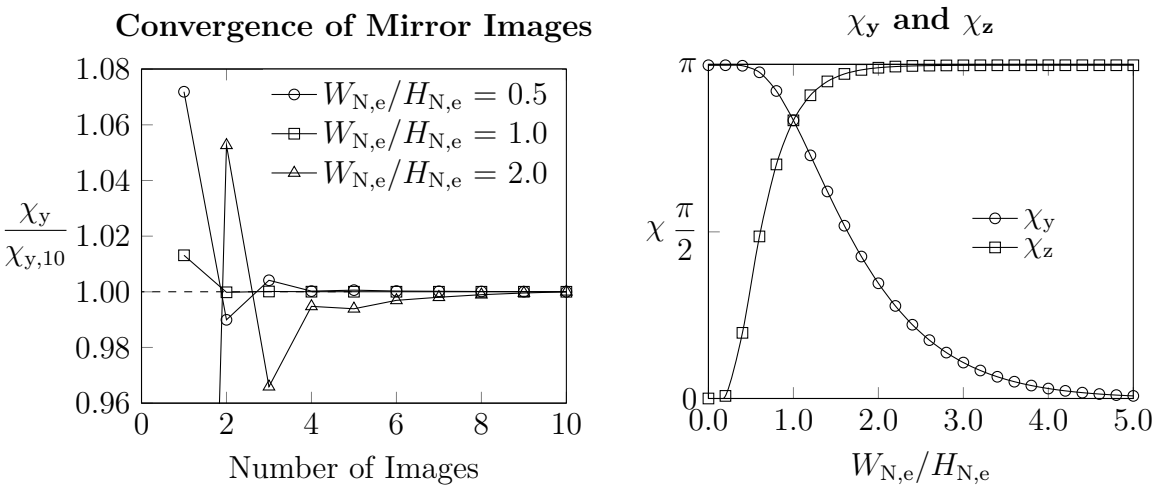

Figure 5.6: Solutions for the summation of χ_y and χ_z. The summation of χ_y converges after 10 images (left). The dependency of χ_y and χ_z is given for different tunnel aspect ratios $W_{N,e}/H_{N,e}$ (right). For $W_{N,e}/H_{N,e} \longrightarrow 0 : \chi_y = \pi$, $\chi_z = 0$; for $W_{N,e}/H_{N,e} \longrightarrow \infty : \chi_y = 0$, $\chi_z = \pi$.

Thus, the effective jet expansion can be formulated by the use of the model and tunnel length scales:

$$\frac{W_{N,0}}{W_{N,e}} = \sqrt{1 - 4\,\chi_y \left(\frac{R_M}{W_{N,e}}\right)^3} \quad \text{and} \quad \frac{H_{N,0}}{H_{N,e}} = \sqrt{1 - 4\,\chi_z \left(\frac{R_M}{H_{N,e}}\right)^3} \tag{5.28}$$

An alternative form is to express the jet expansion related to the blockage ratio:

$$\frac{A_M}{A_{N,e}} = \frac{\pi {R_M}^2}{W_{N,e} H_{N,e}} \quad \longrightarrow \quad R_M = \sqrt{\frac{W_{N,e} H_{N,e}}{\pi} \frac{A_M}{A_{N,e}}} \tag{5.29}$$

The result is:

$$\frac{W_{N,0}}{W_{N,e}} = \sqrt{1 - \chi_y \frac{4}{\pi^{3/2}} \left(\frac{H_{N,e}}{W_{N,e}} \frac{A_M}{A_{N,e}}\right)^{3/2}} \quad \text{and} \quad \frac{H_{N,0}}{H_{N,e}} = \sqrt{1 - \chi_z \frac{4}{\pi^{3/2}} \left(\frac{W_{N,e}}{H_{N,e}} \frac{A_M}{A_{N,e}}\right)^{3/2}} \tag{5.30}$$

The corrected nozzle area and blockage ratio are then:

$$A_{N,0} = W_{N,0}\, H_{N,0} \tag{5.31}$$

$$\frac{A_M}{A_{N,0}} = \frac{A_{N,e}}{A_{N,0}} \frac{A_M}{A_{N,e}} = \frac{W_{N,e}}{W_{N,0}} \frac{H_{N,e}}{H_{N,0}} \frac{A_M}{A_{N,e}} \tag{5.32}$$

The set of equations is now sufficient to solve the dimensions of the expanded jet for a sphere in a rectangular tunnel. The input parameters for a typical application are the nozzle area $A_{N,0}$, the blockage ratio $A_M/A_{N,0}$ and the aspect ratio of the tunnel $W_{N,0}/H_{N,0}$. Therefore, an iterative approach is proposed in order to calculate the dimensions of the expanded jet. The algorithm is given in Figure 5.7. The results are given in Figure 5.8.

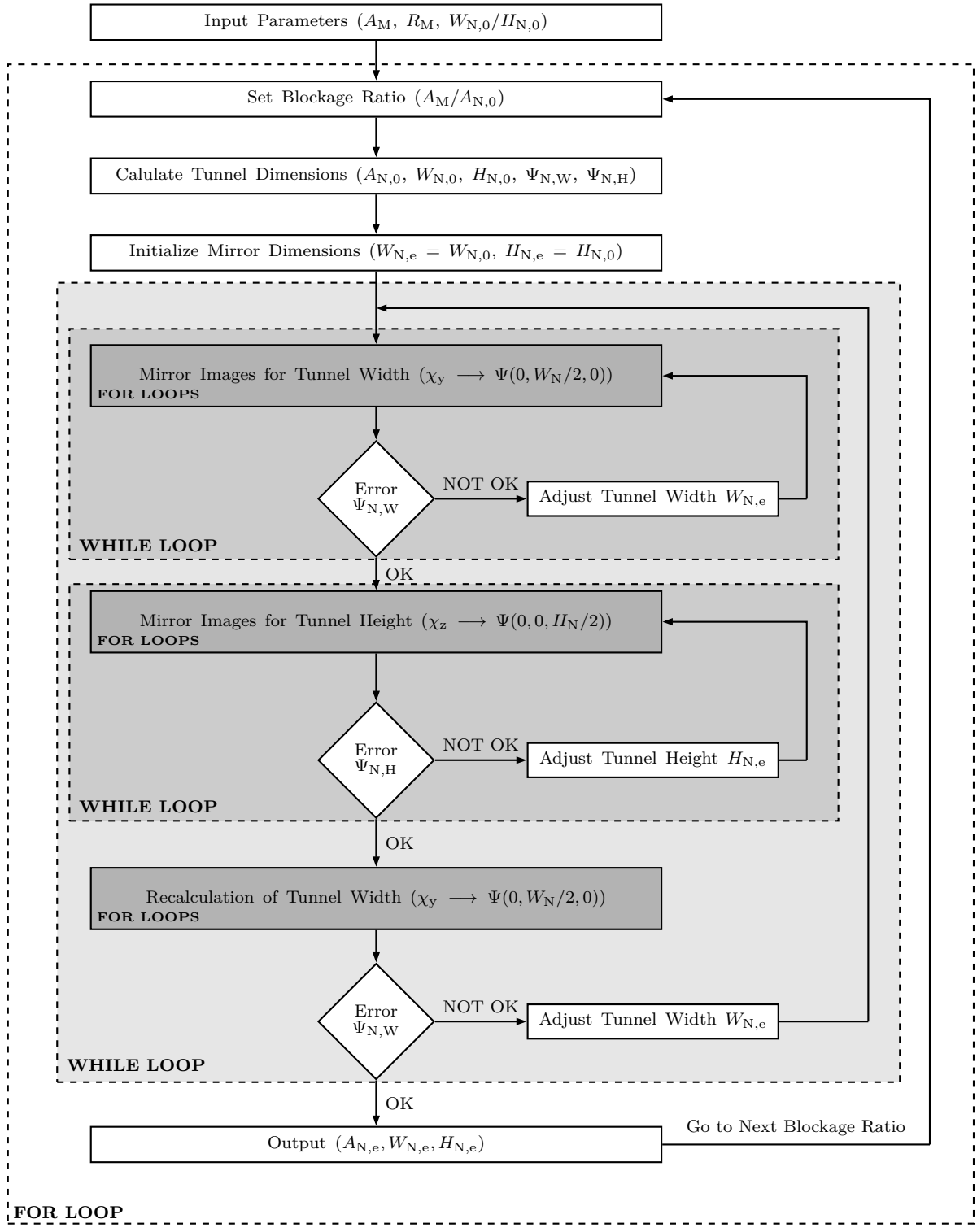

Figure 5.7: Algorithm to calculate the dimensions of the expanded, rectangular jet. An outer for loop performed iterations for different blockage ratios. Three while loops iterate the dimensions of the mirror images in order to match the stream function at the jet boundary.

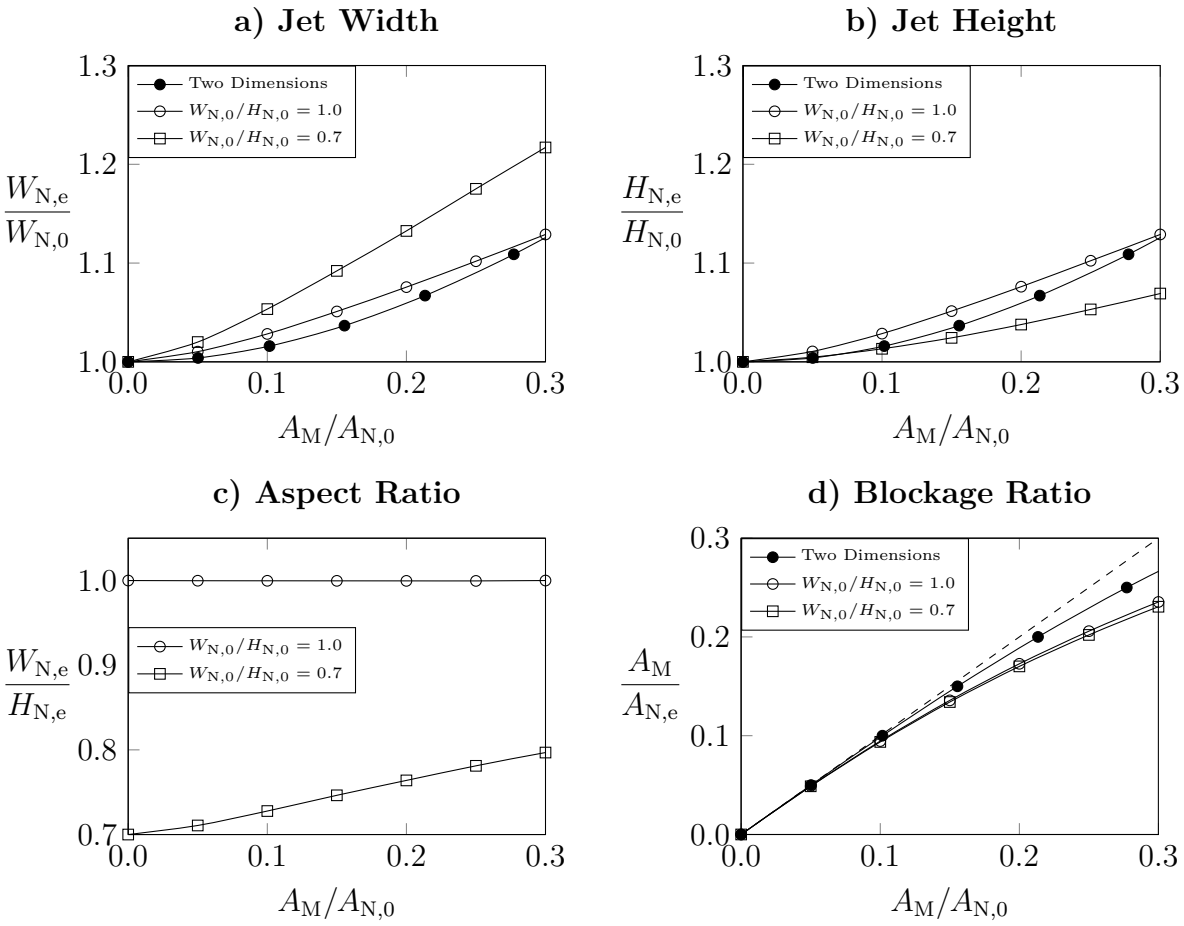

Figure 5.8: Effect of blockage ratio $A_M/A_{N,0}$ on the dimensions of the expanded jet at $x = 0$: a) Increase of jet width; b) Increase of jet height; c) Effect on the aspect ratio of the expanded jet; d) Effective blockage ratio.

5.1.2 Velocity Correction for the Jet Expansion

Method 2.1: Mirror Images at the Model Center

The calculation of the induced velocity by the mirror images at the model center is equivalent to the approach of Lock (1929). Furthermore, the calculation of the resulting velocity interference is rather simple as the lateral components Δu_y and Δu_z are zero. The summation of Δu_x for a rectangular tunnel by Garner et al. (1966) and was introduced in section 2.1.2:

$$\frac{\Delta u_x(x=0)}{u_\infty} = \frac{{R_M}^3}{2} \underbrace{\sum_{m=-\infty}^{\infty} \sum_{n=-\infty}^{\infty}}_{\text{without } m=n=0} (-1)^{m+n} \frac{1}{\left((mW_{N,e})^2 + (nH_{N,e})^2\right)^{3/2}} \tag{5.33}$$

It is worth to mention that the induced velocity for the open jet conditions is calculated from the double infinite summations only of the mirror images. Therefore, the effect of the model $m = n = 0$ is excluded.

The correction of the drag coefficient $C_{\mathrm{D,c}}/C_{\mathrm{D}}$ results from the dynamic pressure correction:

$$\frac{C_{\mathrm{D}}}{C_{\mathrm{D,c}}} = \frac{p_{\mathrm{dyn,c}}}{p_{\mathrm{dyn}}} = \left(\frac{\Delta u_{\mathrm{x}}(x=0)}{u_\infty} \lambda + 1 \right)^2 \tag{5.34}$$

Method 2.2: Mirror Images over the Model Surface

The second method is to calculate the velocity interference in the rectangular open jet test section as the integral velocity over the model area. Therefore, both velocity components $u_{\mathrm{x,c}}$ and $u_{\mathrm{r,c}}$ are used from Table A.4 in the appendix on page 165. The flow field around the sphere without wind tunnel interference is obtained from:

$$\frac{u_{\mathrm{x,c}}(x,y,z)}{u_\infty} = 1 + \frac{{R_{\mathrm{M}}}^3}{2} \frac{r^2 - 2x^2}{(x^2 + r^2)^{5/2}} \tag{5.35}$$

$$\frac{u_{\mathrm{r,c}}(x,y,z)}{u_\infty} = -\frac{3}{2} {R_{\mathrm{M}}}^3 \frac{xr}{(x^2 + r^2)^{5/2}} \tag{5.36}$$

For a specific location (x, y, z) the velocity field of the flow around the sphere in a rectangular tunnel is written for u_{x} and u_{r} in the same way as for method 2.1:

$$\frac{u_{\mathrm{x}}(x,y,z)}{u_\infty} = 1 + \frac{{R_{\mathrm{M}}}^3}{2} \sum_{m=-\infty}^{\infty} \sum_{n=-\infty}^{\infty} (-1)^{m+n} \frac{{r_{\mathrm{m,n}}}^2 - 2{x_{\mathrm{m,n}}}^2}{({x_{\mathrm{m,n}}}^2 + {r_{\mathrm{m,n}}}^2)^{5/2}} \tag{5.37}$$

$$\frac{u_{\mathrm{r}}(x,y,z)}{u_\infty} = -\frac{3}{2} {R_{\mathrm{M}}}^3 \sum_{m=-\infty}^{\infty} \sum_{n=-\infty}^{\infty} (-1)^{m+n} \frac{x_{\mathrm{m,n}} r_{\mathrm{m,n}}}{({x_{\mathrm{m,n}}}^2 + {r_{\mathrm{m,n}}}^2)^{5/2}} \tag{5.38}$$

The coordinates $x_{\mathrm{m,n}}$ and $r_{\mathrm{m,n}}$ in eq. (5.37) and (5.38) can be written as:

$$x_{\mathrm{m,n}} = x \tag{5.39}$$

$$r_{\mathrm{m,n}} = \left({y_{\mathrm{m}}}^2 + {z_{\mathrm{n}}}^2 \right)^{1/2} = \left((y - mW_{\mathrm{N,e}})^2 + (z - nH_{\mathrm{N,e}})^2 \right)^{1/2} \tag{5.40}$$

The substitution with eq. (5.39) and (5.40) yields in:

$$\frac{u_{\mathrm{x}}}{u_\infty} = 1 + \frac{1}{2} {R_{\mathrm{M}}}^3 \sum_{m=-\infty}^{\infty} \sum_{n=-\infty}^{\infty} (-1)^{m+n} \frac{(y - mW_{\mathrm{N,e}})^2 + (z - nH_{\mathrm{N,e}})^2 - 2x^2}{\left(x^2 + (y - mW_{\mathrm{N,e}})^2 + (z - nH_{\mathrm{N,e}})^2 \right)^{5/2}} \tag{5.41}$$

$$\frac{u_{\mathrm{r}}}{u_\infty} = -\frac{3}{2} {R_{\mathrm{M}}}^3 \sum_{m=-\infty}^{\infty} \sum_{n=-\infty}^{\infty} (-1)^{m+n} \frac{x \left((y - mW_{\mathrm{N,e}})^2 + (z - nH_{\mathrm{N,e}})^2 \right)^{1/2}}{\left(x^2 + (y - mW_{\mathrm{N,e}})^2 + (z - nH_{\mathrm{N,e}})^2 \right)^{5/2}} \tag{5.42}$$

From eq. (5.38) the sign of $\pm r_{\mathrm{m,n}}$ indicates the sign of $\pm u_{\mathrm{r}}$. The substitution of $r_{\mathrm{m,n}}$ with eq. (5.40) using ${y_{\mathrm{m}}}^2$ and ${z_{\mathrm{n}}}^2$ eliminates the sign of both the corresponding coordinates. Thus, u_{r} is separated into its components u_{y} and u_{z}:

$$\frac{u_{\mathrm{y}}}{u_\infty} = \frac{y_{\mathrm{m}}}{r_{\mathrm{m,n}}} \cdot \frac{u_{\mathrm{r}}}{u_\infty} \tag{5.43}$$

$$\frac{u_{\mathrm{z}}}{u_\infty} = \frac{z_{\mathrm{n}}}{r_{\mathrm{m,n}}} \cdot \frac{u_{\mathrm{r}}}{u_\infty} \tag{5.44}$$

The velocity components extracted from eq. (5.42) are then:

$$\frac{u_{\mathrm{y}}}{u_\infty} = -\frac{3}{2} {R_{\mathrm{M}}}^3 \sum_{m=-\infty}^{\infty} \sum_{n=-\infty}^{\infty} (-1)^{m+n} \frac{x\,(y - mW_{\mathrm{N,e}})}{\left(x^2 + (y - mW_{\mathrm{N,e}})^2 + (z - nH_{\mathrm{N,e}})^2\right)^{5/2}} \tag{5.45}$$

$$\frac{u_{\mathrm{z}}}{u_\infty} = -\frac{3}{2} {R_{\mathrm{M}}}^3 \sum_{m=-\infty}^{\infty} \sum_{n=-\infty}^{\infty} (-1)^{m+n} \frac{x\,(z - nH_{\mathrm{N,e}})}{\left(x^2 + (y - mW_{\mathrm{N,e}})^2 + (z - nH_{\mathrm{N,e}})^2\right)^{5/2}} \tag{5.46}$$

The velocity correction is based on the integral average of the velocity $\Delta u / u_\infty$ induced by the mirror images. Figure 5.9 depicts the definition of the coordinates φ and θ for a particular surface element $\mathrm{d}A$. The angle φ denotes the angle between the y-axis and the center point of $\mathrm{d}A$ projected on the xy-plane. θ is the angle between the center point of $\mathrm{d}A$ and the z-axis. The principle is to integrate the velocity over the model surface whereas the velocity at the model surface represents the local velocity interference in the

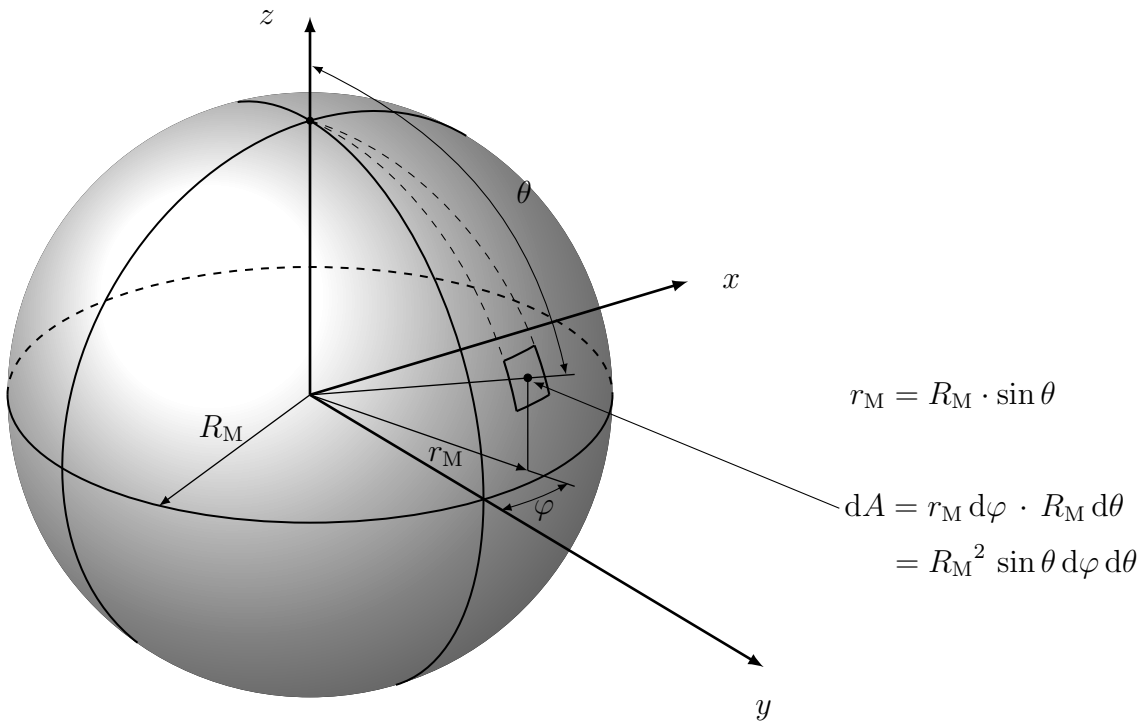

Figure 5.9: Polar coordinates for the integral velocity over the surface of the sphere.

open jet. Due to symmetry conditions the integration of velocity for 1/8 of the sphere surface A is sufficient ($0 \leq \varphi \leq \pi/2; 0 \leq \theta \leq \pi/2$):

$$\frac{\Delta u}{u_\infty} = \frac{1}{A}\int_A \frac{\Delta u(x,y,z)}{u_\infty}\mathrm{d}A = \frac{4}{\pi}\int_{\theta=0}^{\pi/2}\int_{\varphi=0}^{\pi/2} \frac{\Delta u(x,y,z)}{u_\infty}\sin\theta\,\mathrm{d}\varphi\mathrm{d}\theta \tag{5.47}$$

$$\text{with:} \quad \mathrm{d}A = {R_\mathrm{M}}^2\,\sin\theta\,\mathrm{d}\varphi\,\mathrm{d}\theta \tag{5.48}$$

$$A = \pi/4 \cdot {R_\mathrm{M}}^2 \tag{5.49}$$

This approach provided a general, integral velocity correction applicable to all force directions. However, as shown above the jet expansion enforced a longitudinal gradient of velocity interference depending on the local cross section of the model. E.g., the velocity interference for a sphere is smaller at the stagnation point rather than for the model center. Furthermore, the face normal direction of a surface element of the sphere is more drag relevant at the front and more lift and side force relevant in the model center. Thus, a weighting function was applied to the integral velocity considering the projected area of each surface element for the corresponding Cartesian direction $i = x, y, z$:

$$\left(\frac{\Delta u}{u_\infty}\right)_\mathrm{i} = \frac{1}{A}\int_A \frac{\Delta u(x,y,z)}{u_\infty}\mathrm{d}A_\mathrm{i} \tag{5.50}$$

$$\text{with:} \quad \mathrm{d}A_\mathrm{i} = \frac{x_\mathrm{i}}{R_\mathrm{M}}\,\mathrm{d}A \qquad x_\mathrm{i} = x, y, z \tag{5.51}$$

The result was a velocity correction separately for the corresponding directions and, hence, different correction quantities for the drag and lift force coefficient:

$$\frac{C_\mathrm{D}}{C_\mathrm{D,c}} = \left[\left(\frac{\Delta u}{u_\infty}\right)_\mathrm{x}\lambda + 1\right]^2 \qquad \text{and} \qquad \frac{C_\mathrm{L}}{C_\mathrm{L,c}} = \left[\left(\frac{\Delta u}{u_\infty}\right)_\mathrm{z}\lambda + 1\right]^2 \tag{5.52}$$

The solution of the equations above was performed with a numerical approach in MATLAB, see appendix A.4.3 on page 158.

5.1.3 Comparison of the Results

After the description of the extended correction models, the results for the interference corrections for the open jet expansion are presented, firstly for a sphere in a rectangular tunnel and, secondly in comparison to the CFD results from chapter 4. Compared to the method of Lock (1929), the effect of increasing jet cross section in proximity to the model was added. Furthermore, an integral velocity correction was applied, in order to achieve a separate correction for lift and drag.

Sphere in a Rectangular Tunnel

It is worth to mention, that the combination of parallel flow and a dipole in potential flow returned a rather idealized flow field around a sphere and did not contain the rearward,

pressure induced flow separation, which is characteristic for the flow around a "real" sphere. In potential flow, the longitudinal velocity gradient around the model, due to the jet expansion, is compensated between the front and the rear face of the sphere and, hence, the resulting interference is expected to be zero. This is based on the assumption, that wall skin friction is negligible. This situation is expected to change for a "real" sphere as the longitudinal gradient is not compensated due to the rearward separation. The present correction models are based on the assumption, that, the asymptotic theory with blockage conditions remains comparable.

Figure 5.10 presents the results for the correction of both the drag $C_{\mathrm{D,c}}/C_{\mathrm{D}}$ and the lift coefficient $C_{\mathrm{L,c}}/C_{\mathrm{L}}$ for a sphere in rectangular tunnel whereas the aspect ratio $W_{\mathrm{N}}/H_{\mathrm{N}} = 0.7$ of the tunnel was used from the duplex images of the nozzle from chapter 4 with $W_{\mathrm{N}}/H_{\mathrm{N}} = 1.4$. Both the model of Lock (1929) and method 2.1 are based on a velocity correction using the velocity interference in the model center. Thus, the correction for

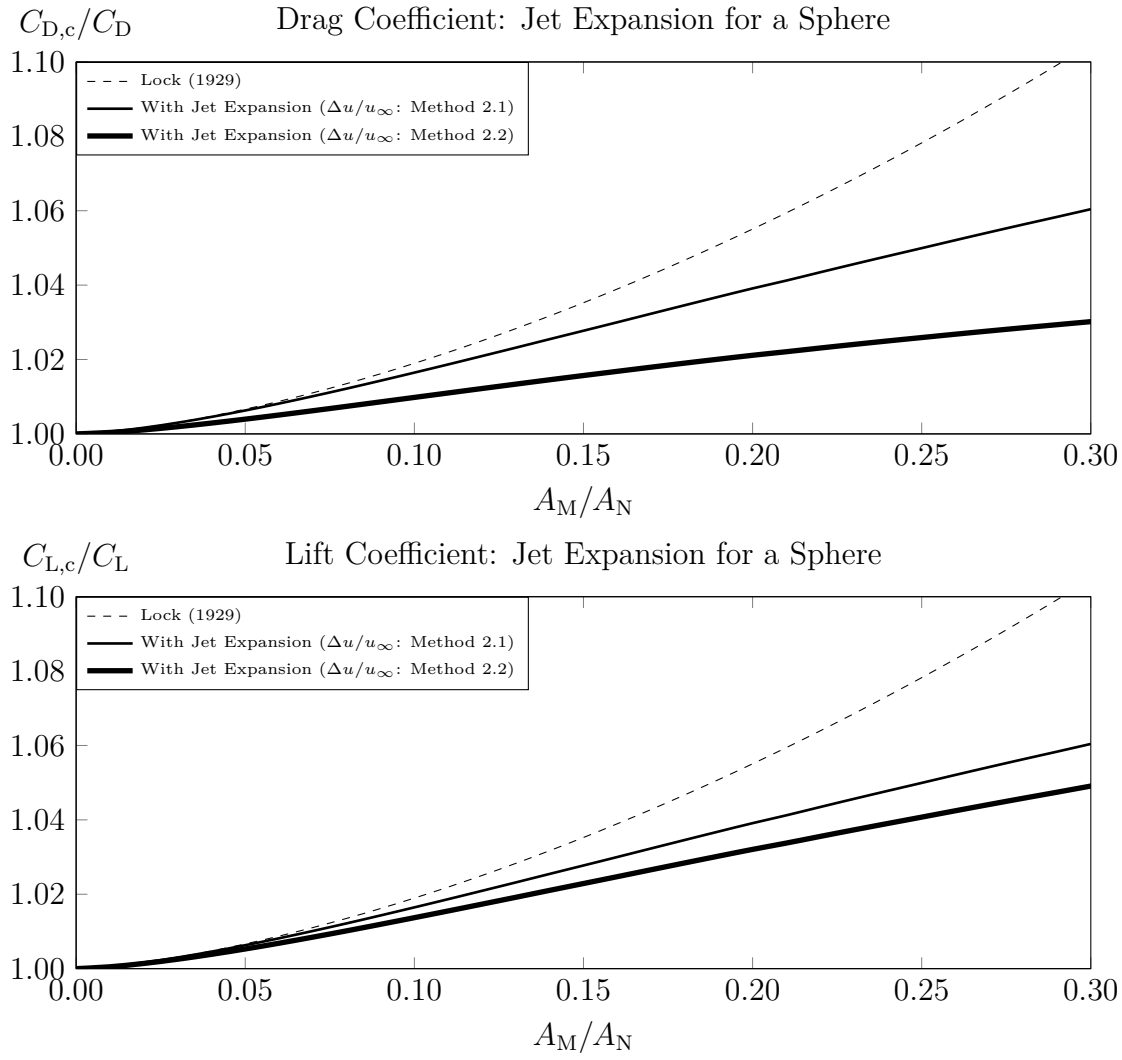

Figure 5.10: Correction of the drag $C_{\mathrm{D,c}}/C_{\mathrm{D}}$ and the lift coefficient $C_{\mathrm{L,c}}/C_{\mathrm{L}}$ for a sphere in a rectangular, duplex tunnel with $W_{\mathrm{N}}/H_{\mathrm{N}} = 0.7$. To represent a sphere, the model shape factor was selected with $\lambda = 1$.

both the drag and the lift coefficients were identical for each model. The remaining difference was the reference blockage ratio A_M/A_N as Lock (1929) uses the blockage ratio of the expanded jet at $x = 0$ whereas the blockage ratio in method 2.1 was determined from the stream function. Thereby, the effective correction in method 2.1 was lower than for the model of Lock (1929). Method 2.2 was based on method 2.1 but added the integral velocity correction, which was separate for drag and lift. The result was a further decrease in effective correction whereas the lift interference was larger than the drag interference. This result was reasonable as the lift effective surface of the sphere was located in regions close to the model center $x = 0$, in which the jet expansion was the largest.

DrivAer Model in a Rectangular Tunnel

The application of the models above to the CFD results required the adjustment of the model shape factor λ. In theory, different methods for the calculation of λ are presented. The original idea of Lock (1929) was to use λ as a factor for the volume of the model compared to the sphere with equivalent frontal area. This principle is adopted by Wickern (2014) or Mercker (2013) by suggesting to additionally include the wake volume of bluff bodies. Based on the volume of the model, the result for a typical automotive body is in the range of $\lambda \approx 2$, Wickern (2014). However, in the present work λ was adjusted in order to achieve the best fit of the potential flow models with CFD for lower blockage ratios $A_M/A_N < 10\,\%$ as the objective was to compare the asymptotic behavior of the wind tunnel corrections with CFD.

Figure 5.11 illustrates the application of the potential flow corrections to the CFD results. The fastback and the notchback results from CFD were excluded for the lift coefficients as the total lift coefficients were low with $C_L = -0.054$ and $C_L = -0.031$ and, hence, the accuracy of the interference in percentage was in the range of $C_{L,c}/C_L \pm 0.1$. For both the drag and the lift coefficients a good agreement was achieved for all methods under investigation by adjusting λ for a blockage ratio of $A_M/A_N \leq 0.1$. Furthermore, for drag, λ was in good agreement with Wickern (2014) if the velocity interference was calculated in the model center (see Lock (1929) and method 2.1). However, for all models λ turned out to be significantly higher in order to match the lift interference. In general, the asymptotic behavior of both method 2.1 and 2.2 was comparable, but λ was adjusted differently. The agreement with CFD was $C_{i,c}/C_i \leq 1\,\%$ within the entire range of investigation whereas the results of the Lock-Model diverged for higher blockage ratios, e.g. $A_M/A_N \approx 20\,\%$.

The main reason for the different results of λ for drag and lift was expected to be the difference in fineness ratio of an automotive body compared to the sphere. The projected effective area of the sphere is equal for drag and lift $A_{ref} = \pi {R_M}^2$. For an automotive body, the lift effective surface area is significantly larger than the frontal area of the model. This explained a larger λ for lift rather than for drag.

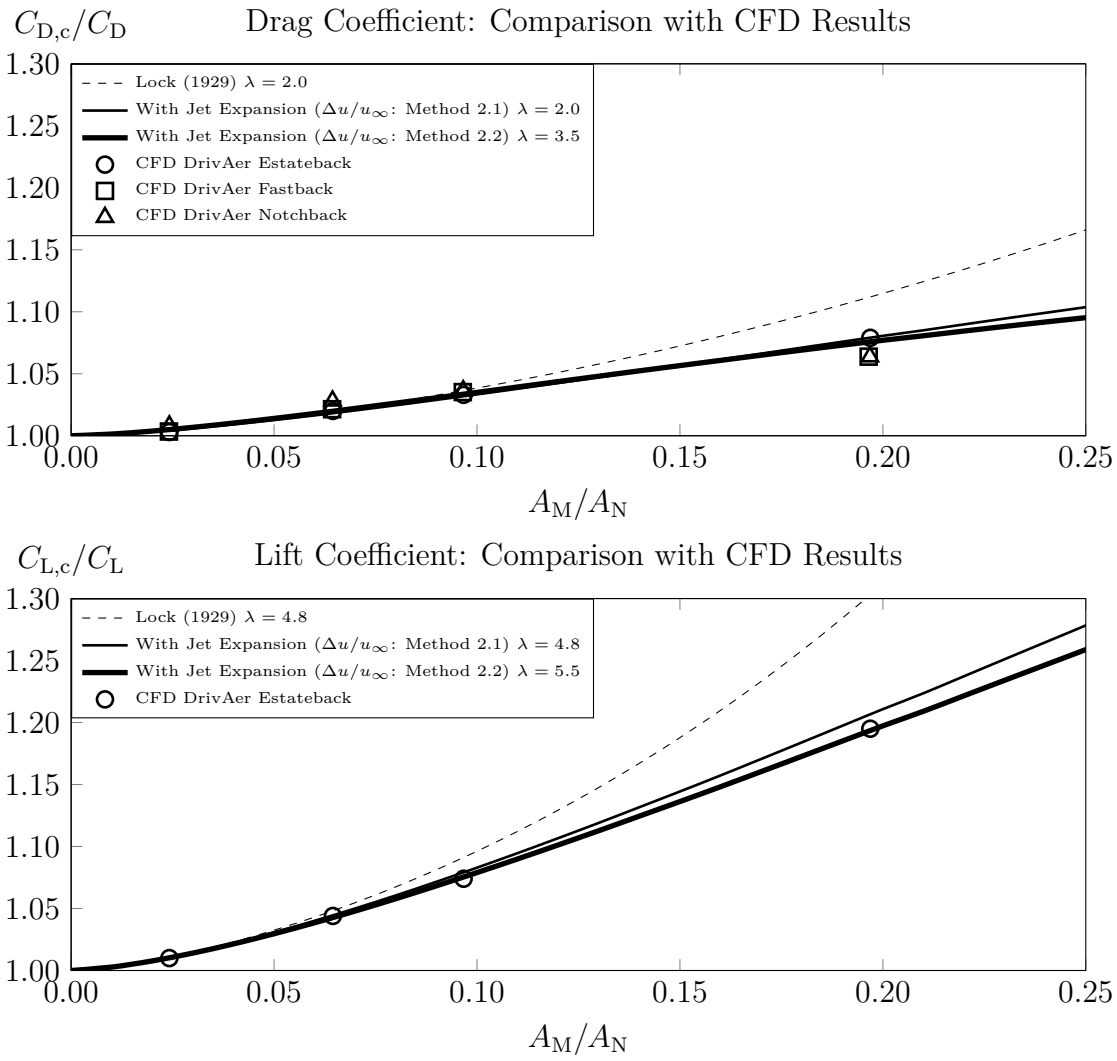

Figure 5.11: Correction of the drag $C_{D,c}/C_D$ and the lift coefficient $C_{L,c}/C_L$ for a sphere in a rectangular, duplex tunnel with $W_N/H_N = 0.7$. The model shape factor λ was adjusted in order to achieve a best fit of the correction models with CFD for low blockage ratios.

5.2 Design Criteria for Automotive, Open Jet Wind Tunnels

This section provides an overview of the most essential results and their consequences for a specific design of an automotive, open jet wind tunnel. The basic idea was to define a series of parameters in order to define a new wind tunnel layout. Therefore, a compromise of accuracy and effort (e.g. costs for investment and operation) was desired. It is worth to mention, that this work does not provide the knowledge about the entire range of relevant parameters for the design of a wind tunnel. The CFD studies, presented in chapter 4, were based on specific assumptions, which certainly affected the results. However, a better understanding of some essential design parameters was obtained.

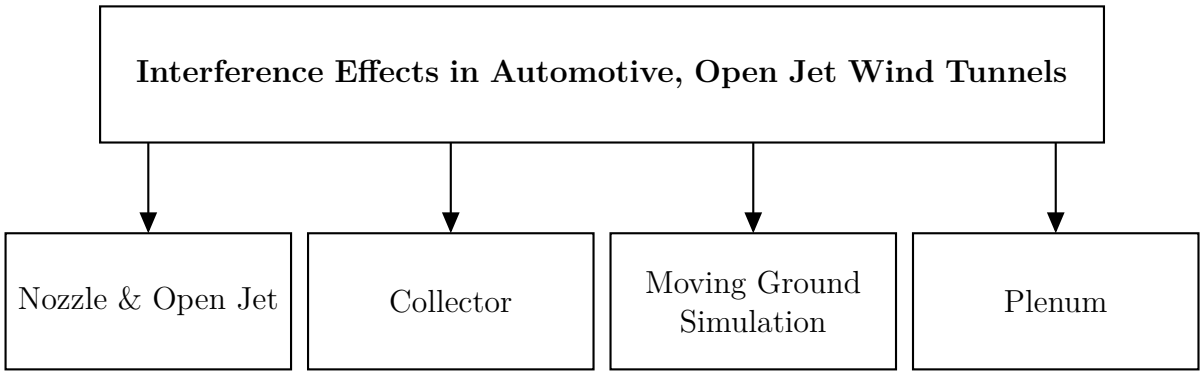

Figure 5.12: Overview of the essential sources for interference effects in open jet wind tunnels.

An overview of the most essential sources for wind tunnel interferences in an open test section is illustrated in Figure 5.12. Three of them were subject of the present work. The conclusions and consequences obtained from the present work concerning the interferences from nozzle and open jet, collector and moving ground simulation are discussed below in section 5.2.1 - 5.2.3. Some basic further considerations, e.g. for plenum interferences, are presented in section 5.2.4.

5.2.1 Nozzle Design

The wind tunnel nozzle is one of the most essential components of a wind tunnel as the decision for a specific cross sectional area of the nozzle A_N defines the solid blockage for a selected model with A_M. The solid blockage ratio $A_\mathrm{M}/A_\mathrm{N}$ is certainly the most common, non-dimensional parameter in order to characterize the relation of the length scales of model and wind tunnel. Effectively, the design of the nozzle defines the dimensions of the open jet and, hence, is part of the discussion concerning the test sections length. E.g., Wickern (2014) suggests not to exceed an effective test section length of three hydraulic jet diameters in order to restrict jet instabilities with an adequate portion. Thus, it is worth to mention that the decision for a specific nozzle dimension is always connected to the required test section length, defined by the collector position.

The present work included nozzle dimensions covering a range of blockage ratio of $2.4\,\% \leq A_\mathrm{M}/A_\mathrm{N} \leq 19.7\,\%$. The investigations involved two general interference effects – the nozzle and the open jet interference. The open jet interference turned out to be the only effect, which was not sufficiently eliminated with decreasing blockage ratio, at least not for a nozzle with a realizable cross section. E.g. the remaining drag deficit due to the jet expansion for the estateback was $\Delta C_\mathrm{D} \approx 0.006$ in a tunnel with $A_\mathrm{N} = 33.6\,\mathrm{m}^2$. The consequence was that a correction of the open jet interference was required. An alternative approach to eliminate a subsequent jet expansion correction is the "self-correcting open jet wind tunnel" presented by Wickern (2014). The principle is to compensate the drag decreasing effects of the open jet with the drag increasing effects of the nozzle by selecting an appropriate longitudinal model position x_c. In general, the self-correcting approach

from Wickern (2014) was confirmed in the CFD for the nozzle method and (partially) for the plenum method. However, on the one hand no compensation was achieved in CFD for lift at the self-correcting model position for drag and, hence, a subsequent lift correction was required. On the other hand, the model position in a real facility is always connected to the location of wind tunnel balance whereas the wheel base center is typically located in the x-center of the balance and the turntable[1]. In CFD, the self-correcting model position was different for the specific rear ends of the DrivAer even though the blockage ratio was identical. Thus, the latter model position in a real facility is not universal but must be adjusted for the specific model under investigation in order to avoid the requirement of drag corrections. This is not expected to be very practicable as, firstly, the optimal model position must be determined and, secondly, an error due to a inaccurate model position is likely.

Based on the results, it is recommended to operate the wind tunnel with the plenum method and, for a selected nozzle, to locate the model at a position x_c, for which the gradient induced by the proximity of the nozzle is sufficiently decayed, e.g. $\Delta C_\mathrm{D} \leq 0.001$. Therefore, the model position x_c was determined to be $x_\mathrm{c} \geq 4.8\,\mathrm{m}$ for a nozzle with $A_\mathrm{N} = 22.4\,\mathrm{m}^2$. Consequently, the force coefficients measured with this approach require to be corrected in order to account for the jet expansion effect. The jet expansion correction can either be applied using the classical solid blockage correction from Lock (1929) or using the methods 2.1 or 2.2 developed in this work. The application of the correction methods presented in Figure 5.11 on the CFD data at $x_\mathrm{c} = 6.0\,\mathrm{m}$ is shown in Table 5.1.

Table 5.1: Effects of the open jet interference on ΔC_D, $\Delta C_\mathrm{L,f}$ and $\Delta C_\mathrm{L,r}$ for different blockage ratios and rear ends. The table presents uncorrected data as well as corrected data using the approach of Lock (1929), method 2.1 and 2.2. The corrections apply the model shape factors λ as presented in Figure 5.11.

		$A_\mathrm{M}/A_\mathrm{N} = 6.4\,\%$			$A_\mathrm{M}/A_\mathrm{N} = 9.7\,\%$			$A_\mathrm{M}/A_\mathrm{N} = 19.7\,\%$		
		ΔC_D	$\Delta C_\mathrm{L,f}$	$\Delta C_\mathrm{L,r}$	ΔC_D	$\Delta C_\mathrm{L,f}$	$\Delta C_\mathrm{L,r}$	ΔC_D	$\Delta C_\mathrm{L,f}$	$\Delta C_\mathrm{L,r}$
Uncorr.	EB	-0.006	0.001	0.008	-0.010	0.001	0.008	-0.023	0.013	0.020
	FB	-0.004	0.003	-0.001	-0.008	0.004	0.000	-0.016	0.011	-0.006
	NB	-0.006	0.002	-0.004	-0.008	0.006	-0.002	-0.017	0.012	-0.008
Lock	EB	-0.001	-0.004	0.003	0.001	-0.008	0.000	0.008	-0.013	-0.005
	FB	0.001	0.000	0.000	0.001	-0.003	0.004	0.010	-0.009	0.005
	NB	-0.001	-0.002	-0.003	0.001	0.000	0.000	0.009	-0.006	-0.004
Meth. 2.1	EB	-0.001	-0.004	0.004	0.000	-0.006	0.001	-0.001	-0.005	0.003
	FB	0.000	0.000	0.000	0.000	-0.002	0.004	0.002	-0.003	0.001
	NB	-0.001	-0.001	-0.003	0.000	0.001	0.000	0.001	0.000	-0.005
Meth. 2.2	EB	-0.001	-0.004	0.004	0.000	-0.006	0.001	-0.002	-0.004	0.004
	FB	0.001	0.000	0.000	0.000	-0.002	0.003	0.002	-0.002	0.001
	NB	-0.001	-0.001	-0.003	0.000	0.001	0.000	0.000	0.001	-0.005

[1]Assumption: The aerodynamic forces are measured with an external, underfloor balance

Proposing an appropriate nozzle cross sectional area for a wind tunnel facility is rather difficult without specifying a particular accuracy and correction effort. However, the data presented in Table 5.1 offers the opportunity to get an overview from the results of the CFD studies and the potential flow correction approaches. Up to a blockage ratio of $A_M/A_N \leq 9.7\,\%$ the corrected drag data from all methods under investigation were in the range of ± 0.001. For the highest blockage ratio $A_M/A_N = 19.7\,\%$ only method 2.1 and 2.2 were in the range of accuracy of CFD of $\Delta C_D \approx \pm 0.002$ and $\Delta C_{L,f} \approx \Delta C_{L,r} \approx \pm 0.005$. The method from Lock (1929) yielded in differences of up to $\Delta C_D \approx \pm 0.010$, which was caused by the difference in asymptotic prediction compared to CFD. Based on this knowledge, it is suggested to choose a nozzle cross section of $A_N \geq 22.4\,\mathrm{m}^2$, for which all correction methods returned adequate results.

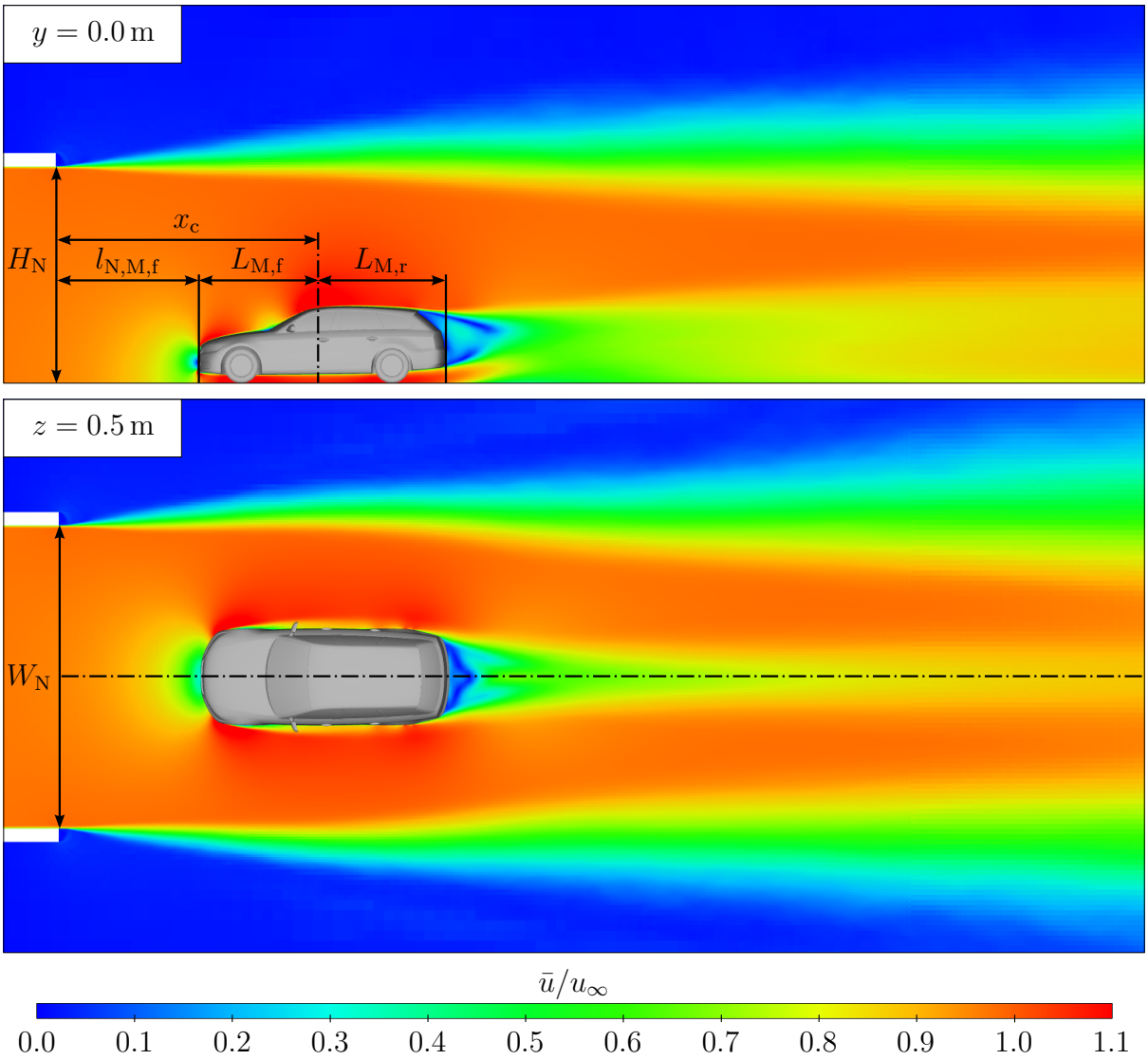

Figure 5.13: Flow field $\bar{u}/u_\infty$ in the planes $y = 0.0\,\mathrm{m}$ (top) and $z = 0.5\,\mathrm{m}$ (bottom) for the recommended nozzle configuration with $A_N = 22.4\,\mathrm{m}^2$, $W_N/H_N = 1.4$ and $x_c = 4.8\,\mathrm{m}$. $L_{M,f} = 2.2\,\mathrm{m}$ and $L_{M,r} = 2.4\,\mathrm{m}$ denote characteristic model lengths.

An example is presented in Figure 5.13 using a nozzle with $A_N = 22.4\,m^2$ ($W_N/H_N = 1.4$ and a model location of $x_c = 4.8\,m$. It is recommended to use the distance $l_{N,M,f}$ between nozzle exit and model front instead of x_c to be more independent from particular model lengths.

Summarizing the most essential results for the nozzle design, the following dimensions are recommended for a DrivAer characteristic production car in full scale:

- $A_N = 22.4\,m^2$ with $A_M/A_N = 9.7\,\%$ and $W_N/H_N = 1.4$
- $l_{N,M,f} = 2.6\,m$ with $x_c = 4.8\,m$, $L_{M,f} = 2.2\,m$ and $L_{M,r} = 2.4\,m$

5.2.2 Collector Design and Test Section Length

The CFD studies on collector interferences were based on a rather generic collector geometry. It was well known that real designs for a wind tunnel collector are often very complex in terms of the geometry. General effects of the collector parameters under investigation on the model tested in the wind tunnel were evaluated. The basic idea was to understand the sensitivities of the particular parameters, find analogies between the generic and the generic, converging collector and, finally, determine the test section length, for which collector interferences die out. Therefore, a particular nozzle geometry $A_N = 22.4\,m^2$ and model position $x_c = 4.8\,m$ was selected based on the results for nozzle and open jet interferences. It is worth to mention that the present study did not consider further aspects such as the jet stabilization by the collector and, hence, no recommendation towards a critical test section length, in terms of jet instabilities, could have been derived.

The results from the generic collector with a flap angle of $\alpha_C = 0\,°$ showed that the collector interference was eliminated for all test section lengths under investigation by selecting an appropriate collector cross sectional area A_C/A_N. The effect of the collector was removed with two approaches, firstly, for $A_C/A_N \approx 1.1$ the collector was expected to match the free open jet propagation and, secondly, interferences died out for $A_C/A_N \geq 3.0$. However, a rather short test section, e.g. $L_{TS} = 8.2\,m$ is not recommended for both of these methods. The selection of $A_C/A_N \approx 1.1$ showed large gradients in the aerodynamic forces and, hence, a high sensitivity with respect to the collector area dC_D/dA_C. For $A_C/A_N > 1.6$ the collector was characterized to be "detached" as the open jet attached not at the collector inlet but further downstream. With a further increase of A_C/A_N the effective test section length increased as well. A rather negative effect on the jet-stabilizing effect of the collector is expected if the flow attaches "too far" downstream from the collector inlet. Thus, the only reliable solution using the generic collector was to extend the test section length L_{TS}. For a test section length of $L_{TS} = 15.8\,m$ the effects on the aerodynamic forces were $\Delta C_{D,max} \leq 0.002$ and $\Delta C_{L,f,max} = \Delta C_{L,r,max} \leq 0.005$ and, hence, in the range of accuracy of the CFD simulations.

The upgrade of the generic collector with an additional parameter, the flap angle $\alpha_C > 0\,°$, offered the opportunity to investigate a more realistic collector geometry. The most essential result was certainly the effective extension of test section length due to an increase

of the flap angle α_C. Furthermore, a detailed comparison of the results showed the conformity for the converging collector with the generic collector also for short test sections $L_{TS} = 8.2\,m$. Based on this knowledge, the maximum expected interference for the converging collector was determined for an increasing test section length $L_{TS} \leq 15.8\,m$ for the estateback, which showed the largest interferences.

The results for the maximum interference of the converging collector at different test section lengths are presented in Table 5.2. The consequence is that the test section can be shorter for a collector with a larger flap angle α_C. Considering the accuracy of the simulations ($\Delta C_D \approx \pm 0.002$ and $\Delta C_{L,f} \approx \Delta C_{L,r} \approx \pm 0.005$) the minimum test section length for the estateback was $L_{TS} \approx 11.7\,m$ for $\alpha_C = 30\,°$, $L_{TS} \approx 14.0\,m$ for $\alpha_C = 20\,°$ and $L_{TS} \approx 15.8\,m$ for $\alpha_C = 10\,°$. It is worth to mention that the values in Table 5.2 state the maximum interference. The corresponding cross sections $A_{C,in}/A_N$ are given and increase with the flap angle. Consequently, it is expected, that based on these values increasing or decreasing the cross section of the collector the interference is further reduced.

The recommendation is to choose the test section length and the corresponding collector design carefully as it is connected to the nozzle dimensions. Wickern (2014) proposes not to exceed a test section length of $L_{TS}/D_{N,h} = 3.00$, which corresponds to a test section length of $L_{TS} = 14.0\,m$ for $A_N = 22.4\,m^2$. However, modern facilities sometimes have a test section length $L_{TS}/D_{N,h} > 3.00$. Thus, a reliable recommendation for a maximum test section length in terms of jet stability can not be derived from the results in this work. That is why the suggested design is proposed with $L_{TS} = 14.0\,m$ and $A_{C,in}/A_N = 2.20$ as, from the aerodynamic side, it turned out to be an adequate layout. For a real facility it is recommended to optimize the collector geometry for further aspects as well. These are e.g. design criteria concerning the open jet stability, tunnel resonances and aero-acoustic aspects.

Figure 5.14 illustrates this concept and some essential length scales to characterize the wind tunnel design. The test section length L_{TS} is a very specific value, strictly connected to the specifications applied by the nozzle design, model position and the model itself. To be more independent from the model characteristics it is recommended to use the distance $l_{W,C}$ between the end of the re-circulation (wake) downstream the model and the

Table 5.2: Maximum effects of the collector on ΔC_D, $\Delta C_{L,f}$ and $\Delta C_{L,r}$ for test section lengths L_{TS} and collector angles α_C. The reference was the simulation in the half-infinite jet without collector. $D_{N,h}$ denotes the hydraulic diameter of the wind tunnel nozzle.

	$L_{TS} = 11.7\,m$ $L_{TS}/D_{N,h} = 2.51$ $A_{C,in}/A_N = 1.75$			$L_{TS} = 14.0\,m$ $L_{TS}/D_{N,h} = 3.00$ $A_{C,in}/A_N = 2.20$			$L_{TS} = 15.8\,m$ $L_{TS}/D_{N,h} = 3.39$ $A_{C,in}/A_N = 3.25$		
	ΔC_D	$\Delta C_{L,f}$	$\Delta C_{L,r}$	ΔC_D	$\Delta C_{L,f}$	$\Delta C_{L,r}$	ΔC_D	$\Delta C_{L,f}$	$\Delta C_{L,r}$
$\alpha_C = 10\,°$	-0.024	-0.005	0.017	-0.005	0.001	0.001	-0.001	-0.001	0.004
$\alpha_C = 20\,°$	-0.013	-0.004	0.006	-0.002	-0.002	0.001	0.002	-0.001	0.000
$\alpha_C = 30\,°$	0.000	-0.003	0.002	-0.001	-0.002	0.004	0.002	-0.003	0.000

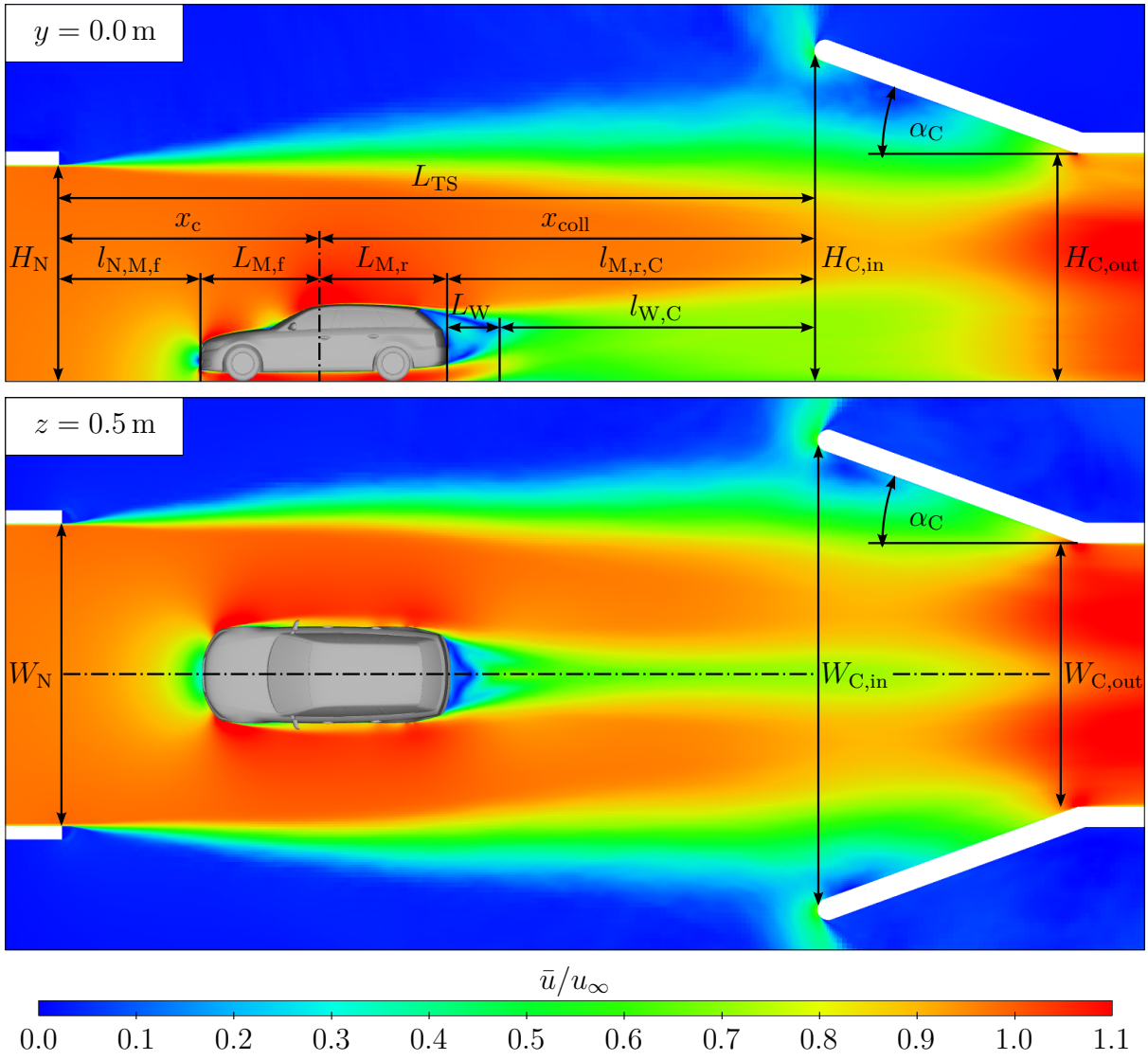

Figure 5.14: Flow field $\bar{u}/u_\infty$ in the planes $y = 0.0\,\mathrm{m}$ (top) and $z = 0.5\,\mathrm{m}$ (bottom) for the recommended collector configuration with $A_{\mathrm{C}}/A_{\mathrm{N}} = 2.20$, $W_{\mathrm{C}}/H_{\mathrm{C}} = 1.4$ and $L_{\mathrm{TS}} = 14.0\,\mathrm{m}$. $L_{\mathrm{M,f}} = 2.2\,\mathrm{m}$, $L_{\mathrm{M,r}} = 2.4\,\mathrm{m}$ and $L_{\mathrm{W}} = 3.3\,\mathrm{m}$ denote characteristic model lengths.

collector inlet or the distance $l_{\mathrm{M,r,C}}$ between the rear end of the model and the collector. Therefore, the wake length L_{W} of the estateback was determined in CFD using the total pressure criteria.

Summarizing the results and consequences from the collector studies, the following parameters were essential for the collector design:

- $l_{\mathrm{W,C}} \geq 1.2\,\mathrm{m}$ and $l_{\mathrm{M,r,C}} \geq 4.5\,\mathrm{m}$ for $\alpha_{\mathrm{C}} = 30\,^\circ$ with $L_{\mathrm{M,r}} = 2.4\,\mathrm{m}$ and $L_{\mathrm{W}} = 3.3\,\mathrm{m}$
- $l_{\mathrm{W,C}} \geq 3.5\,\mathrm{m}$ and $l_{\mathrm{M,r,C}} \geq 6.8\,\mathrm{m}$ for $\alpha_{\mathrm{C}} = 20\,^\circ$
- $l_{\mathrm{W,C}} \geq 5.3\,\mathrm{m}$ and $l_{\mathrm{M,r,C}} \geq 8.6\,\mathrm{m}$ for $\alpha_{\mathrm{C}} = 10\,^\circ$

5.2.3 Moving Ground Simulation

The CFD studies on the moving ground simulation were applied to a selected race car. The results showed large interferences, especially for lift, for the 5-belt moving ground simulation. Thus, from the aerodynamic point of view, a 5-belt system did not provide sufficient flow quality and a single-belt system is recommended. The following consequences are based on the assumption that the desired wind tunnel facility offers the opportunity to test both full scale production cars and race cars. Therefore, the investigations on the moving ground simulation were limited to race car considerations. It is worth to mention, that typical facilities for the development of production cars are equipped with a 5-belt system (or similar) and that a requirement of a single-belt for these cars was not proven. Furthermore, the decision for a particular technique – e.g. 5-belt or single-bet – involves not only aerodynamic flow quality but further aspects. For example, the experimental setup itself in order to measure the aerodynamic forces. External underfloor balances are typical for full scale applications. Measuring aerodynamic forces on a single-belt with an underfloor balance involves larger parasitic forces than for a 5-belt system if the moving belt is connected to the balance. However, these aspects were not involved in the present work and are not discussed more in detail but are recommended to be considered for the design of a moving ground simulation system.

The results from the moving ground investigations showed that the interferences decay with increasing belt dimensions such as moving belt length L_B and width W_B. The remaining effects were in the range of the averaging accuracy of CFD for rear belt length of $L_\mathrm{B,r} \geq 0.9\,L_\mathrm{M}$ whereas L_M denotes the length of the model. Assuming a typical race car length of $L_\mathrm{M} \approx 5.0\,\mathrm{m}$ this yielded in $L_\mathrm{B,r} \geq 4.5\,\mathrm{m}$. Assuming the model to be located in the center of the moving belt the total belt length is then $L_\mathrm{B} \geq 9.0\,\mathrm{m}$. The corresponding result for the belt width required $W_\mathrm{B} \geq 1.5\,W_\mathrm{M}$ and, hence, $W_\mathrm{B} \geq 3.0\,\mathrm{m}$ for a car with $W_\mathrm{M} \approx 2.0\,\mathrm{m}$. Thus, a moving belt of the size L_B x $W_\mathrm{B} = 9.0\,\mathrm{m}$ x $3.0\,\mathrm{m}$ is recommended. Based on the design recommendations for the nozzle and the collector, this concept was integrated into the concept of the test section length of $L_\mathrm{TS} = 14.0\,\mathrm{m}$, see Figure 5.15.

The selected dimensions were rather theoretic values based on the results from the CFD studies and did not involve further aspects such as the assembly space of the specific components, e.g the diameter of the front and rear rollers of the moving belt. Furthermore, the elimination of boundary layer of the on-coming flow at the nozzle exit is an essential step in order to simulate the aerodynamics of ground vehicles and is an essential part of the moving ground simulation. Possible solutions are a boundary layer suction, scoop, tangential blowing or combinations of these solutions. However, the integration of a boundary layer treatment certainly affects the layout of the test section. The upstream integration of e.g. a boundary layer suction must be considered in terms of its consequences on the package due to the assembly space. It is recommended to include these aspects into the design package of a potential facility as they were not sufficiently investigated in the present work.

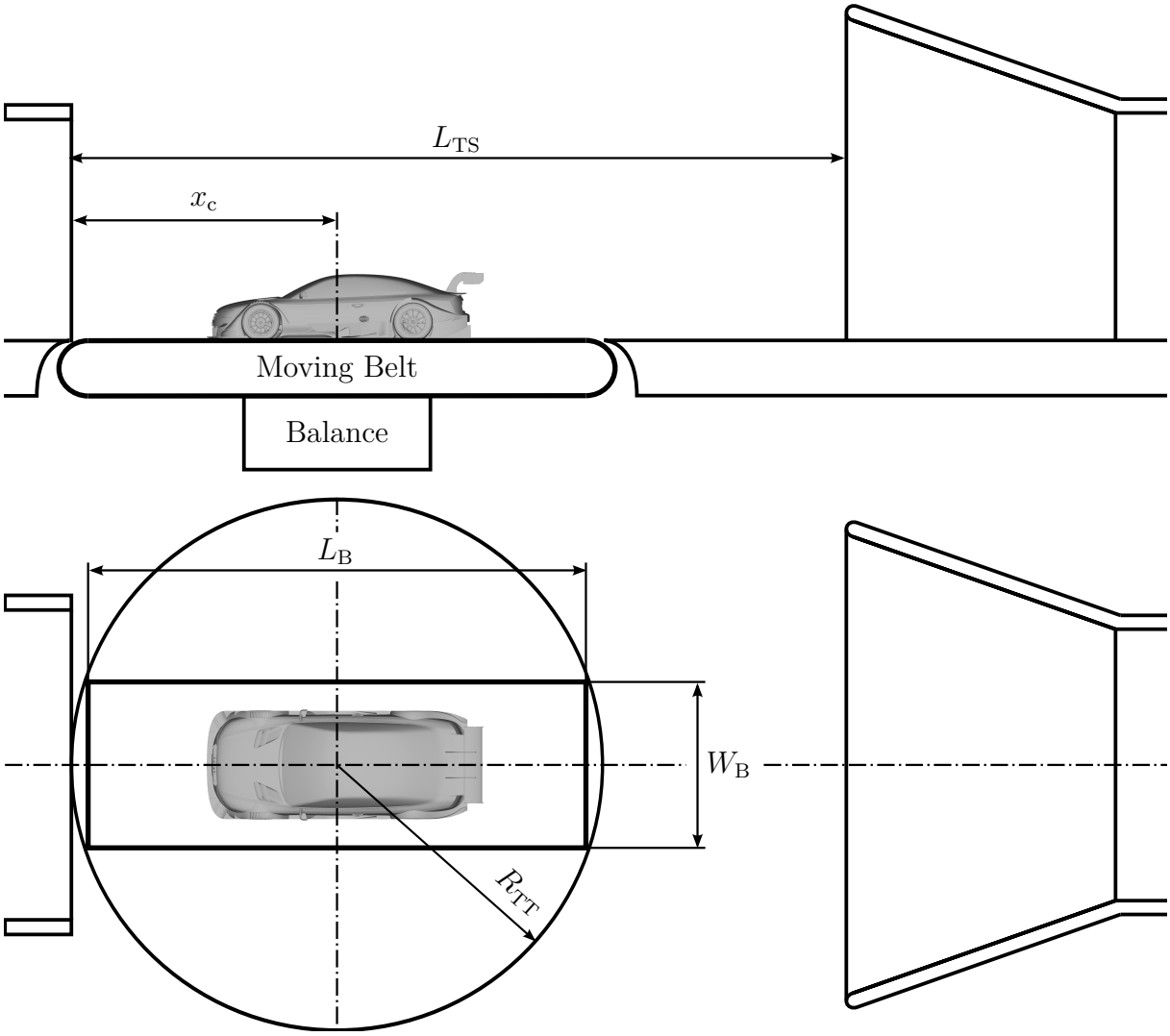

Figure 5.15: Schematic illustration of the integration of the selected moving belt system (single-belt) into the suggested test section layout: $L_{TS} = 14.0\,m$, $x_c = 4.8\,m$, $L_B = 9.0\,m$, $W_B = 3.0\,m$, $R_{TT} = 4.8\,m$.

5.2.4 Summary

Based on the consequences determined for automotive, open jet wind tunnels an example for a final design recommendation is presented in Table 5.3. It is important to mention that this concept involved investigation for a specific model geometry (DrivAer model) for a limited amount of possible parameters and does not include security surcharges, e.g. for the test section length. The test section length L_{TS} was restricted to three hydraulic jet diameters in order to follow the proposal of e.g. Wickern (2014). Real facilities are sometimes equipped with longer test sections, but a recommendation towards a maximum possible test section length for a particular nozzle diameter could not be derived from this work. Further aspects such as package considerations were surely not sufficiently considered as well and, hence, the design proposal mainly based on aerodynamic aspects itself.

Table 5.3: Specifications of the recommended design for an automotive, open jet wind tunnel.

Wind Tunnel Parameters	**Symbol**	**Specification**
Nozzle		
Cross Sectional Area	A_{N}	$22.4\,\mathrm{m}^2$
Width	W_{N}	$5.6\,\mathrm{m}$
Height	H_{N}	$4.0\,\mathrm{m}$
Hydraulic Diameter	$D_{\mathrm{N,h}}$	$4.67\,\mathrm{m}$
Longitudinal Model Position	x_{c}	$4.8\,\mathrm{m}$
Distance to Model Front	$l_{\mathrm{N,M,f}}$	$2.6\,\mathrm{m}$
Aspect Ratio	$W_{\mathrm{N}}/H_{\mathrm{N}}$	1.4
Collector		
Cross Sectional Area Inlet	$A_{\mathrm{C,in}}$	$49.3\,\mathrm{m}^2$
Cross Sectional Area Outlet	$A_{\mathrm{C,out}}$	$20.6\,\mathrm{m}^2$
Width Inlet	$W_{\mathrm{C,in}}$	$8.3\,\mathrm{m}$
Width Outlet	$W_{\mathrm{C,out}}$	$4.9\,\mathrm{m}$
Height Inlet	$H_{\mathrm{C,in}}$	$5.9\,\mathrm{m}$
Height Outlet	$H_{\mathrm{C,out}}$	$4.2\,\mathrm{m}$
Non-Dimensional Cross Sectional Area Inlet	$A_{\mathrm{C,in}}/A_{\mathrm{N}}$	2.2
Non-Dimensional Cross Section Area Outlet	$A_{\mathrm{C,out}}/A_{\mathrm{N}}$	0.9
Aspect Ratio Inlet	$W_{\mathrm{C,in}}/H_{\mathrm{C,in}}$	1.4
Aspect Ratio Outlet	$W_{\mathrm{C,out}}/H_{\mathrm{C,out}}$	1.2
Flap Angle	α_{C}	$20\,^\circ$
Flap Length	L_{C}	$5.2\,\mathrm{m}$
Distance to Model Rear	$l_{\mathrm{M,r,C}}$	$6.8\,\mathrm{m}$
Distance to Wake Closure	$l_{\mathrm{W,C}}$	$3.5\,\mathrm{m}$
Test Section Length	L_{TS}	$14.0\,\mathrm{m}$
Non-Dimensional Test Section Length	$L_{\mathrm{TS}}/D_{\mathrm{N,h}}$	4.0
Moving Ground Simulation (Single Belt)		
Belt Length	L_{B}	$9.0\,\mathrm{m}$
Belt Width	W_{B}	$3.0\,\mathrm{m}$
Turntable		
Radius	R_{TT}	$4.8\,\mathrm{m}$

6 Conclusions and Future Work

The present work provides a better understanding for some particular interference effects in automotive, open jet wind tunnels, evaluated with CFD simulations. The effects under investigation were the nozzle, the open jet, the collector and the moving ground interferences in order to draw recommendations for the design of a modern facility. A summary of the main results and aspects for future work are presented in section 6.1 and 6.2.

6.1 Conclusions

The basic idea was to evaluate open jet wind tunnel interferences for automotive bodies using DDES simulations with *OpenFOAM®*. Therefore, the DrivAer reference model was selected for the investigations on nozzle, open jet and collector interferences and the Audi RS5 DTM car for the studies on moving ground simulation. The numerical methods, presented in chapter 3, were validated for the simulation of selected automotive bodies (DrivAer, Audi RS5 DTM) in both model and full scale as well as for simulations of the Audi Aeroacoustic Wind Tunnel with and without an Audi A4 Series production car inside the test section. The grid refinement within the free shear layers of the open jet turned out to be of crucial importance as it affected the open jet propagation. However, the grid density, especially close to the nozzle exit, was limited due to local CFL-number considerations. The validation of wind tunnel interferences was based on both the comparison of flow field data (hot-wire probes and static pressure gradient) and aerodynamic force coefficients and showed a good agreement of CFD with the experiments. In particular, this included the effect of the longitudinal model position x_c on vehicle aerodynamics for both the plenum and the nozzle method.

Based on the validation of the numerical setup, three different CFD domains were created for the numerical wind tunnel studies. The open road domain represented the flow around the model without wind tunnel constraints whereas the half-infinite wind tunnel (without collector) and the finite wind tunnel domain (with collector) were used to simulate the model in wind tunnel conditions. Consequently, the differences in the results between open road and wind tunnel conditions were evaluated to be open jet wind tunnel interferences. The most essential results concerning interferences due to nozzle and open jet, collector and moving ground simulation are summarized below. Furthermore, the consequences derived from the CFD investigations are discussed towards a recommended design for a future, automotive, open jet facility. It is worth to mention that the results were entirely based on simulations at $u_\infty = 38.89\,\mathrm{m/s}$ and a cross-flow angle $\beta = 0\,^\circ$.

Nozzle and Open Jet Interferences

The CFD simulations in the half-infinite wind tunnel domain included both the effects from nozzle and open jet interferences. Therefore, a generic, rectangular nozzle of variable cross section A_N but without a converging region was used in order to remain independent from a particular stream-wise nozzle curvature. Furthermore, the aspect ratio of the nozzle remained constant with $W_N/H_N = 1.4$. The CFD simulations of the full scale DrivAer model with estateback, fastback and notchback were applied to different test section conditions such as four nozzle cross sections[1] $11.0\,\mathrm{m}^2 \leq A_N \leq 89.6\,\mathrm{m}^2$ and varying longitudinal model positions $3\,\mathrm{m} \leq x_c \leq 9\,\mathrm{m}$. In general, the "theoretical approach towards the self-correcting open jet wind tunnel" presented by Wickern (2014) was confirmed for both the nozzle and the plenum method of dynamic pressure determination. Accordingly, for some particular model locations x_c the drag decreasing effect due to the open jet expansion was compensated with the drag increasing effect of the nozzle. The nozzle interference decayed with increasing distance x_c between the nozzle exit plane and the model, especially for the plenum method. However, "far away" from the nozzle, a deficit in drag remained for all blockage ratios under investigation. This interference (open jet expansion) decayed with decreasing blockage ratio, but with a different asymptotic trend as predicted in the classical solid blockage correction presented by Lock (1929). However, up to a blockage ratio of $A_M/A_N \approx 10\,\%$ both approaches CFD and Lock (1929) showed a good agreement for the correction of drag, if a model shape factor $\lambda = 2$ as proposed by Wickern (2014) was applied.

Collector Interferences

Based on the CFD results for the nozzle and open jet interferences, one particular nozzle configuration with $A_N = 22.4\,\mathrm{m}^2$ and $A_M/A_N = 9.7\,\%$ was selected in order to evaluate the collector interferences. On the one hand, this cross section was experienced to be an adequate compromise between effort (e.g. costs) and accuracy and on the other hand the jet expansion correction for drag was consistent in CFD and Lock (1929). Furthermore, the longitudinal model position was set to $x_c = 4.8\,\mathrm{m}$, for which the nozzle interference using the plenum method decayed to $\Delta C_D \approx \pm 0.001$. For the CFD studies on collector interferences a generic collector with a flap angle of $\alpha_C = 0\,^\circ$ and a generic, converging collector with $\alpha_C \leq 30\,^\circ$ were designed. The parameters under investigation were the collector inlet area $1.00 \leq A_C/A_N \leq 4.75$ and the test section length[2] $8.2\,\mathrm{m} \leq L_{TS} \leq 18.7\,\mathrm{m}$. The length of the collector flap remained constant with 5.2 m. In general, the experimental results presented by von Schulz-Hausmann and Vagt (1988) were confirmed. Flow field analysis showed, depending on A_C/A_N, an attached or detached flow of the open jet at the collector inlet, whereas detached flow conditions were determined as an effective extension of effective test section length[3] $L_{TS,eff} \geq L_{TS}$. The comparison of the generic, converging collector with the generic collector also indicated an extension

[1] The corresponding blockage ratio was in the range $2.4\,\% \leq A_M/A_N \leq 19.7\,\%$.

[2] The corresponding non-dimensional test section length was $1.8 \leq L_{TS}/D_{N,h} \leq 4.0$.

[3] The effective test section length $L_{TS,eff}$ denotes the "aerodynamic length" depending on the point of flow attachment along the collector/diffusor. In contrast, L_{TS} was defined as the distance between nozzle exit and collector inlet.

of effective test section length with increasing flap angle $\alpha_C > 0\,^\circ$. Thus, the collector interferences decayed "faster" for $\alpha_C > 0\,^\circ$ with increasing test section length compared to $\alpha_C = 0\,^\circ$.

Moving Ground Interferences

The CFD studies on moving ground interferences were a rather idealized approach in order to determine the required moving belt dimensions of a single belt for race car aerodynamics. Accordingly, the parameters under investigation were the moving belt width W_B and length L_B. The open road domain was selected for the investigations and the moving belt dimensions were simulated by varying the floor boundary conditions between static and moving friction walls. The incident flow was undisturbed from any boundary layer treatment. The largest effects on the aerodynamics of the Audi RS5 DTM race car were investigated on front lift for the belt width and on rear lift for the rear belt length. However, the effects decayed with increasing belt dimensions and were evaluated to be negligible for a belt width of $W_\mathrm{B} \approx 3.0\,\mathrm{m}$ and a belt length of $L_\mathrm{B} \approx 9.0\,\mathrm{m}$.

Correction Methods and Design Recommendations

The final step of the present work was to wrap up the results from the CFD studies above in order to provide recommendations for the design of a modern, automotive open jet wind tunnel. The open jet expansion was evaluated to be the only interference effect, which did not sufficiently decay with decreasing blockage ratio. Consequently, a correction method was required for nozzle cross sections of $A_\mathrm{N} < 90\,\mathrm{m}^2$ and blockage ratios of $A_\mathrm{M}/A_\mathrm{N} > 2\,\%$. Therefore, an extended, potential flow correction method based on the approach from Lock (1929) was developed in order to correct the open jet interference. The new method adopted Lock's application of mirror images, but additionally considered the displacement of the jet boundary by the presence of the model by using the stream function Ψ. Furthermore, an extended approach for the calculation of the induced velocity $\Delta u/u_\infty$ as an integral average over the model surface was presented. A better agreement with CFD up to a blockage ratio of $A_\mathrm{M}/A_\mathrm{N} \approx 20\,\%$ was achieved with the new method for all rear ends under investigation whereas the Lock solution was up to $\Delta C_\mathrm{D} \approx 0.010$ off. The recommendation of a particular test section design was still rather challenging as the present work did not cover the entire range of relevant parameters for a practical facility. Nevertheless, some design rules were derived from the CFD studies. The nozzle cross section A_N and the blockage ratio $A_\mathrm{M}/A_\mathrm{N}$ respectively, the longitudinal model position x_c and the test section length L_TS turned out to be the essential parameters in order confine interference effects. A blockage ratio of $A_\mathrm{M}/A_\mathrm{N} \approx 10\,\%$ with $x_\mathrm{c} = 4.8\,\mathrm{m}$ was determined to be adequate for sufficiently accurate results, e.g. $\Delta C_\mathrm{D} = \pm 0.002$, if either the correction method from Lock (1929) or the new approaches were applied. The suggested test section length was restricted to $L_\mathrm{TS} = 14.0\,\mathrm{m}$ by following the recommendation of e.g. Wickern (2014) to not exceed $L_\mathrm{TS}/D_\mathrm{N,h} = 3$ in terms of open jet stability. New facilities partially exceed a length of three hydraulic diameters, e.g. Buckisch et al. (2015), but CFD did not provide the ability to draw conclusions for this aspect. However, for a collector flap angle of $\alpha_C = 20\,^\circ$ and $\alpha_C = 30\,^\circ$ a test section length of $L_\mathrm{TS} = 14.0\,\mathrm{m}$ seemed sufficient.

6.2 Future Work

The design recommendations above are certainly connected to the restrictions of parameters under investigation. One of these parameters was the vehicle geometry defined by the DrivAer reference model. Due to the frontal area of $A_{\mathrm{M}} \approx 2.16\,\mathrm{m}^2$ the DrivAer represents a mid-size production car and, hence, the investigations did not cover higher blockage conditions of e.g. production cars with up to $A_{\mathrm{M}} \approx 3\,\mathrm{m}^2$ (or larger). Further more the model geometry used for the wind tunnel studies was rather simplified (e.g. smooth underfloor, mock-up, closed wheels) and uncertainties regarding the effect of further model details on interference effects remain. Thus, it is recommended to perform additional investigations on higher blockage conditions with detailed production cars in order to draw conclusions on the final design of a real facility, e.g. the test section length required. Furthermore, the simulations were performed for a cross-flow angle of $\beta = 0\,^\circ$. Turning a model in wind tunnel in order to create cross-flow conditions surely increase the effective blockage ratio and should be considered for a new facility.

A second geometric parameter was the nozzle design. Due to the generic shape (no converging region) some assumptions were used, especially for the determination of the dynamic pressure. Consequently, a potential contamination of the pressure taps inside the nozzle was not considered but is of crucial relevance for a real nozzle design. In addition, the nozzle cross section was rectangular and the aspect ratio remained constant with $W_{\mathrm{N}}/H_{\mathrm{N}} = 1.4$. In general, different shapes of the nozzle are possible and are recommended to be considered, e.g. $W_{\mathrm{N}}/H_{\mathrm{N}} > 1.4$ for cross-flow conditions, see e.g. Hennig and Mercker (2011). The same conclusions can be drawn for the collector, which also remained constant in its aspect ratio. The investigations on the generic collector covered a rather simple geometry. A more complex geometry is shown e.g. by Hennig (2017) including "breathers" to extend the effective test section length. A further important aspect concerning the collector is the effect of test section length on open jet stability and tunnel resonances as these effects were not considered in the present work. The maximum realizable test section length $L_{\mathrm{TS}}/D_{\mathrm{N,h}}$ for a particular nozzle dimension remains unknown.

Moving ground simulation is one of the essential techniques in modern facilities to sufficiently establish open road flow conditions in a wind tunnel. Consequently, the boundary layer treatment for nozzle exit flow is part of the moving ground simulation and was entirely not investigated in the present. Furthermore, the decision for a particular moving belt system, e.g. 5-belt or single belt, is rather challenging regarding a compromise between flow quality and measurement accuracy. Modern concepts for moving ground simulation are highly complex and part of the concept for a facility. Its integration inside the test section requires more research.

Finally, it is worth to mention, that the design of an automotive, open jet wind tunnel is always a compromise of different requirements for the particular application. Furthermore, the number of wind tunnel parameters and their combination is quasi-infinite. The present work contains results from more than 300 CFD simulations and does only cover a small amount of potential parameters.

References

Arnette, S. A., Buchanan, T. D., & Zabat, M. (1999). On Low-Frequency Pressure Pulsations and Static Pressure Distribution in Open Jet Automotive Wind Tunnels. *SAE Technical Paper 1999-01-0813*. https://doi.org/10.4271/1999-01-0813

Buckisch, R., Horonori, T., & Knoche, H. (2015). The New Daimler Automotive Wind Tunnel: Acoustic Properties and Measurement System. In J. Wiedemann (Ed.), *Progress in Vehicle Aerodynamics and Thermal Management: Proceedings of the 10th FKFS-Conference* (pp. 1–16). Expert-Verlag.

Collin, C., Indinger, T., & Mueller, J. (2017). Moving Ground Simulation for High Performance Race Cars in an Automotive Wind Tunnel. In *International Journal of Automotive Engineering* (Vol. 8; No. 1, p. 15-21). https://doi.org/10.20485/jsaeijae.8.1_15

Collin, C., Mack, S., Indinger, T., & Mueller, J. (2016). A Numerical and Experimental Evaluation of Open Jet Wind Tunnel Interferences using the DrivAer Reference Model. In *SAE Int. J. Passeng. Cars - Mech. Syst.* (Vol. 9; No. 2, pp. 657–679). https://doi.org/10.4271/2016-01-1597

Collin, C., Mueller, J., Islam, M., & Indinger, T. (2018). On the Influence of Underhood Flow on External Aerodynamics of the DrivAer Model. In J. Wiedemann (Ed.), *Progress in Vehicle Aerodynamics and Thermal Management: 11th FKFS Conference* (pp. 201–215). Cham: Springer International Publishing. https://doi.org/10.1007/978-3-319-67822-1_14

Deutenbach, K.-R. (1995). Influence of Plenum Dimensions on Drag Measurements in 3/4-Open-Jet Automotive Wind Tunnels. *SAE Technical Paper 951000*. https://doi.org/10.4271/951000

ESI-OpenCFD. (2017). *OpenFOAM User Guide.* Retrieved 2017-11-08, from `https://www.openfoam.com/`

Fage, A. (1929). On the Two-Dimensional Flow past a Body of Symmetrical Cross-Section Mounted in a Channel of Finite Breadth. *ARC, R. & M. No. 1223*.

Fage, A., Falkner, V. M., & Walker, W. (1929). Experiments on a series of symmetrical Joukowski sections. *ARC, R. & M. No. 1241*.

Fischer, O., Kuthada, T., Mercker, E., Wiedemann, J., & Duncan, B. (2010). CFD Approach to Evaluate Wind-Tunnel and Model Setup Effects on Aerodynamic Drag and Lift for Detailed Vehicles. *SAE Technical Paper 2010-01-0760*. https://doi.org/10.4271/2010-01-0760

Fischer, O., Kuthada, T., Widdecke, N., & Wiedemann, J. (2007). CFD Investigations of Wind Tunnel Interference Effects. *SAE Technical Paper 2007-01-1045*. https://doi.org/10.4271/2007-01-1045

Garner, H., Rogers, E., Acum, W., & Maskell, E. (1966). *Subsonic Wind Tunnel Wall Corrections, AGARDograph 109* (H. Garner, Ed.). North Atlantic Treaty Organization.

Garry, K. P., Cooper, K. R., Fediw, A., Wallis, S. B., & Wilsden, D. J. (1994). The Effect on Aerodynamic Drag of the Longitudinal Position of a Road Vehicle Model in a Wind Tunnel Test Section. *SAE Technical Paper 940414*. http://dx.doi.org/10.4271/940414

Glauert, H. (1928). The effect of a static pressure gradient on the drag of a body tested in a wind tunnel. *ARC, R. & M. No. 1158*.

Glauert, H. (1933). Wind Tunnel Interference on Wings, Bodies and Airscrews. *ARC, R. & M. No. 1566*.

Guertler, T. (2000). *EADE Correlation Test 1999*. Coventry: 18th EADE Meeting at Mira.

Heft, A. (2014). *Aerodynamic Investigation of the Cooling Requirements of Electric Vehicles*. Verlag Dr. Hut.

Heft, A., Indinger, T., & Adams, N. (2012). Introduction of a New Realistic Generic Car Model for Aerodynamic Investigations. *SAE Technical Paper 2012-01-0168*. https://doi.org/10.4271/2012-01-0168

Hennig, A. (2017). *Eine erweiterte Methode zur Korrektur von Interferenzeffekten in Freistrahlwindkanaelen fuer Automobile*. Springer Fachmedien.

Hennig, A., & Mercker, E. (2011). *EADE Correlation Test 2010. Final Report*. Turin: EADE Meeting at FIAT.

Hennig, A., Michelbach, A., Widdecke, N., & Wiedemann, J. (2012, 01). Optimierung der Laufbandtechnologie im 1:1-Aeroakustik-Fahrzeugwindkanal. In *ATZ - Automobiltechnische Zeitschrift* (Vol. 114, pp. 80–85). https://doi.org/10.1365/s35148-012-0254-x

Hennig, A., Widdecke, N., Kuthada, T., & Wiedemann, J. (2011). Numerical Comparison of Rolling Road Systems. In *SAE Int. J. Engines* (Vol. 4; No. 2, pp. 2659–2670). https://doi.org/10.4271/2011-37-0017

Howell, J., Sherwin, C., Passmore, M., & Le Good, G. (2002). Aerodynamic Drag of a Compact SUV as Measured On-Road and in the Wind Tunnel. *SAE Technical Paper 2002-01-0529*. https://doi.org/10.4271/2002-01-0529

Hupertz, B., Krueger, L., Chalupa, K., Lewington, N., Luneman, B., Costa, P., Kuthada, T., & Collin, C. (2018). Introduction of a New Full-Scale Open Cooling Version of the DrivAer Generic Car Model. In J. Wiedemann (Ed.), *Progress in Vehicle Aerodynamics and Thermal Management: 11th FKFS Conference* (pp. 35–60). Cham: Springer International Publishing. https://doi.org/10.1007/978-3-319-67822-1_3

Islam, M., Decker, F., de Villiers, E., Jackson, A., Gines, J., Grahs, T., Gitt-Gehrke, A., & Comas i Font, J. (2009). Application of Detached-Eddy Simulation for Automotive Aerodynamics Development. *SAE Technical Paper 2009-01-0333*. http://doi.org/10.4271/2009-01-0333

Lacey, J. (2002). A Study of the Pulsations in a 3/4 Open Jet Wind Tunnel. *SAE Technical Paper 2002-01-0251*. http://dx.doi.org/10.4271/2002-01-0251

Lawson, A. A., Dominy, R. G., Sims-Williams, D. B., & Mears, P. (2007). A Comparison Between On-Road and Wind Tunnel Surface Pressure Measurements on a Mid-

Sized Hatchback. *SAE Technical Paper 2002-01-0251*. https://doi.org/10.4271/2007-01-0898

Le Good, G. M., & Passmore, M. A. (1994). Wind Tunnel and On-Road Measurements Compared. In *SAE Conference Proceedings P* (pp. 71–80). Florence: 4th International Conference, New Design Frontiers for More Efficient, Reliable, and Ecological Vehicles.

Lock, C. (1929). The Interference of a Wind Tunnel on a Symmetrical Body. *ARC, R. & M. No. 1275*.

Mack, S., Indinger, T., Adams, N. A., & Unterlechner, P. (2012). The Ground Simulation Upgrade of the Large Wind Tunnel at the Technische Universitaet Muenchen. *SAE Technical Paper 2012-01-0299*. http://dx.doi.org/10.4271/2012-01-0299

Maskell, E. (1961). A Theory of Blockage Effects on Bluff Bodies and Stalled Wings in a Closed Wind Tunnel. *ARC, R. & M. No. 3400*.

Menter, F. R., & Kuntz, M. (2004). Adaptation of Eddy-Viscosity Turbulence Models to Unsteady Separated Flow Behind Vehicles. In R. McCallen, F. Browand, & J. Ross (Eds.), *The Aerodynamics of Heavy Vehicles: Trucks, Buses, and Trains* (pp. 339–352). Springer Verlag.

Mercker, E. (1986). A Blockage Correction for Automotive Testing in a Wind Tunnel with Closed Test Section. In *Journal of Wind Engineering and Industrial Aerodynamics* (Vol. 22; No. 2, pp. 149–167). https://doi.org/10.1016/0167-6105(86)90080-2

Mercker, E. (2013). On Buoyancy and Wake Distortion in Test Sections of Automotive Wind Tunnels. In J. Wiedemann (Ed.), *Progress in Vehicle Aerodynamics and Thermal Management: Proceedings of the 9th FKFS-Conference* (pp. 205–227). Expert Verlag.

Mercker, E., & Cooper, K. (2006). A Two-Measurement Correction for the Effects of a Pressure Gradient on Automotive Open-Jet, Wind Tunnel Measurements. *SAE Technical Paper 2006-01-0568*. https://doi.org/10.4271/2006-01-0568

Mercker, E., Cooper, K. R., Fischer, O., & Wiedemann, J. (2005). The Influence of a Horizontal Pressure Distribution on Aerodynamic Drag in Open and Closed Wind Tunnels. *SAE Technical Paper 2005-01-0867*. http://dx.doi.org/10.4271/2005-01-0867

Mercker, E., Wickern, G., & Weidemann, J. (1997). Contemplation of Nozzle Blockage in Open Jet Wind-Tunnels in View of Different Q Determination Techniques. *SAE Technical Paper 970136*. http://dx.doi.org/10.4271/970136

Mercker, E., & Wiedemann, J. (1996). On the Correction of Interference Effects in Open Jet Wind Tunnels. *SAE Technical Paper 960671*. http://dx.doi.org/10.4271/960671

Miller, D. R., & Comings, E. W. (1957). Static Pressure Distribution in the Free Turbulent Jet. In *Journal of Fluid Mechanics* (Vol. 3; No. 1, pp. 1–16). https://doi.org/10.1017/S0022112057000440

Nijhof, B. C., & Wickern, G. (2003). Reference Static and Dynamic Pressures in Automotive Wind Tunnels. *SAE Technical Paper 2003-01-0428*. http://dx.doi.org/10.4271/2003-01-0428

Ower, E., & Hutton, C. (1929). Investigation of the Boundary Layers and the Drags of Two Streamline Bodies. *ARC, R. & M. No. 1271*.

Pope, S. B. (2000). *Turbulent Flows*. University Press Cambridge. https://doi.org/10.1017/CBO9780511840531

Prandtl, L. (1919). Tragfluegeltheorie. II. Mitteilung. In *Nachrichten von der Gesellschaft der Wissenschaften zu Goettingen, Mathematisch-Physikalische Klasse* (pp. 107–137). http://eudml.org/doc/59045

Shih, T. H., Povinelli, L. A., Liu, N. S., & H., C. K. (2000). A Generalized Wall Function for Complex Turbulent Flows. *NASA TM 2000-209936*.

Shur, M. L., Spalart, P. R., Strelets, M., & Travin, A. K. (1999). Detached-Eddy Simulation of an Airfoil at High Angle of Attack. In W. Rodi & D. Laurence (Eds.), *Engineering Turbulence Modelling and Experiments* (Vol. 4, pp. 669–678). https://doi.org/10.1016/B978-008043328-8/50064-3

Spalart, P. R. (2009). Detached-Eddy Simulation. In *Annual Review of Fluid Mechanics* (Vol. 41; No. 1, pp. 181–202). https://doi.org/10.1146/annurev.fluid.010908.165130

Spalart, P. R., & Allmaras, S. R. (1992). A One-Equation Turbulence Model for Aerodynamic Flows. *30th Aerospace Sciences Meeting and Exhibit, Aerospace Sciences Meetings*. https://doi.org/10.2514/6.1992-439

Spalart, P. R., Deck, S., Shur, M. L., Squires, K. D., Strelets, M. K., & Travin, A. (2006). A New Version of Detached-eddy Simulation, Resistant to Ambiguous Grid Densities. In *Theoretical and Computational Fluid Dynamics* (Vol. 20; No. 3, pp. 181–195). https://doi.org/10.1007/s00162-006-0015-0

Spalart, P. R., Jou, W.-H., Strelets, M., & Allmaras, S. R. (1997). Comments on the Feasibility of LES for Wings and on a Hybrid RANS/LES Approach. In C. Liu & Z. Liu (Eds.), *Advances in DNS/LES* (pp. 137–147).

Technical University of Munich. (2018). *DrivAer Model*. Retrieved 2018-06-19, from `http://www.drivaer.com`

von Schulz-Hausmann, F. K., & Vagt, J.-D. (1988). Influence of Test-Section Length and Collector Area on Measurements in ¾-Open-Jet Automotive Wind Tunnels. *SAE Technical Paper 880251*. http://dx.doi.org/10.4271/880251

Waeschle, A. (2007). The Influence of Rotating Wheels on Vehicle Aerodynamics - Numerical and Experimental Investigations. *SAE Technical Paper 2007-01-0107*. https://doi.org/10.4271/2007-01-0107

Wickern, G. (2001). On the Application of Classical Wind Tunnel Corrections for Automotive Bodies. *SAE Technical Paper 2001-01-0633*. http://dx.doi.org/10.4271/2001-01-0633

Wickern, G. (2014). A Theoretical Approach towards the Self-Correcting Open Jet Wind Tunnel. *SAE Technical Paper 2014-01-0579*. http://dx.doi.org/10.4271/2014-01-0579

Wickern, G., Dietz, S., & Luehrmann, L. (2003). Gradient Effects on Drag Due to Boundary-Layer Suction in Automotive Wind Tunnels. *SAE Technical Paper 2003-01-0655*. http://dx.doi.org/10.4271/2003-01-0655

Wickern, G., & Lindener, N. (2000). The Audi Aeroacoustic Wind Tunnel: Final Design and First Operational Experience. *SAE Technical Paper 2000-01-0868*. http://dx.doi.org/10.4271/2000-01-0868

Wickern, G., & Schwartekopp, B. (2004). Correction of Nozzle Gradient Effects in Open

Jet Wind Tunnels. *SAE Technical Paper 2004-01-0669*. http://dx.doi.org/10.4271/2004-01-0669

Wiedemann, J., Wickern, G., Ewald, B., & Mattern, C. (1993). Audi Aero-Acoustic Wind Tunnel. *SAE Technical Paper 930300*.

Wittmeier, F., & Kuthada, T. (2015, 04). Open Grille DrivAer Model - First Results. In *SAE Int. J. Passeng. Cars - Mech. Syst.* (Vol. 8; No. 1, pp. 252–260). https://doi.org/10.4271/2015-01-1553

Wuest, W. (1961). Verdraengungskorrekturen fuer rechteckige Windkanaele bei verschiedenen Strahlbegrenzungen und exzentrischer Lage des Modells. In *Sonderdr. aus: Zeitschrift fuer Flugwissenschaften: 9.1961* (pp. 15–19). Goettingen: Forschungsbericht / Aerodynamische Versuchsanstalt Goettingen.

Young, A. D., & Squire, H. (1945). Blockage Corrections in a Closed Rectangular Tunnel. *ARC, R. & M. No. 1984*.

Zaccariotto, M. M. (1991). Correlation of Full-Scale Wind Tunnel and Road Measurements of Aerodynamic Forces. *Societe des Ingenieurs de l'Automobile*.

Nomenclature

Symbols

Latin

a	m	Distance between holes for perforated sheets
A^*	m	Cross-sectional area of the nozzle (jet deflection)
A_o	m^2	Open cross-sectional area (perforated sheets)
A_c	m^2	Closed cross-sectional area (perforated sheets)
A_C	m^2	Cross-sectional area of the collector
$A_\mathrm{C,in}$	m^2	Cross-sectional area of the collector inlet
$A_\mathrm{C,out}$	m^2	Cross-sectional area of the collector outlet
$A_\mathrm{jet,\infty}$	m^2	Cross-sectional area of expanded, open jet (Wickern)
A_M	m^2	Frontal area of the model
$A_\mathrm{M,D}$	m^2	Duplex frontal area of the model
$A_\mathrm{M,eff}$	m^2	Effective frontal area of the model from model volume
A_N	m^2	Cross-sectional area of the nozzle
$A_\mathrm{N,0}$	m^2	Cross-sectional area of the undisturbed jet
$A_\mathrm{N,D}$	m^2	Duplex cross-sectional area of the nozzle
$A_\mathrm{N,e}$	m^2	Cross-sectional area of the expanded jet
A_SC	m^2	Cross-sectional area of the settling chamber
c	m	Half-distance between source and sink
C_1	–	Linear Darcy-Forchheimer coefficient
C_2	–	Quadratic Darcy-Forchheimer coefficient
c_p	–	Static pressure coefficient (Mercker-Wiedemann)
$c_\mathrm{p,Mb}$	–	Static pressure coefficient at model front base (Mercker-Wiedemann)
$c_\mathrm{p,Wc}$	–	Static pressure coefficient at wake closure (Mercker-Wiedemann)
c_p	–	Static pressure coefficient
C_D	–	Aerodynamic drag coefficient
C_DES	–	Model constant for DES
$C_\mathrm{D,c}$	–	Corrected aerodynamic drag coefficient
$C_\mathrm{D,ref}$	–	Reference aerodynamic drag coefficient
C_L	–	Aerodynamic lift coefficient
$C_\mathrm{L,f}$	–	Aerodynamic front lift coefficient
$C_\mathrm{L,r}$	–	Aerodynamic rear lift coefficient
C_p	–	Static pressure coefficient

$C_{\mathrm{p,SC}}$	$-$	Static pressure coefficient in the settling chamber
d	m	Diameter of holes for perforated sheets
d	m	Distance to closest wall
D	m^2	Linear porous media coefficient
$D_{\mathrm{N,h}}$	m	Hydraulic diameter of the nozzle
$\tilde{d}$	m	Distance to closest wall (SA-model)
F	m	Quadratic porous media coefficient
F	$\mathrm{kg\,m/s^2}$	Aerodynamic force
f_{d}	$-$	Shielding function for DDES
f_{v1}	$-$	Factor for SA turbulence model
F_{x}	$\mathrm{kg\,m/s^2}$	Aerodynamic force in x-direction
F_{y}	$\mathrm{kg\,m/s^2}$	Aerodynamic force in y-direction
F_{z}	$\mathrm{kg\,m/s^2}$	Aerodynamic force in z-direction
G	$-$	Glauert factor
H	m	Height
H_0	m	Geometric parameter for perforated sheets
H_{C}	m	Collector height
$H_{\mathrm{C,in}}$	m	Collector height at inlet
$H_{\mathrm{C,out}}$	m	Collector height at outlet
H_{M}	m	Model height
H_{N}	m	Nozzle height
$H_{\mathrm{N,0}}$	m	Height of the undisturbed jet
$H_{\mathrm{N,D}}$	m	Duplex nozzle height
$H_{\mathrm{N,e}}$	m	Height of the expanded jet
H_{WDU}	m	Height of wheel drive unit
k	$-$	Wake factor
l	m	Length
L_{B}	m	Moving belt length
$L_{\mathrm{B,f}}$	m	Moving belt length front
$L_{\mathrm{B,r}}$	m	Moving belt length rear
L_{M}	m	Model length
$l_{\mathrm{M,r,C}}$	m	Length from model rear end to collector inlet
$L_{\mathrm{M,f}}$	m	Length from front end to the center of the model
$L_{\mathrm{M,r}}$	m	Length from rear end to the center of the model
$l_{\mathrm{N,M,f}}$	m	Length from nozzle to the model front end
L_{T}	m	Total length (model + wake)
L_{TS}	m	Test section length
$L_{\mathrm{TS,eff}}$	m	Effective test section length
L_{turb}	m	Turbulence length scale
L_{W}	m	Wake length
$l_{\mathrm{W,C}}$	m	Length from wake closure to collector
m	$-$	Index of mirror image (potential flow)
M	$\mathrm{m^4/s}$	Dipole moment in potential flow (3D)
n	$-$	Index of mirror image (potential flow)
N	$-$	Number of holes of perforated sheets

p	$^{kg}/_{m\,s^2}$	Relative, static pressure
p_∞	$^{kg}/_{m\,s^2}$	Relative, static pressure of undisturbed flow
p_{dyn}	$^{kg}/_{m\,s^2}$	Dynamic pressure in wind tunnel conditions
$p_{dyn,c}$	$^{kg}/_{m\,s^2}$	Corrected dynamic pressure in wind tunnel conditions
$p_{dyn,N}$	$^{kg}/_{m\,s^2}$	Dynamic pressure at the nozzle inlet
$p_{dyn,NM}$	$^{kg}/_{m\,s^2}$	Dynamic pressure for nozzle method
$p_{dyn,PM}$	$^{kg}/_{m\,s^2}$	Dynamic pressure for plenum method
$p_{dyn,ref}$	$^{kg}/_{m\,s^2}$	Dynamic pressure at reference point for tunnel calibration
$p_{dyn,SC,ref}$	$^{kg}/_{m\,s^2}$	Dynamic pressure in settling chamber at reference conditions
p_N	$^{kg}/_{m\,s^2}$	Static pressure at the nozzle inlet
P_{ref}	$-$	Reference point
p_{SC}	$^{kg}/_{m\,s^2}$	Static pressure in the settling chamber
Q	$^{m^3}/_{s}$	Source or sink strength in potential flow (3D)
r	m	Coordinate in radial direction
r_d	$-$	Function for DDES
$r_{m,n}$	m	r-coordinate of 3D mirror image
R_M	m	Model Radius
R_n	m	Radius (Mercker-Wiedemann)
R_N	m	Nozzle radius (Mercker-Wiedemann)
R_C	m	Collector radius (Mercker-Wiedemann)
Re	$-$	Reynolds number
R_{TT}	m	Radius of the turntable
t	m	Thickness
t	m	Time
T_U	$-$	Turbulence intensity
$\bar{u}$	$^{m}/_{s}$	Average flow velocity
u	$^{m}/_{s}$	Flow velocity
u^*	$^{m}/_{s}$	Flow velocity (jet deflection)
u_∞	$^{m}/_{s}$	Flow velocity of on-coming flow undisturbed by the model
u_c	$^{m}/_{s}$	Corrected flow velocity in wind tunnel conditions
u_{eff}	$^{m}/_{s}$	Effective, local flow velocity in wind tunnel conditions
u_N	$^{m}/_{s}$	Flow velocity at the nozzle inlet
u_{NM}	$^{m}/_{s}$	Flow velocity for nozzle method
u_{PM}	$^{m}/_{s}$	Flow velocity for plenum method
u_r	$^{m}/_{s}$	Velocity component in r-direction
$u_{r,c}$	$^{m}/_{s}$	Corrected velocity component in r-direction
u_{Real}	$^{m}/_{s}$	Flow velocity in real, infinite conditions
u_{Real}	$^{m}/_{s}$	Reference flow velocity
u_{SC}	$^{m}/_{s}$	Flow velocity in the settling chamber
u_{WT}	$^{m}/_{s}$	Flow velocity under wind tunnel constraint
u_x	$^{m}/_{s}$	Velocity component in x-direction
$u_{x,c}$	$^{m}/_{s}$	Corrected velocity component in x-direction
u_y	$^{m}/_{s}$	Velocity component in y-direction
u_z	$^{m}/_{s}$	Velocity component in z-direction
V_{eff}	m^3	Effective model volume (Mercker-Wiedemann)

V_{M}	m^3	Model volume
$V_{\mathrm{M,real}}$	m^3	Real model volume
$V_{\mathrm{M,virtual}}$	m^3	Virtual model volume
V_{T}	m^3	Total volume (model + wake)
W	m	Width
W_0	m	Geometric parameter for perforated sheets
W_{B}	m	Moving belt width
W_{C}	m	Collector width
$W_{\mathrm{C,in}}$	m	Collector width at inlet
$W_{\mathrm{C,out}}$	m	Collector width at outlet
W_{M}	m	Model width
W_{N}	m	Nozzle width
$W_{\mathrm{N,0}}$	m	Width of the undisturbed jet
$W_{\mathrm{N,D}}$	m	Duplex nozzle width
$W_{\mathrm{N,e}}$	m	Width of the expanded jet
W_{WDU}	m	Width of wheel drive unit
x	m	Cartesian coordinate in stream-wise direction
x_{c}	m	Distance between nozzle exit model center
x_{coll}	m	Distance between model center and collector
x_{fb}	m	x-coordinate of model front base
$x_{\mathrm{M,c}}$	m	Distance between nozzle exit and model center (Mercker-Wiedemann)
$x_{\mathrm{M,f}}$	m	Distance between nozzle exit and model front end
$x_{\mathrm{m,n}}$	m	x-coordinate of 3D mirror image
x_{ref}	m	x-coordinate of reference point
x_{s}	m	Distance to source or sink
y	m	Cartesian coordinate in lateral, horizontal direction
y_{n}	m	y-coordinate of mirror image (potential flow)
y^+	m	Non-dimensional wall distance
y_{ref}	m	y-coordinate of reference point
z	m	Cartesian coordinate in lateral, vertical direction
z_{m}	m	z-coordinate of mirror image (potential flow)
z_{ref}	m	z-coordinate of reference point

Greek

α	$^\circ$	Angle of attack
α_C	$^\circ$	Collector flap angle
$\alpha_\mathrm{u,z}$	$^\circ$	Vertical flow angle
θ	$^\circ$	Cross-flow angle
Γ	$\mathrm{m^2/s}$	Circulation
Γ_NM	$\mathrm{m^2/s}$	Circulation for nozzle method
Γ_PM	$\mathrm{m^2/s}$	Circulation for plenum method
Γ	$\mathrm{m^2/s}$	Circulation
Δ	m	Grid spacing filter
$\Delta C_\mathrm{D,Av}$	$-$	Backward average of drag coefficient
$\Delta C_\mathrm{D,c}$	$-$	Cooling drag coefficient
$\Delta C_\mathrm{D,max}$	$-$	Maximum induced drag coefficient
$\Delta C_\mathrm{D,HB}$	$-$	Induced drag by horizontal buoyancy
$\Delta C_\mathrm{L,c}$	$-$	Cooling lift coefficient
$\Delta C_\mathrm{L,f,c}$	$-$	Cooling front lift coefficient
$\Delta C_\mathrm{L,f,max}$	$-$	Maximum induced front lift coefficient
$\Delta C_\mathrm{L,max}$	$-$	Maximum induced lift coefficient
$\Delta C_\mathrm{L,r,c}$	$-$	Cooling rear lift coefficient
$\Delta C_\mathrm{L,r,max}$	$-$	Maximum induced rear lift coefficient
$\Delta C_\mathrm{D,W}$	$-$	Induced drag by wake interference (Mercker-Wiedemann)
$\Delta C_\mathrm{L,Av}$	$-$	Backward average of lift coefficient
Δx	m	Grid length in x-direction
Δy	m	Grid length in y-direction
Δz	m	Grid length in z-direction
Δp_NM	$\mathrm{kg/m\,s^2}$	Reference pressure drop for nozzle method
Δp_PM	$\mathrm{kg/m\,s^2}$	Reference pressure drop for plenum method
Δt	s	Time step
Δu	$\mathrm{m/s}$	Induced velocity by wind tunnel interference
Δu_x	$\mathrm{m/s}$	Induced x-velocity by wind tunnel interference
ε_c	$-$	Blockage factor collector
ε_NM	$-$	Blockage factor nozzle method
ε_PM	$-$	Blockage factor plenum method
$\varepsilon_\mathrm{q,NM}$	$-$	Blockage factor dynamic pressure (nozzle method)
$\varepsilon_\mathrm{q,PM}$	$-$	Blockage factor dynamic pressure (plenum method)
ε_s	$-$	Blockage factor jet expansion
ε_w	$-$	Blockage factor wake
θ	$^\circ$	Angle (polar coordinate)
κ	$-$	von Kármán constant
λ	$-$	Model shape factor
μ	$\mathrm{kg/m\ s}$	Dynamic viscosity
ν	$\mathrm{m^2/s}$	Kinematic viscosity
$\tilde{\nu}$	$\mathrm{m^2/s}$	Turbulent viscosity (SA-model)
ν_SGS	$\mathrm{m^2/s}$	Turbulent viscosity (SGS-model)

ν_t	$\mathrm{m^2/s}$	Turbulent viscosity
ϱ	$\mathrm{kg/m^3}$	Density
τ	$-$	Tunnel shape factor
τ_2	$-$	Tunnel shape factor for nozzle blockage
$\tau_{2,\mathrm{NM}}$	$-$	Tunnel shape factor for nozzle blockage (nozzle method)
$\tau_{2,\mathrm{PM}}$	$-$	Tunnel shape factor for nozzle blockage (plenum method)
τ_NG	$-$	Tunnel shape factor for nozzle gradient
ϕ	$^\circ$	Angle (polar coordinate)
Φ	$\mathrm{m^2/s}$	Potential function in potential flow (3D)
χ_y	$-$	Tunnel summation factor for y-component
χ_z	$-$	Tunnel summation factor for z-component
Ψ	$\mathrm{m^3/s}$	Stream function in potential flow (3D)
Ψ_c	$\mathrm{m^3/s}$	Corrected stream function (without wind tunnel interference)
Ψ_r	$\mathrm{m^3/s}$	r-component of vectorial stream function
Ψ_y	$\mathrm{m^3/s}$	y-component of vectorial stream function
Ψ_z	$\mathrm{m^3/s}$	z-component of vectorial stream function

Abbreviations

AAWK	Audi Aeroacoustic Wind Tunnel
CFD	Computational Fluid Dynamics
CFL	Courant-Friedrichs-Lewy
DDES	Delayed Detached-Eddy Simulation
DES	Detached-Eddy Simulation
DNS	Direct Numerical Simulation
DrivAer	Automotive, aerodynamic reference model
EADE	European Aerodynamic Data Exchange
EB	Estate Back
Exp.	Experiment
FB	Fastback
FKFS	Forschungsinstitut für Kraftfahrwesen und Fahrzeugmotoren Stuttgart
FWT	Finite Wind Tunnel
GS	Grid Scale
HIWT	Half-Infinite Wind Tunnel
LES	Large Eddy Simulation
LUST	Linear-Upwind Stabilized Transport
NB	Notchback
NM	Nozzle Method
OR	Open Road
PISO	Pressure-Implicit with Splitting of Operators
PM	Plenum Method
RANS	Reynolds-averaged Navier Stokes Equations
SGS	Sub-Grid Scale
SA	Spalart-Allmaras
SC	Settling Chamber
TS	Test Section
TUM	Technical University of Munich
WDU	Wheel Drive Unit
WT	Wind Tunnel
WTA	Wind Tunnel A (= large model wind tunnel) of TUM

List of Figures

List of Tables

Appendix

A.1 Methods to Correct Open Jet Wind Tunnel Interferences

A.1.1 Nozzle Interferences

The Method of Mercker et al.

$$\frac{u_{\mathrm{x}}(x,r)}{u_\infty} = 1 + \frac{A_{\mathrm{M}}}{4\pi}\frac{x}{\left(x^2+r^2\right)^{3/2}} \tag{A.1}$$

$$\frac{u_{\mathrm{NM}}}{u_\infty} = \frac{1}{A_{\mathrm{N}}}\int_0^{A_{\mathrm{N}}}\frac{u_{\mathrm{x}}(x=-x_{\mathrm{s}},r)}{u_\infty}\,\mathrm{d}A = \frac{1}{A_{\mathrm{N}}}\int_0^{2\pi}\int_0^{R_{\mathrm{N}}}\frac{u_{\mathrm{x}}(x=-x_{\mathrm{s}},r)}{u_\infty}r\,\mathrm{d}r\,\mathrm{d}\phi \tag{A.2}$$

$$\frac{u_{\mathrm{NM}}}{u_\infty} = \frac{1}{A_{\mathrm{N}}}\int_0^{2\pi}\int_0^{R_{\mathrm{N}}} r - \frac{A_{\mathrm{M}}}{4\pi}\frac{r x_{\mathrm{s}}}{\left(x_{\mathrm{s}}^2+r^2\right)^{3/2}}\,\mathrm{d}r\,\mathrm{d}\phi \tag{A.3}$$

$$\frac{u_{\mathrm{NM}}}{u_\infty} = \frac{1}{A_{\mathrm{N}}}\int_0^{2\pi}\left[\int_0^{R_{\mathrm{N}}} r\,\mathrm{d}r - \frac{A_{\mathrm{M}}x_{\mathrm{s}}}{4\pi}\int_0^{R_{\mathrm{N}}}\frac{r}{\left(x_{\mathrm{s}}^2+r^2\right)^{3/2}}\,\mathrm{d}r\right]\mathrm{d}\phi \tag{A.4}$$

$$\int_0^{R_{\mathrm{N}}} f_1(r)\,\mathrm{d}r = \int_0^{R_{\mathrm{N}}} r\,\mathrm{d}r = \frac{1}{2}\left[r^2\right]_0^{R_{\mathrm{N}}} = \frac{1}{2}\left[R_{\mathrm{N}}^2 - 0^2\right] = \frac{1}{2}R_{\mathrm{N}}^2 \tag{A.5}$$

$$\int_0^{R_{\mathrm{N}}} f_2(r)\,\mathrm{d}r = \int_0^{R_{\mathrm{N}}}\frac{r}{\left(x_{\mathrm{s}}^2+r^2\right)^{3/2}}\,\mathrm{d}r = \frac{1}{2}\int_0^{R_{\mathrm{N}}}\frac{2r}{\left(x_{\mathrm{s}}^2+r^2\right)^{3/2}}\,\mathrm{d}r \tag{A.6}$$

$$u(r) = x_\mathrm{s}^2 + r^2, \qquad \frac{\mathrm{d}u}{\mathrm{d}r} = u' = 2r \tag{A.7}$$

$$\int_0^{R_\mathrm{N}} f_2(r)\,\mathrm{d}r = \frac{1}{2}\int_0^{R_\mathrm{N}} \frac{u'}{u^{3/2}}\,\mathrm{d}r = \frac{1}{2}\int_0^{R_\mathrm{N}} \frac{1}{u^{3/2}}\,\mathrm{d}r = \left[-\frac{1}{u^{1/2}}\right]_0^{R_\mathrm{N}} \tag{A.8}$$

$$\int_0^{R_\mathrm{N}} f_2(r)\,\mathrm{d}r = \left[-\frac{1}{\left(x_\mathrm{s}^2 + r^2\right)^{1/2}}\right]_0^{R_\mathrm{N}} = \left[\frac{1}{|x_\mathrm{s}|} - \frac{1}{\left(x_\mathrm{s}^2 + R_\mathrm{N}^2\right)^{1/2}}\right] \tag{A.9}$$

$$\frac{u_\mathrm{NM}}{u_\infty} = \frac{1}{A_\mathrm{N}}\int_0^{2\pi}\left[\frac{1}{2}R_\mathrm{N}^2 - \frac{A_\mathrm{M}x_\mathrm{s}}{4\pi}\left(\frac{1}{|x_\mathrm{s}|} - \frac{1}{\left(x_\mathrm{s}^2 + R_\mathrm{N}^2\right)^{1/2}}\right)\right]\mathrm{d}\phi \tag{A.10}$$

$$\frac{u_\mathrm{NM}}{u_\infty} = \frac{2\pi}{A_\mathrm{N}}\left[\frac{1}{2}R_\mathrm{N}^2 - \frac{A_\mathrm{M}x_\mathrm{s}}{4\pi}\left(\frac{1}{|x_\mathrm{s}|} - \frac{1}{\left(x_\mathrm{s}^2 + R_\mathrm{N}^2\right)^{1/2}}\right)\right] \tag{A.11}$$

$$\frac{u_\mathrm{NM}}{u_\infty} = \frac{2\pi}{A_\mathrm{N}}\left[\frac{1}{2}R_\mathrm{N}^2 - \frac{A_\mathrm{M}}{4\pi}\left(1 - \frac{x_\mathrm{s}}{\left(x_\mathrm{s}^2 + R_\mathrm{N}^2\right)^{1/2}}\right)\right] \tag{A.12}$$

$$\frac{u_\mathrm{NM}}{u_\infty} = \frac{\pi R_\mathrm{N}^2}{A_\mathrm{N}} - \frac{A_\mathrm{M}}{2A_\mathrm{N}}\left(1 - \frac{x_\mathrm{s}}{\left(x_\mathrm{s}^2 + R_\mathrm{N}^2\right)^{1/2}}\right) \quad \text{with:} \quad A_\mathrm{N} = \pi R_\mathrm{N}^2 \tag{A.13}$$

$$\frac{u_\mathrm{NM}}{u_\infty} = 1 - \frac{A_\mathrm{M}}{2A_\mathrm{N}}\left(1 - \frac{x_\mathrm{s}}{\left(x_\mathrm{s}^2 + R_\mathrm{N}^2\right)^{1/2}}\right) \tag{A.14}$$

The Method of Wickern et al.

The axial velocity component for the flow around a doublet is given by the substitution of Q in eq. (2.15) on page 12 with eq. (2.21):

$$\frac{u_{\mathrm{x}}(x,y,z)}{u_\infty} = \frac{1}{4}t^3\left(\left(\frac{c}{t}\right)^2+1\right)^{1/2}\left[\frac{x+c}{\left((x+c)^2+y^2+z^2\right)^{3/2}} - \frac{x-c}{\left((x-c)^2+y^2+z^2\right)^{3/2}}\right]+1 \tag{A.15}$$

Thus the induced velocity at the location (x,y,z) is calculated from the mirror images:

$$\begin{aligned}\frac{\Delta u}{u_\infty} = \frac{\Delta u_{\mathrm{x}}(x,y,z)}{u_\infty} = \frac{1}{4\pi^{3/2}}&\left(\left(\frac{c}{t}\right)^2+1\right)^{1/2}\left(\frac{H_{\mathrm{N}}}{W_{\mathrm{N}}}\right)^{3/2}\left(\frac{A_{\mathrm{M}}}{A_{\mathrm{N}}}\right)^{3/2}\cdot\\ &\left[\sum_{m=-\infty}^{\infty}\sum_{n=-\infty}^{\infty}(-1)^{m+n}\frac{\frac{x+c}{W_{\mathrm{N}}}}{\left(\left(\frac{x+c}{W_{\mathrm{N}}}\right)^2+\left(\frac{y}{W_{\mathrm{N}}}-m\right)^2+\left(\frac{z}{W_{\mathrm{N}}}-n\frac{H_{\mathrm{N}}}{W_{\mathrm{N}}}\right)^2\right)^{3/2}}\right]-\\ &\left[\sum_{m=-\infty}^{\infty}\sum_{n=-\infty}^{\infty}(-1)^{m+n}\frac{\frac{x-c}{W_{\mathrm{N}}}}{\left(\left(\frac{x-c}{W_{\mathrm{N}}}\right)^2+\left(\frac{y}{W_{\mathrm{N}}}-m\right)^2+\left(\frac{z}{W_{\mathrm{N}}}-n\frac{H_{\mathrm{N}}}{W_{\mathrm{N}}}\right)^2\right)^{3/2}}\right]\end{aligned} \tag{A.16}$$

The tunnel shape factor $\tau_{2,\mathrm{NM}}$ is then:

$$\begin{aligned}\tau_{2,\mathrm{NM}}(x_{\mathrm{c}}) = \frac{1}{4\pi^{3/2}}&\left(\frac{H_{\mathrm{N}}}{W_{\mathrm{N}}}\right)^{3/2}\cdot\\ &\int_{A_{\mathrm{N}}}\left[\sum_{m=-\infty}^{\infty}\sum_{n=-\infty}^{\infty}(-1)^{m+n}\frac{\frac{x_{\mathrm{c}}+c}{W_{\mathrm{N}}}}{\left(\left(\frac{x_{\mathrm{c}}+c}{W_{\mathrm{N}}}\right)^2+\left(\frac{y}{W_{\mathrm{N}}}-m\right)^2+\left(\frac{z}{W_{\mathrm{N}}}-n\frac{H_{\mathrm{N}}}{W_{\mathrm{N}}}\right)^2\right)^{3/2}}\right]\frac{\mathrm{d}A}{A_{\mathrm{N}}}-\\ &\int_{A_{\mathrm{N}}}\left[\sum_{m=-\infty}^{\infty}\sum_{n=-\infty}^{\infty}(-1)^{m+n}\frac{\frac{x_{\mathrm{c}}-c}{W_{\mathrm{N}}}}{\left(\left(\frac{x_{\mathrm{c}}-c}{W_{\mathrm{N}}}\right)^2+\left(\frac{y}{W_{\mathrm{N}}}-m\right)^2+\left(\frac{z}{W_{\mathrm{N}}}-n\frac{H_{\mathrm{N}}}{W_{\mathrm{N}}}\right)^2\right)^{3/2}}\right]\frac{\mathrm{d}A}{A_{\mathrm{N}}}\end{aligned} \tag{A.17}$$

A.2 Experimental Data

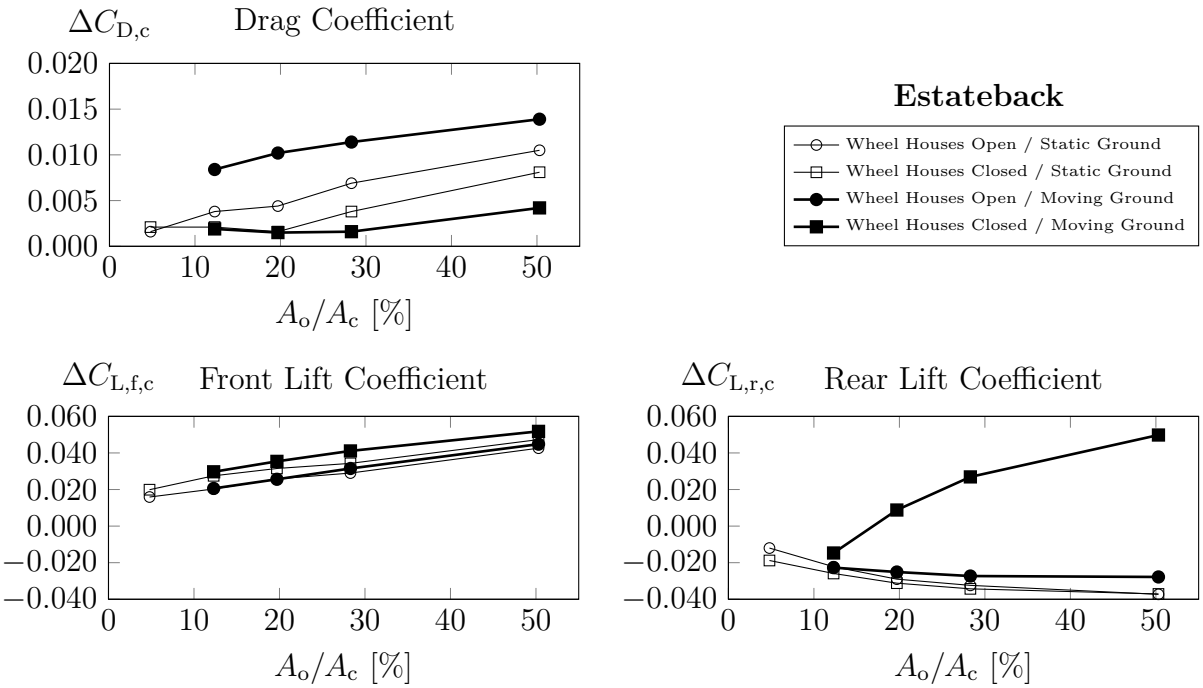

Figure A.1: DrivAer with estateback: Effects of underhood flow on aerodynamic force coefficients for drag $\Delta C_{\mathrm{D,c}}$, front lift $\Delta C_{\mathrm{L,f,c}}$ and rear lift $\Delta C_{\mathrm{L,r,c}}$ as presented by Collin et al. (2018). $A_\mathrm{o}/A_\mathrm{c}$ denotes the openness ratio of the perforated sheets.

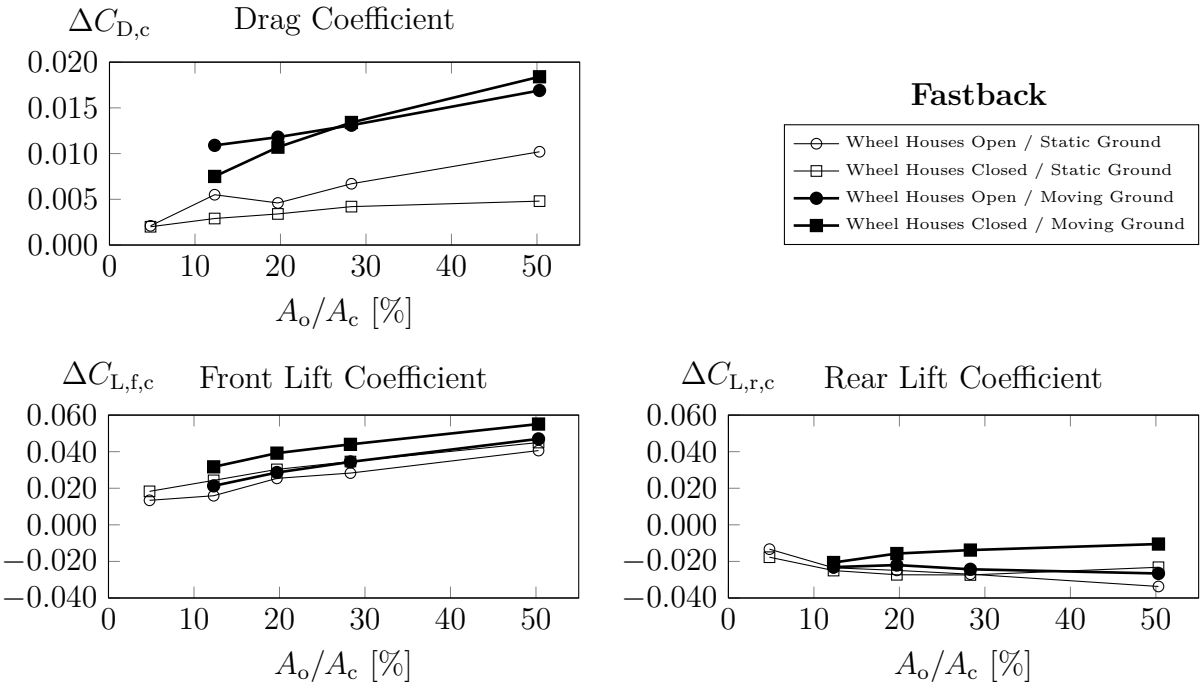

Figure A.2: DrivAer with fastback: Effects of underhood flow on aerodynamic force coefficients for drag $\Delta C_{\mathrm{D,c}}$, front lift $\Delta C_{\mathrm{L,f,c}}$ and rear lift $\Delta C_{\mathrm{L,r,c}}$ as presented by Collin et al. (2018). $A_{\mathrm{o}}/A_{\mathrm{c}}$ denotes the openness ratio of the perforated sheets.

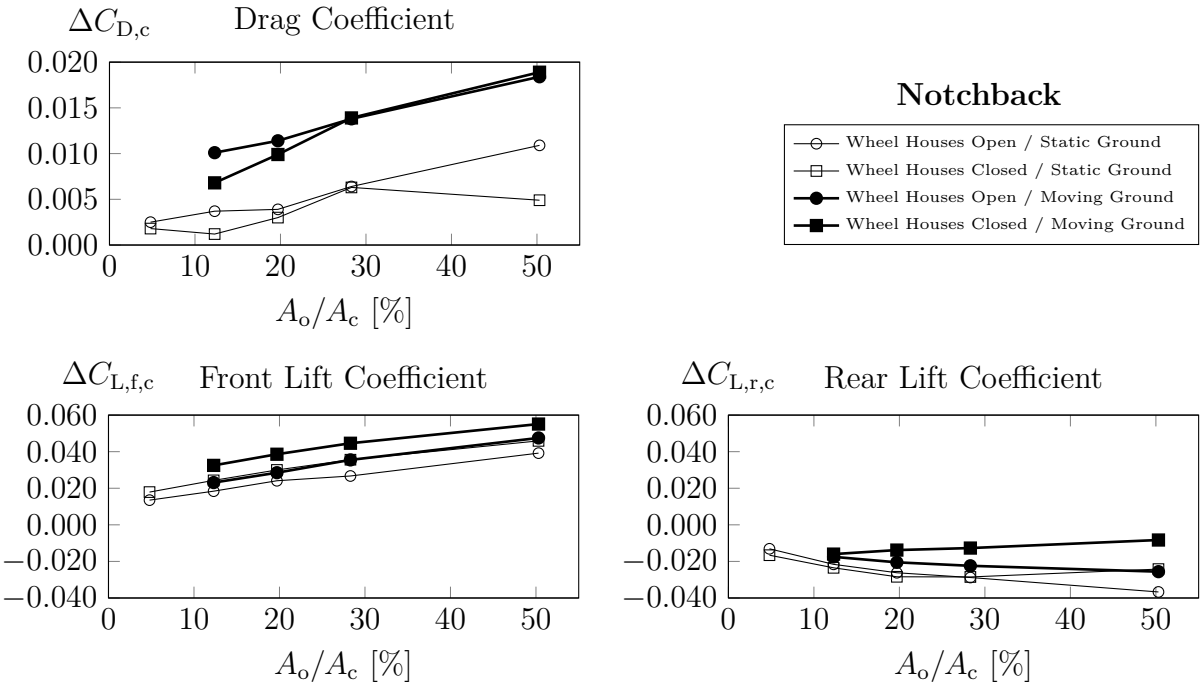

Figure A.3: DrivAer with notchback: Effects of underhood flow on aerodynamic force coefficients for drag $\Delta C_{\mathrm{D,c}}$, front lift $\Delta C_{\mathrm{L,f,c}}$ and rear lift $\Delta C_{\mathrm{L,r,c}}$ as presented by Collin et al. (2018). $A_{\mathrm{o}}/A_{\mathrm{c}}$ denotes the openness ratio of the perforated sheets.

A.3 CFD Simulations

A.3.1 Grid Study

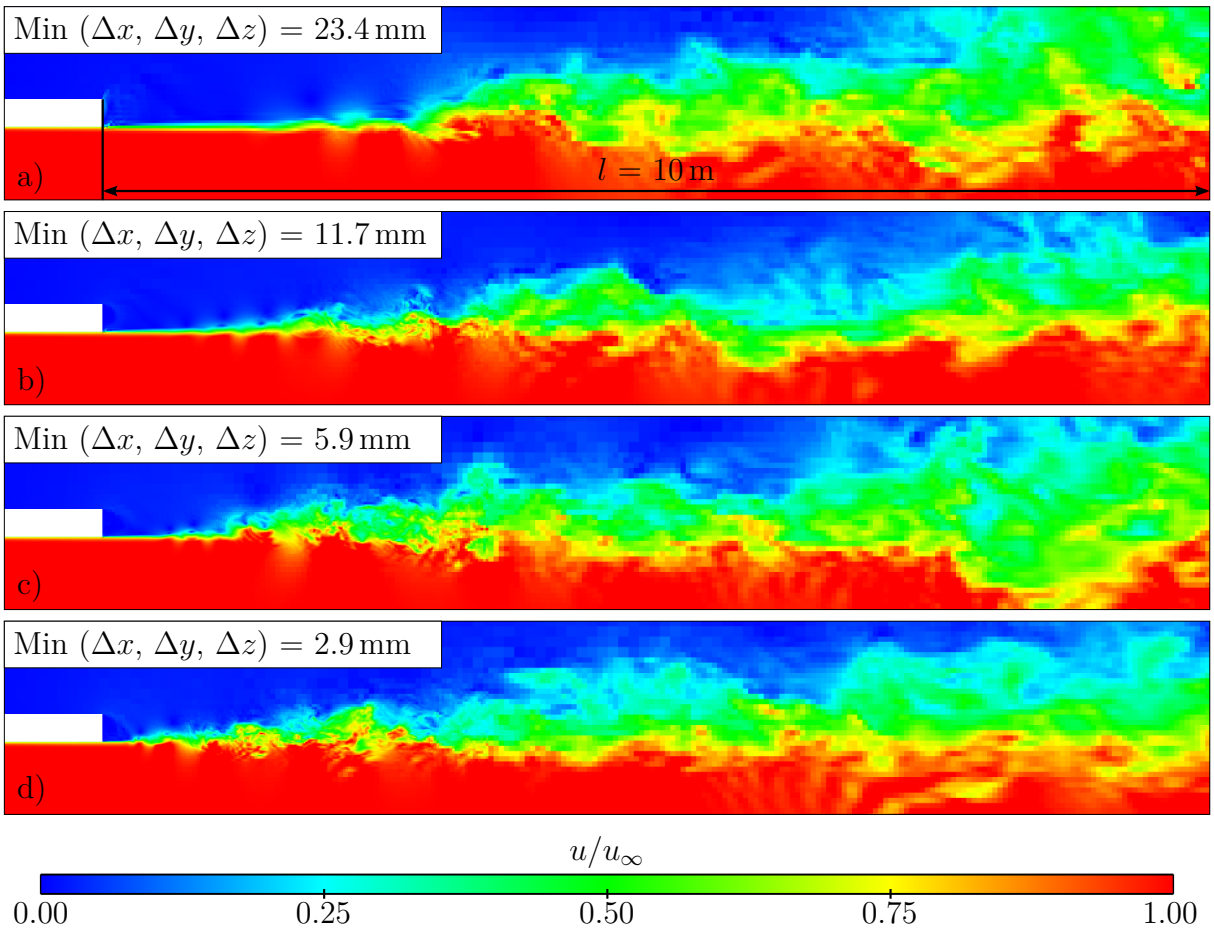

Figure A.4: Unsteady velocity field u/u_∞ for different grid resolutions Δx, Δy, Δz within the free shear layer downstream a nozzle with 11 m^2: a) 23.4 mm; b) 11.7 mm; c) 5.9 mm; d) 2.9 mm.

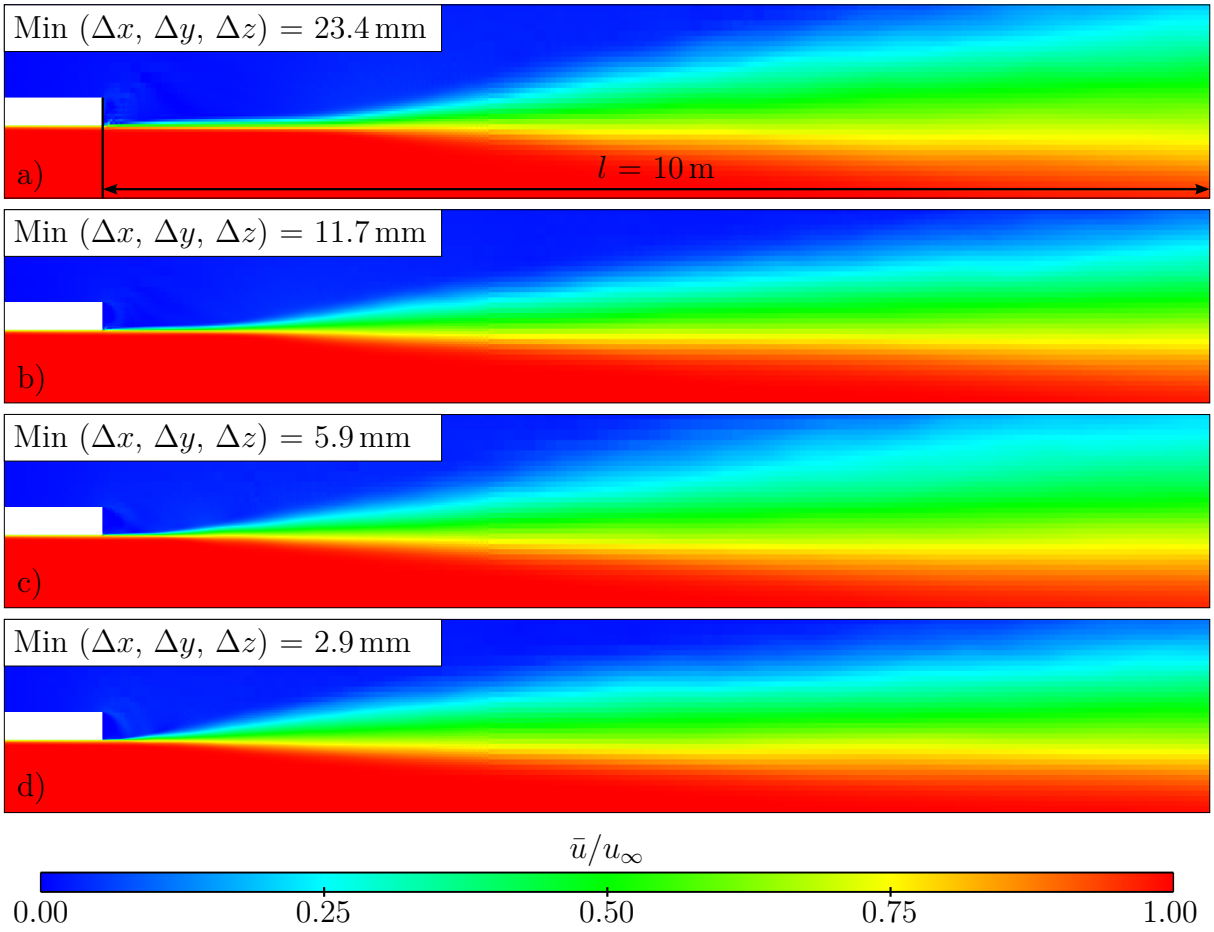

Figure A.5: Average velocity field u/u_∞ for different grid resolutions Δx, Δy, Δz within the free shear layer downstream a nozzle with $11\,\mathrm{m}^2$: a) 23.4 mm; b) 11.7 mm; c) 5.9 mm; d) 2.9 mm.

A.3.2 Nozzle and Open Jet Interferences

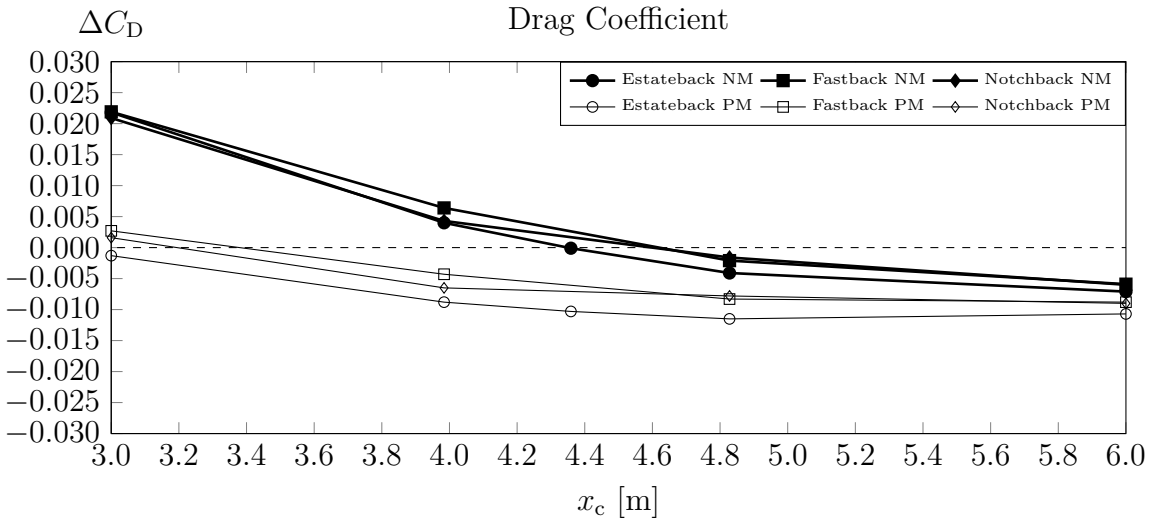

Figure A.6: Drag coefficients ΔC_D for the DrivAer referring to open road conditions. The curves represent different rear end shapes for a nozzle with $A_N = 22.4\,m^2$ and $A_M/A_N = 9.7\,\%$.

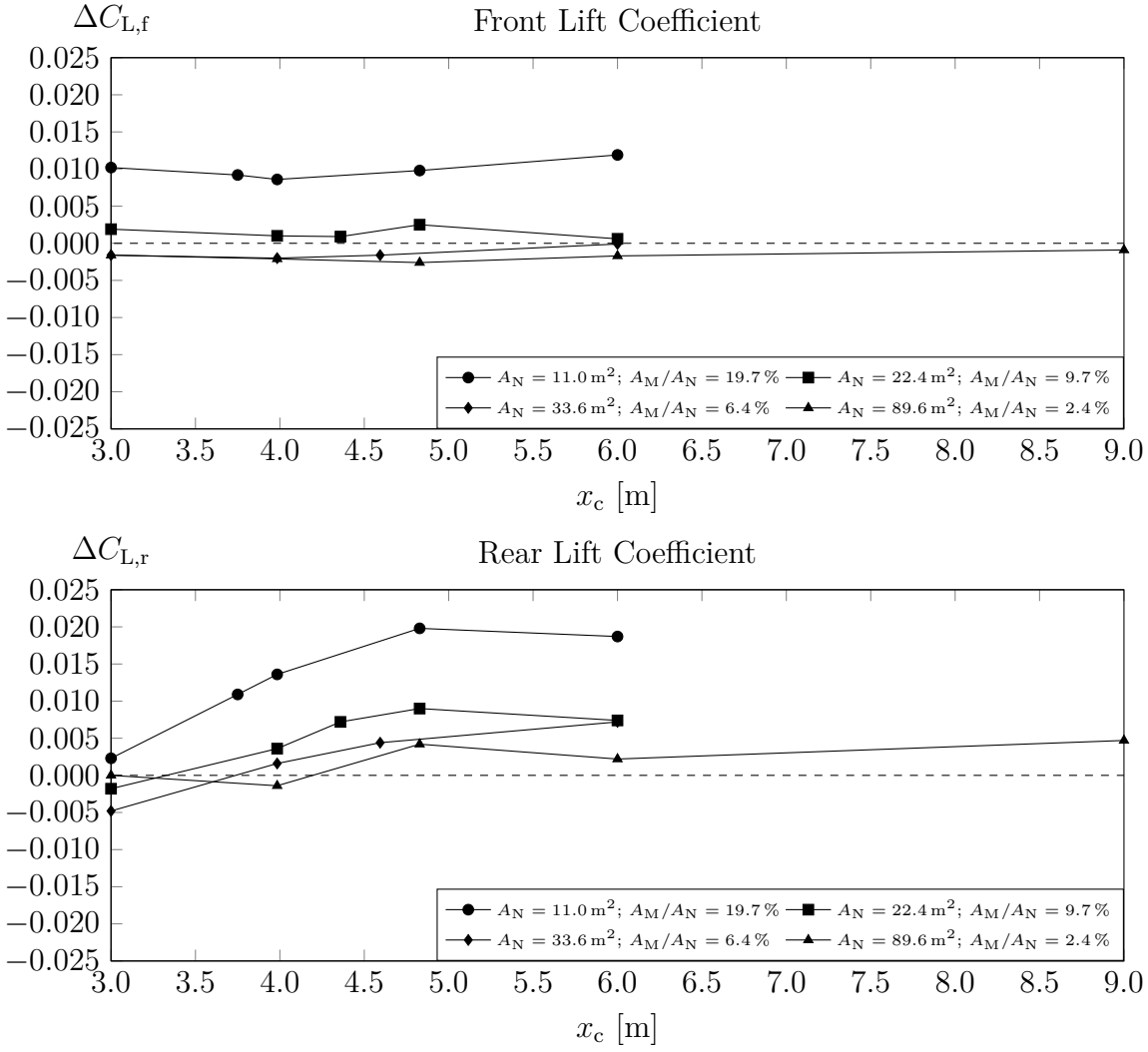

Figure A.7: Nozzle method: Lift coefficients $\Delta C_{\mathrm{L,f}}$ and $\Delta C_{\mathrm{L,r}}$ for the DrivAer estateback referring to open road conditions. The curves represent dependency on the longitudinal model position x_{c} for different blockage ratios $A_{\mathrm{M}}/A_{\mathrm{N}}$.

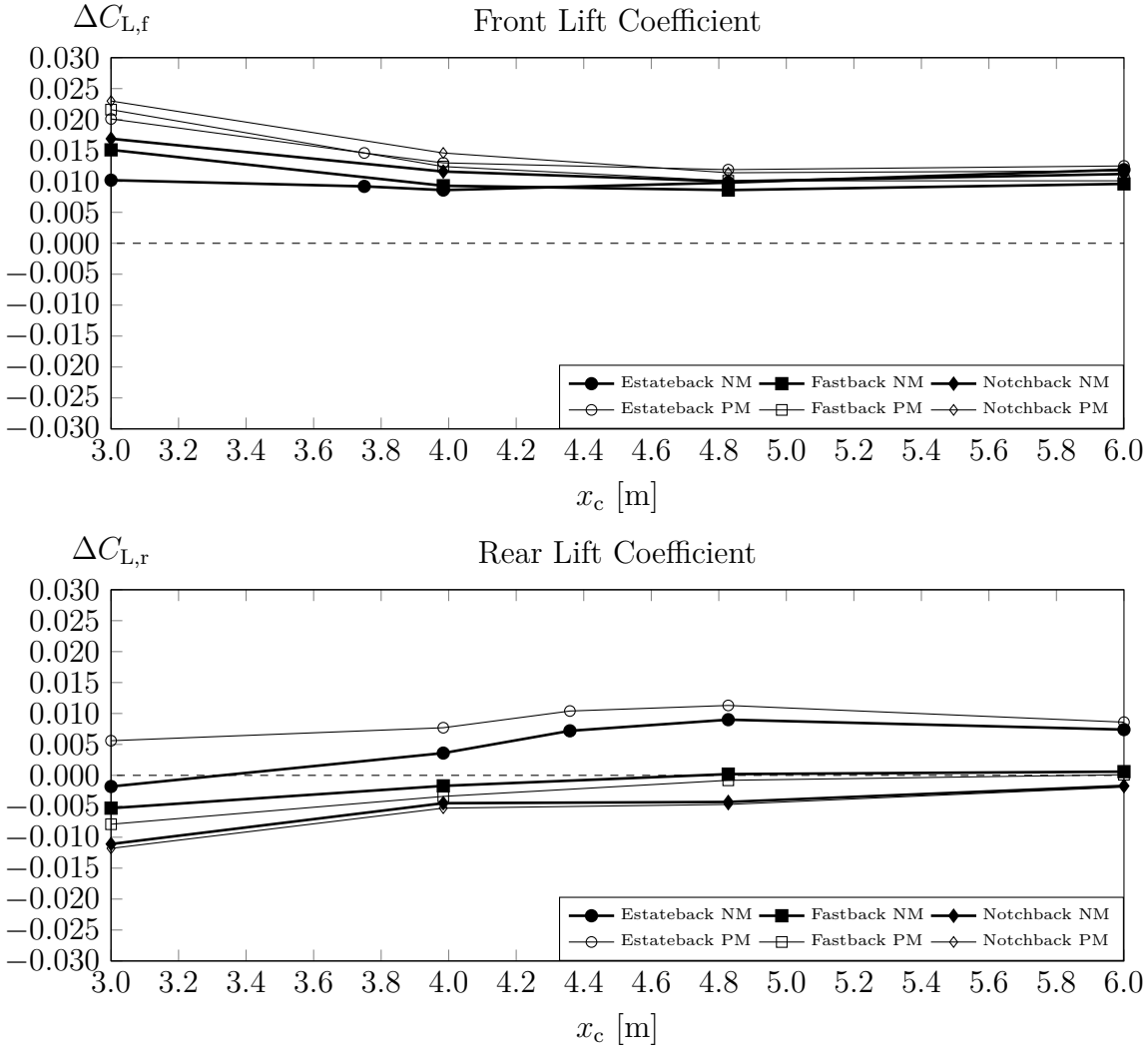

Figure A.8: Lift coefficients $\Delta C_{\mathrm{L,f}}$ and $\Delta C_{\mathrm{L,r}}$ for the DrivAer referring to open road conditions. The curves represent for different rear end shapes for a nozzle with $A_{\mathrm{N}} = 22.4\,\mathrm{m}^2$ and $A_{\mathrm{M}}/A_{\mathrm{N}} = 9.7\,\%$.

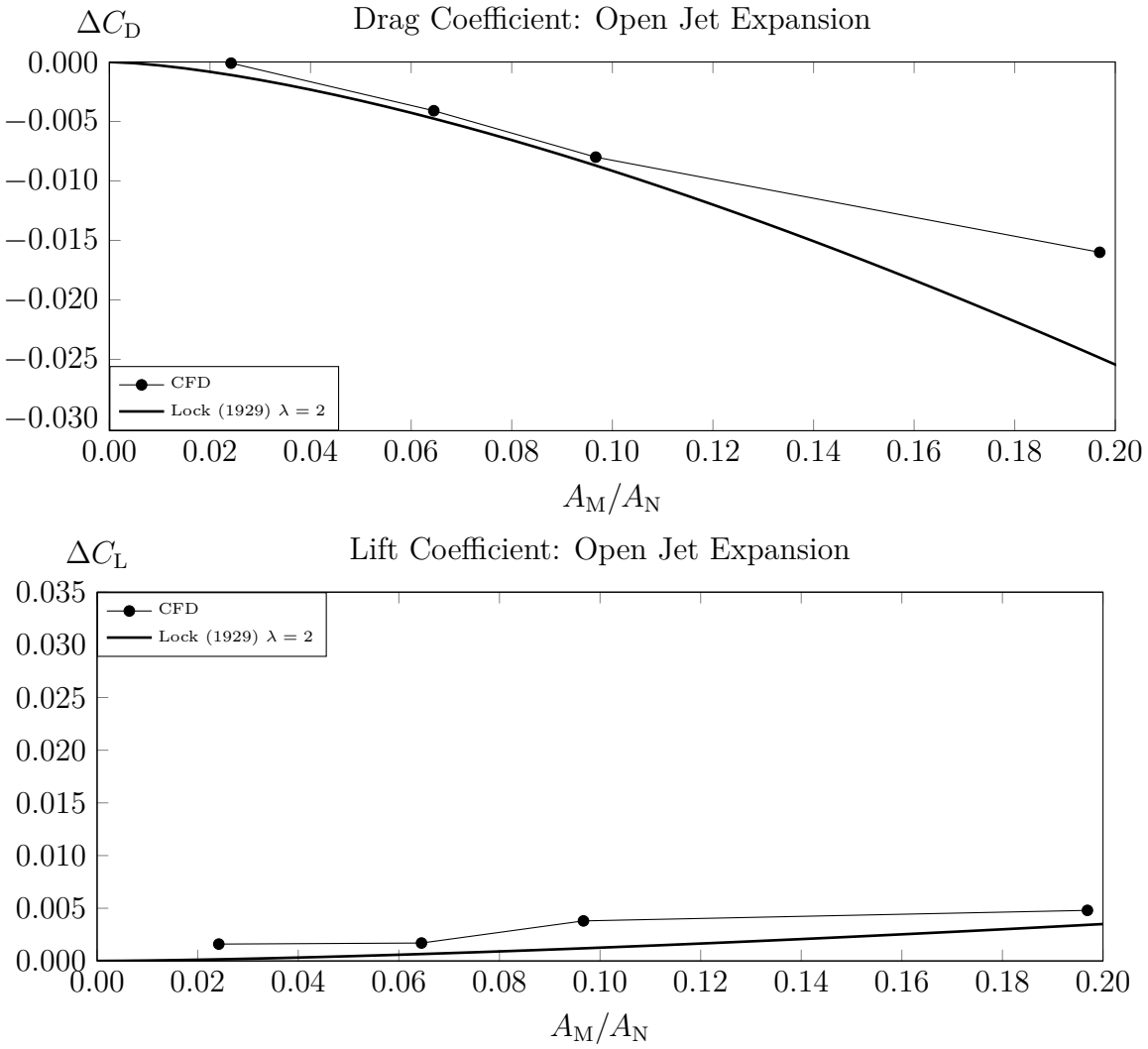

Figure A.9: Fastback: Effect of open jet expansion on drag ΔC_D and lift coefficient ΔC_L depending on the blockage ratio $A_\mathrm{M}/A_\mathrm{N}$. The curves denote the results from CFD and the classical correction from Lock (1929) using $\lambda = 2$ as proposed by Wickern (2014).

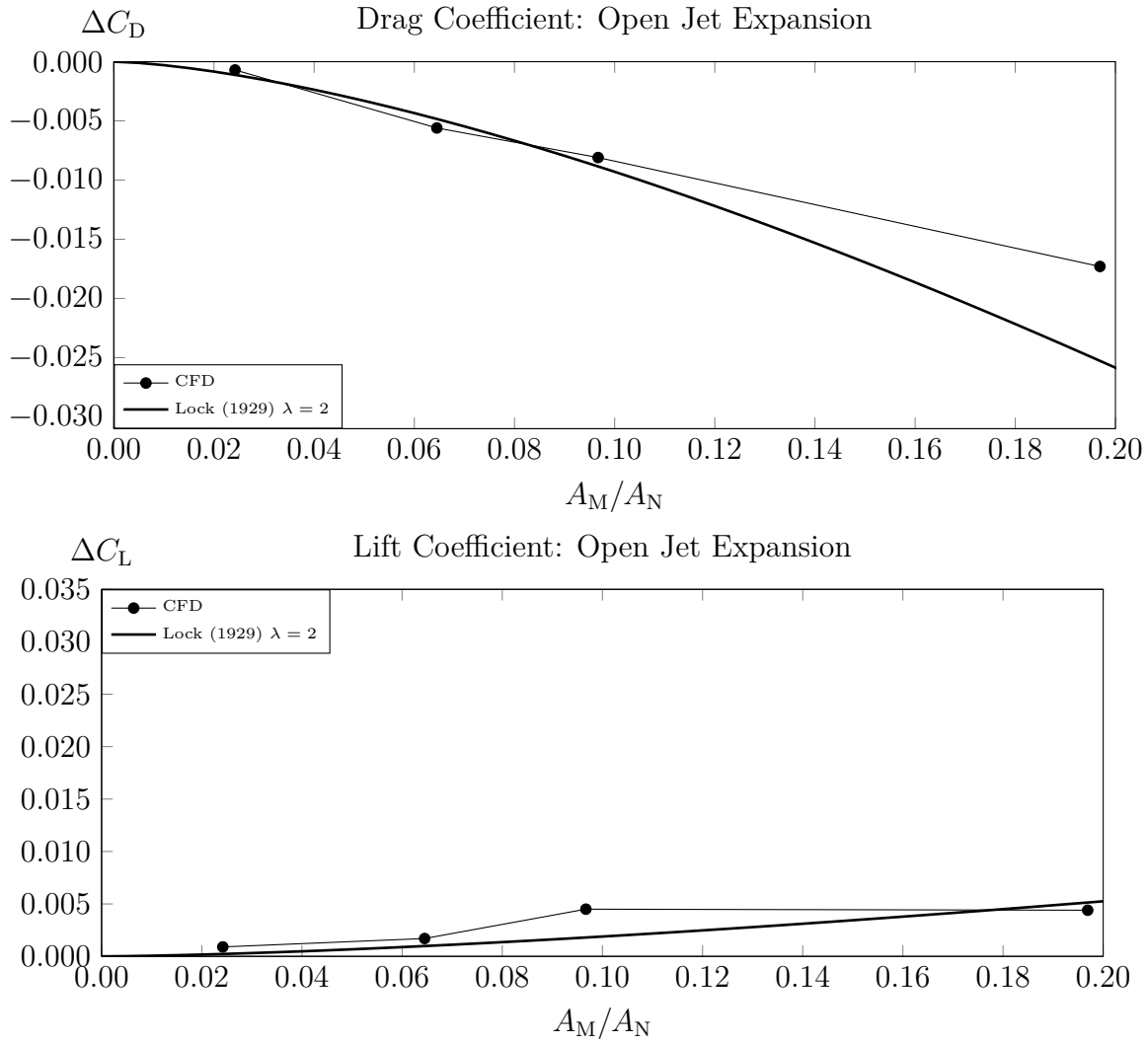

Figure A.10: Notchback: Effect of open jet expansion on drag ΔC_D and lift coefficient ΔC_L depending on the blockage ratio $A_\mathrm{M}/A_\mathrm{N}$. The curves denote the results from CFD and the classical correction from Lock (1929) using $\lambda = 2$ as proposed by Wickern (2014).

A.3.3 Collector Interferences

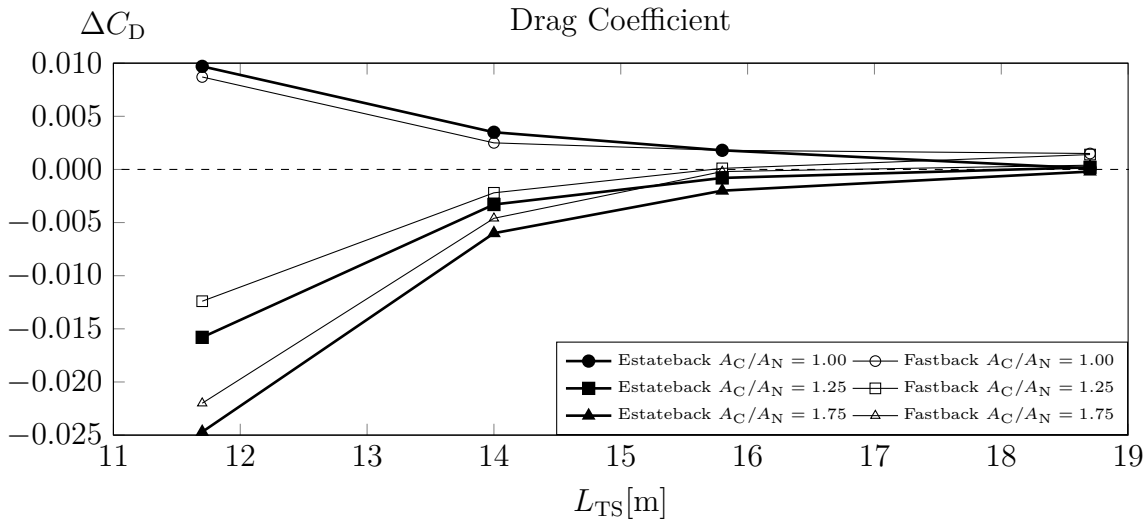

Figure A.11: Drag coefficient ΔC_D for the DrivAer with estateback and fastback referring to the half-infinite wind tunnel $A_\mathrm{N} = 22.4\,\mathrm{m}^2$ and $x_\mathrm{c} = 4.8\,\mathrm{m}$. The curves represent different test section lengths L_TS.

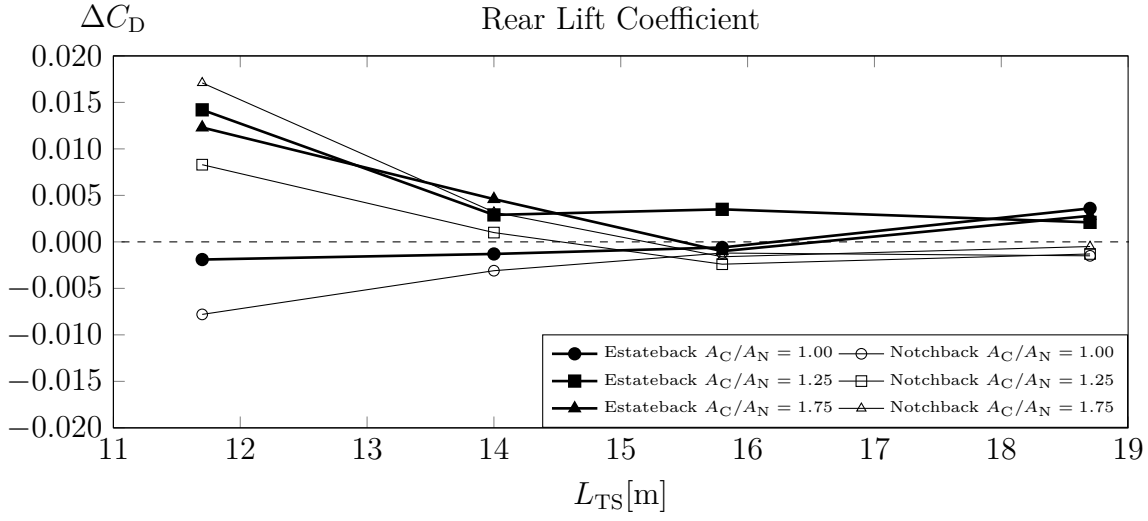

Figure A.12: Rear lift coefficient $\Delta C_\mathrm{L,r}$ for the DrivAer with estateback and fastback referring to the half-infinite wind tunnel $A_\mathrm{N} = 22.4\,\mathrm{m}^2$ and $x_\mathrm{c} = 4.8\,\mathrm{m}$. The curves represent different test section lengths L_TS.

A.4 MATLAB Scripts

A.4.1 Summation of Images for a Rectangular Tunnel

```
% Input
number_of_images            = 100;
height                      = 1;
width_to_height_ratio_min   = 0.01;
width_to_height_ratio_max   = 5.00;
width_to_height_ratio_step  = 0.01;

% Prepare Export
DATname_1                   = 'expansion_rectangular_chi_y.dat';
fileID_1                    = fopen(DATname_1,'w');
DATname_2                   = 'expansion_rectangular_chi_z.dat';
fileID_2                    = fopen(DATname_2,'w');
fprintf(fileID_1,'%f %f\r\n',0,pi);
fprintf(fileID_2,'%f %f\r\n',0,0);

% Run Loops for aspect ratios
for width_to_height_ratio = width_to_height_ratio_min : ...
    width_to_height_ratio_step : width_to_height_ratio_max

    width = width_to_height_ratio * height;
    % Initialize chi_y and chi_z
    chi_y = 0;
    chi_z = 0;

    % Outer loop for index m (columns)
    for m = -number_of_images : 1 : number_of_images
        % Inner loop for index n (rows)
        for n = -number_of_images : 1 : number_of_images
            chi_y = chi_y + (-1)^(m+n) * (1/2 - m)/((1/2 - m)^2 + (n * ...
                height / width)^2);
            chi_z = chi_z + (-1)^(m+n) * (1/2 - n)/((1/2 - n)^2 + (m / ...
                height * width)^2);
        end
    end

    fprintf(fileID_1,'%f %f\r\n',width_to_height_ratio,chi_y);
    fprintf(fileID_2,'%f %f\r\n',width_to_height_ratio,chi_z);

end

fclose(fileID_1);
fclose(fileID_2);
```

A.4.2 Expanded Jet Dimensions

```
% Input
model_area                        = 2*2.16585;
number_of_images                  = 100;
tunnel_width_to_height_ratio_psi = 0.7;
error_limit_psi                   = 0.005;
delta_step                        = 0.001;
blockage_ratio_psi_min            = 0.01;
blockage_ratio_psi_max            = 0.8;
blockage_ratio_psi_step           = 0.01;

% Calculate Global Variables
model_radius                      = sqrt( model_area / pi );

% Prepare Export
string_width_to_height_ratio_psi = ...
    strrep(num2str(tunnel_width_to_height_ratio_psi),'.','_');

DATname_1                         = ['expansion_rectangular_iteration_' ...
    string_width_to_height_ratio_psi '_width.dat'];
fileID_1                          = fopen(DATname_1,'w');

DATname_2                         = ['expansion_rectangular_iteration_' ...
    string_width_to_height_ratio_psi '_height.dat'];
fileID_2                          = fopen(DATname_2,'w');

DATname_3                         = ['expansion_rectangular_iteration_' ...
    string_width_to_height_ratio_psi '_width_to_height_ratio.dat'];
fileID_3                          = fopen(DATname_3,'w');

DATname_4                         = ['expansion_rectangular_iteration_' ...
    string_width_to_height_ratio_psi '_blockage_ratio.dat'];
fileID_4                          = fopen(DATname_4,'w');

fprintf(fileID_1,'%f %f\r\n',0,1);
fprintf(fileID_2,'%f %f\r\n',0,1);
fprintf(fileID_3,'%f %f\r\n',0,tunnel_width_to_height_ratio_psi);
fprintf(fileID_4,'%f %f\r\n',0,0);

% Run Blockage Loops
for blockage_ratio_psi = ...
    blockage_ratio_psi_min:blockage_ratio_psi_step:blockage_ratio_psi_max

    display(blockage_ratio_psi);

    % Calculate Tunnel Dimensions and Jet Boundary
    tunnel_area_psi    = model_area / blockage_ratio_psi;
    tunnel_height_psi  = sqrt( tunnel_area_psi / ...
        tunnel_width_to_height_ratio_psi );
    tunnel_width_psi   = tunnel_width_to_height_ratio_psi * ...
        tunnel_height_psi;
```

```
43      psi_jet_boundary_y = tunnel_width_psi^2 / 8;
44      psi_jet_boundary_z = tunnel_height_psi^2 / 8;
45
46      % Initialize Mirror Dimensions and Stream Function
47      tunnel_width       = tunnel_width_psi;
48      tunnel_height      = tunnel_height_psi;
49      delta_psi_y        = -1;
50
51      % Outer While Loop To Calculation Expandet Jet Dimensions at x = 0
52      while abs(delta_psi_y) > error_limit_psi
53
54          % Initialize psi to Calculate Width of Expanded Jet
55          psi  = 0;
56
57          % Inner Loop to Calculate Width of Expanded Jet
58          while psi < psi_jet_boundary_y
59
60              % Decide for Direction of Step y
61              if delta_psi_y < 0
62                  tunnel_width = tunnel_width + delta_step * 2;
63              else
64                  tunnel_width = tunnel_width - delta_step * 2;
65              end
66
67              % Initialize chi_y
68              chi_y   = 0;
69
70              % Outer For-Loop for Mirror Images in Columns (= y)
71              for m = -number_of_images:1:number_of_images
72
73                  % Inner For-Loop for Mirror Images in Rows (= z)
74                  for n = -number_of_images:1:number_of_images
75
76                      % Calculate Summations of chi_y
77                      chi_y = chi_y + (-1)^(m+n) * (1/2 - m)/((1/2 - m)^2 ...
                            + (n * tunnel_height / tunnel_width)^2);
78
79                  end
80
81              end
82
83              % Calculate the Stream Function at the Jet Boundary
84              psi = tunnel_width^2 / 8 - model_radius^3 * chi_y / 2 / ...
                    tunnel_width;
85
86          end
87
88          % Initialize psi to Calculate Height of Expanded Jet
89          psi  = 0;
90
91          % Inner Loop to Calculate Height of Expanded Jet
92          while psi < psi_jet_boundary_z
93
94              % Increase Tunnel Height by Step
```

```
95              tunnel_height = tunnel_height + delta_step * 2;
96
97              % Initialize chi_z
98              chi_z   = 0;
99
100             % Outer For-Loop for Mirror Images in Columns (= y)
101             for m = -number_of_images:1:number_of_images
102
103                 % Inner For-Loop for Mirror Images in Rows (= z)
104                 for n = -number_of_images:1:number_of_images
105
106                     % Calculate Summations of chi_y
107                     chi_z = chi_z + (-1)^(m+n) * (1/2 - n)/((1/2 - n)^2 ...
                            + (m / tunnel_height * tunnel_width)^2);
108
109                 end
110
111             end
112
113             % Calculate the Stream Function at the Jet Boundary
114             psi = tunnel_height^2 / 8 - model_radius^3 * chi_z / 2 / ...
                    tunnel_height;
115
116         end
117
118         % Initialize chi_y
119         chi_y   = 0;
120
121         % Outer For-Loop for Mirror Images in Columns (= y)
122         for m = -number_of_images:1:number_of_images
123
124             % Inner For-Loop for Mirror Images in Rows (= z)
125             for n = -number_of_images:1:number_of_images
126
127                 % Calculate Summations of chi_y
128                 chi_y = chi_y + (-1)^(m+n) * (1/2 - m)/((1/2 - m)^2 + ...
                        (n * tunnel_height / tunnel_width)^2);
129
130             end
131
132         end
133
134         % Re-Calculate the Stream Function with New Tunnel Height
135         psi         = tunnel_width^2 / 8 - model_radius^3 * chi_y / 2 / ...
                tunnel_width;
136
137         % Calculate Error in Psi at y-Jet Boundary
138         delta_psi_y = psi - psi_jet_boundary_y;
139
140     end
141
142     % Calculate Expansion Ratios
143     ratio_tunnel_width              = tunnel_width / tunnel_width_psi;
144     ratio_tunnel_height             = tunnel_height / tunnel_height_psi;
```

```
145     ratio_tunnel_area               = tunnel_width * tunnel_height / ...
            tunnel_width_psi / tunnel_height_psi;
146
147     % Calculate Expanded Tunnel Properties
148     tunnel_width_to_height_ratio    = tunnel_width / tunnel_height;
149     blockage_ratio                  = model_area / tunnel_width / ...
            tunnel_height;
150
151     % Write Results To Output File
152     fprintf(fileID_1,'%f %f\r\n',blockage_ratio_psi,ratio_tunnel_width);
153     fprintf(fileID_2,'%f %f\r\n',blockage_ratio_psi,ratio_tunnel_height);
154     fprintf(fileID_3,'%f ...
            %f\r\n',blockage_ratio_psi,tunnel_width_to_height_ratio);
155     fprintf(fileID_4,'%f %f\r\n',blockage_ratio_psi,blockage_ratio);
156 end
157
158 fclose(fileID_1);
159 fclose(fileID_2);
160 fclose(fileID_3);
161 fclose(fileID_4);
```

A.4.3 Integral Velocity

```
% Input
model_area                          = 2*2.16585;
number_of_images                    = 10;
tunnel_width_to_height_ratio_psi = 1.05;
error_limit_psi                     = 0.005;
delta_step                          = 0.001;
blockage_ratio_psi_min              = 0.01;
blockage_ratio_psi_max              = 0.3;
blockage_ratio_psi_step             = 0.01;
delta_phi                           = pi/2/90;
delta_theta                         = pi/2/90;
lambda                              = 3.5;

% Calculate Global Variables
model_radius                        = sqrt( model_area / pi );

% Prepare Export
string_width_to_height_ratio_psi = ...
    strrep(num2str(tunnel_width_to_height_ratio_psi),'.','_');
string_lambda                       = strrep(num2str(lambda),'.','_');

DATname_1                           = ['lambda_' string_lambda '_W_H_' ...
    string_width_to_height_ratio_psi '_width.dat'];
fileID_1                            = fopen(DATname_1,'w');

DATname_2                           = ['lambda_' string_lambda '_W_H_' ...
    string_width_to_height_ratio_psi '_height.dat'];
fileID_2                            = fopen(DATname_2,'w');

DATname_3                           = ['lambda_' string_lambda '_W_H_' ...
    string_width_to_height_ratio_psi '_width_to_height_ratio.dat'];
fileID_3                            = fopen(DATname_3,'w');

DATname_4                           = ['lambda_' string_lambda '_W_H_' ...
    string_width_to_height_ratio_psi '_blockage_ratio.dat'];
fileID_4                            = fopen(DATname_4,'w');

DATname_5                           = ['lambda_' string_lambda '_W_H_' ...
    string_width_to_height_ratio_psi '_q_correction_x.dat'];
fileID_5                            = fopen(DATname_5,'w');

DATname_6                           = ['lambda_' string_lambda '_W_H_' ...
    string_width_to_height_ratio_psi '_q_correction_y.dat'];
fileID_6                            = fopen(DATname_6,'w');

DATname_7                           = ['lambda_' string_lambda '_W_H_' ...
    string_width_to_height_ratio_psi '_q_correction_z.dat'];
fileID_7                            = fopen(DATname_7,'w');

```

```
42 DATname_8                          = ['lambda_' string_lambda '_W_H_' ...
       string_width_to_height_ratio_psi '_q_correction.dat'];
43 fileID_8                          = fopen(DATname_8,'w');
44
45 fprintf(fileID_1,'%f %f\r\n',0,1);
46 fprintf(fileID_2,'%f %f\r\n',0,1);
47 fprintf(fileID_3,'%f %f\r\n',0,tunnel_width_to_height_ratio_psi);
48 fprintf(fileID_4,'%f %f\r\n',0,0);
49 fprintf(fileID_5,'%f %f\r\n',0,1);
50 fprintf(fileID_6,'%f %f\r\n',0,1);
51 fprintf(fileID_7,'%f %f\r\n',0,1);
52 fprintf(fileID_8,'%f %f\r\n',0,1);
53
54 % Declare Variables
55
56
57 % Run Blockage Loops
58 for blockage_ratio_psi = ...
       blockage_ratio_psi_min:blockage_ratio_psi_step:blockage_ratio_psi_max
59
60     display(blockage_ratio_psi);
61
62     % Calculate Tunnel Dimensions and Jet Boundary
63     tunnel_area_psi    = model_area / blockage_ratio_psi;
64     tunnel_height_psi  = sqrt( tunnel_area_psi / ...
           tunnel_width_to_height_ratio_psi );
65     tunnel_width_psi   = tunnel_width_to_height_ratio_psi * ...
           tunnel_height_psi;
66     psi_jet_boundary_y = tunnel_width_psi^2 / 8;
67     psi_jet_boundary_z = tunnel_height_psi^2 / 8;
68
69     % Initialize Mirror Dimensions and Stream Function
70     tunnel_width       = tunnel_width_psi;
71     tunnel_height      = tunnel_height_psi;
72     delta_psi_y        = -1;
73
74     % Outer While Loop To Calculation Expandet Jet Dimensions at x = 0
75     while abs(delta_psi_y) > error_limit_psi
76
77         % Initialize psi to Calculate Width of Expanded Jet
78         psi  = 0;
79
80         % Inner Loop to Calculate Width of Expanded Jet
81         while psi < psi_jet_boundary_y
82
83             % Decide for Direction of Step y
84             if delta_psi_y < 0
85                 tunnel_width = tunnel_width + delta_step * 2;
86             else
87                 tunnel_width = tunnel_width - delta_step * 2;
88             end
89
90             % Initialize chi_y
91             chi_y   = 0;
```

```
92
93              % Outer For-Loop for Mirror Images in Columns (= y)
94              for m = -number_of_images:1:number_of_images
95
96                  % Inner For-Loop for Mirror Images in Rows (= z)
97                  for n = -number_of_images:1:number_of_images
98
99                      % Calculate Summations of chi_y
100                     chi_y = chi_y + (-1)^(m+n) * (1/2 - m)/((1/2 - m)^2 ...
                            + (n * tunnel_height / tunnel_width)^2);
101
102                 end
103
104             end
105
106             % Calculate the Stream Function at the Jet Boundary
107             psi = tunnel_width^2 / 8 - model_radius^3 * chi_y / 2 / ...
                    tunnel_width;
108
109         end
110
111         % Initialize psi to Calculate Height of Expanded Jet
112         psi  = 0;
113
114         % Inner Loop to Calculate Height of Expanded Jet
115         while psi < psi_jet_boundary_z
116
117             % Increase Tunnel Height by Step
118             tunnel_height = tunnel_height + delta_step * 2;
119
120             % Initialize chi_z
121             chi_z   = 0;
122
123             % Outer For-Loop for Mirror Images in Columns (= y)
124             for m = -number_of_images:1:number_of_images
125
126                 % Inner For-Loop for Mirror Images in Rows (= z)
127                 for n = -number_of_images:1:number_of_images
128
129                     % Calculate Summations of chi_y
130                     chi_z = chi_z + (-1)^(m+n) * (1/2 - n)/((1/2 - n)^2 ...
                            + (m / tunnel_height * tunnel_width)^2);
131
132                 end
133
134             end
135
136             % Calculate the Stream Function at the Jet Boundary
137             psi = tunnel_height^2 / 8 - model_radius^3 * chi_z / 2 / ...
                    tunnel_height;
138
139         end
140
141         % Initialize chi_y
```

```
142         chi_y   = 0;
143
144         % Outer For-Loop for Mirror Images in Columns (= y)
145         for m = -number_of_images:1:number_of_images
146
147             % Inner For-Loop for Mirror Images in Rows (= z)
148             for n = -number_of_images:1:number_of_images
149
150                 % Calculate Summations of chi_y
151                 chi_y = chi_y + (-1)^(m+n) * (1/2 - m)/((1/2 - m)^2 + ...
                        (n * tunnel_height / tunnel_width)^2);
152
153             end
154
155         end
156
157         % Re-Calculate the Stream Function with New Tunnel Height
158         psi         = tunnel_width^2 / 8 - model_radius^3 * chi_y / 2 / ...
                    tunnel_width;
159
160         % Calculate Error in Psi at y-Jet Boundary
161         delta_psi_y = psi - psi_jet_boundary_y;
162
163     end
164
165     % Calculate Expansion Ratios
166     ratio_tunnel_width              = tunnel_width / tunnel_width_psi;
167     ratio_tunnel_height             = tunnel_height / tunnel_height_psi;
168     ratio_tunnel_area               = tunnel_width * tunnel_height / ...
            tunnel_width_psi / tunnel_height_psi;
169
170     % Calculate Expanded Tunnel Properties
171     tunnel_width_to_height_ratio    = tunnel_width / tunnel_height;
172     blockage_ratio                  = model_area / tunnel_width / ...
            tunnel_height;
173
174     % Write Results To Output File
175     fprintf(fileID_1,'%f %f\r\n',blockage_ratio_psi,ratio_tunnel_width);
176     fprintf(fileID_2,'%f %f\r\n',blockage_ratio_psi,ratio_tunnel_height);
177     fprintf(fileID_3,'%f ...
            %f\r\n',blockage_ratio_psi,tunnel_width_to_height_ratio);
178     fprintf(fileID_4,'%f %f\r\n',blockage_ratio_psi,blockage_ratio);
179
180     delta_u_x = 0;
181     delta_u_y = 0;
182     delta_u_z = 0;
183     A_sum     = 0;
184     A_x_sum   = 0;
185     A_y_sum   = 0;
186     A_z_sum   = 0;
187
188     % Integration of velocity by mirror images over sphere surface
189     % Outer loop for theta
190     for theta=delta_theta/2:delta_theta:pi/2- delta_theta/2;
```

```
191
192         % Inner loop for phi
193         for phi=delta_phi/2:delta_phi:pi/2-delta_phi/2;
194
195             % Calculation of cartesian coordinates from polar coordinates
196             x       = model_radius * sin(theta) * sin(phi);
197             y       = model_radius * sin(theta) * cos(phi);
198             z       = model_radius * cos(theta);
199
200             % Integration of the surface area
201             delta_A = model_radius^2 * sin(theta) * delta_phi * ...
                    delta_theta;
202             A_sum   = A_sum + delta_A / (pi / 2 * model_radius^2);
203             A_x_sum = A_x_sum + delta_A * x / (pi / 4 * model_radius^2) ...
                    / model_radius;
204             A_y_sum = A_y_sum + delta_A * y / (pi / 4 * model_radius^2) ...
                    / model_radius;
205             A_z_sum = A_z_sum + delta_A * z / (pi / 4 * model_radius^2) ...
                    / model_radius;
206
207             % Initialize velocity
208             chi_x = 0;
209             chi_y = 0;
210             chi_z = 0;
211
212             % Outer For-Loop for Mirror Images in Columns (= y)
213             for m = -number_of_images:1:number_of_images
214                 % Inner For-Loop for Mirror Images in Rows (= z)
215                 for n = -number_of_images:1:number_of_images
216                     % Exclude the model itself: m=0, n=0
217
218                         % Calculate Summations of chi_y
219                     chi_x     = chi_x + (-1)^(m+n) * ( ...
                            (y-m*tunnel_width)^2 + (z-n*tunnel_height)^2 - 2 ...
                            * x^2 ) / (( x^2 + (y-m*tunnel_width)^2 + ...
                            (z-n*tunnel_height)^2 )^2.5);
220                     chi_y     = chi_y + (-1)^(m+n) * ( x * ...
                            (y-m*tunnel_width) ) / (( x^2 + ...
                            (y-m*tunnel_width)^2 + (z-n*tunnel_height)^2 )^2.5);
221                     chi_z     = chi_z + (-1)^(m+n) * ( x * ...
                            (z-n*tunnel_height) ) / (( x^2 + ...
                            (y-m*tunnel_width)^2 + (z-n*tunnel_height)^2 )^2.5);
222                     if (m==0) && (n==0)
223                         u_c_x = 1 + model_radius^3 / 2 * (-1)^(m+n) * ( ...
                                (y-m*tunnel_width)^2 + (z-n*tunnel_height)^2 ...
                                - 2 * x^2 ) / (( x^2 + (y-m*tunnel_width)^2 ...
                                + (z-n*tunnel_height)^2 )^2.5);
224                         u_c_y = - 1 * model_radius^3 * 3 / 2 ...
                                *(-1)^(m+n) * ( x * (y-m*tunnel_width) ) / ...
                                (( x^2 + (y-m*tunnel_width)^2 + ...
                                (z-n*tunnel_height)^2 )^2.5);
225                         u_c_z = - 1 * model_radius^3 * 3 / 2 ...
                                *(-1)^(m+n) * ( x * (z-n*tunnel_height) ) / ...
```

```
                                (( x^2 + (y-m*tunnel_width)^2 + ...
                                (z-n*tunnel_height)^2 )^2.5);
226                         end
227                     end
228                 end
229                 u_x       = 1 + model_radius^3 / 2 * chi_x;
230                 u_y       = - 1 * model_radius^3 * 3 / 2 * chi_y;
231                 u_z       = - 1 * model_radius^3 * 3 / 2 * chi_z;
232                 u         = sqrt( u_x^2 + u_y^2 + u_z^2 );
233                 u_c       = sqrt( u_c_x^2 + u_c_y^2 + u_c_z^2 );
234                 delta_u   = u - u_c;
235                 delta_u_x  = delta_u_x + delta_A * x / (pi / 4 * ...
                       model_radius^2) / model_radius * delta_u;
236                 delta_u_y  = delta_u_y + delta_A * y / (pi / 4 * ...
                       model_radius^2) / model_radius * delta_u;
237                 delta_u_z  = delta_u_z + delta_A * z / (pi / 4 * ...
                       model_radius^2) / model_radius * delta_u;
238
239             end
240         end
241         q_corr_x = (delta_u_x * lambda + 1)^2;
242         q_corr_y = (delta_u_y * lambda + 1)^2;
243         q_corr_z = (delta_u_z * lambda + 1)^2;
244         fprintf(fileID_5,'%f %f\r\n',blockage_ratio_psi, 1/q_corr_x);
245         fprintf(fileID_6,'%f %f\r\n',blockage_ratio_psi, 1/q_corr_y);
246         fprintf(fileID_7,'%f %f\r\n',blockage_ratio_psi, 1/q_corr_z);
247
248 end
249
250 fclose(fileID_1);
251 fclose(fileID_2);
252 fclose(fileID_3);
253 fclose(fileID_4);
254 fclose(fileID_5);
255 fclose(fileID_6);
256 fclose(fileID_7);
257 fclose(fileID_8);
```

A.5 Potential Flow Equations

Table A.3: Potential flow equations for parallel flow as well as for source/sink and dipole singularities in two dimensions

	$u_\mathrm{x}(x,y)$	$u_\mathrm{y}(x,y)$	$\Phi(x,y)$	$\Psi(x,y)$
parallel flow	u_∞	0	$u_\infty x$	$u_\infty y$
source sink	$\frac{Q}{2\pi}\frac{x}{x^2+y^2}$	$\frac{Q}{2\pi}\frac{x}{x^2+y^2}$	$\frac{Q}{2\pi}\ln\sqrt{x^2+y^2}$	$\frac{Q}{2\pi}\arctan\left(\frac{y}{x}\right)$
dipole	$-\frac{M}{2\pi}\frac{x^2-y^2}{(x^2+y^2)^2}$	$-\frac{M}{2\pi}\frac{2xy}{(x^2+y^2)^2}$	$\frac{M}{2\pi}\frac{x}{x^2+y^2}$	$-\frac{M}{2\pi}\frac{y}{x^2+y^2}$

Table A.4: Potential flow equations for parallel flow as well as for source/sink and dipole singularities in three dimensions

	$u_\mathrm{x}(x,y,z)$ $u_\mathrm{x}(x,r)$	$u_\mathrm{r}(x,y,z)$ $u_\mathrm{r}(x,r)$	$\Phi(x,y,z)$ $\Phi(x,r)$	$\Psi(x,y,z)$ $\Psi(x,r)$
parallel flow	u_∞	0	$u_\infty x$	$\frac{1}{2}u_\infty(y^2+z^2)$
	u_∞	0	$u_\infty x$	$\frac{1}{2}u_\infty r^2$
source sink	$\frac{Q}{4\pi}\frac{x}{(x^2+y^2+z^2)^{3/2}}$	$\frac{Q}{4\pi}\frac{(y^2+z^2)^{1/2}}{(x^2+y^2+z^2)^{3/2}}$	$-\frac{Q}{4\pi}\frac{1}{(x^2+y^2+z^2)^{1/2}}$	$-\frac{Q}{4\pi}\frac{x}{(x^2+y^2+z^2)^{1/2}}$
	$\frac{Q}{4\pi}\frac{x}{(x^2+r^2)^{3/2}}$	$\frac{Q}{4\pi}\frac{r}{(x^2+r^2)^{3/2}}$	$-\frac{Q}{4\pi}\frac{1}{(x^2+r^2)^{1/2}}$	$-\frac{Q}{4\pi}\frac{x}{(x^2+r^2)^{1/2}}$
dipole	$\frac{M}{4\pi}\frac{1-3\frac{x^2}{x^2+y^2+z^2}}{(x^2+y^2+z^2)^{3/2}}$	$-\frac{3M}{4\pi}\frac{x\,(y^2+z^2)^{1/2}}{(x^2+y^2+z^2)^{5/2}}$	$\frac{M}{4\pi}\frac{x}{(x^2+y^2+z^2)^{3/2}}$	$-\frac{M}{4\pi}\frac{y^2+z^2}{(x^2+y^2+z^2)^{3/2}}$
	$\frac{M}{4\pi}\frac{1-3\frac{x^2}{x^2+r^2}}{(x^2+r^2)^{3/2}}$	$-\frac{3M}{4\pi}\frac{xr}{(x^2+r^2)^{5/2}}$	$\frac{M}{4\pi}\frac{x}{(x^2+r^2)^{3/2}}$	$-\frac{M}{4\pi}\frac{r^2}{(x^2+r^2)^{3/2}}$